High-resolution, space spectropolarimeters for a wide ultra-violet range : design and tests

Maëlle Le Gal

PSL
UNIVERSITÉ PARIS

THÈSE DE DOCTORAT
DE L'UNIVERSITÉ PSL

Préparée à l'Observatoire de Paris

Spectropolarimètres spatiaux haute résolution pour un grand domaine ultra-violet: conceptions et tests

Soutenue par
Maëlle Le Gal
Le 3 Septembre 2021

École doctorale n°127
Ecole Doctorale Astronomie et Astrophysique d'Ile de France

Spécialité
Astronomie et astrophysique

Composition du jury :

Claude Catala Directeur de recherche, LESIA	*Président du Jury*
Frans Snik Professeur adjoint, Université de Leiden	*Rapporteur*
Marianne Faurobert Professeure, Université Côte d'Azur	*Rapporteure*
Yael Nazé Chargée de recherche, Université de Liège	*Membre du Jury*
Frank Brachet Ingénieur docteur, CNES	*Membre du Jury*
Coralie Neiner Directrice de recherche, LESIA	*Directrice de thèse*
Martin Pertenais Ingénieur docteur, DLR	*Directeur de thèse*
Arturo López Ariste Directeur de recherche, IRAP	*Invité*
Norbert Champion Ingénieur de recherche, LERMA	*Invité*

l'Observatoire de Paris | PSL

High-resolution, space spectropolarimeters for a wide ultra-violet range: design and tests

Acknowledgment

First, I would like to acknowledge my supervisors, Coralie Neiner and Martin Pertenais, for directing my PhD studies and for carefully reviewing this thesis manuscript. Thank you for helping me during these 4 years.

I would also like to thank Frans Snik, Marianne Faurobert, Claude Catala, Yael Nazé and Frank Brachet, for agreeing to be part of my PhD thesis jury. Thank you for taking the time to read this manuscript. Thanks to Arturo López Ariste and Norbert Champion to be part of this journey as well.

In addition, I would like to thank Arturo López Ariste for collaborating extensively with me on reflection polarimeters. Thank you for welcoming me many times in Toulouse and for helping me to understand many of the problems related to polarimetry.
I am particularly grateful to Norbert Champion for spending a lot of time (months!) on the optical transmission polarimeter experiment with me. Thanks also to Lydia Tchang-Brillet for letting me use the UV spectrometer for the time necessary for my thesis (which was much longer than expected).
Thank you to Jean-François Mariscal for having hosted me at LATMOS part-time for a few years in order to carry out the reflection polarimeter experiment.
I would also like to show my gratitude to Juan Larruquert for providing me with the optical indices I needed, and for welcoming me in his laboratory to show me his UV facilities. Moreover, I would like to thank Avi Bendavid and Philip Martin from CSIRO and REOSC for lending me material samples to test with my experiments.
Special thank you to Frank Brachet, referent of my thesis at CNES, for following my thesis with attention. Thanks to CNES for financing this thesis.
Many thanks to Marion Bonafous and Jean-Michel Reess for their advices and help on the optical experiments, and thanks to Jérome Parisot and Cyrille Blanchard for the ones on the thermal and vacuum chambers.
I would also like to sincerely thank Youssef Younes and Jean-Philippe Amans for designing the mechanical benches for my experiments, and Claude Collin and Vartan Arslanyan for building them. Thanks to Napoleon Nguyen Tuong for studying the impact of the mounts

during thermal cycles, and for the help on the mechanical benchs.
Thanks to Matthieu Louvel de Monceau, Hanna Lahmar, and Emilien Denoual for having worked with me on problems related to UV polarimeters during their internships in our team.
Many thanks to Aurélien Bour and Pierre Baudoz for taking the time to test my plates using a Shack-Hartmann. Thanks also to Pierre Baudoz for the discussions on the interpretation of the interference fringes.
Additional thanks go to Manuel Ortiz, Moustapha Dekkali, and Daniel Dias for their advices and the realization of the vacuum passages for the electric cables of the motors of my experiments.
I also want to mention here Constance Imad for managing all the administration of my thesis, and Goran Greblo and Sudagar Vassin for solving all my computer problems.

On a more personal level, I would like to thank all the people of LESIA and in particular all the persons of building 10 for the moments and laughs shared together. Also, I would like to thank all the people of LATMOS for welcoming me with open arms.
My personal thanks for supporting me these last years go to my family and all my amazing friends. Special thanks to Hélène, Lucie, and Arielle who have been there every day. And last but not least, thanks for literally everything to Julien, without who I would not have done it.

Acronyms

Au	Gold
B_4C	Boron carbide
CaF_2	Calcium fluoride
CLASP	Chromospheric Lyman-Alpha Spectro-Polarimeter
CNES	Centre Natinal d'Etudes Spatiales
D2 or ^2H	Deuterium
DOP	Degree of polarisation
ELT	Extremely Large Telescope
ESA	European Space Agency
ESPaDOnS	Echelle SpectroPolarimetric Device for the ObservatioN of Stars
FUV	Far UltraViolet
H2D2	high-end deuterium lamp
IRAP	Institut de Recherche en Astrophysique et Planétologie
LAM	Laboratoire d'Astrophysique de Marseille
LESIA	Laboratoire d'Etudes Spatiales et d'Instrumentation en Astrophysique
LiF	Lithium Fluoride
LUVOIR	Large Ultraviolet Optical InfraRed surveyor
MICADO	Multi-AO Imaging Camera for Deep Observations
MIDEX	Medium-Class Explorers Missions
MgF_2	Magnesium Fluroide
MUV	Mid UltraViolet
NASA	National Aeronautics and Space Administration
NUV	Near UltraViolet
Pt	Platinium
R&T	Research and Technology
SiC	Silicon carbide
SiO_2	Silicon dioxide
SNR	Signal to Noise Ratio
ta-C	Tetrahedral amorphous Carbon
TRL	Technical Readiness Level
UV	UltraViolet
WUPPE	Wisconsin Ultraviolet Photo-Polarimeter Experiment

Summary

Several space mission projects, such as LUVOIR, Arago, PolStar, and CASSTOR, plan to use a spectropolarimeter operating in the ultraviolet (UV) range. The main goals of these instruments is the study of stars and their environments, in particular their magnetic fields and magnetospheres, as well as the interstellar medium and exoplanets. However, high-resolution spectropolarimeters operating over a wide spectral range only exist on instruments on Earth and in the visible or infrared wavelength ranges.
The work carried out in this thesis aims at studying prototype polarimeters in order to design and optimize them over the wavelengths of interest. Several wavelength ranges were considered, depending on the studied instruments, between 90 and 400 nm. Two prototypes were studied: one using birefringent materials and operating by transmission, and one operating exclusively by reflection. An optimization method was developed to maximize the efficiency of the polarimeters for the chosen wavelength ranges. The performance is evaluated considering both the transmission, a real challenge in the UV, and the polarimetric efficiencies. Some polarimeters have been designed with this optimization method for specific missions. Finally, three experiments were set up to test these two prototypes optically and thermally. Two experiments were designed to test the transmission polarimeter. First, it was tested in the UV and in vacuum in order to measure the polarimetric efficiencies of the prototype under its operating conditions. This experiment was subject to many technical difficulties, and real experimental expertise was gained in these wavelength ranges. This experiment does not allow us to conclude about the exact performance of the polarimeter, but it has allowed us to pinpoint many of the technical issues that will arise in the design of such an instrument. By considering all these topics, a future experiment will be able to better test the polarimeter. Then, examples of the modulator used in this polarimeter underwent a series of thermal cycles to study the resistance of molecular bonding of its plates. Indeed, molecular bonding of birefringent materials is fragile due to the anisotropic expansion of the materials with temperature. These tests showed that a vast majority of the studied prototypes resisted temperature variations well, but some bonding broke. The results do not seem correlated with the parameters of the samples and indicate a high dependence of the bonding strength on the manufacturing conditions. Some studies of the strength of molecular bonding are underway and further work should focus on optimizing and reproducing the bonding conditions to strengthen the bonding.
Finally, the third experiment tests a prototype by reflection using gold mirrors. This exper-

iment also allows us to measure the polarimetric properties of some materials foreseen for such polarimeters and thus better simulate the studied polarimeters. The experiment has so far only been carried out in the visible range, but it has been designed to be inserted later into a vacuum tank in order to conduct UV tests. The alignment of the prototype by reflection has been identified as a real technical challenge that will require careful attention in the future to improve the performances of this prototype.
The methods used to optimize and design the polarimeters as well as the experiments carried out and their results are presented in this thesis.

Résumé

Plusieurs projets de missions spatiales, tels que LUVOIR, Arago, PolStar ou CASSTOR, prévoient l'utilisation d'un spectropolarimètre fonctionnant dans le domaine de l'ultra-violet (UV). Parmi les objectifs principaux de ces instruments on trouve l'étude des étoiles et leurs environnements, en particulier leurs champs magnétiques et leurs magnétosphères, ainsi que le milieu interstellaire et les exoplanètes. Cependant, les spectropolarimètres haute résolution fonctionnant sur une large gamme spectrale n'existent que sur des instruments sur Terre et dans le domaine des longueurs d'onde visibles ou infrarouges.
Le travail réalisé au cours de cette thèse vise à étudier des prototypes de polarimètres afin de les concevoir et de les optimiser sur les longueurs d'onde UV d'intérêt. Plusieurs gammes de longueurs d'onde ont été considérées, en fonction des instruments étudiés, entre 90 et 400 nm. Deux prototypes de polarimètres ont été étudiés : un prototype utilisant des matériaux biréfringents et fonctionnant par transmission et un prototype fonctionnant exclusivement par réflexion. Une méthode d'optimisation a été développée pour maximiser l'efficacité des polarimètres pour les gammes de longueurs d'onde choisies. La performance est évaluée en prenant en compte la transmission, véritable challenge de l'UV, ainsi que l'efficacité polarimétrique. Quelques polarimètres ont été conçus avec cette méthode d'optimisation pour des missions spécifiques. Enfin, trois expériences ont été mises en place pour tester ces deux prototypes sur les plans optique et thermique.
Deux expériences ont été conçues pour tester le polarimètre par transmission. Tout d'abord, il a été testé dans l'UV et sous vide afin de mesurer l'efficacité du prototype dans ses conditions de fonctionnement. De nombreux problèmes techniques sont venus compliqués cette expérience, et une réelle expertise expérimentale a été acquise sur les expériences dans ces domaines de longueur d'onde. Cette expérience ne permet pas de conclure quant aux performances exactes du polarimètre mais a permis d'identifier de nombreuses questions techniques qui se présenteront dans la conception d'un tel instrument. En prenant en compte tous ces sujets, une prochaine expérience pourra permettre de mieux tester le polarimètre. Ensuite, des exemplaires du modulateur utilisé dans ce polarimètre ont été soumis à une série de cycles thermiques pour étudier la résistance de l'adhésion moléculaire de ses lames. En effet, l'adhésion moléculaire de matériaux biréfringents est fragile en raison de l'expansion anisotropique des matériaux avec la température. Ces tests ont montré qu'une grande majorité des exemplaires étudiés résistaient bien aux variations de température, mais certaines adhésions ont rompu. Les résultats ne semblent pas corrélés avec les paramètres des exem-

plaires et indiquent une grande dépendance de la résistance de l'adhésion à ses conditions de fabrication. Quelques études de résistance de l'adhésion moléculaire sont en cours et la suite de ce travail devra se concentrer sur l'optimisation et la reproductibilité des conditions d'adhésion pour son renforcement.
Enfin, la troisième expérience permet de tester un prototype par réflexion utilisant des miroirs en or. Cette expérience permet également de mesurer les propriétés polarimétriques de certains matériaux pressentis pour de tels polarimètres par réflexion et ainsi mieux simuler les polarimètres étudiés. L'expérience n'a pour l'instant pu être réalisée que dans le visible mais a été conçue pour être par la suite insérée dans une cuve sous vide afin de faire des tests dans l'UV. L'alignement du prototype par réflexion a été identifié comme un véritable challenge technique qui nécessitera une grande attention dans le futur pour améliorer les performances de ce prototype.
Les méthodes utilisées pour l'étude et la conception des polarimètres ainsi que les expériences réalisées et leurs résultats sont présentés dans cette thèse.

Contents

List of Figures

Chapter 1

Introduction to polarimetry

The history of polarization began in 1669 when Erasmus Bartholinus first observed an image duplicated by an Iceland spar [2]. This is the first known observation of what is now called birefringence (see Section 1.2.1). Huygens described this phenomenon and proposed an explanation of what would be called polarized light in 1678 [20]. It was not until Malus, in 1808, that further work was done on this subject [36]. He observed the light reflected on the windows of the Luxembourg Palace and used an Iceland spar to see it fade with the rotation of the crystal. He had just discovered the polarization of light by reflection. He officially introduced the term "polarized light". In 1811, Arago built the first device to determine whether light is polarized: a polariscope [1]. In 1812, Brewster studied the light reflected by glass as a function of its incidence angle [5]. He observed that there was an angle of incidence for which he was able to extinguish the light with an Iceland spar and succeeded in establishing the relationship between the two: this is what is known today as the Brewster angle (see Section 1.2.3) [34]. Polarimetry was then extensively studied in the 19th century, and became a useful tool in the 20th century, in particular in astronomy and chemistry.

This Chapter is an introduction to polarization and polarimetry. Polarization is first described, then the conventions used along this thesis are defined in Section 1.1. Some useful components to study polarization are introduced in Section 1.2. Finally, methods and tools to design polarimeters are presented in Section 1.3.

1.1 Polarization

This Section defines the notion of polarization. It is mainly based on [45].

1.1.1 Definition

Light can be considered as an electromagnetic wave. It is composed of an electric field E and a magnetic field B, vibrating orthogonally to light propagation axis. The direction of vibration of the electric field E is called the polarization of the light wave. If the vibration has no particular direction, it is said to be unpolarized. If the vibration occurs in a plane, it is linearly polarized. If the vibration rotates around the axis of propagation of light, it is circularly polarized. In all cases, it is possible to project this vibration in the plane orthogonal to the wave propagation. This projection forms an ellipse. If the light is unpolarized, the ellipse will have a zero radius, and will be represented by a point, as can be seen in Figure 1.1a. If the light is linearly polarized, the projection forms a line as shown in Figure 1.1b. In the case of circular polarization, the ellipse is a circle, as seen in Figure 1.1b. Finally, in the general case of polarized light, the projection is an ellipse and its characteristics (dimensions and angles) represents the polarization.

1.1.2 Stokes convention and Mueller matrices

There are several formalisms to describe and study polarization. In this thesis, to process the data and do the calculations, the Stokes convention has been chosen. The Stokes convention makes it possible to use matrix calculations via Mueller matrices and therefore simplifies the data processing. The Stokes parameters can be computed in several different ways. They are introduced here through the parameters of the ellipse of polarization. This definition only allows to describe 100% polarized light. However, the Stokes parameters can also describe unpolarized or partially polarized light. In these cases, the Stokes parameter should be defined from the components of the electric field. The Stokes vector computed from the ellipse of polarization is defined by:

$$\vec{S} = \begin{pmatrix} I \\ Q \\ U \\ V \end{pmatrix} = \begin{pmatrix} a^2 + b^2 \\ (a^2 - b^2)cos(2\theta) \\ (a^2 - b^2)sin(2\theta) \\ 2abm \end{pmatrix} \tag{1.1}$$

where a and b are the axis of the ellipse, θ is the angle of the ellipse, and m is the sign of the rotation of the circular polarization. The ellipse and its characteristics are illustrated in Figure 1.2

The coefficient I corresponds to the intensity of the light. The coefficients Q and U correspond to its linear polarization (respectively along the reference axis and along an axis at 45° from it) and the coefficient V corresponds to its circular polarization. The 4

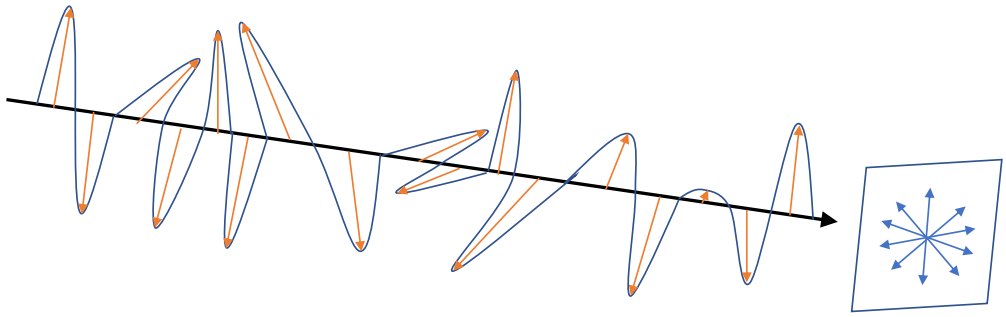

(a) *Unpolarized electromagnetic wave.*

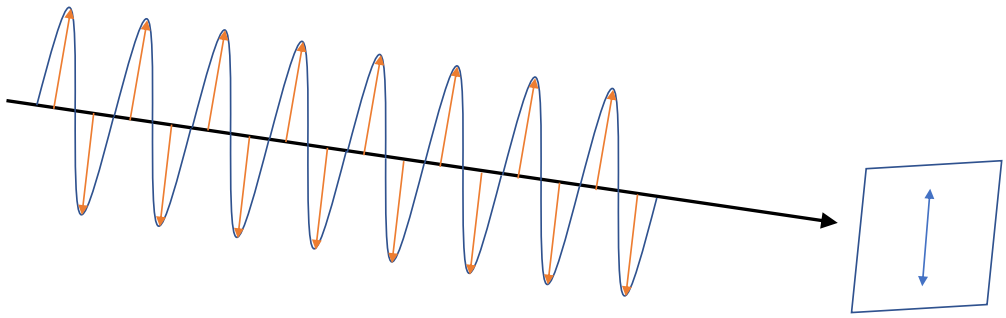

(b) *Linearly polarized electromagnetic wave.*

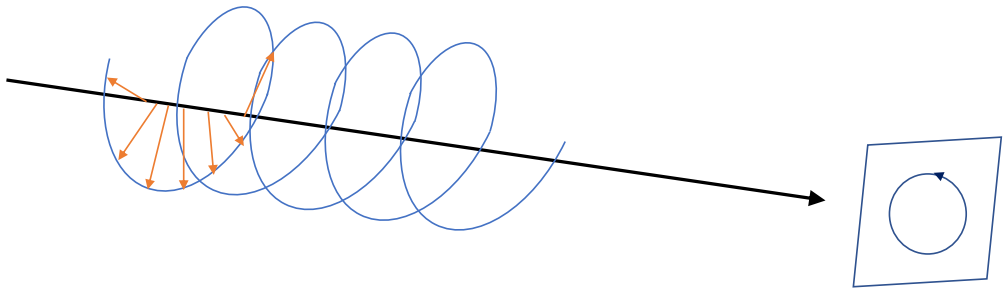

(c) *Circularly polarized electromagnetic wave.*

Figure 1.1: *Three states of polarization are represented. 1.1a illustrates an unpolarized electromagnetic wave. 1.1b illustrates a linearly polarized electromagnetic wave and 1.1c illustrates a circularly polarized electromagnetic wave.*

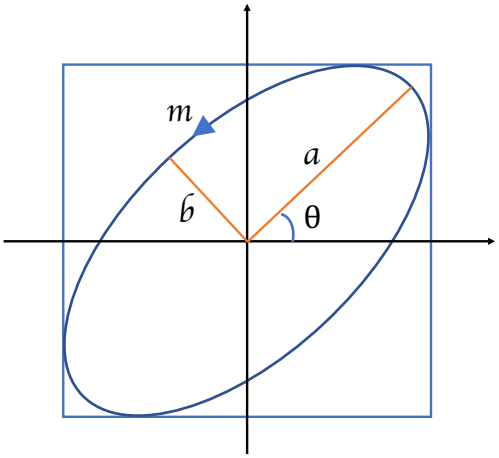

Figure 1.2: *The ellipse of polarization and its characteristics are illustrated. a and b are the axis of the ellipse, θ is the angle of the ellipse, and m is the sign of the rotation.*

components can thus describe all possible polarization states.
If the wave is fully polarized, the Stokes parameters verify the following equation:

$$I^2 = Q^2 + U^2 + V^2. \tag{1.2}$$

If the wave is totally depolarized, coefficients Q, U, and V are null:

$$U = V = Q = 0. \tag{1.3}$$

If the wave is partially polarized, Stokes parameters verify the following equation:

$$Q^2 + U^2 + V^2 = I_p^2 < I^2. \tag{1.4}$$

where I_p is the intensity of the polarized light.
We call the degree of polarization (DOP) the ratio:

$$DOP = \frac{I_p}{I}. \tag{1.5}$$

The important advantage of using Stokes vectors is to study polarization through matrix calculations. Indeed, each optical component, or each object interacting with light can be modeled by a matrix. For each component, its matrix defines the way the component modifies the polarization: it is called the Mueller matrix. The Mueller matrix M_i of a component i is defined by:

$$\vec{S}_{out} = M_i.\vec{S}_{in} \tag{1.6}$$

.

If N components are in the optical path of the light, the Mueller matrices of these components are multiplied to obtain the total modification of the polarization. We obtain:

$$\begin{aligned}\vec{S}_{out} &= M_N ... M_1 . \vec{S}_{in} \\ &= \prod_{i=N}^{1} M_i . \vec{S}_{in}\end{aligned} \tag{1.7}$$

Since matrix multiplication is non-commutative, the order of the N components is important.

In addition, if we rotate a component relative to the incoming light, its effect on polarization will be different and so will be its Mueller matrix. If we call M the Mueller matrix before the rotation and M_m the Mueller matrix after a rotation by an angle m, we can define M_m by :

$$M_m = R(-m).M.R(m) \tag{1.8}$$

with is the rotation matrix defined by:

$$R(m) = \begin{pmatrix} 1 & 0 & 0 & 0 \\ 0 & cos(2m) & sin(2m) & 0 \\ 0 & -sin(2m) & cos(2m) & 0 \\ 0 & 0 & 0 & 1 \end{pmatrix} \tag{1.9}$$

It is important to note that all these equations are wavelength dependent. The Mueller matrices are in general different from one wavelength to another.

This method can therefore easily model the impact of optical components on polarization. This technique is widely used in astrophysics in particular, and it was used in the work presented in this thesis.

1.2 Polarization components

In this Section, optical components and properties that will be used in the remainder of the thesis are presented. The majority of this Section is inspired from [35], [10].

1.2.1 Birefringence

Birefringence is an anisotropic property of certain transparent media. The Iceland spar mentioned in the introduction is one of them. The refractive index of the birefringent medium is not uniform and depends on the direction of polarization of the light in the material. As usual, the refractive index also depends on the wavelength λ. Birefringence is due to the structure of the material: it has a non-cubic crystal structure. This particular structure affects the speed of light in the material depending on the structure's orientation and creates a slow axis and a fast axis in the material. Light polarized parallel to the slow axis is slowed down more than light polarized parallel to the fast axis: different polarization

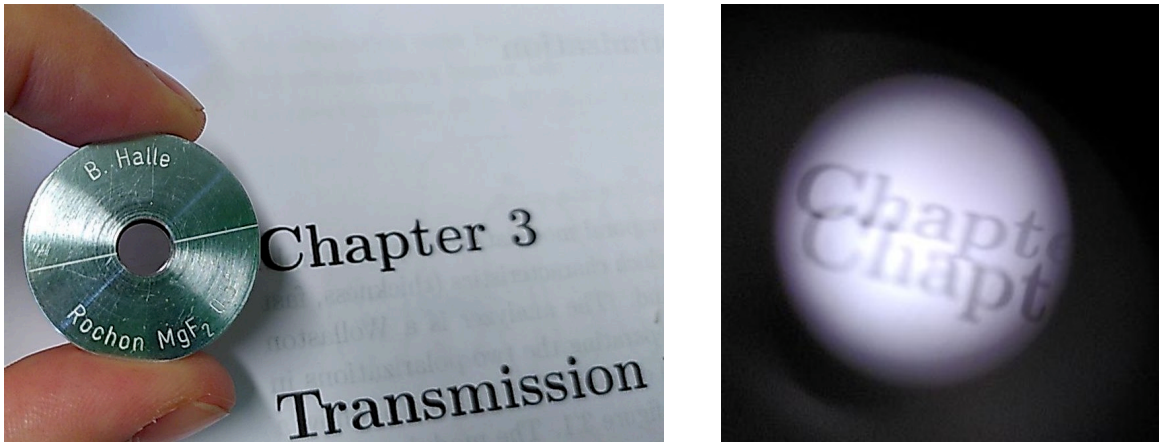

(a) **(b)**

Figure 1.3: *Picture 1.3a displays an optical component made of MgF_2, a birefringent crystal, next to a text printed on a paper. On picture 1.3b, the same text is seen through the optical component. The light is split in two orthogonal polarizations by the optical component and two images can be observed.*

inputs undergo different refractions in the material. This results in a splitting of the images in most cases, as can be seen in Figure 1.3. This phenomenon is called birefringence and it occurs naturally in some crystals. It can also be generated by a mechanical or thermal stress applied on a material. Some liquid crystals can also become birefringent, depending on the electric current applied to them.

Birefringence is commonly used to delay one polarization with respect to the other. This property is used to produce retarders, as explained in Section 1.2.2. Birefringence is also used to physically separate the orthogonal polarizations, as it will be explained in Section 1.2.3. In Figure 1.3, a component using birefringence to separate orthogonal polarizations is illustrated. In picture 1.3a, the component is showed next to a printed text. In picture 1.3b, the same text is seen through the optical component. As one can seen, the image of the text is duplicated: the two images are formed by the two orthogonal polarizations of the light.

1.2.2 Retarders or waveplates

Waveplates or retarders are optical components that create a delay between the light going through the two axes of polarization defined by the fast and slow axes of the plates. These plates are made of birefringent material. Quarter-wave plates and half-wave plates are commonly used in optics. The quarter-wave plate creates a delay of $\pi/2$, i.e. a quarter of a wavelength, between the two components of polarization defined by the plate axis. In particular, the use of a quarter-wave plate can transform a linear polarization into a circular polarization and vice versa. The half-wave plate creates a delay of π, i.e. half a wavelength.

The Mueller matrix of a waveplate with an axis α versus the reference angle of polarization and inducing a delay ϕ at wavelength λ is:

$$D(\alpha,\lambda) = \begin{pmatrix} 1 & 0 & 0 & 0 \\ 0 & cos^2(2\alpha) + sin^2(2\alpha)cos(\phi) & sin(4\alpha)sin^2(\phi/2) & -sin(2\alpha)sin(\phi) \\ 0 & sin(4\alpha)sin^2(\phi/2) & sin^2(2\alpha) + cos^2(2\alpha)cos(\phi) & cos(2\alpha)sin(\phi) \\ 0 & sin(2\alpha)sin(\phi) & -cos(2\alpha)sin(\phi) & cos(\phi) \end{pmatrix} \tag{1.10}$$

1.2.3 Polarizers

Linear polarizers

A linear polarizer is an optical component that transmits light only at a given polarization. The light coming out of the polarizer is linearly polarized along the axis of the polarizer. There are several types of linear polarizers, such as grating polarizers which are made of long parallel metal wires. They transmit light polarized perpendicularly to the wires and reflect the light polarized along other directions. Other polarizers work by absorption: their crystals aborb light polarized along one polarization and transmit the rest of the light.

Prisms

Another way to polarize light is to use birefringent prisms. By using the birefringence of some materials, orthogonal polarizations can be separated. The two output beams are called the ordinary and extraordinary beams. The ordinary beam corresponds to the polarization perpendicular to the optical axis of the crystal. The extraordinary beam corresponds to the polarization parallel to the plane formed by the optical axis and the direction of propagation of light. There are many different prisms, the two that are used in this thesis are the Rochon prism and the Wollaston prism. The Rochon prism does not deflect the ordinary beam but deflects the extraordinary beam. The two beams thus have different optical paths. It is particularly useful to create a linear polarization, aligned on the optical axis. The Wollaston prism deflects both the ordinary and extraordinary beams symmetrically. When measuring the two beams, it is useful because the two beams follow optical paths of the same length, so that the measurements respect a symmetry that we do not have with the Rochon prism. Figure 1.4 presents several types of polarization splitters, including the Rochon and Wollaston prisms.

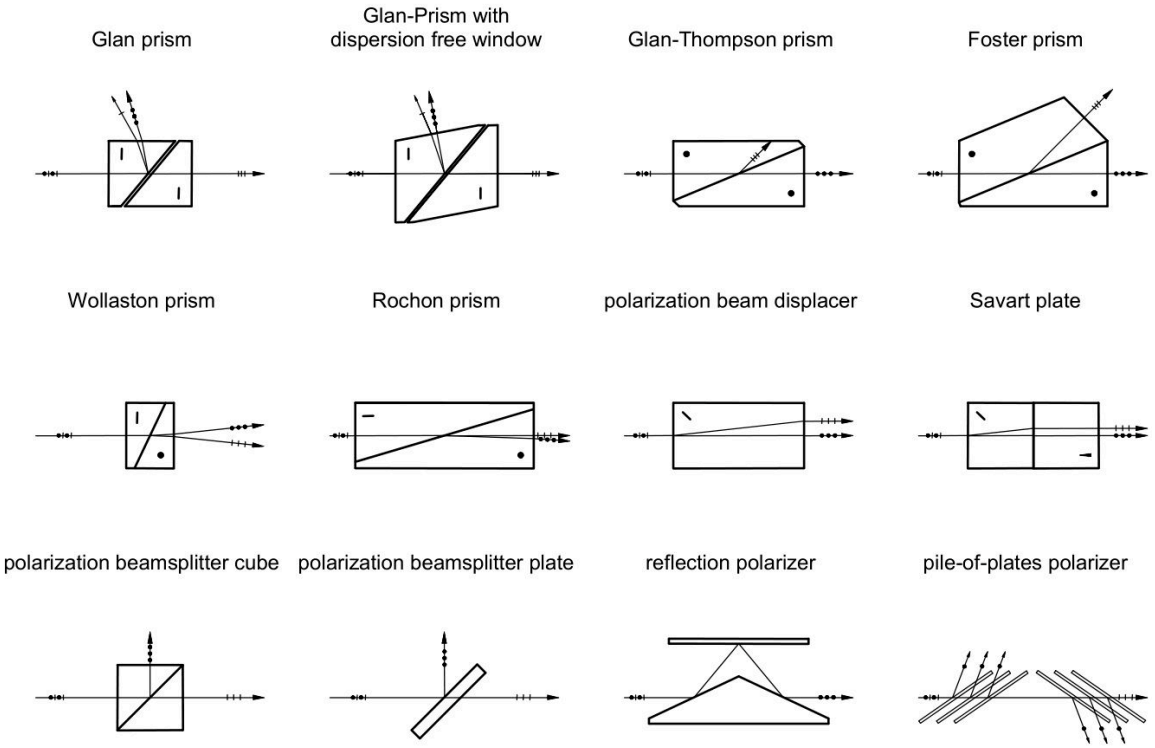

Figure 1.4: *Several types of polarization splitters are presented. Credit: Bernhard Halle Nachfl. GmbH (https://www.b-halle.de/products/polarizers.html).*

Brewster angle

The Brewster angle $\theta_{Brewster}$ is the angle for which the light reflected by a crystal is fully polarized. Brewster showed that this angle is defined by:

$$\theta_{Brewster} = arctan(\frac{n_2}{n_1}) \tag{1.11}$$

with n_1 the index of the medium where the light is propagating and n_2 the index of the crystal [5]. This angle is therefore dependent on wavelength and on the optical index of the crystal. This law does not apply to metals, but a similar principle in the case of metallic mirrors will be presented in Chapter 4 of this thesis.

Mueller matrix of a perfect polarizer

A perfect polarizer can be described by the following Mueller matrix:

$$P(\beta) = \frac{1}{2}\begin{pmatrix} 1 & cos(2\beta) & sin(2\beta) & 0 \\ cos(2\beta) & cos^2(2\beta) & cos(2\beta)sin(2\beta) & 0 \\ sin(2\beta) & cos(2\beta)sin(2\beta) & sin^2(2\beta) & 0 \\ 0 & 0 & 0 & 0 \end{pmatrix} \tag{1.12}$$

where β is the angle of the polarizer axis. The polarizer output is a light wave polarized along the axis defined by β.

1.2.4 Integrating spheres

An integrating sphere is an optical component mainly used for the production of a uniform light source. The inner surface of the sphere has a highly reflective and diffusive coating. The rays entering the sphere are diffused and reflected many times before exiting it. These multiple reflections destroy all spatial characteristics, including polarization. An integrating sphere can thus be used as a depolarizer to create a non-polarized source.

1.2.5 Other components

Many other components have an effect on polarization. Some components are very difficult to model and their Mueller matrices are not easy to compute. For example, a mirror creates both a phase shift between the components of the light and a polarizing effect: it does not reflect the components of the light with the same reflectivities. Therefore, the calculation of the Mueller matrix of a plane mirror is not straigthforward. It will be detailed in Chapter 4. Other components such as elliptical or parabolic mirrors need to be studied in detail to determine their Mueller matrices, as for instance in the article by Rodriguez-Herrera et al. [51].

1.3 Polarimetry

Polarimetry is the measure of polarization. The complexity of polarimetry lies in the fact that we can only measure the intensity of light I on current detectors. Since traditional sensors (CCD, CMOS, MCP, etc) are not sensitive to the polarization of light but only to its intensity, the information of the polarization state Q, U, or V must be encoded into I. To do this, the polarimeter creates a modulation: a variation of the intensity which unravels the polarization information. Polarimetry uses photometric measurements to find the polarization. A polarimeter is composed of a modulator and an analyzer. The modulator encodes the polarization information into the measurable intensity and the analyzer, by

transmitting only the light polarized in one direction, decomposes the light in that direction. The modulator can transmit light, as in the case of the polarimeter studied in Chapter 3, or reflect it as studied in Chapter 4. There are several types of modulation: temporal, spatial, or spectral.

1.3.1 Temporal modulation

All the polarimeters studied in this thesis use temporal modulation. Temporal modulation involves successive measurements of the intensity by the detector with a different amount of encoded polarization. The modulator takes several angular positions m around the optical axis and rotates the polarization. The analyzer filters the polarized light along a given direction. To measure the polarization state, one needs at least four measurements, which means four angular positions of the modulator. However, using a larger number of measurements, i.e. a larger number of modulation angles or simply redundantly using 4 optimal angles, is often used to improve the quality of the results [52]. The temporal modulation principle is illustrated in Figure 1.5.

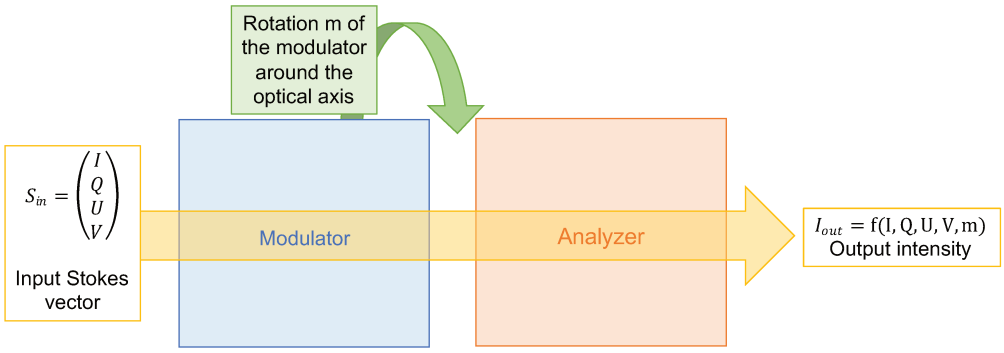

Figure 1.5: *General principle of a polarimeter using temporal modulation.*

1.3.2 Spatial and spectral modulations

Many other polarization measurement techniques exist, notably techniques using spatial or spectral modulation. These techniques are presented in article [58].

One technique to note is the case of spatial modulation along the slit. These polarimeters work under the same principle as the ones using temporal modulation: they have a modulator and an analyzer. Instead of rotating the modulator in time, the modulator is a prism which introduces a phase shift depending on the height of the beam on the prism [47, 62]. Indeed, the light beam passes through a thickness e of the prism that depends on the height x, resulting in a phase shift between polarizations dependent on the height. The light is then filtered in one direction by the analyzer. As a consequence, the output intensity depends on

x. A spatial modulation is thus created. The spatial modulation principle is illustrated in Figure 1.6.

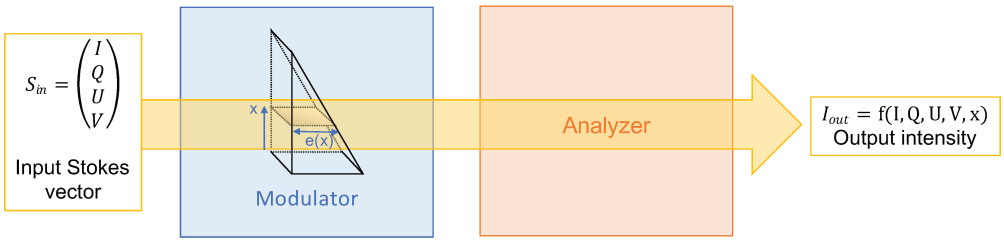

Figure 1.6: *General principle of a polarimeter using spatial modulation.*

Another technique of spatial modulation consists in placing a grid of micro-polarizers in front of a CCD sensor, with different angular positions. However, this technique is not suitable for our applications, especially in the FUV where it is limited by the transmission of materials [18].

1.3.3 Study of a polarimeter

In this Section, the method used to study and optimize polarimeters is presented [65]. First the specific matrices (Mueller, modulation, and demodulation) of the polarimeter are introduced. Then, the efficiencies and figures of merit quantifying the correct operation of the polarimeter are presented. Only temporally modulated polychromatic polarimetry is considered in this Section.

Mueller matrix

As seen in the previous Section, each component of an optical bench can be modeled by a Mueller matrix. By multiplying these matrices together, the complete system can be simulated. Thus the Mueller matrix of a polarimeter can be determined by multiplying the Mueller matrix of its modulator and analyzer, as in equation 1.13. The order is important, it must respect the path of the light. In the case of a temporal modulation, the global Mueller matrix depends on the modulation angle m.

$$M_{polarimeter}(m, \lambda) = M_{analyzer}(\lambda).M_{modulator}(m, \lambda) \tag{1.13}$$

(De)Modulation

The complete Mueller matrix of the polarimeter characterizes the effect of the polarimeter on the input polarization S_{in} into the output polarization S_{out}. Since the output Stokes vector S_{out} is not directly accessible, the Mueller matrix is not sufficient to deduce the input

Stokes vector S_{in}. The Stokes vector should be related to intensity measurements in order to extract its parameters.

Since only intensities are measured, only the first component of S_{out} is useful, it gives the total intensity measured by the detector. The modulation matrix O is defined, as a matrix of dimensions 4xN, by combining every first line of the Mueller matrix of the polarimeter for each of the N modulation angles.

This modulation matrix **O** allows us to write an equation for the measurement process:

$$\mathbf{I_{out}} = \begin{pmatrix} I'_{m_1} \\ I'_{m_2} \\ \vdots \\ I'_{m_N} \end{pmatrix} = \mathbf{O} * \mathbf{S_{in}}, \tag{1.14}$$

where $\mathbf{I_{out}}$ is the vector of the series of N intensity measurements recorded for each angle m of modulation and $\mathbf{S_{in}}$ is the input Stokes vector. To retrieve the Stokes vector, the demodulation matrix **D**, is defined by the pseudo-inverse of the modulation matrix **O** [13]:

$$\mathbf{D} = (\mathbf{O}^T * \mathbf{O})^{-1} * \mathbf{O}^T \tag{1.15}$$

where O^T is the transpose of the modulation matrix O. For a non-square modulation matrix, there is an infinity of demodulation matrices. The pseudo-inverse is the one that minimized the noise propagation. The input Stokes vector can be retrieved using equation 1.16:

$$\mathbf{S_{in}} = \mathbf{D} * \mathbf{I_{out}} \tag{1.16}$$

Therefore the initial Stokes vector S_{in} can be directly computed from the N intensity measurements I_{out}. The demodulation matrix is also used to determine the efficiency of the polarimeter as defined in the next paragraph.

Efficiencies

In order to quantify the proper operation of the polarimeter, polarimetric efficiencies are defined using equation 1.17:

$$\epsilon_i = (n. \sum_{j=1}^{n} D_{i,j})^{-1/2} \tag{1.17}$$

This equation defined mathematically in [13] gives the proportion of signal dedicated to a polarization measurement. It is the ratio between the signal to noise ratio (SNR) in the polarization parameters and the SNR in the intensity. [13] shows that these efficiencies verify

the following equations:

$$\begin{aligned} \epsilon_I &\leq 1 \\ \epsilon_Q^2 + \epsilon_U^2 + \epsilon_V^2 &\leq 1 \end{aligned} \tag{1.18}$$

We wish to have the best SNR possible for the polarization measurements, so we aim to design polarimeters with the highest possible efficiency values. Using equations 1.18, it is easy to find that the optimum efficiencies to retrieve Q, U, and V simultaneously with the same SNR is $\frac{1}{\sqrt{3}}$. To design polarimeters, we define an optimization parameter $\Delta\epsilon$:

$$\Delta\epsilon = \sqrt{(\frac{1}{\sqrt{3}} - \epsilon_Q)^2 + (\frac{1}{\sqrt{3}} - \epsilon_U)^2 + (\frac{1}{\sqrt{3}} - \epsilon_V)^2} \tag{1.19}$$

To approach the most efficient polarimeter, we try to minimize this parameter. ϵ_Q, ϵ_U, ϵ_V, and $\Delta\epsilon$ depend on wavelength λ.

Figure of merit

The study of polarimeters using the previously defined efficiencies does not consider the transmission of the polarimeter. Indeed, the efficiencies define the proportion of SNR used for polarimetry, but remain independent of the amount of signal transmitted by the polarimeter. In order to consider the transmission of the polarimeter in the design, a figure of merit is introduced :

$$\kappa(\lambda) = E(\lambda).\sqrt{T(\lambda)} \tag{1.20}$$

with $E = \frac{\epsilon_Q + \epsilon_U + \epsilon_V}{3}$, i.e. the mean of the polarimetric efficiencies and T is the transmission of the polarimeter. Using the square root on transmission maximizes the importance of transmission in the equation. Indeed, maximizing the flux is essential in polarimetry.

1.3.4 Spectropolarimetry

Spectrometry is the measurement of the intensity of light as a function of wavelength. Spectropolarimetry is the fusion between polarimetry and spectrometry, i.e. the study of the polarization of light as a function of wavelength. As a first step, the spectrometric and polarimetric parts of a spectropolarimeter can be studied separately. In particular the polarimeter can be studied independently of the spectrometer. This will be done in this thesis. The spectrometry part will not be discussed, and only the study of UV polarimeters will be treated. Nevertheless parameters of the polarimeters are studied over the spectrum, and in particular, efficiencies and figures of merit are studied as a function of the wavelength. The optimization process focuses on the average values of the spectrum.

For more details on polarimetry for astronomical use, these references are highly recommended: [11, 25, 59, 64].

1.4 Introduction to the thesis and plan

Spectropolarimetry is burgeoning in the field of astrophysics, thanks to ground-based spectropolarimeters in the visible and infrared wavelength domains. The need for UV spectropolarimetry is clear for many astrophysical studies. To escape the terrestrial atmosphere which absorbs most of the UV waves, UV spectropolarimeters are being studied in the framework of space missions. High-resolution (HR) spectropolarimeters on a wide UV range have never been tested, and for some wavelength ranges, they have never been studied. This thesis is part of this context, with the objective of increasing the Technology Readiness Level (TRL) of UV polarimeter prototypes. Two prototypes in particular have been studied: a prototype by transmission using birefringent materials, and a prototype by reflection using mirrors.

This thesis has 5 Chapters. In this first Chapter the basic knowledge of polarization was reviewed and the methods that are used in the remainder of the thesis to study polarimetry were presented.

Chapter 2 places this thesis in its astrophysical context before getting into the heart of the thesis. Science objectives and space missions for which the polarimeters have been studied during this thesis are presented.

Chapter 3 focuses on a prototype of polarimeter working by transmission. This principle of polarimeter is already well known [46] and the theory carried out focuses mainly on the design and optimization methods. Two experiments have been set up to test this polarimeter. The first experiment objective is to test the polarimeter optically to characterize its performance. The second experiment tests the polarimeter thermally, to see if this prototype would survive in space conditions. Both experiments and their results are presented in Chapter 3.

Chapter 4 focuses on a prototype for a reflective polarimeter. This type of polarimeter is innovative and reaches wavelengths never studied before in polarimetry (down to 90 nm in the present case). The theory of this new type of polarimeters is detailed and a test experiment has been set up. The experiment is also detailed in Chapter 4.

Finally, in Chapter 5, I summarize the results obtained in this thesis and suggests future work to continue to progress on the development of UV spectropolarimeters.

Chapter 2

Context in astrophysics

The concept of spectropolarimetry appeared thanks to Pieter Zeeman who demonstrated the existence of polarized spectral lines under the effect of magnetic fields in 1896 [68]. High-resolution spectropolarimeters have been studied extensively since the 1990's, particularly for applications in astronomy. This Chapter first introduces the science achievable with UV spectropolarimetry and its use in astronomy. Then, some space missions considering UV spectropolarimeters are presented. The design and optimization of polarimeters for these missions will be addressed in this thesis.

2.1 Spectropolarimetry for astrophysics

Spectropolarimetry can be useful to study many astronomical objects. For example, planets and exoplanets reflect light from their host stars and polarize it. This polarization gives information about the (exo)planets: their atmospheres, their orbital configurations, etc. Spectropolarimetry is also particularly useful to characterize the magnetic field of stars. Indeed, under the effect of a magnetic field, the Zeeman effect is observed in stellar lines as explained in Section 2.1.1: a spectral line splits into several shifted lines with different polarizations. Magnetic fields can be computed from the measurement of these polarized lines. Some astrophysical applications of UV spectropolarimetry are detailed in Section 2.1.2.

In recent years, many spectropolarimeters have been designed. For example, on the ground, ESPaDOnS [38] and SPIRou [15] at the Canada France Hawaii Telescope (CFHT) make high-resolution spectropolarimetry measurements possible in the visible and infrared wavebands. (Neo)Narval [7] on the Bernard Lyot Telescope (TBL) at the Pic du Midi in France and HARPSPol [49] on the 3.6 m telescope at the La Silla observatory in Chile both work in the visible range, and SPiP will soon be installed at TBL for the infrared range [24]. A polarimetric mode was also set up at the Robert Stobie Spectrograph on the Southern African Large Telescope (SALT), and is working down to 320 nm [50]. In the UV light however, it is essential to send the instruments into space to get rid of the terrestrial atmosphere. The interest of the UV range for spectropolarimetry is synthesized in Section 2.1.3. Only one

UV spectropolarimeter studying stars have flown in space so far: the Wisconsin Ultraviolet Photo-Polarimeter Experiment (WUPPE) [42]. WUPPE flown twice for a few days only in the 90's in the space Shuttles Columbia and Endeavour. It had a 50-cm telescope and collected low-resolution (∼330) spectropolarimetric measurements for 121 objects from 140 to 330 nm. Some space missions to study specific spectral features of the Sun have also been launched. In the UV, the Chromospheric Lyman-Alpha Spectro-Polarimeter (CLASP) and CLASP2 obtained first spectropolarimetric measurements of the Sun with a 27-cm telescope on a sounding rocket [67], [61]. Their Stokes I, Q, and U measurements concentrated on a very narrow spectral band (around Ly_α at 121.567 nm for CLASP and around 280 nm for CLASP2) with a resolution of 12000. No high-resolution spectropolarimeter working on a wide spectral band and measuring all polarizations (I, Q, U, and V) has been launched yet, but many projects are under study. Some of these projects have been studied in this thesis and are presented in Section 2.2.

2.1.1 Zeeman effect

Spectrometry consists in the decomposition of the studied light intensity according to the wavelength. The study of spectral lines gives important information on the observed subject. Spectral lines result from the excitation or de-excitation of an atom. A spectral line in emission is created by the de-excitation of an atom. A light source is composed of excited atoms. The atoms emit light energy to return to a neutral (non-excited) state. The energy released is in the form of a light wave characterized by:

$$E_0 = \frac{hc}{\lambda_0} \tag{2.1}$$

where E_0 is the released energy, h the Planck constant, c the speed of light, and λ_0 the wavelength of the released wave. The energy levels of an atom are quantified, that means they can only take a discrete number of energy states. Therefore, a light source always emits the same energies defined by equation 2.1, with the same wavelength. In the case of an absorption spectrum, we observe a neutral gas that is illuminated by a source. The atoms of the gas absorb light energy specific to their energy quantization, with the same formula as equation 2.1. The spectrum studied is continuous with darker lines corresponding to the absorption wavelengths of the gas.

The Zeeman effect, named after Pieter Zeeman (Nobel prize 1902), designates the division of an energy level specific to an atom into several energy levels in the presence of a magnetic field [28]. The Zeeman effect is illustrated in Figure 2.1. Without magnetic field, the levels of energy are degenerated and the released energy E_0 has a wavelength λ_0. In the presence of a magnetic field, the degenerescence is lifted and the energy released or absorbed by an atom can correspond to several different energies leading to several wavelengths. For instance, the levels E_0, E_1, and E_2 in Figure 2.1 lead to the emission of light at wavelengths λ_0, λ_1, and

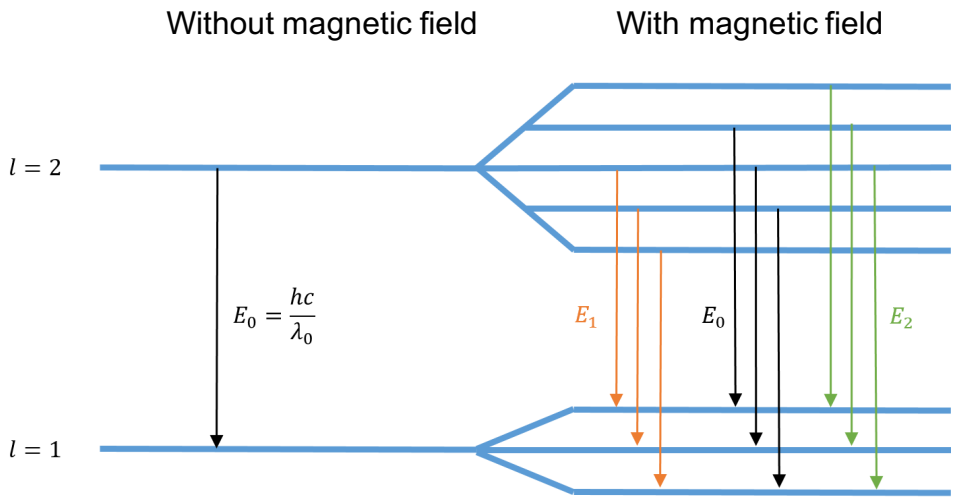

Figure 2.1: *Representative scheme of the Zeeman effect. On the left, the energy released by an excited atom without a magnetic field follows the energy quantization, and only one energy is released. On the right, under the effect of a magnetic field, the energy levels are divided and several energies are released. Credit: Martin Pertenais.*

λ_2. Triplets are common, but there may be more energy levels depending on the considered atomic transition. In concrete terms, this means that in the presence of a magnetic field, there will be a division of the absorption line into several lines slightly shifted in wavelength with respect to each other. Unless the magnetic field is strong, this effect is not really visible in spectrometry because the shift of the lines is very small. Indeed, the separation between the central wavelength and the external wavelengths $\Delta\lambda$ is given by equation 2.2:

$$\Delta\lambda = 4.67.10^{-13} g \lambda_0^2 B \tag{2.2}$$

where g is the Landé factor of the line, λ_0 the central wavelength, and B the magnetic field.

Therefore in most cases, and especially in the UV where λ_0 is small, the Zeeman splitting will only lead to a tiny broadening of the spectral line. Most instruments do not have a sufficient spectral resolution to resolve this tiny Zeeman splitting.

However, each line resulting from a Zeeman splitting is polarized differently. In a Zeeman triplet, the central line is linearly polarized whereas the external lines are circularly polarized, each one in an opposite direction. This polarization information are used to detect the Zeeman effect.

For instance, typical profiles of Stokes I and V as a function of wavelength in the case of a Zeeman effect are presented in Figure 2.2. The spectral lines are not well separated, as can be seen in the intensity profile I. The line separation is small, and therefore difficult to measure in a noisy spectrum. The polarization signal visible in Stokes V however is easier to measure. Using the weak-field approximation, the polarization created in the lines is directly

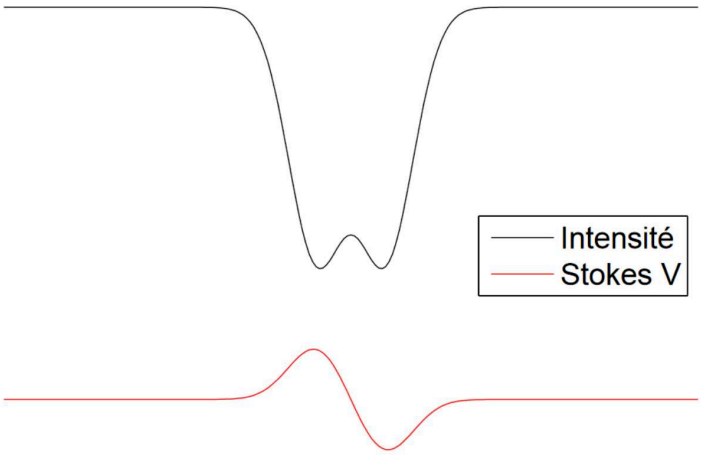

Figure 2.2: *Stokes I and V profiles as a function of wavelength in case of a spectral line in absorption in the presence of a magnetic field. Credit: Martin Pertenais.*

related to the magnetic field by:

$$B_{long} = 2.1410^{11} \frac{\int vV(v)dv}{\lambda gc \int [1 - I(v)]dv} \tag{2.3}$$

with B_{long} the longitudinal magnetic field, λ_0 the central wavelength, g the Landé factor of the line, c the speed of light, and v the velocity.

To summarize, measuring spectral line polarization is more sensitive than measuring a line splitting in Stokes I. This is why spectropolarimetry is a more powerful tool than spectrometry. In addition, the higher the spectral resolution, the more details can be obtained in the Stokes profiles and thus in the magnetic mapping of a celestial object. Moreover, the larger the wavelength coverage of the instrument, the more spectral lines can be studied and thus the higher the SNR can be obtained in the polarization measurements.

The measured polarization signals are generally very weak. In order to maximize the SNR, the Least Square Deconvolution (LSD) method can be used: if the electromagnetic field is weak and the lines all come from the same source under the same conditions, all spectral lines can be used simultaneously by performing a weighted sum [14]. The SNR of the Zeeman signature averaged over N spectral lines increases by $\sqrt{N}$ at first order. To this aim, it is necessary to perfectly know the intensity spectrum of the source, i.e. the position and amplitude of its lines. One then uses the Stokes profiles averaged over a spectrum rather than from a single line to determine the magnetic field. The efficiency of this method relies in measurements over wide spectral bands, making it possible to have as many spectral lines as possible used in the average.

Finally, while the Zeeman effect is most commonly used in spectropolarimetry, other polarization effects exist. For example, the Hanle effect has been successfully used for the Sun, but not applied for other stars yet. In addition, polarization can appear without

the presence of a magnetic field, for example through scattering. In astrophysics this is particularly relevant for any non-spherical geometry, e.g. a circumstellar disk.

Below, I present some examples of the main scientific cases from some space missions for high-resolution large-waveband UV spectropolarimetry. More details on those cases and additional ones can be found in the articles [4, 41, 54].

2.1.2 Examples of sciences cases

Stellar Physics

Spectropolarimetry is mainly used to measure stellar magnetic fields. As discussed above, by measuring the Zeeman effect in the spectral lines of a star, we can retrieve its magnetic field. A cartography of the magnetic field of a star can be constructed using Zeeman-Doppler imaging [27, 55, 56]. The polarization measurements are related to the longitudinal component of the magnetic field, i.e. they depend on the direction of the magnetic field with respect to the line-of-sight. When a star rotates, if the magnetic axis is not aligned with the rotation axis, the longitudinal component of the field changes with the stellar rotation phase. This rotational modulation of polarization is used to reconstruct the full magnetic field strength and configuration even if we measure only the longitudinal component of the field. This technique has already been widely used to study the field at the surface of stars in the visible domain. In addition, measuring the full Stokes vector (I, Q, U, V), i.e. linear polarization in addition to circular polarization, more details of the magnetic field of a star can be characterized..

Using UV spectropolarimetry, these magnetic field studies are not limited to the surface of the star, but can be applied to the medium and flows around the star (stellar wind, chromosphere, corona,...) which are only detectable in the UV. In particular, the UV range includes resonance lines of various highly ionized species (C IV, Si IV, Al III, N V, O VI...), that are sensitive to the stellar wind and probe different heights above the photosphere. In addition, linear polarisation and depolarisation processes in circumstellar environments, e.g. in accretion or decretion disks, will be very interesting to study.

Interstellar Medium

The interstellar medium (ISM) is the medium that composes the space between stars in galaxies. It is mainly composed of gas and dust and can be found in 3 different phases. The first phase is composed of hot ionized gas at a temperature of $10^6 - 10^7$ K. It is characterized by the presence of O VI (doublet at 103.19 and 103.76 nm) and C IV (many lines from 94.81 to 155.08 nm). The second phase is colder, it has a temperature between 6.10^3 and 10^4 K and is composed of neutral or ionized gas. It can be studied through the spectral lines O I (many lines from 92.20 to 135.85 nm) and N I (90.52 to 183.67 nm). The last cold phase has a temperature between 10 and 200 K and is composed of neutral gas, including H I (91.46 to 121.57 nm) and C I (94.52 to 199.36 nm)[26]. The study of the ISM thus requires

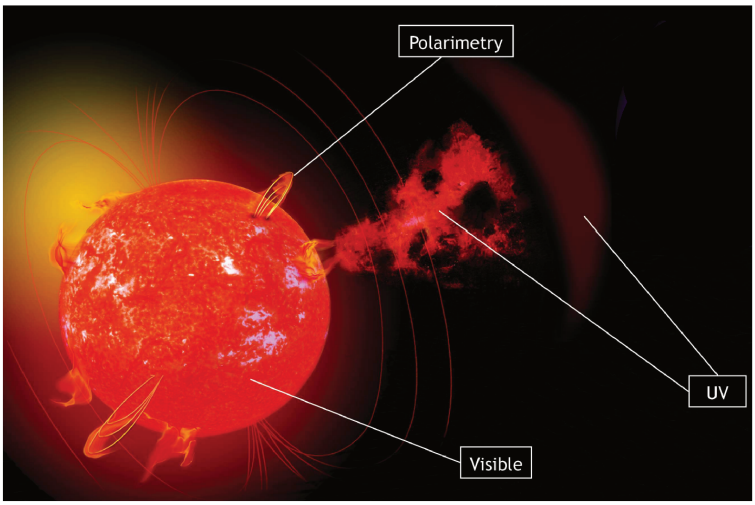

Figure 2.3: *Image of a star with its magnetic field, its winds, and a coronal mass ejection. Credit: Sylvain Cnudde (LESIA).*

high resolution UV spectrometry to separate the spectral lines from different phases and to observe all three phases.

Moreover, UV spectropolarimetric studies of the ISM can characterize the magnetic fields for all three phases. In particular, the size distribution of dust grains and their composition are fundamental to the micro-physics of ISM heating and cooling, whereas the magnetic field in the ISM controls the transport of the heat and cosmic rays on large scales. These factors are crucial to understand the dynamics of the gas in the ISM and can provide useful information for the models of stellar formation.

(Exo)planets

The planets, moons, or small celestial objects, whether they are inside or outside our solar system, reflect the light of their host stars. The unpolarized light from the star is linearly polarized during this reflection. In particular, the polarization rate varies with the angle between the object, the star, and the observer. The properties of the object studied, such as the composition of its atmosphere, the size of its particles, or the roughness of its surface also influence the polarization of the light. For example, the polarimetric study of Jupiter's moon, Io, by WUPPE showed that it is covered with 25% SiO_2 frost. Polarization variations can also provide important insight about the observed object. Periodic variations can be significant for planetary rings or moons for example. On the other hand, irregular temporal variations give information about cloud patterns or temperature variations. The scattering of light on the object is mainly due to the Rayleigh scattering which is very strong at low wavelengths of the UV. Moreover, the observations of planets around 210-220 nm will be used to detect the presence of carbon, undetectable in the visible or infrared light.

2.1.3 Particular interest of ultraviolet

As described in the previous Sections, the UV wavelength range is particularly important for many astrophysical studies because it is particularly rich in atomic and molecular transitions. For stellar physics, measurements in the visible are used to characterize the surface of the star and to determine its properties such as magnetic field, temperature, and rotation, while measurements in the UV give information on the environment of the star and can be used to measure the stellar wind, magnetosphere etc. It is therefore by combining observations in the visible and in the UV that we can establish a complete map of the properties of the star and its environment, and establish links between causes (spots, magnetic footpoints,...) and consequences (coronal mass ejections, disks,...). The study of the phases of the ISM is mainly done in the UV because the ionic components of the ISM radiates in the FUV. Finally, for the study of planets and exoplanets, the UV is an important domain, because the Rayleigh scattering is particularly strong at these wavelengths. It also covers the spectral lines of carbon, allowing to detect the presence of this chemical element in the atmosphere of the observed object.

2.2 Space mission projects

This thesis was conducted in the framework of a Centre National d'Etudes Spatiales (CNES) Research and Technology (R&T) study "UV spectropolarimetry" set up in 2012. This R&T has notably accompanied the Arago project, an M-class space mission proposed to ESA, and the POLLUX instrument proposed for the LUVOIR flagship mission to NASA. This thesis was built around the three polarimeters of POLLUX. The main goal of the thesis is to increase the TRL of a wide-band UV spectropolarimeter. The work done in this thesis also led to the design of the polarimeters of CASSTOR, a nanosatellite demonstrator, and PolStar, a mission proposed to NASA. All these missions are presented in this Section.

2.2.1 Arago

Arago is a space project imagined by the UVMag consortium to respond to ESA's calls for M-class space missions. The objective of Arago is to study the cycle of matter in the Milky Way as well as star-planet interactions via the study of magnetospheres (see Section 2.1). Arago is a Cassegrain telescope of 1.3-m diameter equipped with a spectropolarimeter operating between 119 and 888 nm with a spectral resolution of 25000 in the UV and 35000 in the visible. Both circular and linear polarizations are measured, i.e. full Stokes parameters I, Q, U, and V. The technical specifications allow for detection up to Ly_α. This makes it possible to study stars and their environments as well as exoplanets. More science cases are detailed in [41]. Arago was studied by Martin Pertenais during his thesis, which led him to elaborate the complete optical design of the spectropolarimeter, with the help of Laurent Parès [46]. My thesis builds on this work to study future UV space polarimeters.

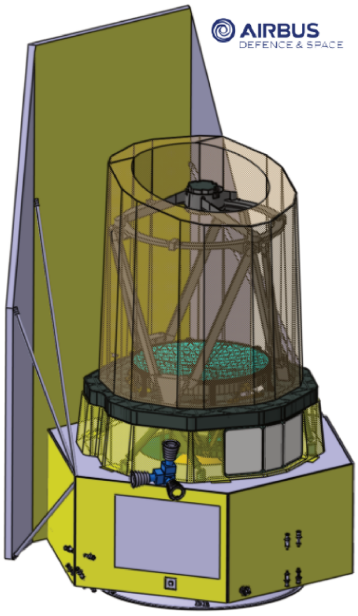

Figure 2.4: *Arago global scheme including the telescope, the sunshield, the instrument and the platform. Credit: Airbus Defense & space.*

2.2.2 POLLUX onboard LUVOIR

LUVOIR is a space telescope project of 15-m diameter for its version A, equiped with 4 instruments. LUVOIR Ultraviolet Multi Object Spectrograph (LUMOS) is a spectrometer covering a wide spectral range from 100 to 1000 nm and a large field of view. The High Definition Imager (HDI) is an instrument capturing images from near UV to near IR. Extreme Coronagraph for Living Planetary Systems (ECLIPS) is a coronagraph with a very fine contrast. It works over several wavelength ranges between 200 nm and 2 μm. Finally, POLLUX is a high-resolution UV spectropolarimeter working from 90 to 400 nm. LUVOIR would thus be a real observatory in space and could contribute to research in almost all astronomical topics with its wide spectral range and its diversity of instruments. More information is available in [4]. LUVOIR is a project proposed for the 2020 Astrophysics decadal Survey of NASA. For version B, the diameter of the telescope would be 8 m, and LUVOIR would have only 3 instruments. In this case, POLLUX would not be integrated to the space mission, but a polarimetric module would be added on LUMOS in order to do UV spectropolarimetry.

POLLUX is the result of a European collaboration, led by France, in particular by LESIA, Laboratoire d'Astrophysique de Marseille (LAM), and CNES. This spectropolarimeter works at very high resolution R = 120 000. In order to optimize the measurements on the whole wavelength range, POLLUX includes 3 channels: the near UV (NUV), the mid UV (MUV), and the far UV (FUV). Each channel has its own spectropolarimeter. The spectrometers were developed at LAM by Eduard Muslimov [40]. The polarimeters were developed in the framework of this thesis. For the NUV channel, between 200 and 400 nm, a transmission

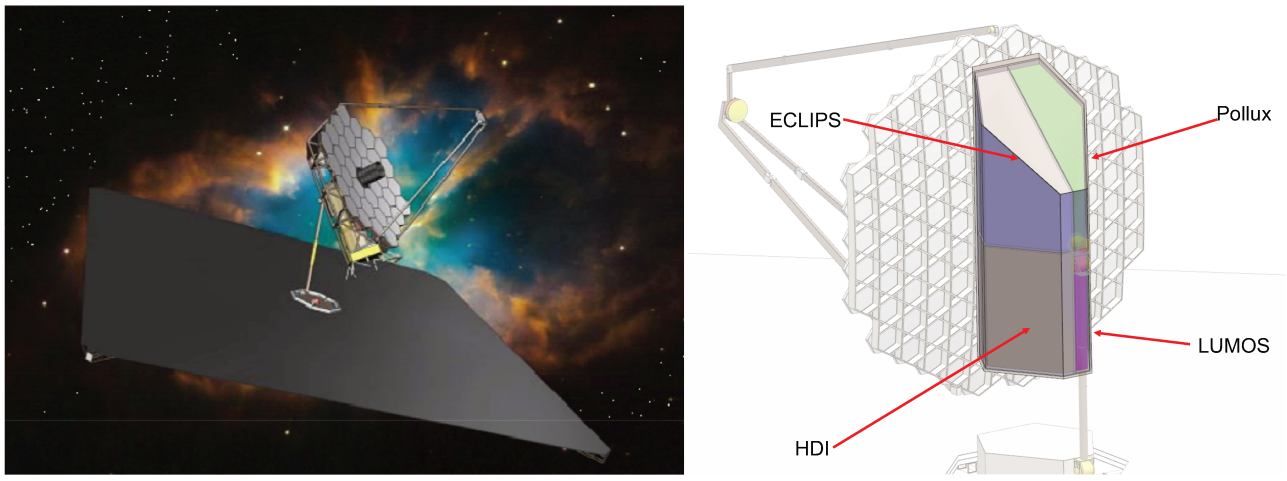

(a) (b)

Figure 2.5: *Picture 2.5a is an artist view of LUVOIR in space. Picture 2.5b represents the telescope with the 4 instruments onboard. Credits: NASA.*

polarimeter is considered, as previously studied for Arago for instance. For the FUV channel, between 90 and 120 nm, birefringent materials do not transmit light anymore. Therefore, an innovative concept of polarimeter by reflection is studied. Finally, for the MUV channel, between 118.5 and 200 nm, both designs can be considered: by reflection and by transmission. For now, only the transmissive one has been studied. The transmission polarimeters have been studied and tested and are presented in Chapter 3. The FUV reflection polarimeter is presented in Chapter 4.

The technical specifications reached by POLLUX make it possible to study all the scientific cases mentioned in the previous Section. Spectral lines in the FUV as well as the high resolution necessary for the study of ISM are reached with POLLUX. Moreover, thanks to the telescope's large diameter, LUVOIR can extend studies to further distances, outside our galaxy, in particular in the Magellanic Clouds.

2.2.3 CASSTOR

CASSTOR is a nano-satellite currently under development at LESIA in partnership with CNES and LAM. CASSTOR is a 12-cm telescope with a UV spectropolarimeter. The instrument works between 135 and 291 nm. Previously, the instrument was planned for a use between 220 and 400 nm, so that the polarimeter was studied for this waveband. It is a flight demonstrator for UV polarimeters in space. In particular, it will increase the TRL of the transmissive UV polarimeter. The nano-satellite will also demonstrate the feasibility of the science by making the first UV spectropolarimetric measurements on a few tens hot stars. The nano-satellite is in a 12U configuration, i.e. 20x20x30 cm^3. The launch is planned

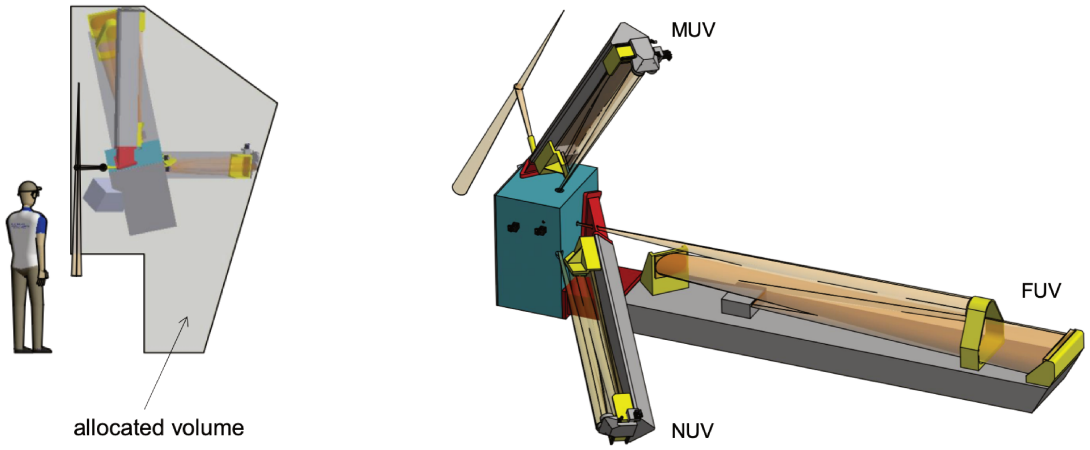

(a) (b)

Figure 2.6: *Model views of POLLUX representing the volumes of the instrument. Scheme 2.6a represent a human next to the instrument to show the proportion. In Figure 2.6b, the three spectropolarimetric channels are illustrated inside the instrument. Credit: David Montgomery (UKRI STFC)*

in 2025. The study of the polarimeter of the instrument is presented in Chapter 3 of this thesis.

2.2.4 PolStar

PolStar is an Medium-Class Explorer mission project (MIDEX) for NASA. PolStar is a MUV spectropolarimeter, working from 121 to 200 nm at high resolution (R=30 000) and from 121 to 320 nm at low resolution (R=20). The telescope is a 60-cm Cassegrain telescope. The polarimeter is a transmission polarimeter which will be detailed in Chapter 3 of this thesis. PolStar will be used mainly for the study of hot star environments as well as ISM and exoplanet studies. In particular, the 3D magnetic and wind environment of stars will be measured. More information can be found in [54].

2.2.5 Summary of the instruments requirements

Table 2.1 summarizes the requirements for the studied instruments. The requirements have been chosen in order to benefit the greatest number of scientific studies. For instance, we could have given priority to some Stokes parameters compared to others to improve the polarization measurement for some science objectives, but this would have prevented the proper conduct of other studies. It is a scientific choice to measure all Stokes parameters with the same efficiency. In the same spirit, it was decided not to favor certain wavelengths over others to allow all scientific cases to acquire the data necessary for their goals.

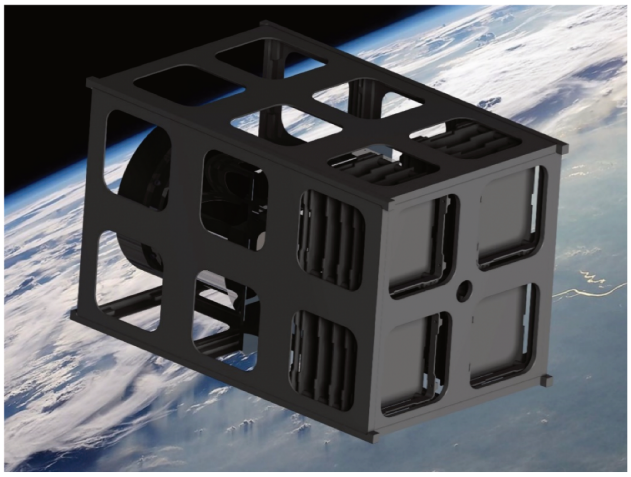

Figure 2.7: *Simulated image of CASSTOR in space. Credit: Adrien Saada (LESIA)*

Requirements	Arago	POLLUX	CASSTOR	PolStar
Missions	a 1.3-m space telescope for an ESA M mission project	LUVOIR, a 15-m telescope project for NASA	a 12-cm telescope nanosat by CNES, LESIA, and LAM	a 60-cm Cassegrain telescope MIDEX mission for NASA
Wavelength range (nm)	123-888	3 ranges NUV: 200-400 MUV: 118.5-200 FUV: 90-120	135-291 (studied here: 220-400)	121-300
Polarization goals	Measurements of linear (Q,U) and circular (V) polarization with equal efficiencies			
Polarization sensitivity	10^{-3}	10^{-4}	10^{-3}	10^{-3}
Science goals	Magnetic fields of stars	Magnetic fields of stars, study of exoplanets, ISM...	Magnetic fields of stars, instrument demonstrator	Magnetic fields of stars

Table 2.1: *Summary of the requirements for the instruments studied in this thesis.*

Chapter 3

Transmission polarimetry

3.1 Introduction

As seen in Chapter 1, optical polarimeters usually consist of two components: a modulator and an analyzer. When working in transmission (as opposed to reflection), the birefringence of the materials used is the key characteristic to develop polarimeters. In case of a polarimeter using temporal modulation, the modulator is often a quarter waveplate, rotating around the optical axis and modulating the input polarization. The analyzer is usually a linear polarizer or a birefringent prism, permitting the measurement of the intensity for this linear polarization. In ultra-violet, few birefringent materials are available. MgF_2 and SiO_2 are the main birefringent material transmitting in ultra-violet.

A UV polarimeter has already flown on CLASP, it was made with a MgF_2 half wave plate and two reflective analyzers and was working at Lyman-alpha (121.567 nm) [67]. This polarimeter has proven to work efficiently at this specific wavelength. Polarimeters working on a large waveband both in UV and optical light have been studied for X-shooter as well as for Arago [48, 57]. Experiments have shown that these prototypes work in the visible range [46]. The work displayed in this Chapter aims at optimizing these prototypes for a wide bandwidth in the ultraviolet as well as demonstrating their performances in the ultraviolet via experiments reproducing space conditions (vacuum and thermal conditions).

First, the method used to compute this polarimeter as well as some optical design made for several space missions are presented in Section 3.2. Then two experiments are detailed. To test the polarimetric properties in the ultra-violet range of a prototype, a bench was set up to create any polarization at the input of our prototype. The experiment is presented in Section 3.3, and its results are presented in Section 3.4. Finally, the modulator underwent thermal cycles to test its thermal resistance. This experiment is presented in Section 3.5.

3.2 Optical design and optimization

3.2.1 General design

Design

The design of a transmitting polarimeter using temporal modulation is quite standard. The modulator is composed of birefringent plates which characteristics (thickness, fast axis angles) are optimized for the studied waveband. The analyzer is a Wollaston prism. The Wollaston prism has the advantage of separating the two polarizations in a symmetrical manner, transmitting both ordinary and extraordinary beams into a symmetrical optical path. The two beams can then be used together and facilitate the computation of Stokes parameters by compensating errors. The design is illustrated in Figure 3.1. The modulator takes several successive angular positions in time, these positions are called the modulation angles. Those angles can be optimized or chosen evenly distributed, as can be seen further in Section 3.2.2.

The birefringent plates in the modulator rotate the polarization of the incoming light. The Wollaston prism is equivalent to a linear polarizer and measures the linear component of the polarization at the chosen modulation angle. By combining the measurements of all the modulation angles, the incident polarization can be recovered. In practical terms, Mueller matrices are used to obtain a modulation and demodulation matrices. These matrices are explained in detail in Chapter 1 and will be recalled in Section 3.2.2. They are used to compute the input polarization state based on measured intensities, and vice versa. The greater the number of measurements, the greater the accuracy of the polarization measurement to a certain extent. The number of measurements can be increased by increasing the number of modulation or by repeating 4 optimal modulation angles [52].

The modulator is composed of several birefringent plates. The optimization of the polarimeter also consists in reducing the number of its plates in order to increase its transmission.
The plates have a minimum thickness of 0.3 mm. Indeed, this 0.3 mm thickness corresponds to the thinnest plates that can be accurately polished with such materials. If plates with thicknesses smaller than 0.3 mm are required anyway, then double plates have to be used. By assembling two plates with crossed axes, we can simulate a thin plate thanks to the difference in thickness between the two plates. The phase shifts created by plates add up only if their axes are identical. It is easy to prove using the Mueller matrix presented in equation 1.10, that a plate with an axis angle of $\alpha + \frac{\pi}{2}$ and introducing a phase shift ϕ has the same effect on the polarization that a plate with an axis angle α and introducing a phase shift $-\phi$. The phase shift from the second plate can thus be subtracted from the first one. The phase shift is given by:

$$\phi = \frac{2\pi}{\lambda} e \Delta n \tag{3.1}$$

with λ the wavelength, e the thickness of the plate and Δn the birefringence of the material. Therefore, a plate with a thickness $e + \Delta e$ induces a phase shift $\phi + \Delta\phi$, where ϕ is the phase shift created by the thickness e and $\Delta\phi$ is the one created by the thickness Δe. The double plates can thus be considered as the equivalent plate with an axis angle of α and inducing a global phase shift $\phi_{eq} = \phi + \Delta\phi - \phi = \Delta\phi$. These plates are called quasi zero-order retarder. However, double plates decrease transmission by increasing the number of diopters and thus, by adding Fresnel reflections. Many optimisations have been studied to have a single plate around 0.3mm and thus avoid these double plates, but none of them has led to suitable results. The double plates option is therefore the final solution.

Finally, in all these considerations, one must also take into account the possibility to use molecular bonding for these plates. The best way to maximize transmission is to glue these plates to avoid Fresnel reflections. As no glue could be identified that both fit space mission specifications and is transparent in the whole wavelength range, molecular bonding is considered instead. Molecular bonding is a technique of bonding of materials by simple contact of their surfaces. If the surfaces are sufficiently well polished and parallel, intermolecular bonds are formed between the two materials, and stick them together. However, this bonding can be fragile to temperature changes and is not proven to be resistant to space conditions for birefringent material. This topic will be further discussed in Section 3.5. A stack of plates which are not molecularly adhered is said to have airgaps. It is similar as if the stack included plates made of air between 2 real plates.

The only design parameter of the Wollaston prism is the output angle between the two output beams. It is determined according to the instrument studied. Indeed, the requirement on the separation induced by the prism is determined so that the separation is large enough to separate completely the ordinary and extraordinary beams, but also is small enough not to overlap with orders of the spectrometer, or to fall off the detector. The Wollaston prism is then designed outside the optimization of the polarimeter.

Materials

In the ultra-violet range, few birefringent materials are available. MgF_2 and SiO_2 are the two well-known birefringent materials transmitting in ultra-violet.
MgF_2 is the main considered material as its transmission is over 90% for wavelengths larger than 200 nm (for a 5-mm plate, see Figure A.1 in Appendix A) - the main loss being the Fresnel reflection. Its transmission decreases until approximately 50% at 120 nm but its birefringence is equal to 0 at 119.5 nm (see Figure A.4 in Appendix A). Therefore MgF_2 is not suitable for a polarimeter in the FUV. However, it can be used in the MUV and the NUV. SiO_2 is also considered, but its cutoff wavelength being 185 nm (see Figure A.6 in Appendix A), it is a solution only for a polarimeter above this wavelength. Thus, SiO_2 is only considered for a use in the NUV. All information on materials can be retrieved in Appendix A.

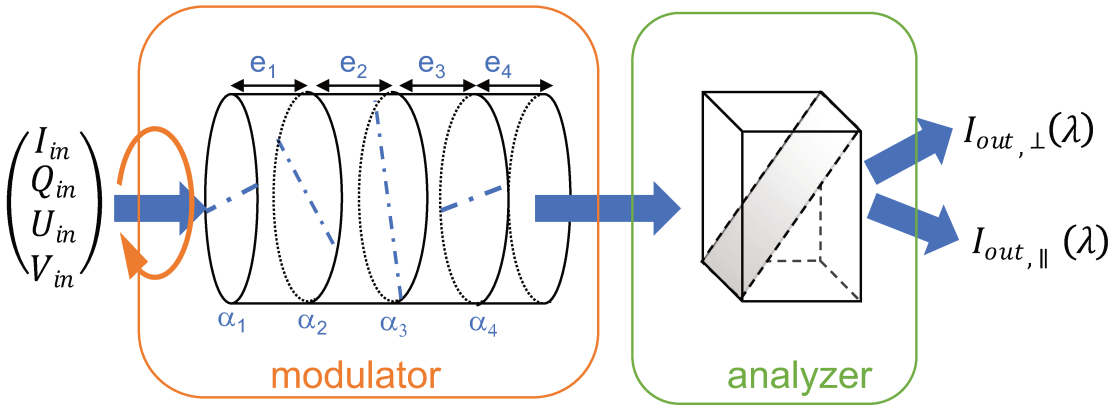

Figure 3.1: *Scheme of the transmitting polarimeter.I_{in}, Q_{in}, U_{in}, and V_{in} are the input Stokes parameters. e_1, e_2, e_3, and e_4 are the thicknesses of the plates. α_1, α_2, α_3, and α_4 are the angles of the axis of the corresponding plates. $I_{out,\parallel}$ and $I_{out,\perp}$ are the two outputs of the polarimeter.*

Errors

To perfectly simulate the performance of the polarimeter, an error study is essential. In particular, reflections from the instrument will create errors in the polarization measurement. Indeed, by passing several times through all or part of the polarimeter, the reflected light will not follow the desired polarization path, and will therefore distort the measurements. These reflections can be studied and simulated in order to be included in the design of the instrument. Studies of these fringes have been done in some articles for X-shooter for instance [60]. A study of these fringes was started by Emilien Denoual, as part of his master's thesis. An article is in preparation on this study (Denoual et al). The study of these fringes in our polarimeters should be conducted in the next steps of the instrument development. The fringes will not be considered in the optimization and designs presented here.

However, to limit these problems, it is essential to reduce the reflections to a minimum. To do so, molecular bonding, mentioned earlier, is a very effective solution. Indeed, the use of molecular bonding reduces the number of diopters from 8 to 2 in the case of two double plates for the modulator. This considerably reduces reflections. Molecular bonding is discussed further in Section 3.5.

Other sources of errors such as the uncertainty of the optical indices or the accuracy and repeatability of the alignment of the plates fast axis angles are also important sources of error which should be studied. This work has not been completed within the framework of this thesis and should be done for the complete study of the instrument.

3.2.2 Methods

Efficiencies computation

As seen in Chapter 1, the polarimeter can be modelled by Mueller matrices. The Mueller matrix of a plate with a fast axis α is:

$$D(\alpha,\lambda)=\begin{pmatrix}1 & 0 & 0 & 0\\ 0 & cos^2(2\alpha)+sin^2(2\alpha)cos(\phi) & sin(4\alpha)sin^2(\phi/2) & -sin(2\alpha)sin(\phi)\\ 0 & sin(4\alpha)sin^2(\phi/2) & sin^2(2\alpha)+cos^2(2\alpha)cos(\phi) & cos(2\alpha)sin(\phi)\\ 0 & sin(2\alpha)sin(\phi) & -cos(2\alpha)sin(\phi) & cos(\phi)\end{pmatrix} \tag{3.2}$$

where ϕ is the phase shift and is defined by:

$$\phi=\frac{2\pi.e.\Delta n}{\lambda} \tag{3.3}$$

with e is the thickness of the plate, λ the studied wavelength, and Δn the birefringence at λ.
The Mueller matrix of a linear polarizer with a β axis is:

$$P(\beta)=\frac{1}{2}*\begin{pmatrix}1 & cos(2\beta) & sin(2\beta) & 0\\ cos(2\beta) & cos^2(2\beta) & cos(2\beta)sin(2\beta) & 0\\ sin(2\beta) & cos(2\beta)sin(2\beta) & sin^2(2\beta) & 0\\ 0 & 0 & 0 & 0\end{pmatrix} \tag{3.4}$$

By using the rotation matrix R seen in Chapter 1, it is now possible to calculate the global Mueller matrix of the polarimeter:

$$\begin{aligned}M_{polarimeter}(\beta,m,\lambda)&=P(\beta)*R(-m)*\prod_{k=1}^{Z}D(\alpha_k,\lambda)*R(m)\\&=P(\beta)*R(-m)*M_{plates}*R(m)\end{aligned} \tag{3.5}$$

where m represents the modulation angles, N the number of plates, and M_{plates} is the Mueller matrix of the combination of Z plates.
The Mueller matrix being calculated as a function of the modulation angle m, it is easy to calculate the modulation matrix O. It is constructed by taking the first row of the Mueller matrix (the intensity) for each of the modulation angles:

$$O(\lambda)=\begin{pmatrix}M_{polarimeter}(m_1,\lambda)(1,1:4)\\ \vdots\\ M_{polarimeter}(m_N,\lambda)(1,1:4)\end{pmatrix} \tag{3.6}$$

with N the number of modulation angles.

Using this modulation matrix, the demodulation matrix and efficiencies coefficients as defined by [13] can be computed as seen in Chapter 1.

Optimization

To optimize the polarimeter, a local optimization implemented in Matlab and using a sequential quadratic programming method has been used. This optimization depends on a starting point. It was launched with random starting points as many times as possible (from 1000 to $\sim$ 10 000 times). The parameters used to optimize the polarimeter are the number of plates, their thicknesses, and their fast axis angles. The angular positions are generally evenly distributed around the optical axis. At first, I decided to optimize them. The optimization of these angles increases slightly the efficiencies, and breaks the symmetry of the measurements. However, in practice, these particular angles constraint the alignment of the modulator and make it more difficult to align. It was noted in particular in the experiments described in Section 3.3. It is therefore recommended to favor modulation angles evenly distributed around the optical axis. The same conclusions were found in [52]. Nonetheless, in some cases, the optimization of these angles is preferred, in particular to reduce the number of angles (to a minimum of 4) or in the case where only one polarization (the ordinary beam) is retrieved. In the first experiment presented in this Chapter, in Section 3.3, these angles were optimized.

Figure of merit

The more plates the polarimeter has, the more efficient it is but also the more absorbing it is. To include transmission in the choice of modulator, a figure of merit was introduced according to the following formula:

$$\kappa = E * \sqrt{T} \tag{3.7}$$

where κ is the figure of merit, E is the mean of the polarization efficiencies as defined in [13] and T is the global transmission of the modulator.
This figure of merit is a criterion of selection considering both efficiency and transmission. Polarimeters are then optimised to obtain the largest possible figure of merit. We want to have a transmission as close to 1 as possible, and efficiencies as close to 0.57 as possible. The optimisation then consists in having the largest figure of merit. In the best case it is equals to 0.57. For each studied design, the transmission for a modulator is considered both for the case with airgaps or with molecular bonding.

3.2.3 POLLUX NUV

The NUV polarimeter for POLLUX has to be designed to work from 180 to 400 nm. Both SiO_2 and MgF_2 are considered. Configurations with two and three plates are considered for both materials. To calculate the figures of merit, both configurations with molecular

bonding and airgaps were considered. Figure 3.2 shows the figure of merit obtained for the NUV for all the studied configurations. As one can see, the figures of merit for a modulator studied with SiO_2 are significantly lower than the ones with MgF_2. The loss of efficiency around 190nm for SiO_2 corresponds to its birefringence reaching 0. It does not reach 0 on the curve because of the wavelength resolution. With plates in molecular bonding, configurations with two and three plates are quite similar. The three plates configuration is slightly better at the edge of the waveband. Nevertheless, for configurations with airgaps, the figures of merit for a two plates modulator is higher than the one with 3 plates as the transmission is much better. The two-plates configuration is preferred as it presents less risk due to the molecular bonding and also limits spurious reflections compared to the three-plates version. The final modulator for POLLUX's NUV channel is then a block of two MgF_2 plates with the following configurations:

- Plate 1: angle of fast axis 32.6°and thickness 12.8 μm
- Plate 2: angle of fast axis 147.3°and thickness 3.7 μm

The efficiencies of this polarimeter is presented in Figure 3.3. The efficiencies fluctuate around the optimal efficiency. The efficiencies of Q and U are identical because the modulation angles are symmetrical with respect to the polarization axes.

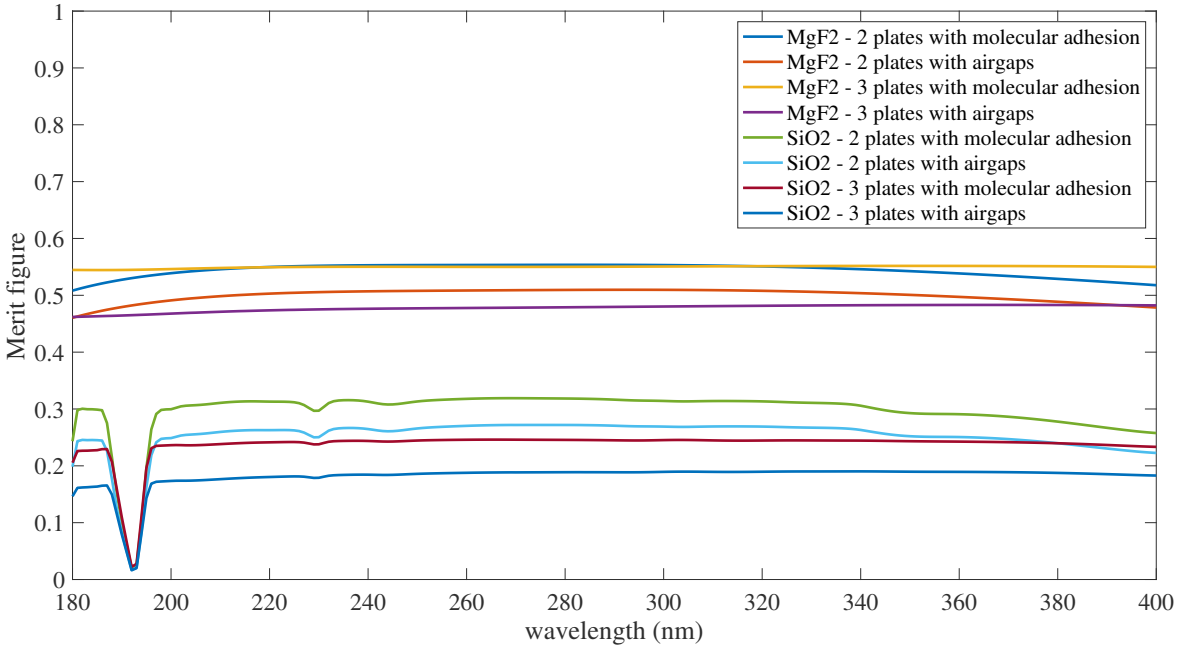

Figure 3.2: *Figure of merit of all the configurations studied for the NUV channel of POLLUX.*

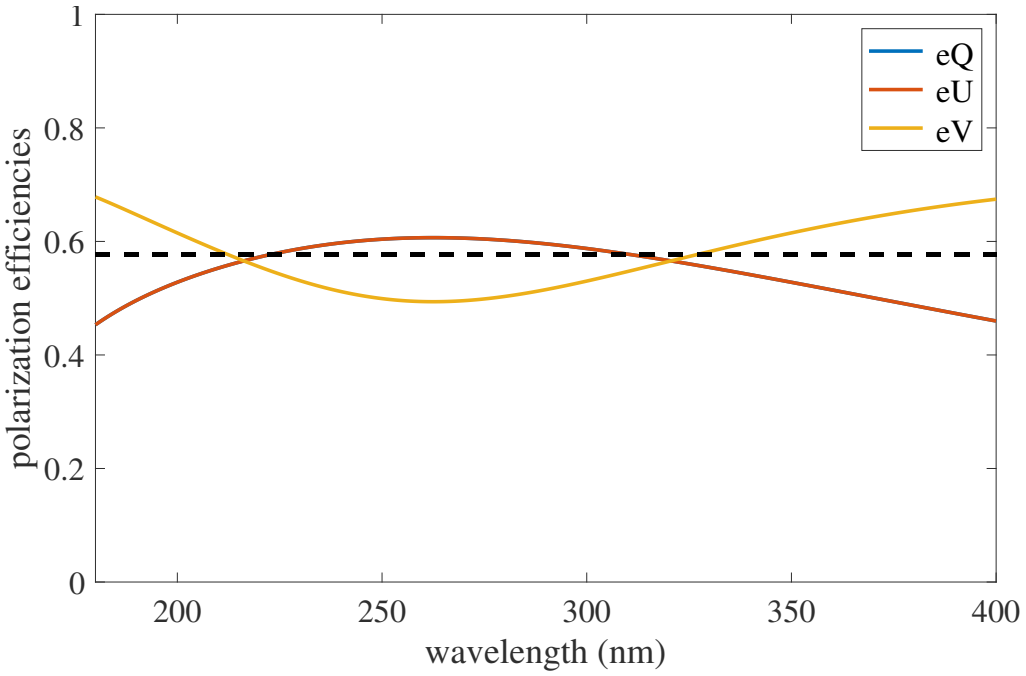

Figure 3.3: *Efficiencies for the 2-MgF_2-plates modulator chosen for the NUV channel of POLLUX. Q and U have the same efficiency curve.*

3.2.4 POLLUX MUV

For the MUV channel, only MgF_2 is considered, as SiO_2 does not transmit at these wavelengths. For this wavelength range, the efficiencies obtained with 3 plates are no different than with 2 plates. The transmission with two plates is though better for both configurations with or without molecular bonding. The final modulator for POLLUX's MUV channel is a block of two MgF_2 plates with the following configurations:

- Plate 1: angle of fast axis 6.4°and thickness 9.6 μm
- Plate 2: angle of fast axis 70.0°and thickness 3.3 μm

The efficiencies for this modulator is presented in Figure 3.4. The efficiencies drop to 0 at 119.5 nm as the birefringence is at 0: the polarimeter does not have any effect on the polarization state at this wavelength.

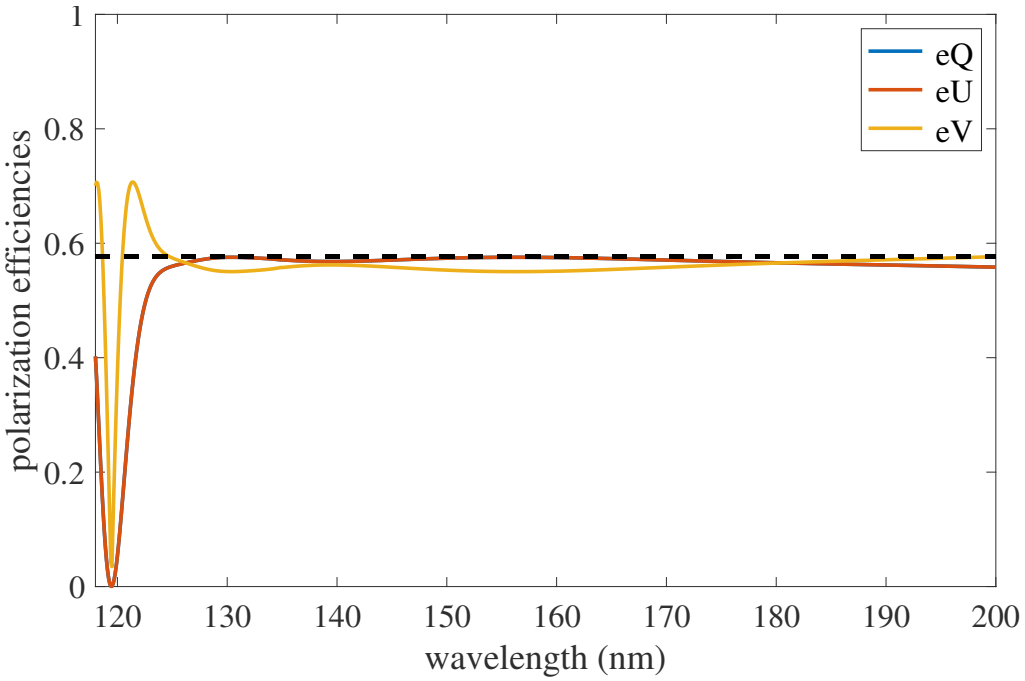

Figure 3.4: *Efficiencies for the 2-MgF_2-plates modulator chosen for the MUV channel of POLLUX. Q and U have the same efficiency curve.*

3.2.5 CASSTOR

For CASSTOR's polarimeter, the studied wavelength range is 220 - 400 nm. A two-plates solution has been found with MgF_2. The addition of a third plate does not improve the efficiency and decrease the flux. Based on the study of the NUV polarimeter of POLLUX, the SiO_2 solution has not been explored. The parameters of these plates are:

- Plate 1: angle of fast axis 2.2°and thickness 5.63 μm
- Plate 2: angle of fast axis 66.1°and thickness 16.97 μm

Figure 3.5 shows the efficiencies found for this polarimeter. The efficiencies are very closed to the optimal efficiency all over the spectrum.

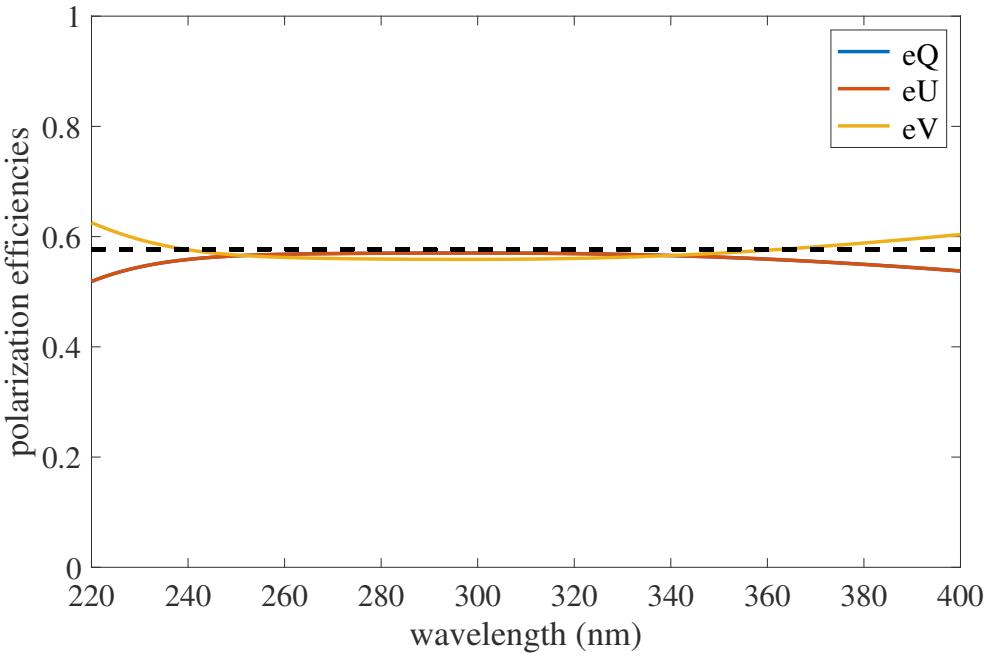

Figure 3.5: *Efficiencies for the 2-MgF_2-plates modulator chosen for CASSTOR. Q and U have the same efficiency curve.*

3.2.6 PolStar

As presented in Chapter 2, PolStar is a FUV spectropolarimeter measuring polarization in the range 121 - 320 nm. For these wavelengths, SiO_2 is not considered. The optimization was therefore based on two parameters: two or three plates. Figure 3.6 shows the efficiency calculated for the two configurations for both plates at optical contact or with airgaps.

The figures of merit are quite similar to the NUV of POLLUX. The figures of merit presented in Figure 3.6 show that a configuration with three plates is slightly preferable in the case of plates in molecular bonding. However, the two plates configuration is much better in the case of plates with air gaps which is the baseline for PolStar. Considering also that the parallel plates in the airgaps configurations will create polarized fringes as seen in Section 3.2.1, the configuration with two plates is preferable. The efficiencies are presented in Figure 3.7. The parameters of the plates are:

- Plate 1: angle of fast axis 20.1°and thickness 10 μm
- Plate 2: angle of fast axis 83.7°and thickness 3.2 μm

.

The POLLUX NUV and MUV polarimeters as well as the CASSTOR and PolSTAR polarimeters have been designed. They are all made of MgF_2, and consist of two plates. The

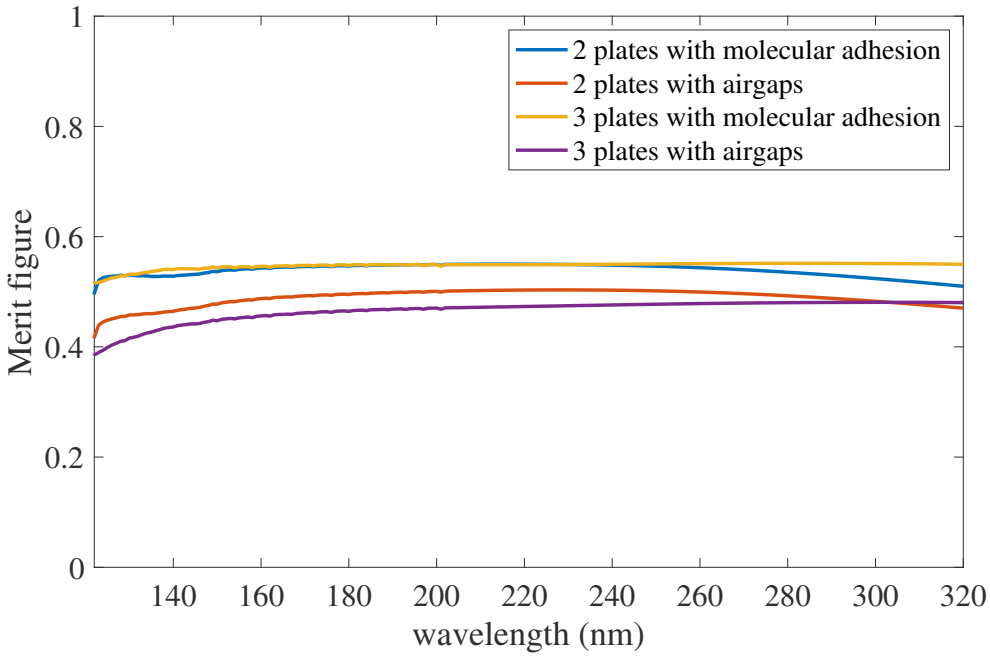

Figure 3.6: *Figures of merit for the studied modulators for PolStar.*

plates can be either optically adhered or comports airgaps. The molecular bonding version is preferred to increase the transmission of the polarimeter, nevertheless the airgaps version might be more robust. It has been shown that SiO_2 polarimeter were less efficient. All polarimeters achieve excellent polarimetric efficiencies around the optimum efficiency. The MUV polarimeter of POLLUX does not reach a waveband down to 118 nm. For wavelength under 121 nm, reflective polarimeter should be considered.

3.3 UV optical test facilities

In order to prove that these theoretical prototypes work in the UV range, we set up an experiment to test a prototype polarimeter under UV spectropolarimetry conditions. This experiment was mounted at the entrance of a high resolution vacuum-ultraviolet spectrometer at LERMA, a laboratory of the Paris Observatory. The goal of the experiment is to make spectropolarimetric measurements to prove the efficiency of the polarimeter. In order to test the polarimeter, the polarization response of the polarimeter must be characterized and its experimental modulation matrix measured. Indeed, the experimental matrix can differ from the theoretical one, as it takes into account the instrumental polarization or the misalignment of the bench. To do this, 100% Q, 100% U and 100% V polarized light are sent successively and the output intensity is measured for all modulation angles. Then, some

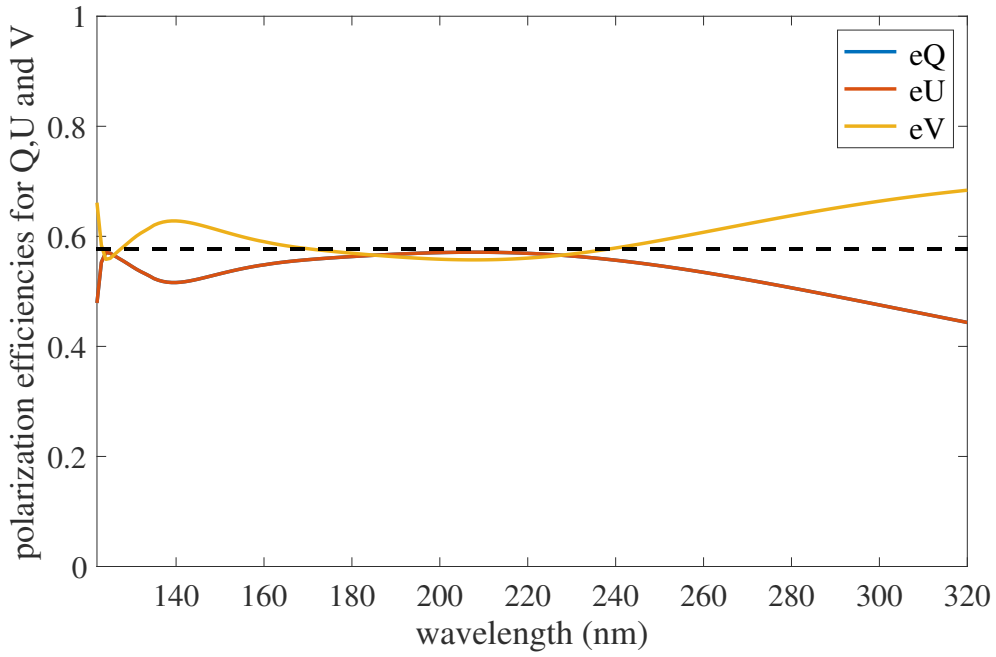

Figure 3.7: *Efficiencies for the 2-MgF_2-plates modulator chosen for PolStar. Q and U have the same efficiency curve.*

specific polarizations are measured across the spectrum.
The VUV spectrometer used is a high-resolution Rowland spectrometer and is presented in Section 3.3.1. The modulator used for this experiment is the one optimized for the POLLUX NUV channel. Although presented previously, its particular characteristics for this experiment are detailed in Section 3.3.2.

3.3.1 Test bench

The spectrometer of LERMA is a Rowland grating spectrometer: the entrance slit, the grating, and the detector are on the same circle called Rowland circle [43]. The circle of this spectrometer has a diameter of 10.6 m, for a 23-cm diameter grating and a detector of about 80 cm long. The grating is curved and creates an image of the slit on the detector. The detector consists of two photosensitive sheets placed side by side on a curved detector holder. The measured spectrum has a 20 nm long bandwidth with a resolution up to R = 200.000. Figure 3.8 shows a graphic of this spectrometer. This experiment has been achieved with the great help of Norbert Champion, the engineer in charge of the spectrometer.

The polarimeter test bench must be designed to fit at the entrance of the spectrometer and create an image on the entrance slit of the spectrometer. The spectrometer can be seen in the background of the picture in Figure 3.9. It is the big green vacuum chamber. At the

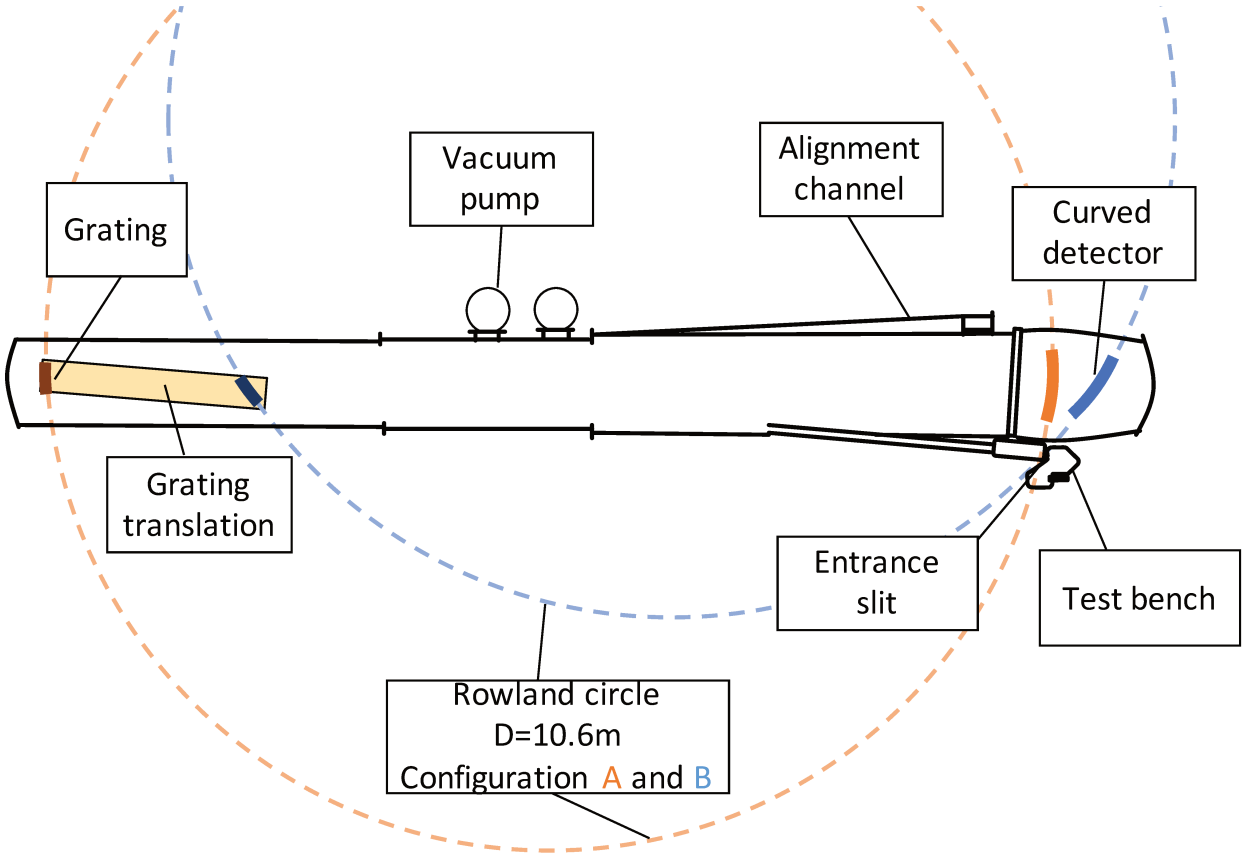

Figure 3.8: *Scheme of the Rowland spectrometer.*

foreground of the same picture, one can see the vacuum chamber in which the test bench stands at the input of the spectrometer.

The bench must first be equipped with a UV source, a linear polarizer, and a quarter-wave plate in order to create any polarized input. Since conventional linear polarizers do not exist in the UV at these wavelengths, a Rochon prism is used, set to its ordinary output. This choice is not ideal because in addition to reducing the transmission by its thickness, it splits the beam in two, dividing the flux by two. Reflection polarizers were considered and then discarded because the output light is only partially polarized and its polarizing effect is optimized for certain wavelengths, which introduces a strong chromatic effect. A diaphragm is used to block the extraordinary beam.

At the entrance of the polarization optics, rays must be parallel in order to separate properly the two orthogonal polarization beams and to create a homogeneous phase shift. To create these parallel beams, off-axis parabolic mirrors are used. The mirrors are coated by a supplier with a Al/MgF_2 coating insuring a high reflectivity at our studied wavelength. The curves of reflectivity are presented in the Appendix A. The use of lenses has not been considered in view of the low transmission of materials at these wavelengths. However, after

Figure 3.9: *Picture of the spectrometer with the test bench at the input. The spectrometer is the green chamber, the test bench is the aluminum chamber in the foreground.*

the experiment and in view of Section 3.4.2, this choice can be reconsidered.

The final test bench is shown in Figure 3.10. The optical design of the bench has been greatly constrained by the mechanics of the spectrometer. Indeed, the spectrometer being very closed, no solution permitting the measurement of both the ordinary and extraordinary beams simultaneously was found. The two beams are then measured one after the other. Therefore, the beams cannot be used together but should be considered as independent measurements. Also, the needed components were difficult to find and compromises were made. Indeed, by working under vacuum and in the UV range, a large number of components had to be tailor-made or vacuum-adapted.

Here is a list of the components used in the experiment:

- Source: Deuterium H2D2 Light Source L15094 from Hamamatsu. Spectral distribution from 115 to 400 nm, with an optimum from $\sim$ 130 to $\sim$ 170 nm. The spectrum of the source is presented in Appendix A. The study focuses on the 143-163 nm wavelength range as this is inside the brightest part of the H2 spectrum.

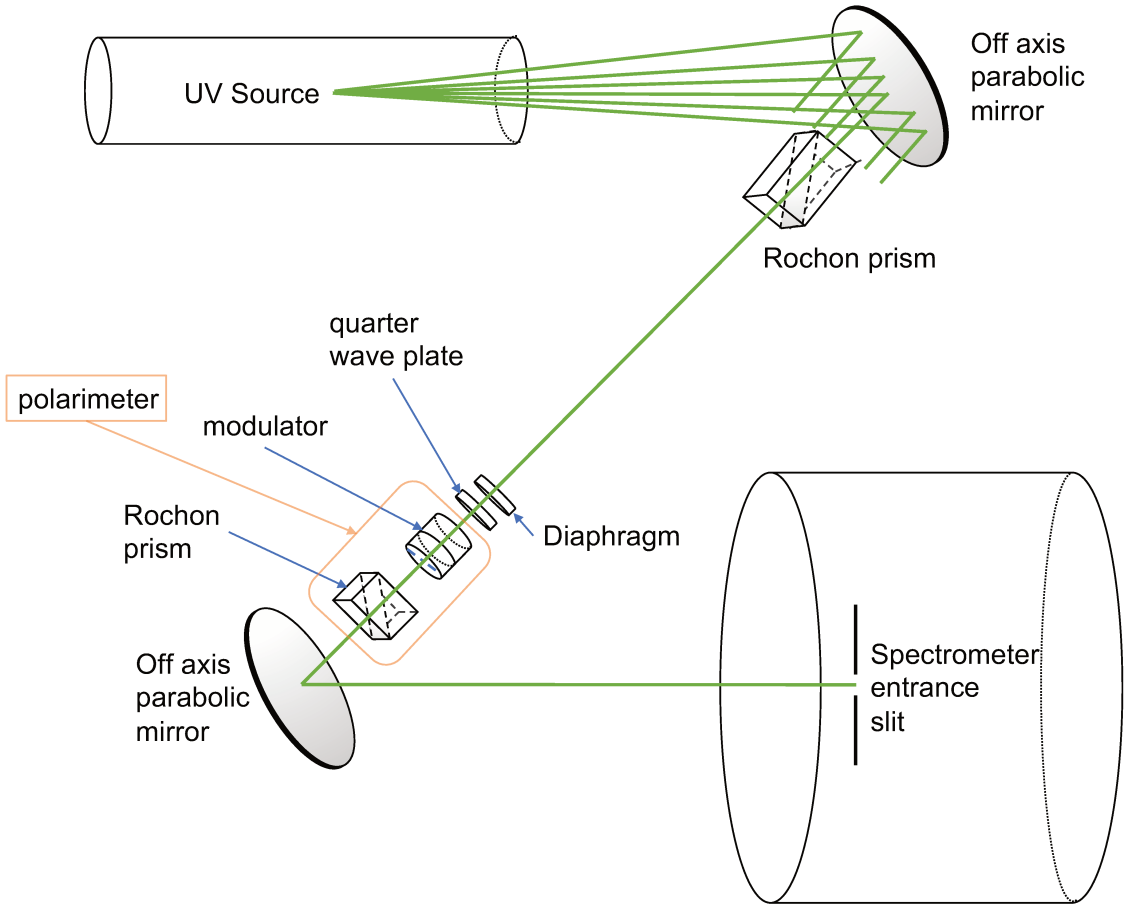

Figure 3.10: *Optical design of the test bench.*

- Quarter-wave plate: from the B. Halle catalog, designed for use in UV and optimized for 157 nm. The shift as a function of the wavelength is shown in the appendix A. The plate induces a slight chromatic effect.
- Polarizer: Rochon prism custom made by the company B. Halle, made in MgF_2. Length 13.5 mm and 4 mm diameter, making a 2.5°angle between ordinary and extraordinary beams.
- Off-axis parabolic mirrors: To decrease the price, we have chosen off-axis parabolic mirrors at Thorlabs with a coating of Al/MgF_2 made by eSource Optics for the first set of measure (ordinary beam), then Acton Optics for the second set of of measure (extraordinary beam), (see Section 3.3.2). The coating was more or less the same in both cases and insure a good reflectivity in UV, the curves are presented in AppendixA. As the Rochon prisms have a very small aperture, to ensure the required separations, the focal length of the mirror was chosen the shortest possible in order to concentrate the light as much as possible, but was mechanically constrained by the spectrometer.

- Electronic rotator: URS50BPPV6 from Newport, vacuum compatible. The repeatability of the rotator is 0.003°, and the accuracy is 0.02°.

- Vacuum chamber: it was designed by Youssef Younes (GEPI, Observatoire de Paris) and built partly by an external supplier and partly by Vartan Arslanyan and Claude Collin at the LESIA workshop. The mechanical part of the bench was not an easy task as it had to be vacuum compatible and allow the polarimeter to be controlled from outside. Indeed, in order not to break the vacuum too often, the modulation angles as well as a translation of the polarimeter had to be controllable from the outside of the chamber. The modulator is therefore mounted on a rotary motor, which can be controlled with a computer. Therefore, the modulator rotation is performed even when the chamber is under vacuum. The entire polarimeter, i.e. the modulator in the rotator and the analyzer, is mounted on a translation axis. This axis - controllable from outside the chamber - had to be created in order to make light intensity measurements without the polarimeter: they are the intensity calibration measurements.

- Grating - Aluminum concave grating with a curvature radius of 10.685 m and 3600 grooves/mm

- Detector: Photostimulated luminescence screen IPTR2040, fujifilm

- Image Scanner Starion FLA9000N, fujifilm.

Figure 3.11 shows a top view of the open chamber. All the components are represented inside the vacuum chamber.

3.3.2 Polarimeter

The NUV modulator, although not optimized for these wavelengths, was used for this experiment. However, the modulation angles were re-optimized for the wavelengths of the experiment. As the optical bench does not transmit both ordinary and extraordinary beams, the beams were measured independently. Therefore, the acquisitions are considered as independent measurements, making the modulation and demodulation matrices twice as large. The optimization of the modulation angles also reduced the number of angles to 4. This choice was important because the lifetime of the mirrors of the experiment was very limited (see Section 3.4.2). Each modulation angle represents 9 full days of measurements. The modulation angles used are: 125.9°, 13.9°, 158.7°and 50.6°. The theoretical efficiency of this modulator is shown in Figure 3.12.

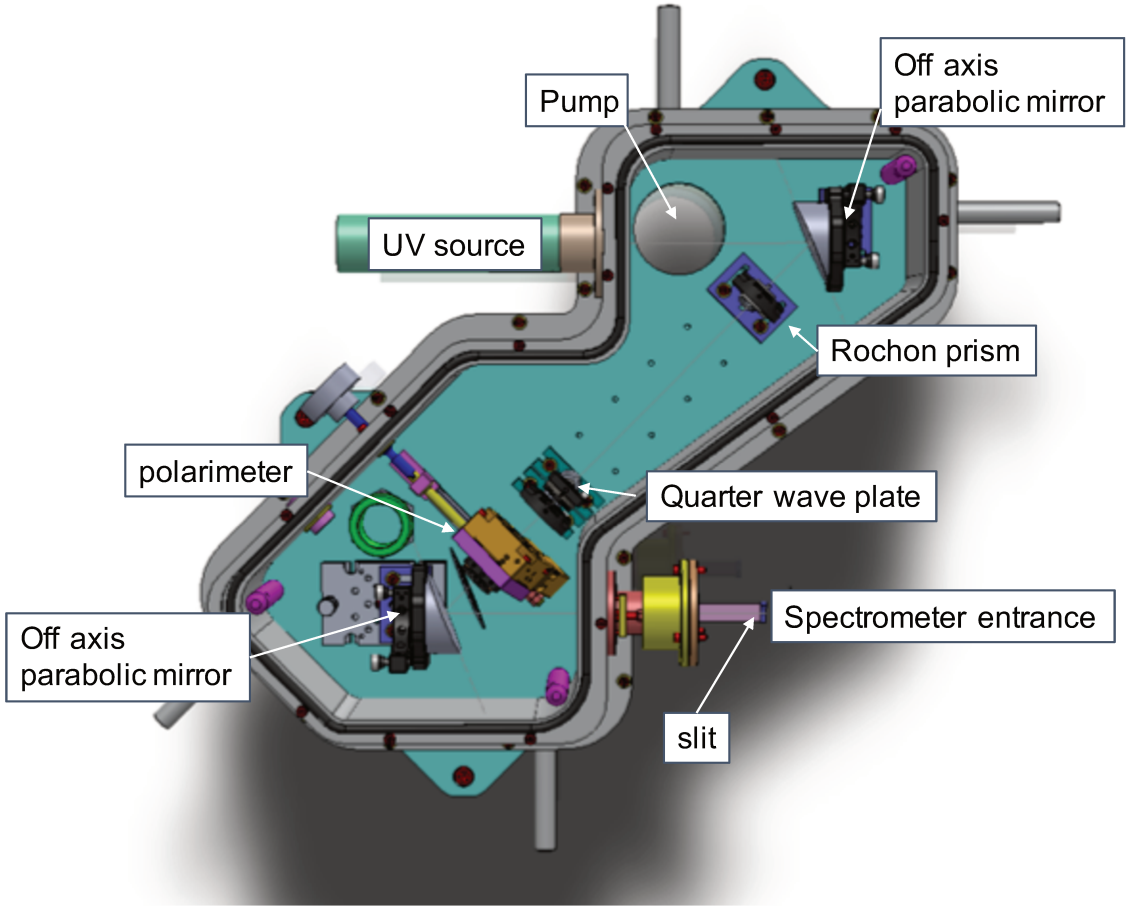

Figure 3.11: *Top view scheme of the mechanical test bench.*

3.4 Acquisition and processing

3.4.1 Protocol

As explained before, the ordinary and extraordinary beams could not be measured in parallel because of the small aperture of the spectrometer. As a result, the experiment has been made in two parts: the ordinary beam was first measured completely, then the bench was realigned to measure the extraordinary beam. Once the ordinary beam has been aligned, the first step was to measure the transmission of the polarimeter, then to test the answer of the experiment to different exposure time. The modulation matrix was then measured and finally specific polarizations were acquired. This same procedure was then applied to the extraordinary beam. A calibration measurement is made before and after each measurement. Indeed, the measurements being very long, the intensity of the lamp can strongly vary. To limit this effect as much as possible, the lamp is switched on 15 minutes before the beginning of the experiments to warm it up. Finally, the schedule of the measurements is always the

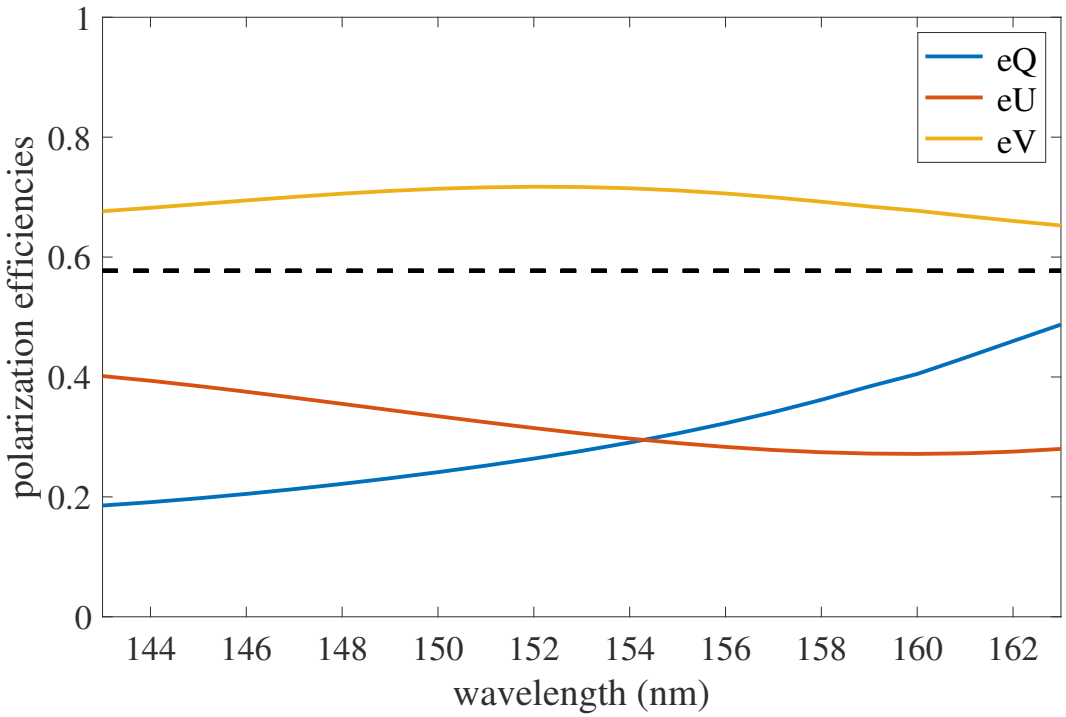

Figure 3.12: *Efficiencies for the NUV modulator adapted to the experiment from 143 to 163 nm.*

same: 10 minutes of calibration, 1h30 of measurement, 10 minutes of calibration, 1h30 of measurement, 10 minutes of calibration for the ordinary beam, and 1h of calibration, 3h of measurement and 1h of calibration for the extraordinary beam. Between each measurement, it takes only a few minutes, the time to make the necessary changes in the bench. After each acquisition, the vacuum is broken in order to extract the detector and change the optical configurations not accessible from the outside. The vacuum takes about 5 hours to recover an acceptable value ($\sim 10^{-6}$ mbar), so only one acquisition is made per day.

3.4.2 Loss due to the darkening of a mirror

After a few weeks of experiments, we noticed a great decrease of flux in our measurements. The observation of the optics lead to the discovery of a dark stain on the first mirror, close to the source, at the place where the flux hits it, as one can see in Figure 3.13. This stain seems to be the source of the flux loss. Two explanations were considered for this darkening: color center or contamination.

Contamination: The darkening of the mirror might have been caused by the burning of a deposit on the surface of the mirror resulting from a contamination of the chamber from

Figure 3.13: *Picture of the dark stain on the first mirror. The stain is encircled in red. The contrast has been optimized in order to make the spot more visible. In real light, the spot is slightly less visible.*

other objects (mounts, motor...) or an unsuccessful cleaning process after the manufacturing of the mirror.

Color centers: The color centers are produced by an absorption of light in a material with punctual imperfections. Indeed, contrary to a perfect material, a material containing imperfections will capture or give up electrons more easily. It is this phenomenon that will color the material.

It has been shown that annealing can eliminate color center, though the temperature of annealing has to be adapted to the material. We asked our supplier about the temperature we could use without damaging the mirror: 100°C. The mirror was heated at 82°C for 48 hours to see if the darkening disappeared. Unfortunately, this did not bring any change to the mirror. Based on this study, no conclusion can be made on the nature of this darkening. Indeed, it should be noted that the temperature of 82°C does not damage the mirror but is not necessarily the right temperature to remove eventual color centers in the materials of this mirror. The right temperature depends on materials, their structures but as seen in [9], a suitable temperature to remove color centers for Terbium Gallium Garnet crytals (known as TGG crystals) is 900°C. The order of magnitude of temperature required to remove the color centers is likely well above the conceivable temperatures for this mirror. The mirror was then sent to a private laboratory specialized in material analysis. Three kind of analysis were performed. First a spectromolecular analysis was performed in order to analyze a potential contamination dissolved in dichloromethane. This revealed a very low presence

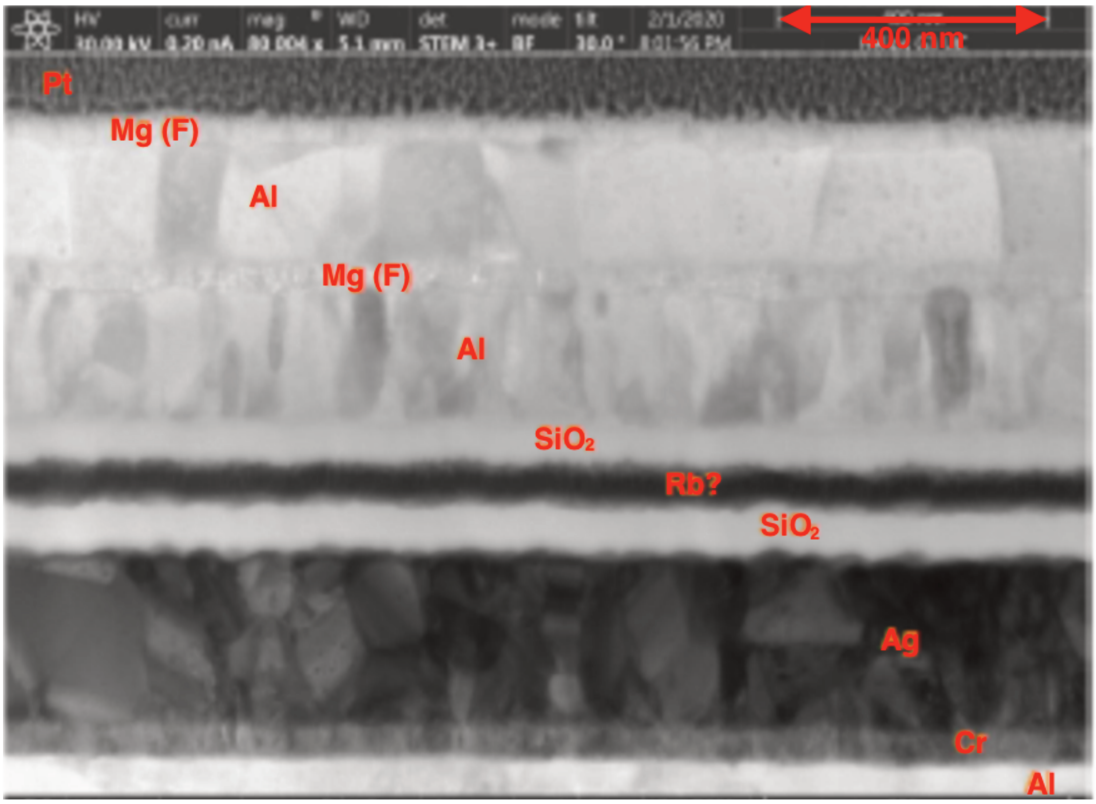

Figure 3.14: *Results of the analysis of the darkened mirror using a Scanning Transmission Electron Microscopy. Credit: Soditech.*

of silicon. The company could not conclude in favor of a contamination by silicon due to the very small amount found and they could not affirm that it was not a reaction from their own analyses. Also, the dissolution of the alleged contamination did not remove any darkening, as the color seemed inside the mirror. Two other more in-depth analyses were performed. First, the mirror was observed using a Scanning Electron Microscopy (SEM). Then a slide was analyzed using a Scanning Transmission Electron Microscopy (STEM). These analyses highlight many components inside the mirror: carbon, magnesium, fluorine, aluminum, silicon, platinum, oxygen, ribidium, silver, and chromium. These analyses did not reveal any contamination during the experiment, but tend to conclude that the mirror contains many contaminants in depth other than the theoretical aluminum and magnesium fluoride. This structure studied with STEM is showed in Figure 3.14.
The mirrors being ruined anyway, a contact cleaning with ethanol and optical paper was carried out (usually unthinkable for a use in UV). This cleaning removed a good part of the stain and increased the measured intensity by a factor 4. However, it is not clear if this is due to external contamination that was removed or if it is the mirror coating that was abraded. In addition, scratches are inevitable. This solution is not viable.

As no conclusion could be made from the analyses carried out, this effect could not be removed. A new intensive cleaning of the vacuum chamber and all components was made. New mirrors were ordered, and the goal was to perform the experiment before observing the mirror darkening. The darkening appeared again with the new mirrors. The use of mirrors seemed obvious for reasons of flux optimization. However, in view of the problems encountered during this experiment, the use of high quality MgF_2 lenses for intense light flux should be considered in the future.

3.4.3 Spectrum extraction and spectral calibration

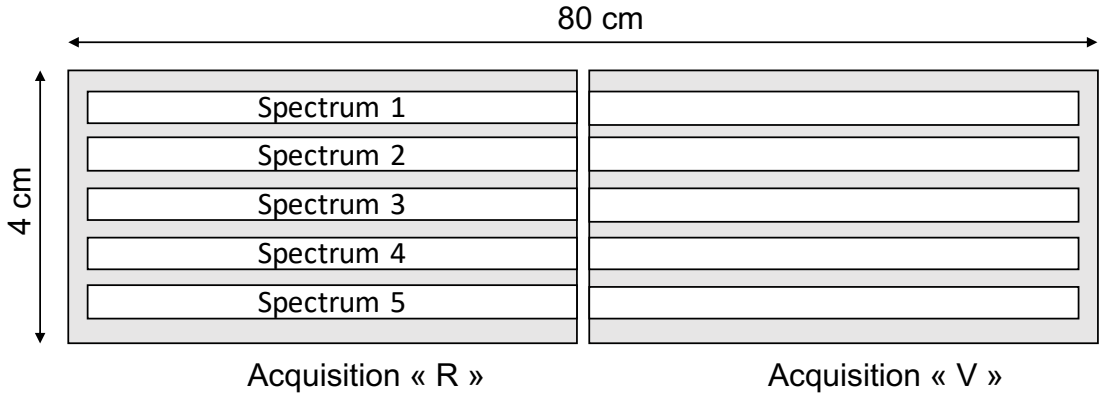

Figure 3.15: *Scheme of the photosensitive sensors. The proportions are distorted to make the drawing more readable.*

In Figure 3.15, a standard acquisition is shown as an example: 5 spectra and two photosensitive sheets are measured for each acquisition. The sensors are next to each other and measure different part of the spectrum. The photosensitive sheet "R", for red, is the one with the longest wavelength and the "V", for violet, is the one with the shortest wavelength. Each detector records a spectrum with a bandwidth of 10 nm. The two detectors together measure a 20 nm bandwidth spectra. In each acquisition, several spectra can be made in the height. *The two sensors with several spectra are called an acquisition. A spectrum inside one acquisition is called a measurement.*

The extraction of the five spectra from the image as well as the formatting of the spectra requires some processing. The method is detailed in the following paragraphs. First, we need to detect the beginning and end of each spectrum for each column of the image. The spectra being very noisy in the violet, the detection is not always correctly done. Then, a fit is used to extract the edges of the spectrum based on the edges detected for each column of the spectra. The detection of the edges is presented in Figure 3.16. Once the spectra are detected, it is easy to extract and rotate them. One detected spectrum is shown in

Figure 3.17. The image is distorted to emphasize the misalignments produced by the extraction method. Indeed, the slightly curved spectra could not be unwind with this extraction method. The curvatures are less than 1°and thus are considered negligible. Following the extraction of this spectrum, the edges are cut, to avoid considering non-complete lines over the entire spectrum. Then the lines are correlated one by one to ensure the verticality of the spectral lines and not to lose resolution. As the spectral distortion is not perfectly linear, the correlation was not done on the entire spectrum but by bins of 100 pixels. The spectra are now ready to be vertically summed. All spectra have been summed over 600 pixels.
All spectra are calibrated in wavelength to the same reference spectrum before being processed. The reference undergoes a polynomial spectral calibration based on 32 (resp. 58) spectral line references for the "R" photosensitive sheet (resp. "V") converting pixels to nanometers. The resolution achieved is 5.10^{-3} nm. The continuum is the level of the flux outside the spectral lines. The continuum is not homogenous over the spectrum depending on the transmission of the bench and on the source. Its extraction is presented in Figure 3.18.

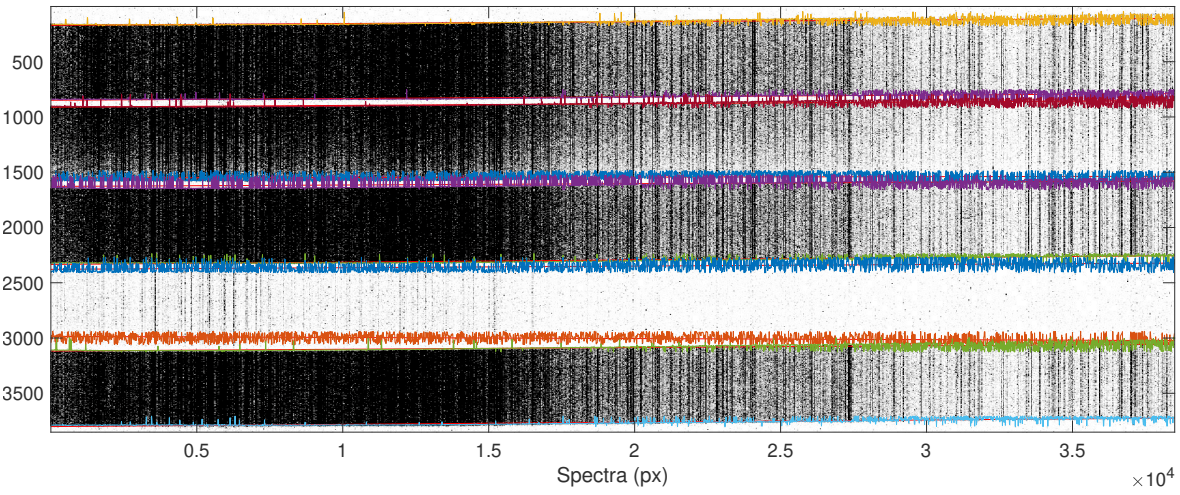

Figure 3.16: *Extraction of the five spectra from an acquisition. The image is stretched vertically to be more visible. Only one sensor is presented here. The contrast is enhanced in order to make the five spectra visible at the expense of spectral line visibility.*

3.4.4 Calibrations

During the experiment, for the ordinary beam (resp. extraordinary beam) spectra 1, 3 and 5 (resp. spectra 1 and 3) are calibrations and spectra 2 and 4 (resp. spectrum 2) are measurements. Calibrations are exposed 10 minutes (resp. 1h) and are taken without polarimeter. They depend on the polarization components present in the chamber and are

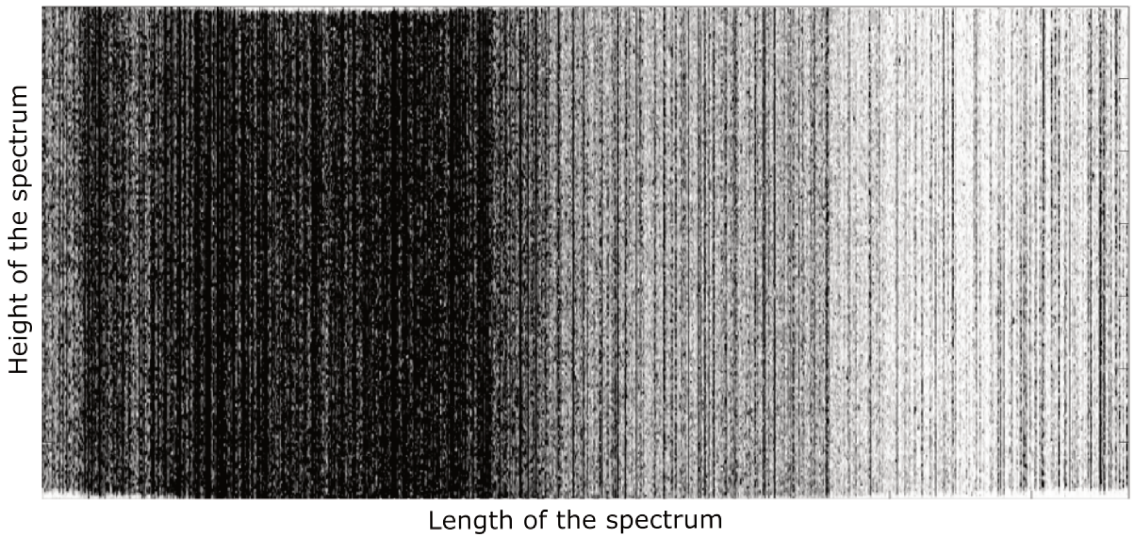

Figure 3.17: *A spectrum extracted from an image acquisition. The image is stretched vertically to be more visible.*

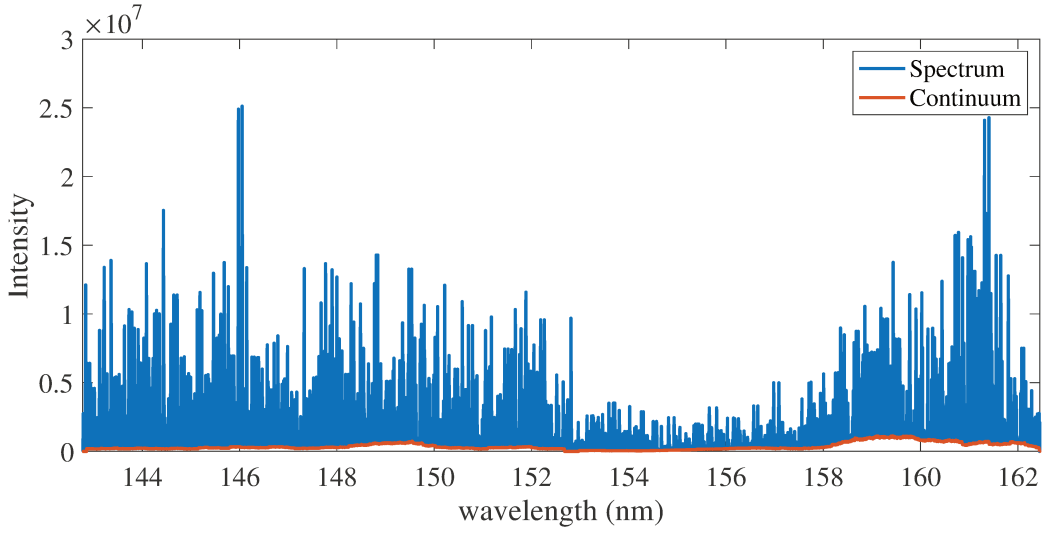

Figure 3.18: *A spectrum summed over its height and its continuum are presented.*

therefore not comparable from one acquisition to another, but they are identical inside one acquisition. These calibrations also are a measure of the flux going inside the polarimeter: by multiplying them with the transmission of the polarimeter, the calibrations define the Stokes parameter I. The evolution of the light flux as a function of time can be observed from these calibrations. Indeed, the light flux can change due to the fluctuations of the lamp, but also the darkening of the mirror. Using these calibrations, the response of the test bench can

be studied. It defines the linearity in intensity and exposure time, but also the repeatability of the measurements.

Transmission

The transmission of the polarimeter is shown in Figure 3.19. This transmission takes into considerations the analyzer (and the loss of 50% of the flux) and the modulator. Transmission was measured as the ratio of a spectrum with a polarimeter to a spectrum without a polarimeter. The measurement of this transmission incorporates several problems. First, to make this measurement, the incoming intensity should be unpolarized. However, even if the polarization optics have been removed from the optical path for these measurements, there is no guarantee that the light leaving the lamp and after reflection from a mirror is unpolarized. Furthermore, when the polarization optics are added to the optical path, the optical path is slightly modified, and the transmission is impacted.

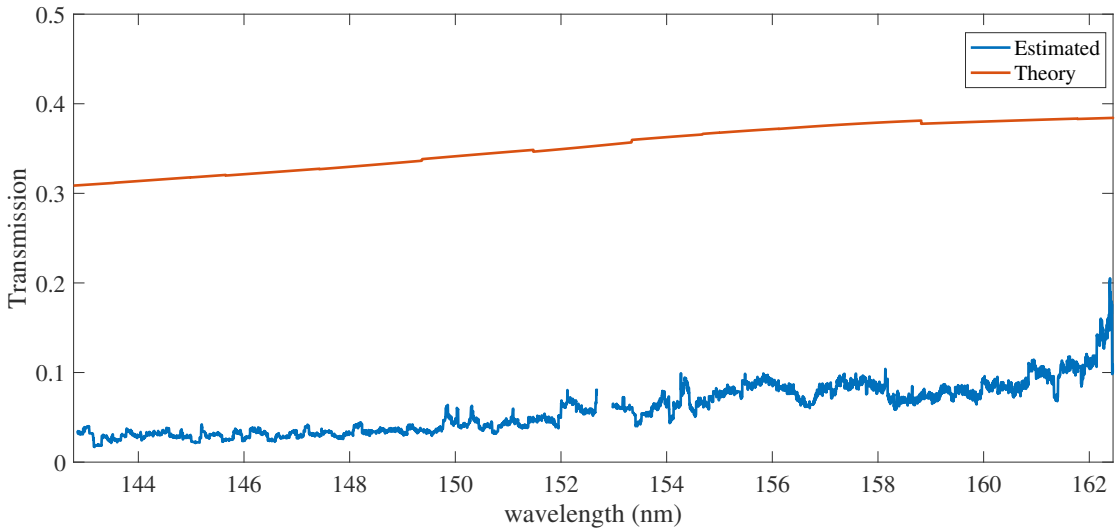

Figure 3.19: *Transmission of the polarimeter. The blue line corresponds to the experimental transmission. The red line corresponds to the theoretical transmission.*

The measured transmission was re-evaluated with the measurements obtained during the experiments to better fit our theoretical model. These measurements were made only for the ordinary part of the experiment. The transmission could not be measured during the extraordinary part of the experiment, it was simulated to fit our theoretical model. The re-evaluated ordinary transmission and the extraordinary transmission are identical. The re-evaluation of the transmission has no impact on the polarization measurement.

The experimental transmission is between 0.02 and 0.2 whereas the theoretical transmission is between 0.3 and 0.4. This can be explained partly by the alignments. We also have

suspicions about the condition of the optics used for the polarimeter. Indeed, by observing the effect that the radiation from the source had on the first collimation mirror 3.4.2, one can wonder about the impact it has on all our optics.

Linearity

During the experiment, several integration times were used to adapt our acquisition to some very low intensity measurement as well as the decrease of intensity due to the darkening of the mirror. To control these changes, a calibration with different integration times was acquired. 5 spectra without polarimeter were measured with the following integration times:

1. 10 minutes
2. 20 minutes
3. 1 hour 30 minutes
4. 3 hours
5. 6 hours

To exploit the results of our experiment, it is important to determine a linearity between these measurements. Almost all the measurements last 1h30 (respectively 3h) and the calibrations 10 minutes (respectively 1h) for the ordinary beam (respectively the extraordinary beam).

The linearity of the measurement was studied both in time and in intensity.

- **Linearity in time**
  The first idea is to check if a measurement lasting 1h30 is the same as the sum of 9 measurements of 10 minutes. In Figure 3.20, the 5 spectra are displayed normalized to a 1h30 exposition. This means the spectrum of 10 minutes has been multiplied by 9, the one of 20 minutes by 4.5, the one of 1h30 by 1, the one of 3 hours by 0.5 and the one of 6 hours by 0.25. As one can see, the spectra do not match each other. Therefore, the multiplying coefficients are not linear in time. In Figure 3.21, one can see a superposition of the 5 spectra normalized by their continuum. As one can see, the superposition is much better than in Figure 3.20, even though notable differences can still be observed in the spectral lines. There are two possible reasons for this problem: variation in the intensity of the source and variation in the response of the photostimulated screen. The linearity of the screen response will be studied in the next Section . For more visibility, Figures 3.20 and 3.21 show a little part of the spectrum, it has been observed that the study is similar over the full spectrum.

  This study shows that even though ratios between the spectra are not linear, they do follow a relationship between exposure time and intensity. In table 3.22, ratios

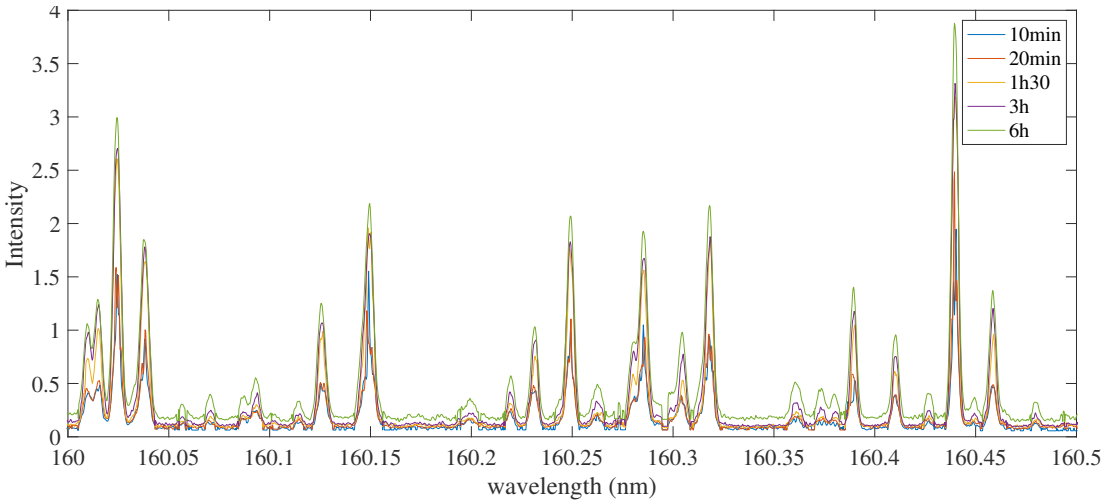

Figure 3.20: *Superposition of spectra of 10 minutes, 20 minutes, 1h30, 3h, and 6h exposure. Each spectra is normalized by its time exposure.*

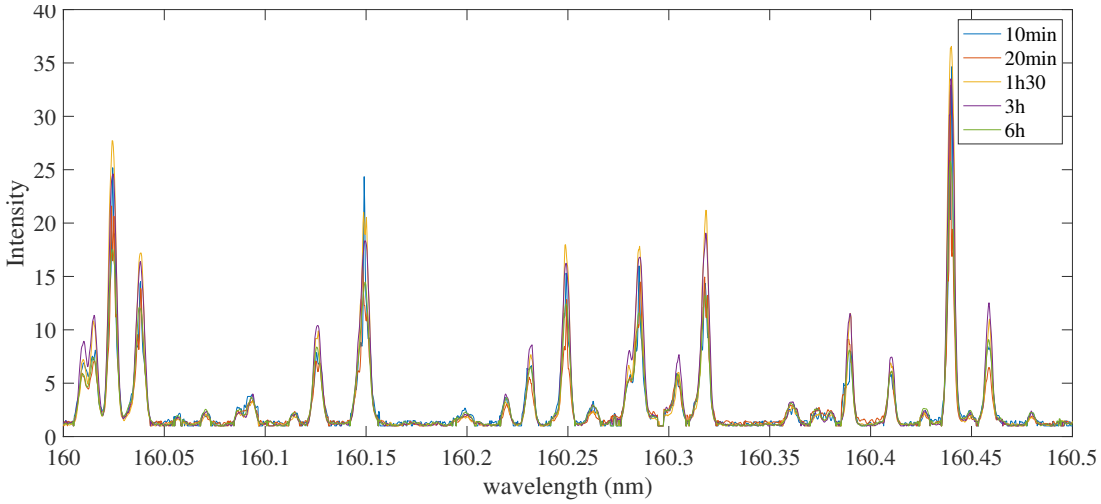

Figure 3.21: *Superposition of spectra of 10 minutes, 20 minutes, 1h30, 3h, and 6h normalized in intensity. Each spectra is normalized by its continuum.*

between spectra and the spectrum of 1h30 are computed. It is clear that the spectrum do not follow a linear variation in time. The tricky part is that the continuum and the full intensity of the spectrum do not vary similarly: the intensity seems to increase more rapidly at high intensity. The linearity in intensity is studied in the next Section. To counter this problem, only continuum variations will be studied to compute the polarization. The spectra of different integration times will be normalized using the curve presented in Figure 3.23. One can see the relationship between exposure times

and average intensities of their continuum. Even though, the relation is not linear, they obey a perfect polynomial equation. Nevertheless, this study lacks of calibrations: it does not consider the variation of intensity over a detector photosensitive sheet.

Integration time T	Time ratio $T/1h30$	Continuum ratio C/C_{1h30}	Intensity ratio I/I_{1h30}
10 minutes	0.11	0.09	0.07
20 minutes	0.22	0.19	0.17
1h30	1	1	1
3h	2	2.20	2.40
6h	6	5.16	6.31

Figure 3.22: *Summary of the ratio between the studied spectra and a spectrum of 1h30 in time and in intensity.*

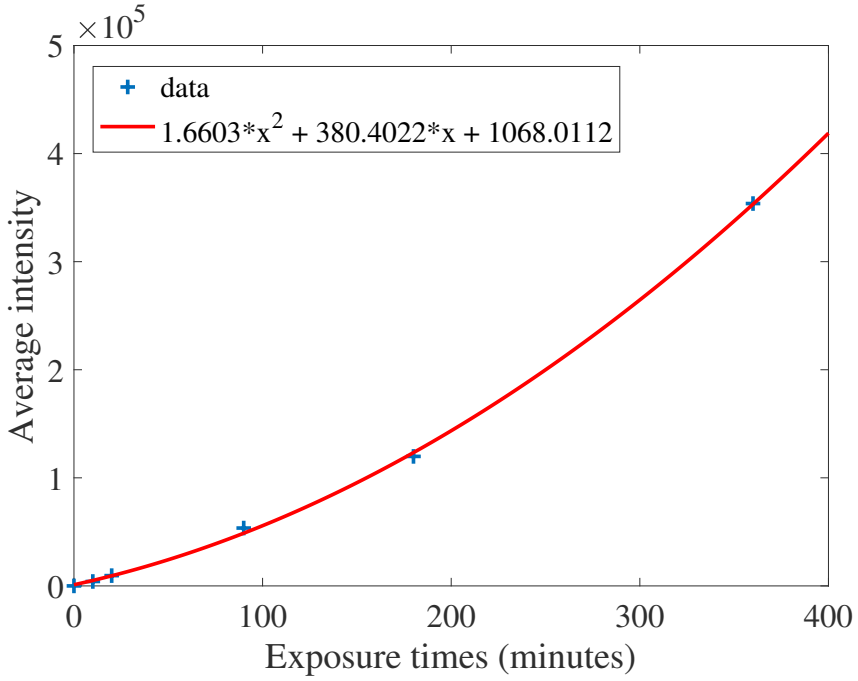

Figure 3.23: *Relation between average intensity of the continuum and exposure time.*

- **Linearity in intensity**
  The previous Section finds a good correlation between the integration time and the average intensity of the continua, but raises questions about the linearity in intensity: indeed, when the continuum is set to the same level once the spectra are calibrated,

the more intense lines still have glaring differences in intensity. In Figure 3.24, one can see the ratio between spectra normalized to their continuum and the normalized 6-hour spectrum as a function of the intensity of the non-normalized studied spectrum.

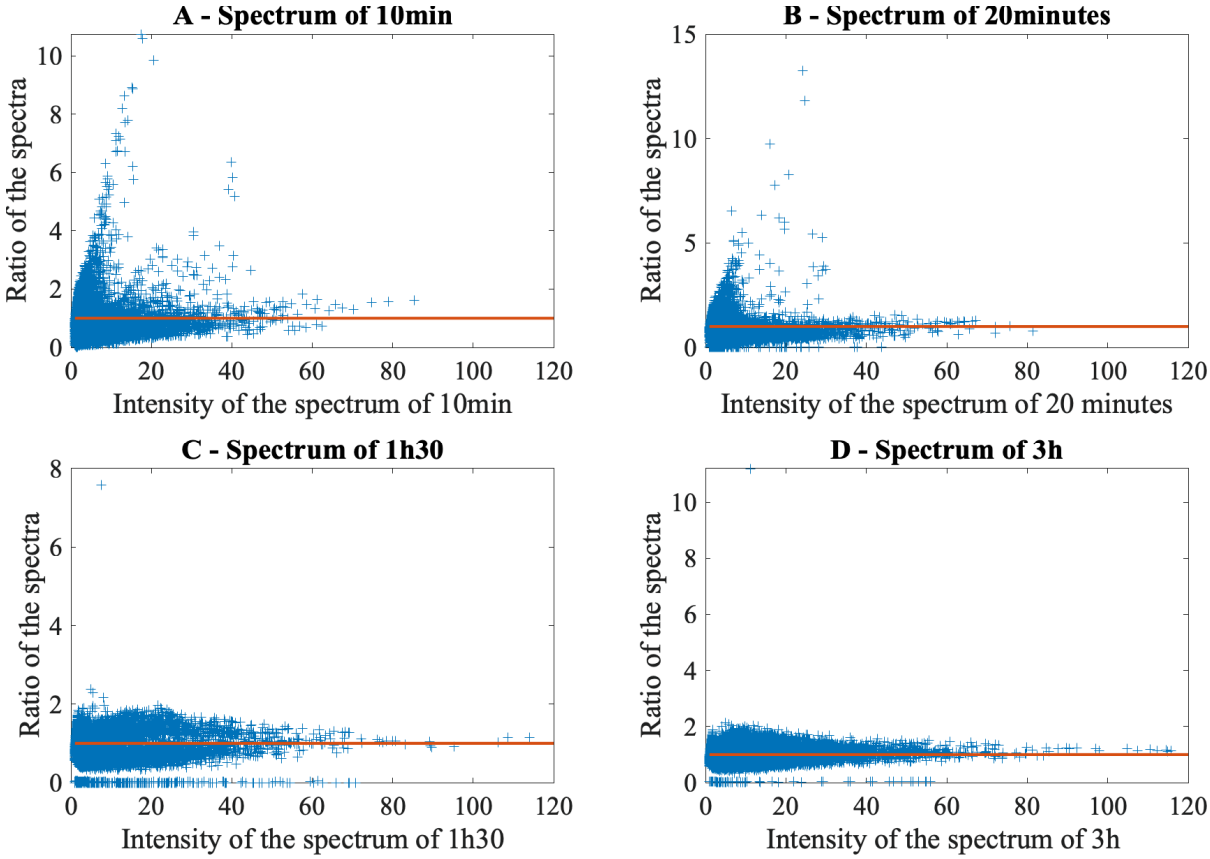

Figure 3.24: *Ratio of the spectra of 10 minutes (A), 20 minutes (B), 1h30 (C), or 3h (D), and of a spectrum of 6h as a function of the intensity of the considered spectrum (A, B, C, or D). The orange line equals to 1.*

All spectra were normalized by their continuum. If acquisitions were linear in intensity, the ratio would be around 1 whatever the intensity of the studied original spectrum. The curves detect some spurious lines in the spectrum of 10 and 20 minutes: indeed, sometimes an artifact creates a false detection of signal, especially for the short exposure times it reaches the same intensities as the recorded spectral lines. Nevertheless, these false lines are less significant on the 6 hours spectrum, this is why it has been chosen as the reference of this study. When spectra are normalized by their continuum, when false lines appear in the short exposure time, the normalized 6hours spectra is at 1, while the studied normalized spectra is above. This creates a line at y=x. These errors do not appear in the 1h30 and 3h00 spectra. However, another problem appears

in these spectra: some points are close to 0. These points are continuum detection errors. Some points are considered as continuum in the 1h30 and 3h spectra, but not in the one of 6h. Normalized points near 1 are then divided by the lines of the 6h spectrum, making a near 0 value. Apart from these problems, we see that the curves follow a straight line close to y=1, no non-linearity in intensity is detected statistically. However, an important spreading of the data points shows the errors caused by the noise are up to 100%.

Repeatability

The repeatability of the measurements is studied here: if the same measurement were performed several times, will they be the same? The repeatability or continuity is the ability to measure the same spectrum when reproducing the same condition on the same photosensitive sheet. We have several sets of data to study the repeatability:

- Each acquisition includes 3 calibrations measurements (spectra 1, 3, and 5 as seen before). Calibrations can be compared within each acquisition.
- Two acquisitions were obtained with two identical spectra to study the repeatability (spectra 1 and 2). In one acquisition, two spectra of 1h30 were recorded. In the other one, 2 acquisitions of 3h were obtained.

We have 10 acquisitions with 3 identical measurements at positions 1, 3, and 5 of the detectors "R" and "V". The measurements differ from one acquisition to another, and only the variation within one acquisition needs to be studied. For this purpose, the measurements are normalized to the first spectrum within each acquisition. The variations for these intensities are shown in Figure 3.25. The data are shown for both plates "R" and "V" in the same colors, R as a solid line and V as a dashed line. Unfortunately, even though we can clearly see that there is a large variation of intensity inside one acquisition, there is no clear tendency on how the intensity changes. This shows the importance of calibrations inside one acquisition. Indeed, within each acquisition the variations seem slow enough to be considered as linear. This shows that our measurements can be calibrated in intensity with these calibrations spectra. The dates of acquisition have been added in the legend to investigate a potential effect of time. A slight correlation seems to appear: the variations seem to decrease as the date increases, even though the correlation is not perfect. This could be explained by the darkening of the mirror which got stronger as the measurements were taken.

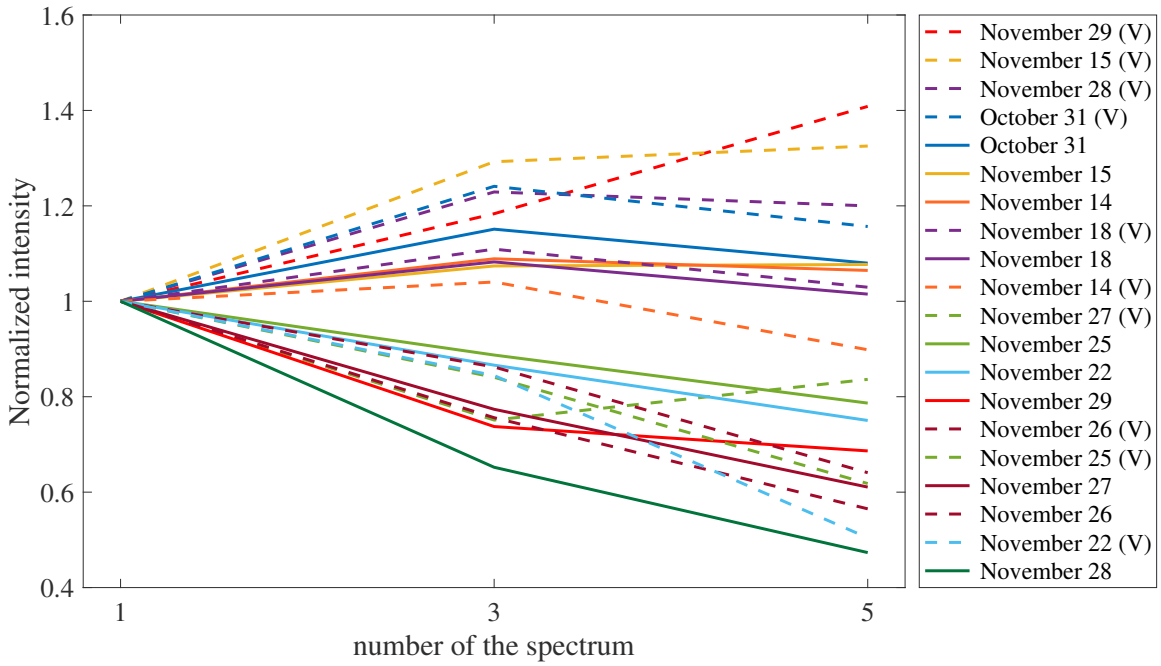

Figure 3.25: *Variation of the mean intensity of the continuum as a function of its number on the detector. Each line corresponds to a different acquisition thus a different date.*

In Figure 3.26, one can see two intensity ratios between two identical spectra. The ratio is constant along the spectrum, with an average around 0.9. The black lines represent the linear fits of the two ratios. Noise is up to 20% on the intensity of the spectrum. On the orange ratio, one can notice an important error around 153 nm up to 60%. This area is between the two detectors "R" and "V", and can therefore be considered as an edge effect. This error is not systematic and will be excluded if appearing on measurement spectra.

3.4.5 Results

(De)modulation matrices and efficiencies

The intensity measured at the polarimeter output is a linear combination of the input Stokes parameters:

$$I_{out}(\lambda) = T(\lambda) * (I_{in}(\lambda) + \alpha_Q(\lambda) * Q_{in}(\lambda) + \alpha_U(\lambda) * U_{in}(\lambda) + \alpha_V(\lambda) * V_{in}(\lambda)) \tag{3.8}$$

where I_{out} is the intensity measured by our experiment, T is the transmission of the polarimeter, I_{in} is the intensity going inside the polarimeter thus, the calibration. $\alpha_{Q/U/V}$ is the coefficient of modulation we want to measure to create our modulation matrix and Q, U and V are the elements of the Stokes vector of the polarized source.

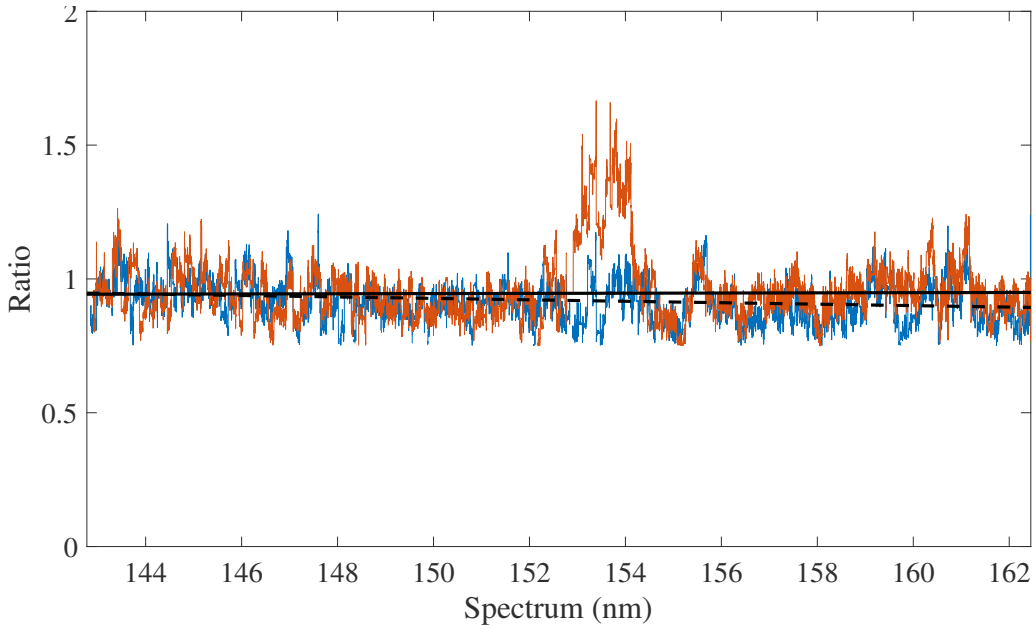

Figure 3.26: *Ratios between two identical spectra on the same acquisition over the spectrum.*

In conventional polarimetry, the beams are combined to retrieve polarimetric information by overcoming nominal intensity problems. The combination of the beams is described in [46]. In our case, as the beams were measured months apart and with different optical alignments, the conventional method cannot be used. In addition, the nominal intensity entering the polarimeter varies with the lamp and the polarization components, so calibrations must be taken into account. Ordinary and extraordinary beams are considered independent. The methods used for the two beams are slightly different:

- Ordinary beam
  For the ordinary beam, the modulation matrix can easily be extracted. The calibrations are a measurement of I_{in}. The transmission was measured. In case of a 100% Q input, $U_{in} = V_{in} = 0$ and $I_{in} = Q_{in}$ then $I_{out} = T * (I_{in} + \alpha_Q I_{in})$. The corresponding modulation coefficient can be extracted directly by using the measured transmission and the calibrations.
  $$\alpha_Q(\lambda) = \frac{I_{out}(\lambda)}{T(\lambda) I_{in}(\lambda)} - 1 \tag{3.9}$$
- Extraordinary beam
  In the case of the extraordinary beam, the extraction of the coefficients is less direct as the calibrations could not be done without the polarimeter. Indeed, the extraordinary beam being deviated by the polarimeter, the bench was aligned with this deviation. Removing the polarimeter misaligned the bench. Thus, no measurement of I_{in} could be made for each polarization measurements. The calibrations in that case were made

with the polarimeter at a specific position, which is designed as the reference position. The calibrations were therefore a polarization measurement. A final measurement was made to "calibrate all the calibrations" together: the calibration measurements were recorded again at the same time as I_{in}: this makes it possible to reintroduce I_{in} with the right calibration made by the polarized measurement I_{ref} . For instance, for $U_{in} = V_{in} = 0$ and $I_{in} = Q_{in}$ we have

$$I_{out}(\lambda) = T(\lambda) * (I_{in}(\lambda) + \alpha_Q(\lambda) * Q_{in}(\lambda)) \tag{3.10}$$

$$\alpha_Q(\lambda) = \frac{I_{out}(\lambda)}{T(\lambda) * I_{in}(\lambda)} - 1 = \frac{I_{out}(\lambda)}{T(\lambda) * I_{ref}(\lambda)} * \frac{I_{ref}(\lambda)}{I_{in}(\lambda)} - 1 \tag{3.11}$$

In Figures 3.27 and 3.28, the experimental modulation and demodulation matrices are illustrated superimposed on the theoretical matrices. The experimental results have been fitted with polynomials in red. The first column of the modulation matrix is not displayed because it is the normalized intensity i.e. constant and equal to 1. Quite strong differences are visible between the experimental results and the theory for some coefficients, especially on the first angles of V, where the experimental measurements differ from the theory by more than 1. However, the coefficients follow a trend very close to the theory. The differences observed between theory and practice can be explained by many factors. First, the experimental matrix takes into account the instrumental polarization. This instrumental polarization is created by the components of the experiment and is not simulated in the theory. The determination of the experimental matrix should improve the polarimetric results by considering this instrumental polarization.

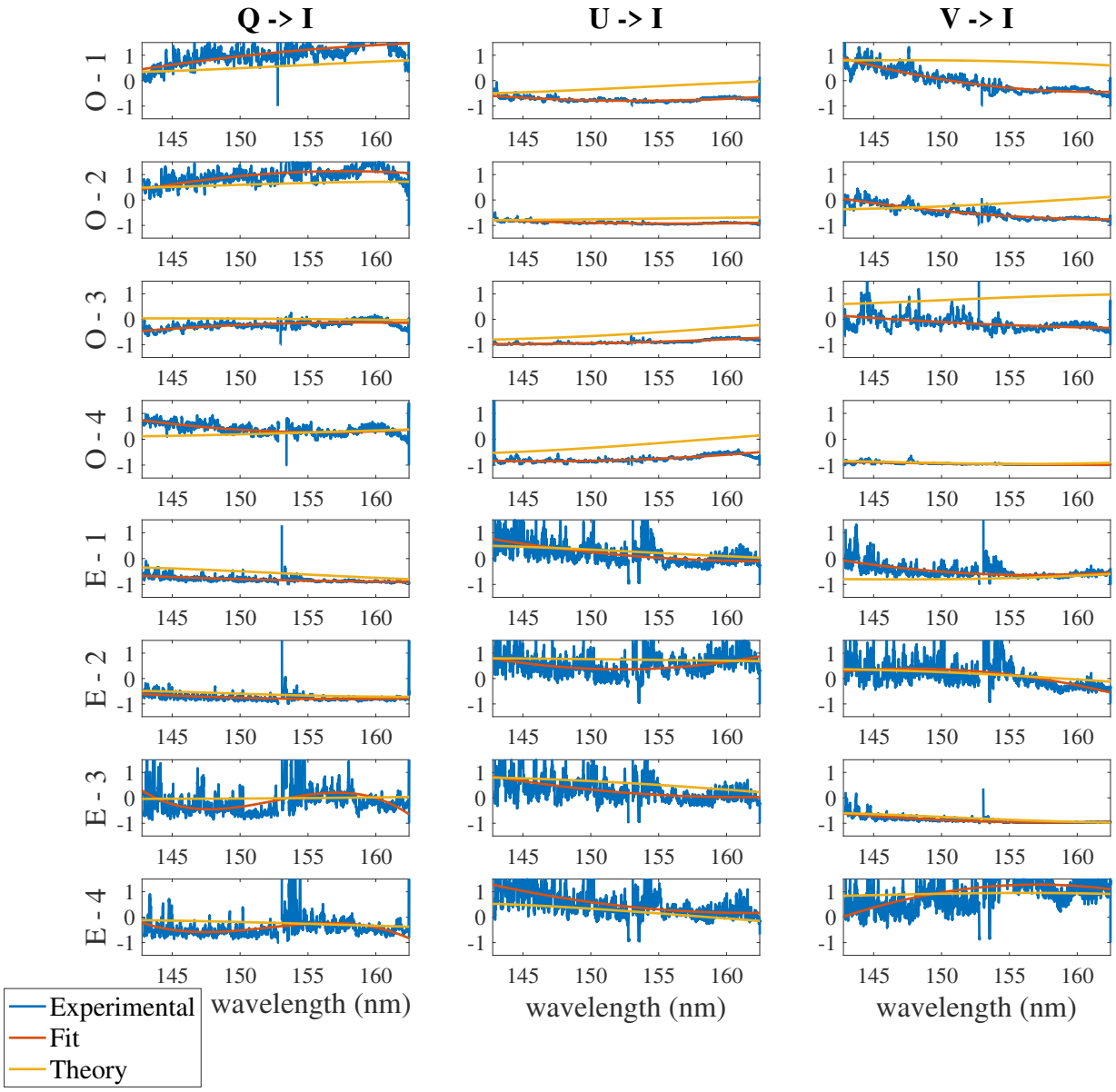

Figure 3.27: *Experimental modulation matrix. The blue line is the experimental matrix computed from the measurements. The red line is the fit of the experimental matrix. The yellow line is the theoretical matrix.*

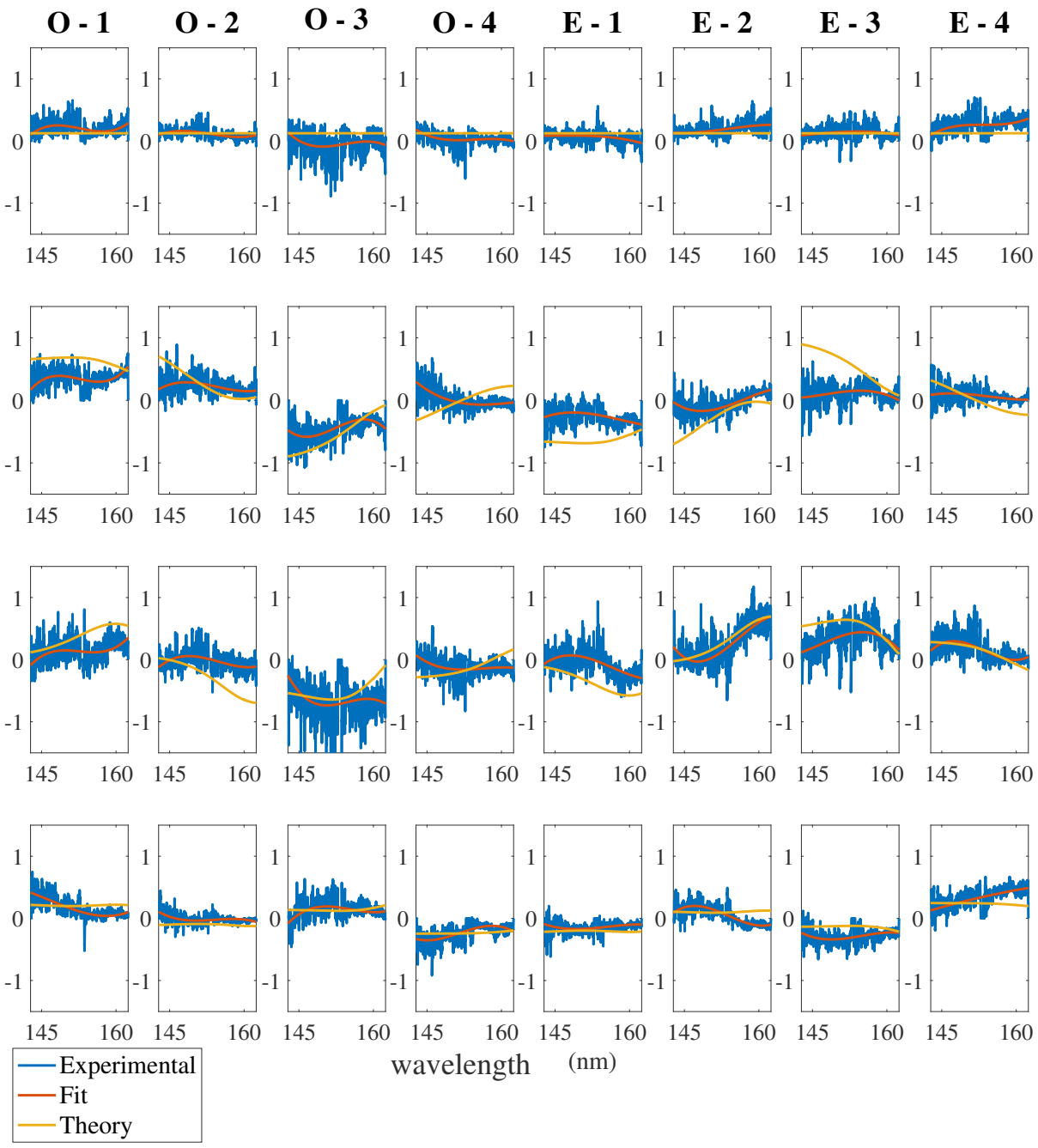

Figure 3.28: *Experimental demodulation matrix. The blue line is the experimental matrix computed from the measurements. The red line is the fit of the experimental matrix. The yellow line is the theoretical matrix. The intensity is at 1/8.*

It is also observed that in many measurements, especially in the extraordinary beam measurements, the noise is very high. This is explained by the low intensity of the measurements due to the many technical problems that occurred during the experiment. Moreover, as seen previously, the uncalibrated measurements showed intensity variations of up to 50%. It is difficult to estimate the intensity errors on the calibrated measurements. Finally, the matrix can differ from the theory due to some alignment errors. Indeed, an error in the alignment of the polarization creates a wrong polarized signal. These errors can easily be estimated but are insignificant compared to the error of intensity measurements.
We also observe that some coefficients, notably the first Q coefficients, are greater than 1 around 160 nm. These measurements have no physical meaning, they correspond to a combination of all the errors cited before.
Figure 3.29 shows the comparison between the theoretically calculated efficiencies and those measured in the experiment. It is observed that for the longest wavelengths, when the intensity is highest, the difference between the theoretical and experimental efficiencies are smaller.

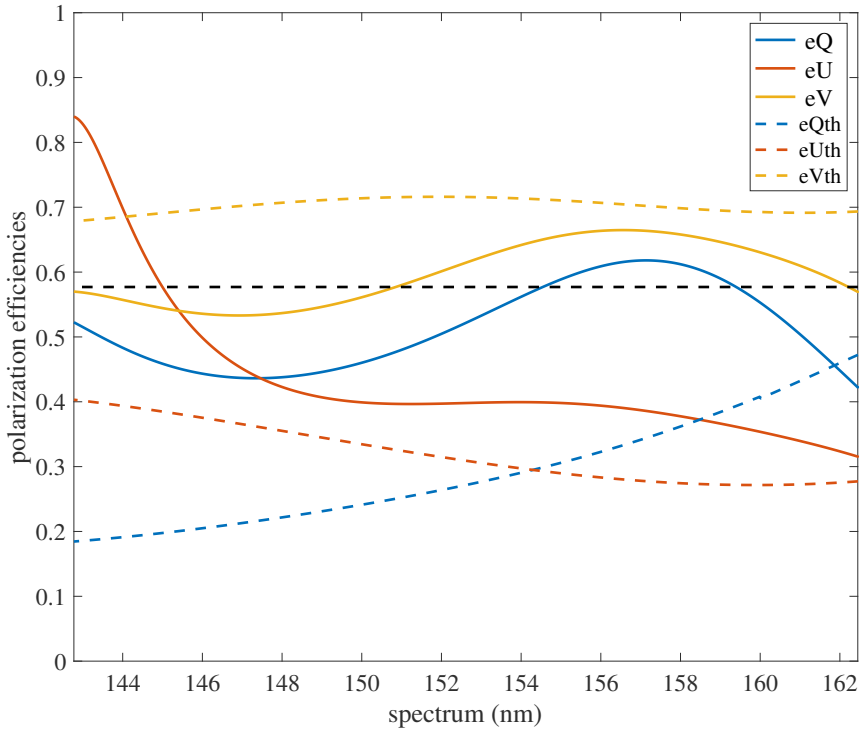

Figure 3.29: *Efficiencies calculated from the experiment and compared to the theoretical ones. The solid lines are the experimental measurements. The dotted lines are the theoretical simulations. The blue lines are the efficiencies for Stokes Q. The red lines are the efficiencies for Stokes U. The yellow lines are the efficiencies for Stokes V.*

Results of polarization measurements

In order to validate the measurements described above, specific polarizations should be measured to check if they are retrieved when using the experimental demodulation matrix and if we can identify the precision of the polarization measurements. Three polarizations were measured that we call polarizations A, B, and C. As these measurements were made at the end of the experiment, when the mirror was damaged, the intensity is very low. The data between 142 and 147 nm were discarded because the signal was not high enough. For polarizations B and C, only the ordinary beam could be measured. Therefore, only the ordinary modulation matrix was used to demodulate the intensity. In Figures 3.30, 3.31, and 3.32, the polarization measurement results are displayed (polarizations A, B, and C). Since the intensity measurements were a bit biased by the transmission measurement, and the measured polarization has a polarization degree of 1, the results are normalized to $Q^2+U^2+V^2$, which should be equal to the intensity I (see equation 1.4). I is forced to 1 and is then not presented. In blue, the Stokes vector found with our experimental demodulation matrix is shown. In orange, the theoretical demodulation matrix was used. In yellow, the theoretical input polarization is shown. For the three measurements A, B, and C, the measurements show better results using the theoretical matrix in orange than the experimental one in blue. This means that the intensity errors are higher than the instrumental polarization and alignment errors. Using the theoretical matrix, the main components of polarization are retrieved. Significant errors are present in the experimental measurements. The measurement of polarization A, made with both the beams of ordinary and extraordinary light, is better than the measurements of polarizations B and C.
Unfortunately, we cannot determine a satisfactory measurement accuracy based on this experiment. However, in all three measurements, the dominant polarization and an approximation of the input polarizations are retrieved.

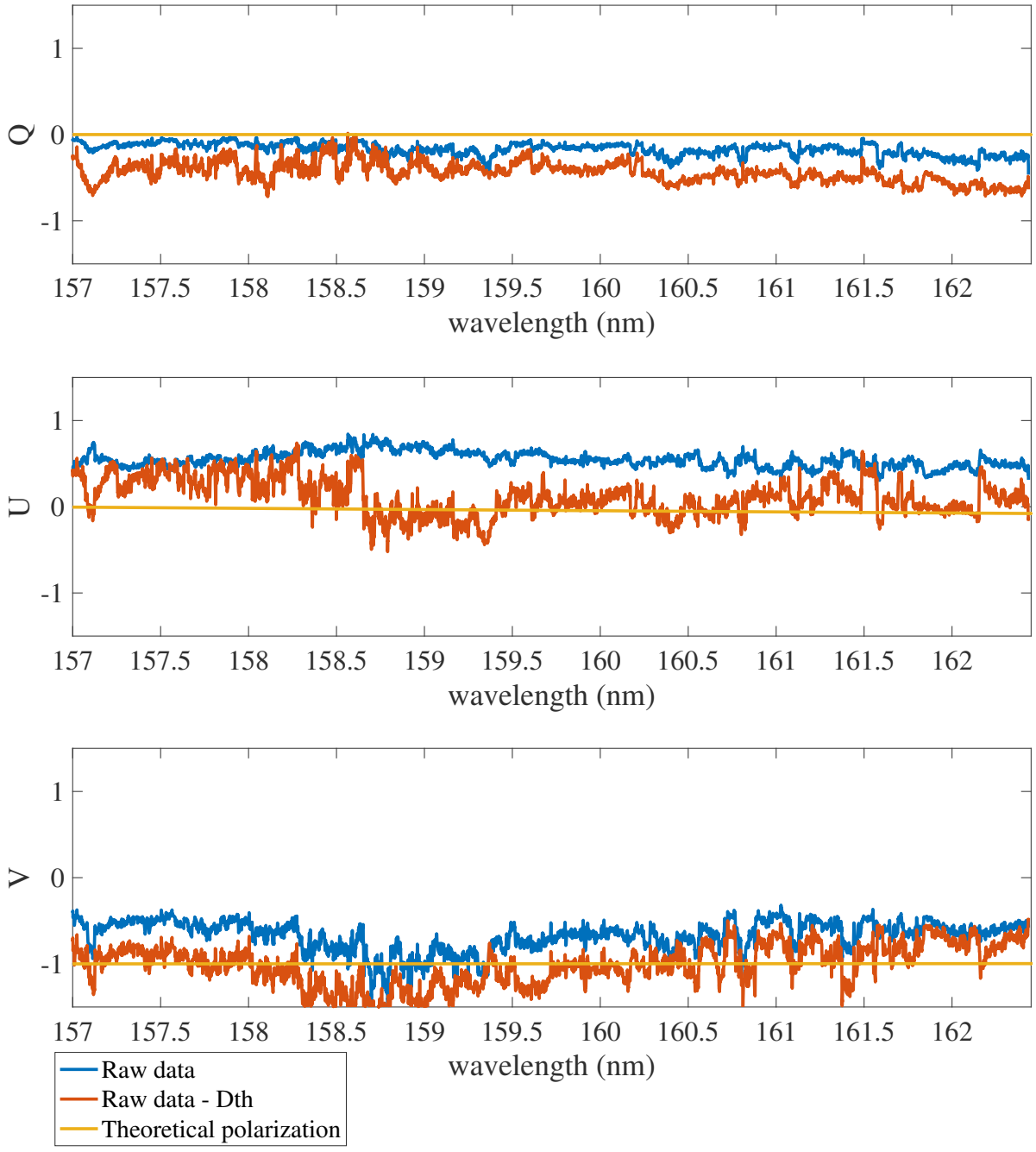

Figure 3.30: *Stokes parameters measured and theoretical for measurement A. The blue line corresponds to the data demodulated with the experimental matrix. The red line corresponds to the data demodulated with the theoretical matrix. The yellow line corresponds to the theoretical polarization input.*

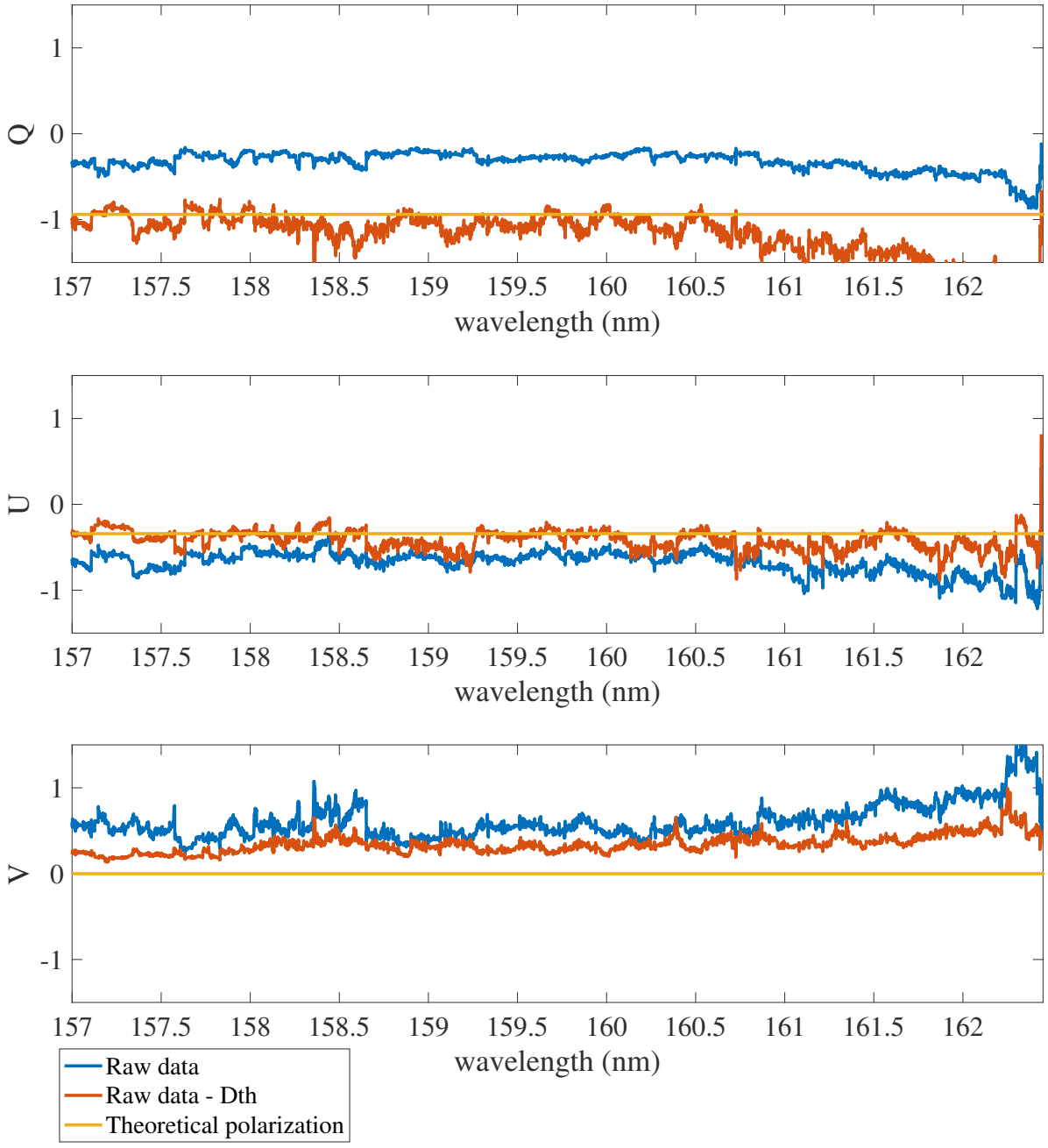

Figure 3.31: *Stokes parameters measured and theoretical for measurement B. The blue line corresponds to the data demodulated with the experimental matrix. The red line corresponds to the data demodulated with the theoretical matrix. The yellow line corresponds to the theoretical polarization input.*

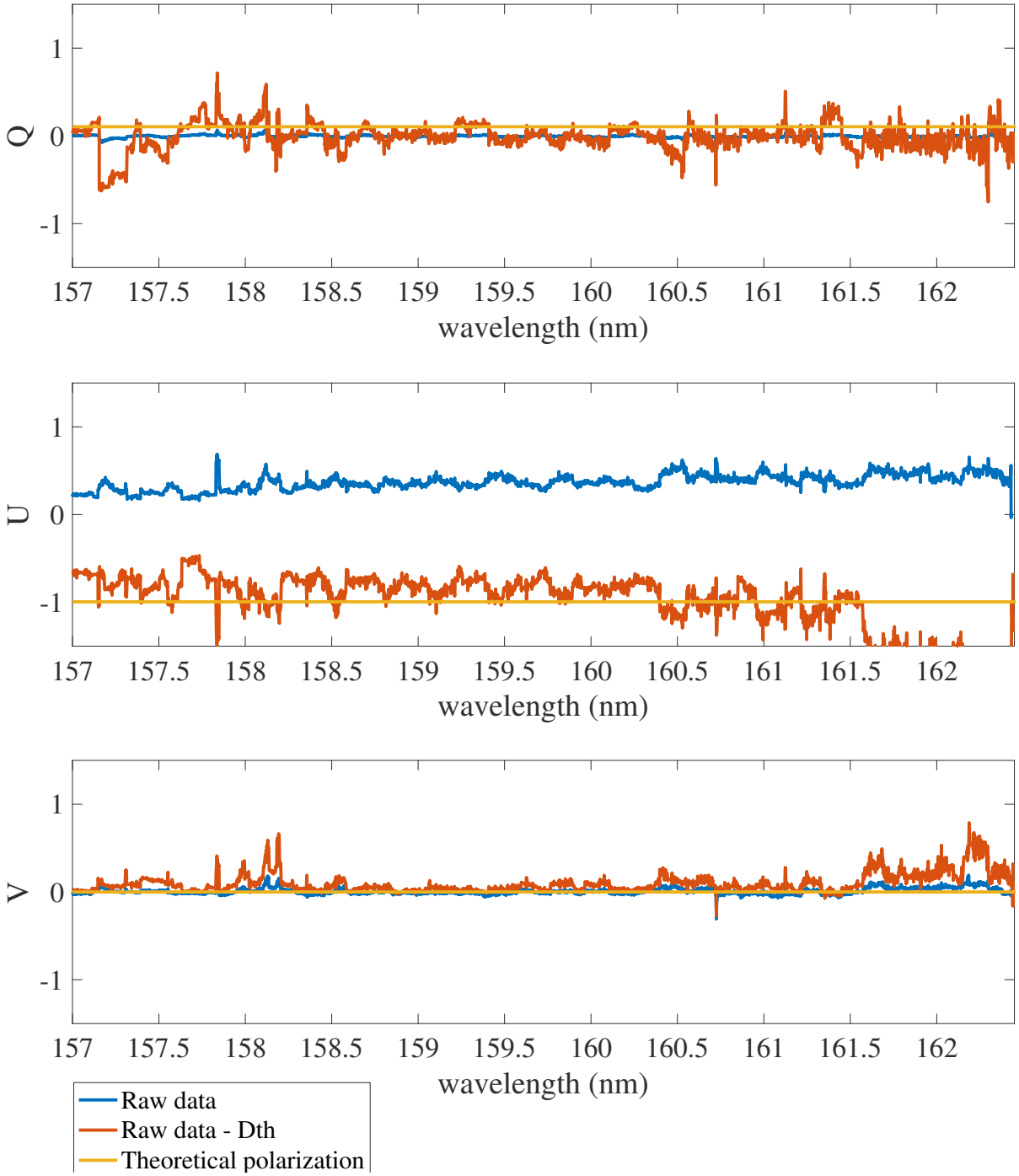

Figure 3.32: *Stokes parameters measured and theoretical for measurement C. The blue line corresponds to the data demodulated with the experimental matrix. The red line corresponds to the data demodulated with the theoretical matrix. The yellow line corresponds to the theoretical polarization input.*

3.4.6 Conclusion

An experiment putting a UV spectropolarimeter in an existing high-resolution spectrometer has been performed. The aim of the experiment was to test the performances of a UV spectropolarimeter in real conditions: under vacuum, in the UV, and with an HR spectrometer. The experimental modulation matrix was measured, and the experimental demodulation matrix was deduced. Then, measurements of particular polarizations have been performed with the polarizations called A, B, and C. These measurements were performed in very poor photometric conditions and do not establish a polarimetric measurement accuracy. The experimental setup underwent many obstacles: the optical design had to be adapted with many constraints to meet the specifications of the spectrometer, the luminous flux was very low due to an obscuration of the collimation mirror creating very noisy spectra in spite of a long exposure time, and an analysis of the results showed a repeatability error of the measurements likely due to the type of detector used in the spectrometer. Although the obtained accuracy is far from the desired one, and despite these (non-exhaustive) obstacles, the dominant polarizations are retrieved. These results are encouraging and should be consolidated by further experiments, building on the valuable expertise gained here. These new tests should be carried out with a spectrometer adapted to the polarimeter. This means the construction of a bench measuring both ordinary and extraordinary beams simultaneously on a CCD or CMOS detector. The use of coated mirrors is discouraged near a UV source, and the use of high quality lenses without impurities is recommended instead.

3.5 Thermal Test

The work presented in this Section was published in the SPIE proceeding by Le Gal, Neiner, Louvel De Monceaux, et al: Thermal tests of birefringent plates in molecular bonding for spatial ultra-violet polarimetry. In: Advances in Optical and Mechanical Technologies for Telescopes and Instrumentation IV. International Society for Optics and Photonics, 2020. p. 1145132.

3.5.1 Definition of the study

As MgF_2 is a birefringent material, it is expected to expand or contract with thermal changes in privileged directions corresponding to the axes parallel and perpendicular to its fast axis. Each of the plates of the modulator having a different fast axis angle, the plates will expand (or retract) in different directions with thermal changes. These plates movements create stress on the molecular bonding. To test the resistance of molecular bonding in space, the polarimeter has to be studied thermally. To take potential changes of design into account and include all possible future polarimeters in our study, we consider the plates in a configuration that will create the most stress to the molecular bonding: 4 MgF_2

plates with their birefringence axes crossed with respect to the adjacent plates. The plates are square with a size of 15 mm and a thickness of 0.3 mm. This is shown in Figure 3.33.

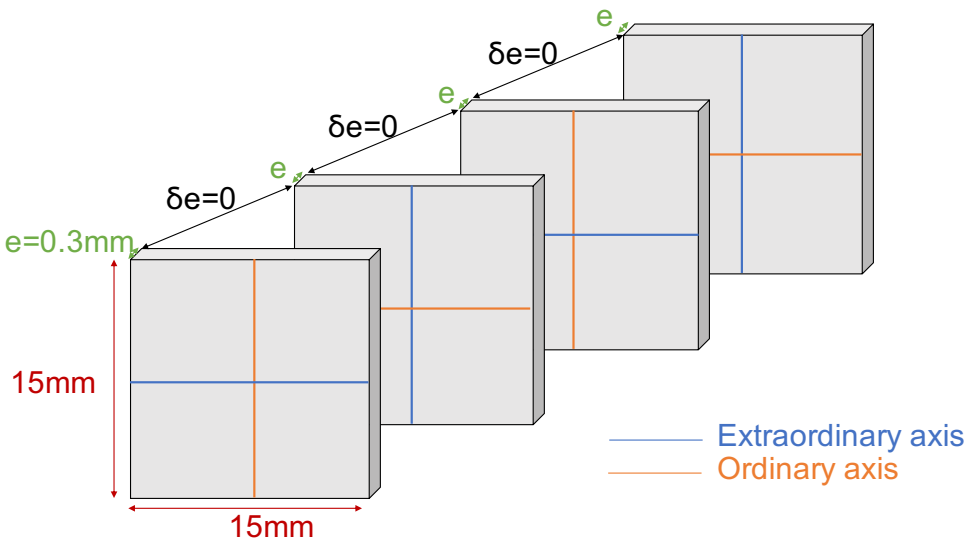

Figure 3.33: *Exploded view of the stack of plates at molecular bonding.*

3.5.2 Thermal testing standard

In order to qualify our prototype for a space mission, we test the modulator respecting JPL[37] and ECSS[16] standards. It was determined that the polarimeter should be validated over a temperature range [-25°C; +55°C] over at least 8 thermal cycles with a slope lower than 5°C/min. The prescribed cycling is described in Figure 3.34. The behaviour of the mechanical support on this temperature range has been studied and is presented in Section 3.5.3. Two experiments were performed. The first experiment, at LESIA at the Paris Observatory, followed one sample of MgF_2 plates in real time with interferometry and is described in Section 3.5.4. Second, we put 7 samples of MgF_2 plates in a thermal vacuum chamber at CNES through 10 thermal cycles. We measured them optically after the cycling using an interferometer and a Shack Hartmann wavefront sensor. This second experiment is described in Section 3.5.5.

3.5.3 Impact of the mechanical mount

The stack of plates is inserted in a mechanical mount provided by B. Halle. The plates are square and maintained in all directions with thin foil acting as spring. The regular mount has one spring in one direction. Some mounts were made especially for the second

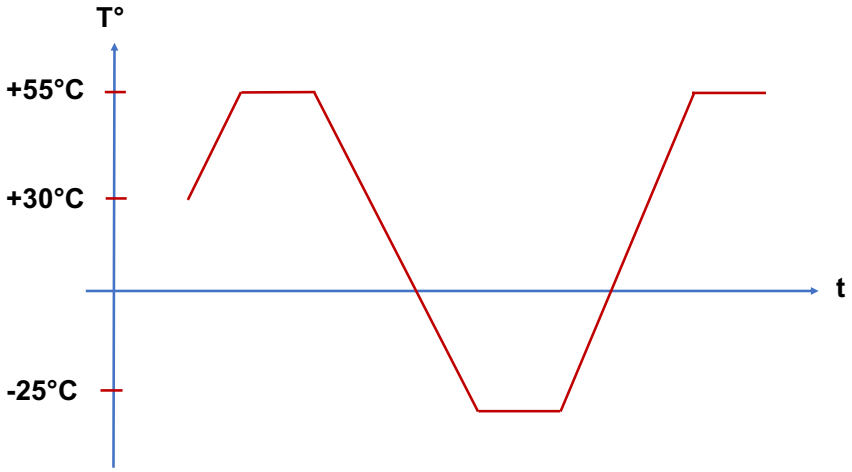

Figure 3.34: *Variation of temperature during a thermal cycle.*

experiment described below and have two springs (in the two lateral directions). In addition, some mounts also have a hole to better evacuate the air when placed in vacuum (those are identified as "vacuum mounts" in Figure 3.45). A study was made by a thermal engineer, N. Nguyen Tuong to ensure that the plates were not constrained by the strength of the springs and that the space available around the plates in the mount was large enough to absorb the dilatation of the plates with the thermal changes. This study concludes that the mechanical mount should not interfere with the plates in the range [-20°C, +20°C]. Results outside of this temperature range are not known yet.

3.5.4 Monitoring of the plate interferences during thermal cycling

The first experiment was performed at LESIA using a thermal enclosure and a real time tracking measurement of the plates. The concept of this experiment is to create interference between the plates and a plane surface - in our case a mirror - and to watch the possible change of the interference figures with the thermal changes. If all plates are at optical contact, the surfaces are perfectly parallel and create fringes with equal inclination (i.e. rings). If a molecular bonding of the stack breaks, the plates are not perfectly parallel anymore and the fringes become of equal thickness (i.e. lines). In addition, if a molecular bonding breaks, the transmitted flux decreases. Another tracking method would thus be to measure the possible loss of flux during thermal cycling. However, due to the unstable flux of the laser used in our experiment, this method was not exploited. The experiment is schemed in Figure 3.35. The pictures in Figure 3.36 show the experiment. On the picture 3.36a, the thermal chamber is located on the left of the image. The plates can be seen through the window. In the foreground, the laser and the beam splitter cube are visible. On the picture 3.36b, the beam splitter cube and the laser are seen on the left of the picture, from another point of view.

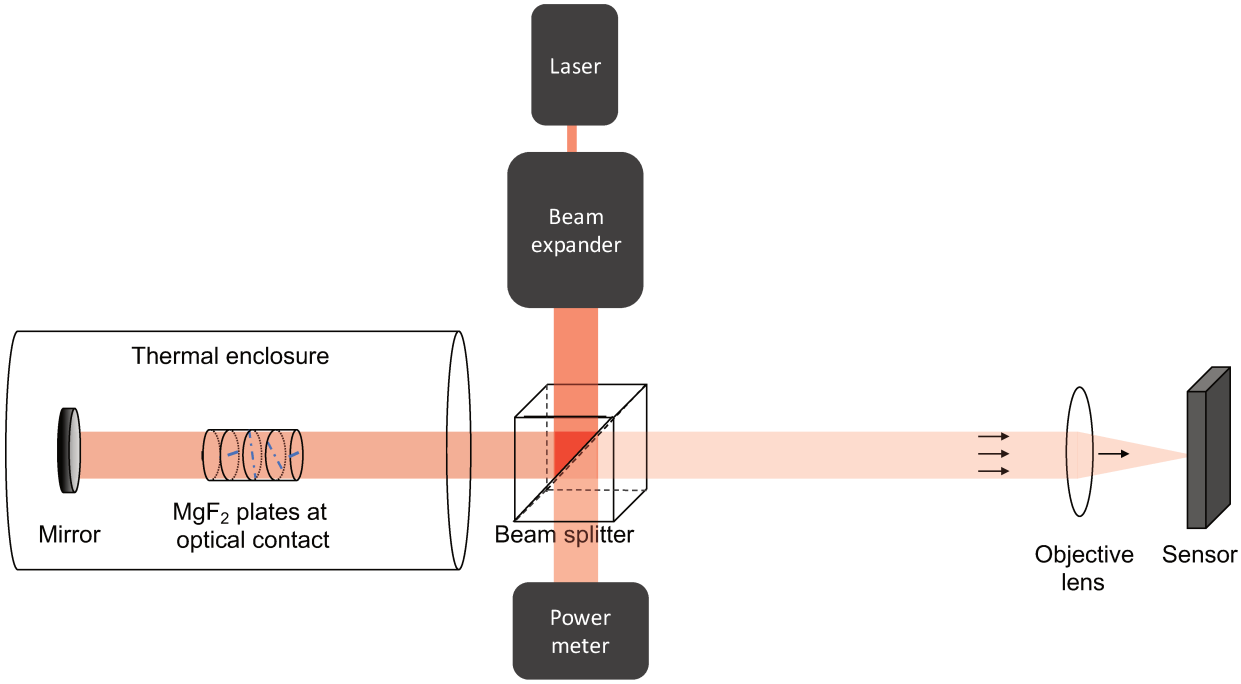

Figure 3.35: *Optical design of the real time experiment at LESIA.*

On the right, one can see the objective as well as the detector making the images of the interferences.

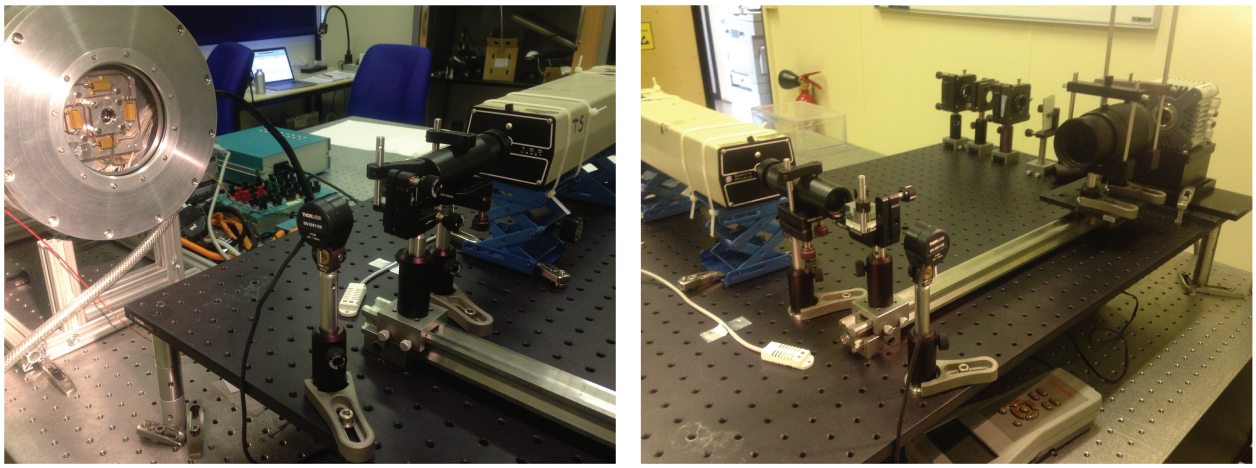

(a) **(b)**

Figure 3.36: *Pictures of thermal tests performed with real-time monitoring of the state of the plates.*

Preliminary tests

First, some preliminary tests have been performed, either with only a mirror in the chamber (and no plates), or with a non-contacted sample (i.e. a stack of plates with airgaps instead of being optically contacted). During these tests, the interference figures were stable over the full thermal range. This shows the mechanical stability of the experiment and will help us to interpret our results with the plates reaction to temperature changes. Examples of results of these first tests are presented in Figures 3.37 and 3.38. One can see that in the case of the plates with airgaps, the interference are fringes of equal thickness as the plates are not perfectly parallels in the mounts.

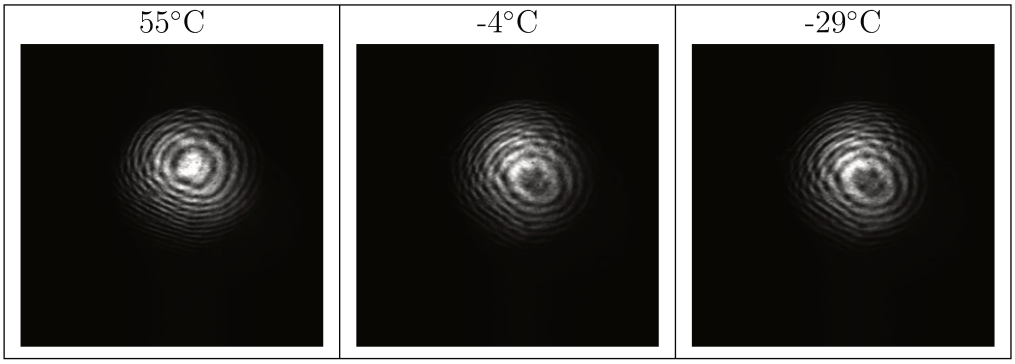

Figure 3.37: *Some interference figures at 3 different temperatures are presented. In this case, only the mirror (and no plates) is in the thermal chamber.*

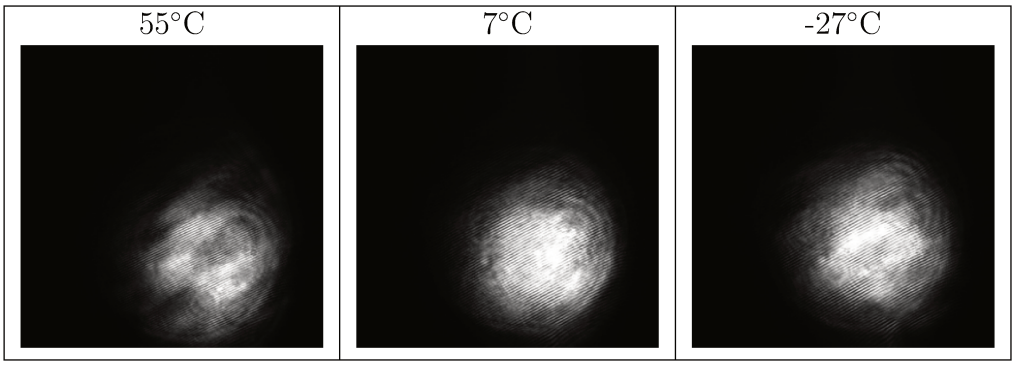

Figure 3.38: *Some interference figures at 3 different temperatures are presented. In this case, the interference are created with a modulator with airgaps. Both the mirrors and the modulator are in the thermal chamber.*

Thermal cycle of the plates at molecular bonding

Now that the experiment has shown that the mechanical parts should not affect our measurement during the thermal cycling, our plates with molecular bonding can be measured. The thermal cycling is presented in Figure 3.39 and the corresponding interferences are shown in Figure 3.40. Between the first rise in temperature (from 30 to 55°C) then cooling down to 18°C, the rings remain fairly stable as one can see in panels 1 to 4 in Figure 3.40. The contrast of the fringes fluctuates slightly during the first rise of temperature. During this first phase, it is suggested that the plates remains unaffected. From 7°C to -10°C, corresponding to panels 5 to 7 in Figure 3.40, the rings are strongly deformed. Indeed, linear fringes are superimposed on the rings: fringes of both equal inclination and equal thickness are visible. This suggests that the plates are deformed under the effect of stress imposed by temperature. However, no anomalies were detected upon visual inspection of the plates, which suggests that at this point the plates were still in molecular bonding. At -22°C (panel 8 in Figure 3.40) the rupture is clear: the rings turn into hyperbola, which means that at least one molecular bonding broke. Visual inspection of the stack of plates confirms this conclusion: fringes are visible as one can see in Figure 3.41. During the last phase of the cycle, when the temperature rises again, we do not retrieve the original fringes. This suggests that the break of bonding is permanent.

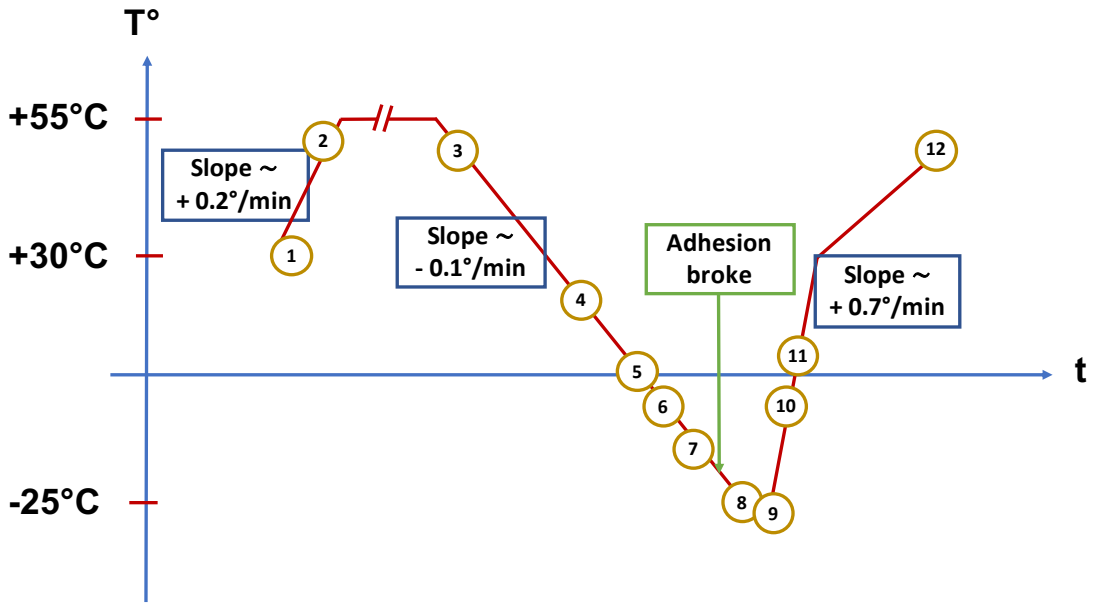

Figure 3.39: *Thermal cycling performed in the experiment described in Section 3.5.4. The numbers 1 to 12 correspond to the interference patterns shown in Figure 3.40.*

While the plates did stand high temperature, they did not survive the thermal changes at low temperature. One of the 3 molecular bonding broke around -15°C. With this experiment

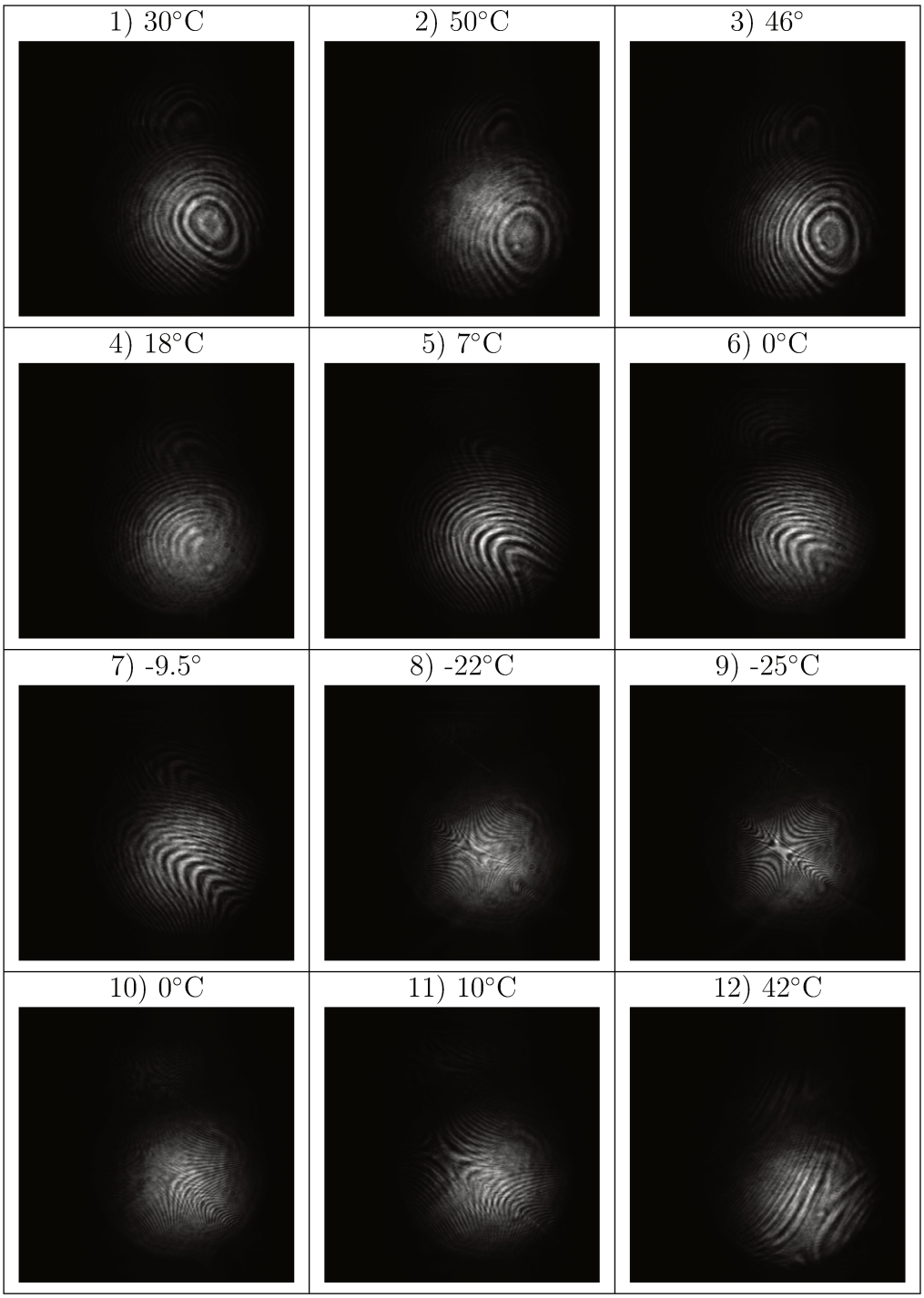

Figure 3.40: *Some interference figures observed at different temperatures are presented. In this case, the interference are created with the modulator with plates in molecular bonding.*

only, it is difficult to establish the particular reason why one molecular bonding broke and not the other two. The bonding broke at -15°C, which is in the range where the mount has

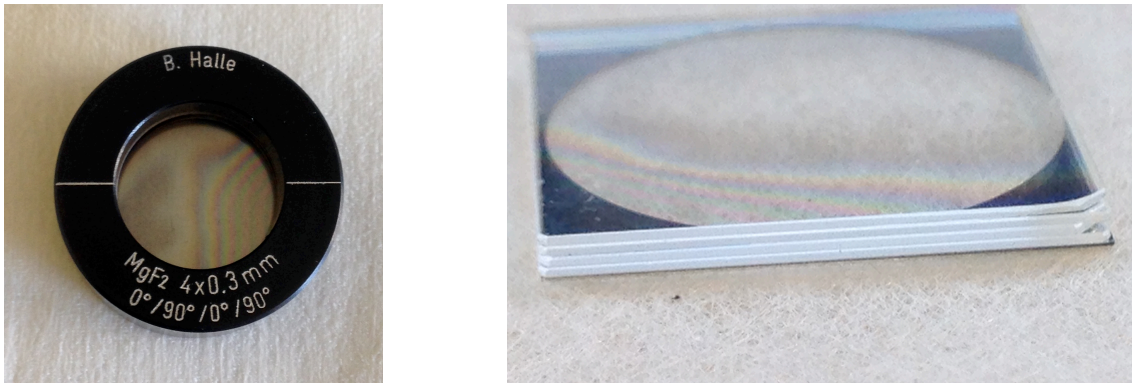

(a) (b)

Figure 3.41: *The plates after thermal cycle described in Section 3.5.4. In subfigure 3.41a fringes are visible by eye directly in the plates. In subfigure 3.41b one can see the plates unmounted after the cycle. The first plate is detached from the stack at the bottom right corner.*

been studied and approved to not harm the plates, so the mount can be excluded a priori as the culprit. The most obvious explanation is that the break could be due to the strength of the molecular bonding, which may not be equal for all 3 molecular bonding. However, the break could also be due to the non-homogeneity of the temperature in the vacuum chamber. Indeed, the temperature in the chamber was set by thermal conduction, which is not easy to perfectly control. Thermal probes follow the temperature changes in various points in the chamber during the cycling and indeed suggest slight differences in temperature between different parts of the chamber. However, two thermal probes broke during the test, making difficult the full comprehension of the thermal homogeneity.

3.5.5 Blind thermal cycling with multiple samples

To complete this first result, and investigate further the resistance of the molecular bonding in better conditions of temperature homogeneity, another experiment was performed at CNES in a thermal vacuum chamber ensuring thermal homogeneity. Several thermal cycles were carried out in order to test various bonding samples and thus determine the cause of the failure. The cycles were carried out in a conventional thermal chamber without real time monitoring. The optics were checked visually before and after the cycles. The temperature was controlled with several thermal probes and ensure the homogeneity of the chamber.
Samples with different parameters were tested. Samples with only 2 plates instead of 4 were produced to check if they would be more resistant. Samples with an additional spring in the mount were produced to see if the way we maintain the sample was causing mechanical stress. In addition, samples without any mount were tested to see the influence of the mounts. The samples are listed in Figure 3.42. 10 cycles were performed in the range -25 to 55°C. The

Plates	Configuration of the plates
A	2 plates without mount
B	2 plates without mount
C	2 plates mounted, one spring
D	4 plates without mount
E	4 plates mounted, two springs
F	2 plates mounted, two springs
G	4 plates mounted, one spring

Figure 3.42: *Description of the 7 samples tested in the thermal cycling experiment described in Section 3.5.5.*

cycle pattern is the same as in the previous experiment. The thermal data recorded during the second cycle are presented in Figure 3.43 as an example. Samples are simply placed in an aluminum cup inside the vacuum chamber. As a first cautious attempt, the first cycles were made with only samples A, B, C and D. E and F were added for the second cycle. Since the samples resisted well, in cycle 3 to 10, all samples were included.

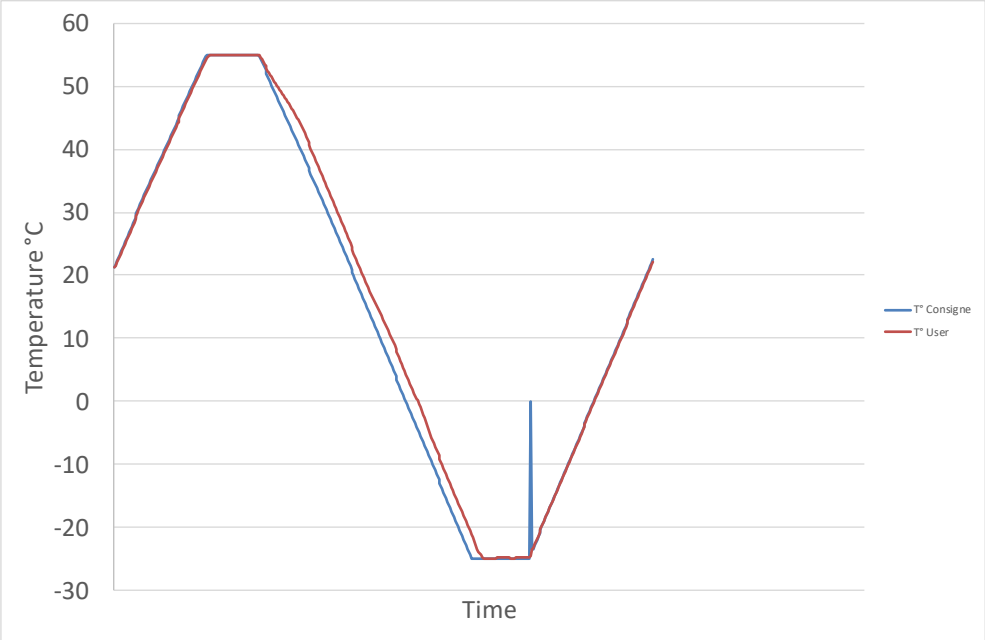

Figure 3.43: *Thermal temperature of the second cycle of the experiment described in Section 3.5.5. The temperature slope of this cycle is 1° C/minute.*

Cycle #1

Given the results obtained with the previous test described in Section 3.5.4, the aim of this first cycle was to test a sample with only 2 plates and a single bonding, which should be more resistant than 4 plates with 3 bonding because it undergoes less stress. In addition, we decided to test samples without mounts, to see if the bonding survived better without mechanical stress. It was therefore decided during this first cycle to use plates A, B, C, and D, i.e. 2 samples of 2 plates without mounts, 1 sample of 2 plates with a regular mount (1 spring), and 1 sample of 4 plates without mount. The temperature cycle was from -25°C to + 55°C with a slope of 3°C/minute and steps of 20 minutes. A visual inspection was carried out at the end of the cycle in order to check the samples. No bonding break was observed on visual inspection.

Cycle #2

As all the samples survived the thermal cycle #1, it was decided for cycle #2 to test a new mount with 2 springs instead of 1 spring, i.e. to add samples E and F: a sample of 4 plates with a mount with 2 springs and a sample of 2 plates with a mount with 2 springs. The temperature cycle was -25°C to +55°C with a slope of 1°C/minute and 20 minute steps. A visual inspection after the cycle determined that no bonding had broken during the cycle.

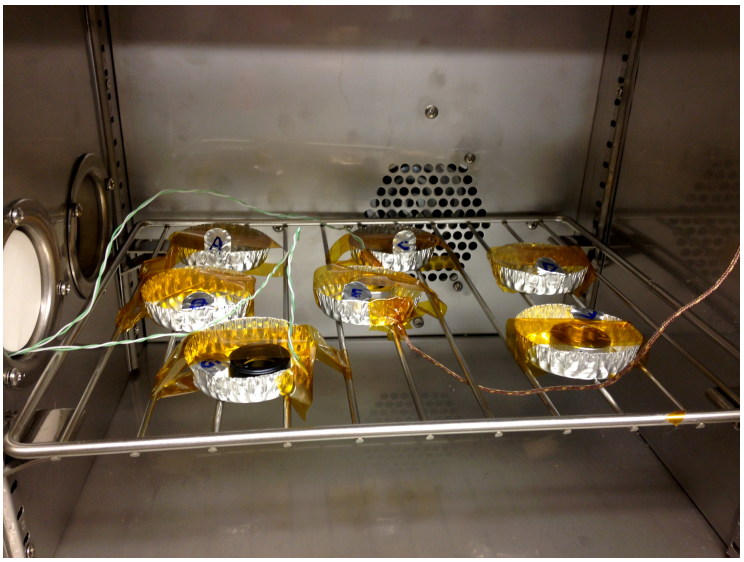

Figure 3.44: *Picture of the thermal chamber with the samples ready for thermal cycling.*

Cycles #3 to #10

As all the samples survived the thermal cycles #1 and #2, it was decided to add the sample G, namely a sample of 4 plates with a regular mount (one spring) identical to the one that

broke in the first experiment at LESIA, and to let the experiment run for 8 consecutive cycles without interruption. The configuration of these cycles is shown in Figure 3.45. The temperature cycles were from -25°C to +55°C with a slope of 1°C/minute and steps of 20 minutes.
In picture 3.44, the 7 samples ready to undergo the thermal cycles 3 to 10 are shown. At the bottom of the chamber, the nitrogen input is visible. Non-polluting tape has been put over the aluminium supports to prevent the plates without mounts, which are very light, from being lifted up by the nitrogen inlet. One can also see the thermal probes allowing the monitoring of temperature in the chamber and on the supports of the plates. Visual inspection after 8 cycles determined that 7 samples had survived the experiment but at least one bonding of sample E broke. Indeed, fringes are visible on the sample, as one can see in Figure 3.46. The shape of the visible interference shows a situation similar to that obtained at LESIA after breaking of the bonding. The interference appears to be in the axis of the extraordinary axis, which is also the axis of one of the retaining springs. Sample E consisted of 4 plates and 3 molecular bonding in a mount with 2 springs. This mount is supposed to put less stress in the plates than mounts with only 1 spring. In addition, we note that sample G (4 plates and a mount with 1 spring, a copy of the sample used in the first experiment at LESIA) survived the 8 thermal cycles. We conclude, like in the first experiment, that the mounts are probably not at the origin of the broken bonding.

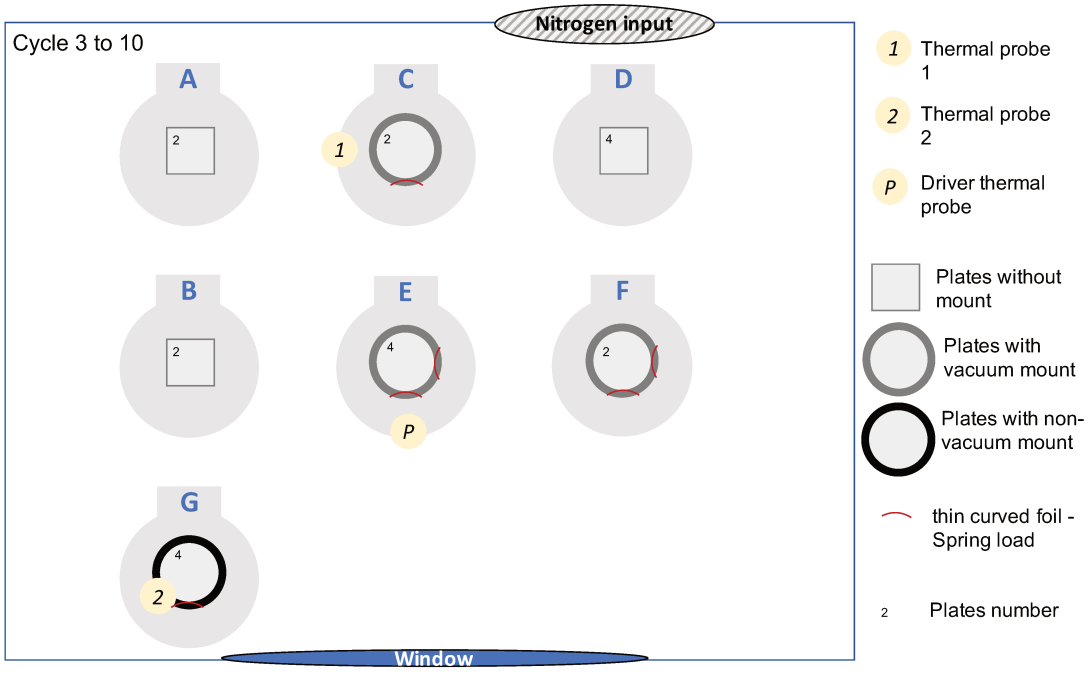

Figure 3.45: *Positions of the samples in the thermal vacuum chamber during cycles 3 to 10 performed at CNES.*

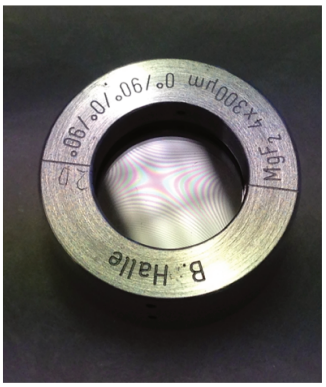

Figure 3.46: *Sample E after cycles #3 to #10. Fringes are clearly visible. At least one of the 3 molecular bonding of sample E broke.*

3.5.6 Conclusion

During these two experiments, one molecular bonding in two samples out of eight broke. All samples with only 2 plates and without mount passed the thermal space qualification. The two samples which failed the thermal cycling had 4 plates in molecular bonding and were in a mount. However, other samples with 4 plates and with mounts have survived. At this point, the cause of the loss of bonding in some cases cannot be determined, but we suspect that the strength of the molecular bonding may not be equal in all samples.

These results are based on a few samples and should therefore be taken with caution. They were obtained as a first attempt to check the feasibility of the use of a stack of birefringent plates in molecular bonding in space missions. However, further experiments should be performed to extend this study. First, many more samples should be tested to obtain statistical results. Indeed, a copy of the sample that broke in experiment 1 was safe in experiment 2. To draw conclusions, the test of many copies in identical conditions should be performed. Second, methods to strengthen the bonding should be studied. Previous work [12, 66] suggests that the conditions under which the bonding is done have a great influence on its resistance. In particular, several parameters applied during the bonding process can be tuned, such as the levels of hydrometry, cleanliness, and polishing of the surfaces. Finally, we tested here whether the plates and their molecular bonding survived thermal changes. In the future it will be useful to also check whether the plates get permanently deformed by these thermal changes, which could impact their optical properties. Even though this preliminary study cannot conclude on the resistance of the modulator with birefringent plates in molecular bonding, our results are encouraging and suggest that, in the worst case, a back-up solution of the modulator with 4 plates organised in optically-contacted pairs could be considered.

3.6 Discussion and conclusion

The work presented here has improved the optimization technique of transmissive modulator. Using this optimization, it is now possible to consider polarimeters with only two birefringent plates for ultraviolet prototypes. This work has led to the design and optimization of polarimeters for LUVOIR, CASSTOR and PolStar space missions with excellent efficiencies. The first experiment carried out shows encouraging results. The first broadband polarimetry measurements in UV has been performed with our transmission prototype. The main components of polarization were retrieved but no conclusion on the accuracy of the measurements can be done for now. Indeed, many technical problems unrelated to the polarimeter have impacted the photometry of our measurements. Moreover, the spectrometer used with photosensitive sensors does not guarantee a repeatability of the measurements. The problems of mirror darkening also suggests the use of MgF_2 lenses may be more appropriate than mirrors to improve the lifetime of this experiment and the quality of the measurements. Finally, the modulator with molecular bonding has been tested at temperature for the first time, and important results have shown weakness at low temperature. This weakness is not repeatable, and its origin is not yet fully understood, however the quality of the molecular bonding is affected. Further work on the strength of molecular bonding as a function of temperature and the molecular bonding manufacturing process will need to be carried out to identify a repeatable process.

Thanks to the expertise gained from the experiments performed in this Chapter, a new experiment to test the accuracy of the polarimeter and a study to strengthen the prototype with molecular bonding with temperature variations will be conducted. These steps are essential to spatialize our polarimeter.

Chapter 4

Reflection polarimetry

4.1 Introduction

Commonly, polarimeters use birefringent materials like magnesium fluoride, as the polarimeter studied in Chapter 3. Even though magnesium fluoride can be used for waveplate almost near its transmission cutoff around 115 nm [23], its small and variable birefringence at these wavelengths makes it challenging to use for a polychromatic polarimeter. Therefore, below ∼123 nm preferably [48], and below 115 nm in any case, one needs to find another way. To measure polarization in the FUV, and as low as 90 nm for POLLUX, one must resort to reflection rather than the usual transmissive methods. Each reflection introduces a phase shift between orthogonal polarizations, as well as a change in the total rate of polarization thanks to the different reflectivities. This makes it possible to use reflection for both the modulator, and the analyzer functions.

A polarimeter made of four reflecting surfaces is studied. Three surfaces are at a fixed position with respect to each other but free to rotate together around the optical axis, they make the modulator. It is made with three surfaces as it is the minimum number that permits not to change the optical axis when rotating the modulator while maximizing the flux. This three-mirror modulator is also called a K-mirror. The analyzer is made of a single reflecting surface (a dielectric crystal or a metal at Brewster angle[1]), which polarizes the incoming light. Contrary to transmissive polarimeters which can use dual-beam polarizers [22, 67], the use of the Brewster angle in this reflective polarimeter implies a single beam output. This reflective polarimeter is studied, simulated, and optimized in Section 4.2.

One of the major difficulties in this study was to find the optical indices (n,k) of the reflective surface at the considered wavelengths. An experiment was set up to measure these optical properties necessary for the study of polarimeters for the identified materials. The principle of the experiment is to measure the polarization of light before, and after refection on a material sample under study. A reflective polarimeter was built for the first time using

[1] A Brewster angle for a metal is defined as the incidence angle at which the reflected beam is optimally polarized, though seldom polarized at 100% contrary to dielectrics.

gold reflection. This experiment is introduced in Section 4.3, and the results are presented in Section 4.4.

4.2 Theory

As a first step, it is necessary to identify materials that can be used for a reflective FUV polarimeter. These materials must be available, their (n,k) data must be known, and they must have a good reflectivity in the FUV. The materials identified are presented in Section 4.2.1. In order to simulate the polarimeter, following the same method as presented in Section 1.3.3, it is necessary to be able to calculate the Mueller matrix of a reflection. This issue is discussed in Section 4.2.2. Finally, the polarimeter can be simulated. Initially, only the analyzer is simulated in order to obtain the best possible efficiency. The simulation of the analyzer is presented in Section 4.2.3. Lastly, the whole polarimeter is simulated in Section 4.2.4. The special case of the POLLUX FUV polarimeter is treated in this Section.
Sections 4.2.2, 4.2.3, and 4.2.4 are largely inspired by Le Gal, Ariste López, Neiner, et al: Simulation, and optimization of a broadband reflective far ultraviolet polarimeter. Applied Optics, 2020, vol. 59, no 30, p. 9320-9327.

4.2.1 Materials

The study of this FUV polarimeter requires the complex optical data (n,k) of materials with good reflectivity in the FUV domain. The GOLD team in Madrid has published numerous papers on materials in the FUV. In particular, papers [6, 29, 32] highlight the high reflectivity of materials such as a Tetrahedral Amorphous Carbon (ta-C), Boron carbide (B_4C), or Silicon carbide (SiC) in the FUV. Other papers, such as [19, 30, 39], show the advantages of using aluminium (Al) with a MgF_2 coating. In theory, bare aluminium would be a perfect metal for the design of a reflective polarimeter. Unfortunately, its oxydation is so rapid that it is very difficult to use without coating. Other materials such as MgF_2, Calcium fluoride (CaF_2), silicon dioxide (SiO_2), or gold (Au) were also simulated, and their data at the required wavelengths were taken from the Palik database [44]. Data for some materials are available in several literature sources but with different values of the complex indices. This difference is interpreted as a high dependence of the optical indices on the manufacturing process of the optics, measurement techniques, and conditions. All optical components used in this Chapter are presented in Annex B.

4.2.2 Simulating a reflection as a Mueller matrix

Mueller matrix of a reflection

To simulate, and optimize a reflective polarimeter, its modulation, and demodulation matrices should be computed from the Mueller matrices of the components, i.e. with Mueller

matrices of a reflection. The Mueller matrix of a reflection $\mathbf{M_R}$ at an incidence angle θ, and for a wavelength λ is given by [8]:

$$\mathbf{M_R}(\theta,\lambda) = \begin{pmatrix} \chi(\theta,\lambda)^2+1 & \chi(\theta,\lambda)^2-1 & 0 & 0 \\ \chi(\theta,\lambda)^2-1 & \chi(\theta,\lambda)^2+1 & 0 & 0 \\ 0 & 0 & 2\chi(\theta,\lambda)\cos(\tau(\theta,\lambda)) & 2\chi(\theta,\lambda)\sin(\tau(\theta,\lambda)) \\ 0 & 0 & -2\chi(\theta,\lambda)\sin(\tau(\theta,\lambda)) & 2\chi(\theta,\lambda)\cos(\tau(\theta,\lambda)) \end{pmatrix} \quad (4.1)$$

with $\chi^2 = r_\parallel^2/r_\perp^2$ the squared ratio of Fresnel amplitude reflection coefficients, and τ the difference of phase shift between p and s polarizations. Both components depends on (n,k), the complex optical indices of the considered material(s). To study the modulation and efficiency of the reflective polarimeter, these two parameters must be known. This matrix is obviously dependent on the angle of incidence θ and the wavelength λ, but also on the material used (optical indices of the substrate, of the coating and of its thickness).

Three cases are presented below, depending on the surface used to reflect (absorbing or not), and with or without a coating. The case of multi-layer coatings were not considered.

Phase shift and amplitude of a reflection on an absorbing surface with a non-absorbing coating

A reflection on an absorbing material creates a phase shift in addition to the polarization-dependent reflectivities. As shown in Figure 4.1, 1 the environment of the instrument is called 1 (vacuum in our case), the one of the coating is called 2, and, the one of the substrate of the surface is called 3. The indices of all the parameters in this Section will refer to this notation. One may notice that the calculation of the refraction angle using Snell-Descartes equations should use the complex optical index to take the absorption into account, and may provide mathematical complex refraction angles [21].

The rate of reflectivities χ and the phase difference τ in this case can be directly found in [3]. Explicitly, they are calculated using the reflection coefficient r:

$$r = \frac{r_{12} + \rho_{23} e^{i(\phi_{23}+2\beta)}}{1 + r_{12}\rho_{23} e^{i(\phi_{23}+2\beta)}} \quad (4.2)$$

with $\beta = 2\pi n_2 \frac{h}{\lambda}\cos(\theta_2)$. r_{12} is the reflection ratio at the interface between 1 and 2. ρ_{23} and ϕ_{23} are the amplitude ratio and phase change at the interface between 2 and 3. The amplitude and phase of this reflection coefficient gives the reflectivities and phases for p or s polarizations, using the appropriate expressions.

Using Born & Wolf equations [3], it is possible to calculate χ and τ, and to retrieve the Mueller matrix of a reflection in the case of a coated reflecting surface.

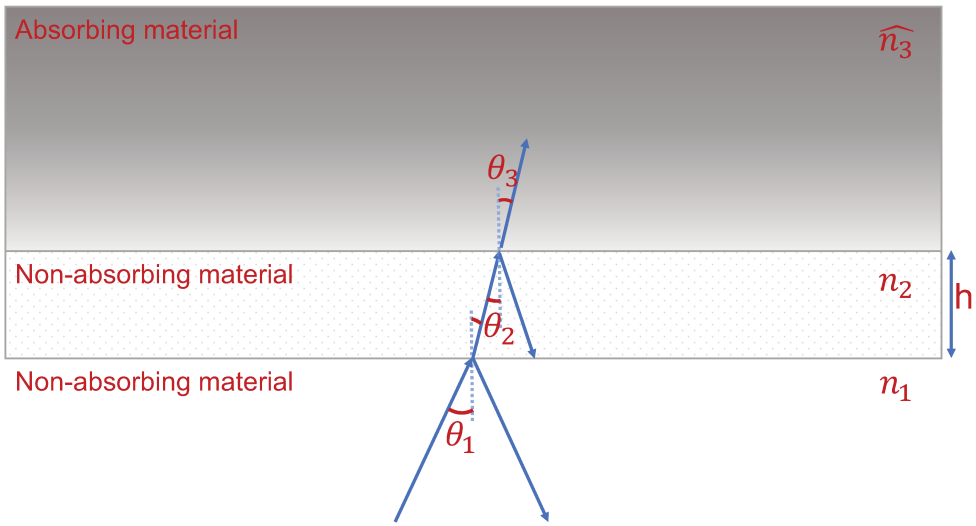

Figure 4.1: *Reflection on a coated absorbing surface.*

Phase shift and amplitude of a reflection on an absorbing surface without coating

Although a particular case of a coated surface, it is worth to recall here also the case of an uncoated substrate which, obviously, can be computed with simpler expressions. These can also be found in [8]:

$$\chi^2 = \frac{f^2 + g^2 - 2f.\sin(\theta_1).\tan(\theta_1) + \sin^2(\theta_1).\tan^2(\theta_1)}{f^2 + g^2 + 2f.\sin(\theta_1).\tan(\theta_1) + \sin^2(\theta_1).\tan^2(\theta_1)} \tag{4.3}$$

and

$$\tan(\tau) = \frac{2g.\sin(\theta_1).\tan(\theta_1)}{\sin^2(\theta_1).\tan^2(\theta_1) - (f^2 + g^2)} \tag{4.4}$$

with θ_1 the angle of incidence, and where

$$f^2 = \frac{1}{2}(n^2 - k^2 - \sin^2(\theta_1) + \sqrt{(n^2 - k^2 - \sin^2(\theta_1))^2 + 4n^2k^2} \tag{4.5}$$

and

$$g^2 = \frac{1}{2}(k^2 - n^2 + \sin^2(\theta_1) + \sqrt{(n^2 - k^2 - \sin^2(\theta_1))^2 + 4n^2k^2} \tag{4.6}$$

help simplifying the expressions. k is defined by $\hat{n} = n + ik$. Other terms use the same notations as above.

Phase shift and amplitude of a reflection on a non-absorbing material (k=0)

In the particular case of a non-absorbing medium – such as a crystal – where k is considered null, the expressions for reflectivities reduce to the well known expressions [3]. In this case

there is no phase shift between the polarizations. Indeed, at each reflection of light coming from vacuum into the crystal, the phase shift is 0, unless the crystal is finite with width d and transparent enough so that multiple reflections occur [53]. Total reflections impose another different phase shift, used in Fresnel rhombs, but this is beyond application in our present study. Therefore, non-absorbing media cannot be used for the modulator but can make a good polarizer.

For any given wavelength, it is indeed possible to find an angle for which the reflected beam is 100% polarized: the Brewster angle $\theta_B = \arctan(n)$. Such a Brewster angle is wavelength dependent, and this complicates its use in a broadband polarimeter if the available materials have very chromatic optical indices. In addition, even if the reflection at the Brewster angle is 100% polarized, the actual reflectivity may be too small, jeopardizing the throughput of any polarimeter based upon it. This has been studied further in Section 4.2.3.

4.2.3 Simulating the analyzer

Polarization contrast and figure of merit

Usually, above 123 nm, beamsplitters are used as transmissive analyzers as they separate the incoming beam into two linear polarization states. This has the advantage of using all the incoming flux, and to have a perfect polarizer, with two 100% polarized beams. Using a reflection is more complicated. First, this FUV analyzer only reflects one linear polarization, so we lose some flux, which is precious in the UV domain. Also, the efficiency of the polarimeter decreases as the output beam is not 100% polarized.

Our goal is to simulate and then optimize the analyzer in order to restrict these two drawbacks. This means to both maximize the degree of polarization and the transmission. Optimizing the degree of polarization means to accentuate the ratio of one linear polarization with respect to its orthogonal polarization. Optimizing the transmission means to retain a sufficient signal-to-noise ratio. Two parameters are going to help us quantify their efficiency. First, we define a contrast as the ratio between p and s polarizations:

$$C = \left|\frac{R_{\parallel} - R_{\perp}}{R_{\parallel} + R_{\perp}}\right| \tag{4.7}$$

where $R_{\parallel}$, and $R_{\perp}$ are the reflectivities of the polarizations for which the electric field is perpendicular or parallel to the plane of incidence. The contrast can help us determine the degree of polarization of the reflection, which is linked to the efficiency of the polarimeter. This is however not sufficient to characterize a good analyzer, since the reflection can be fully polarized but with an extremely low reflectivity. Thus reflectivity should be part of our characterization. To combine both parameters – reflectivity and contrast – a figure of merit

is introduced [17]:

$$\epsilon = C.\sqrt{max(R_{\parallel}, R_{\perp})} = |\frac{R_{\parallel} - R_{\perp}}{R_{\parallel} + R_{\perp}}|\sqrt{max(R_{\parallel}, R_{\perp})} \tag{4.8}$$

The figure of merit helps us quantify and compare analyzers according to both their efficiencies and reflectivities. The square root is used on the reflectivity to minimize its variation and give a larger weight to contrast.

Now that we have a way to quantify the quality of a polarizer, we can study different solutions and compare them. The study is divided in two parts: first, the solutions including only one material (no coating) with only one parameter to study: the incidence angle. Second, the study of a coated substrate, for which there are then two parameters: the incidence angle and the thickness of the coating.

Uncoated surface

For a reflection made with a material without coating, there is just one parameter to consider: the angle of incidence. For a given material and a given wavelength, a particular angle of incidence can be computed that optimizes polarization contrast or transmission or, ideally, both. However, the values of the optimal angle of incidence are very chromatic, and at best, for a given material, a compromise can be found. The previously defined figure of merit in equation 4.8 will help us define that optimal solution, but it will also be used to compare different materials. The contrast alone has also been studied to underline the benefit of the defined figure of merit.

For the spectral range of POLLUX in the FUV and MUV, CaF_2, MgF_2, SiO_2, Au, B_4C, *ta-C*, and SiC have been studied. The contrast as a function of incidence angle and wavelength is shown in Figure 4.2 for all considered materials. The figure of merit as a function of incidence angle and wavelength is given in Figure 4.3.

Figure 4.2 shows that the contrast is sufficiently high for some materials such as CaF_2, MgF_2, SiO_2, Au, and *ta-C* to consider them further. Moreover, the variation of the contrast with wavelength is acceptable in the considered wavelength range. However, in Figure 4.3, one can see that in spite of the good contrast, the reflectivity is not very high and is mostly responsible for the degradation of the efficiency of these polarizers.

To compare our solutions, the mean contrast (Figure 4.4), and figure of merit (Figure 4.5) averaged over the considered wavelength range are plotted as a function of incidence angle. On those graphs, one can see very clearly that even though *ta-C* is not the best analyzer based on contrast, reaching almost 0.7, it is the best choice when based on the figure of merit for which it hits 0.6. CaF_2 and SiO_2 seem to be good back-up solutions since they have good figures of merit almost reaching 0.6. One may notice that they also have a very good contrast, around 0.9 for CaF_2 and 0.8 for SiO_2. The figure of merit helps us to choose *ta-C* reflection as the analyzer for POLLUX, as it is the best compromise between

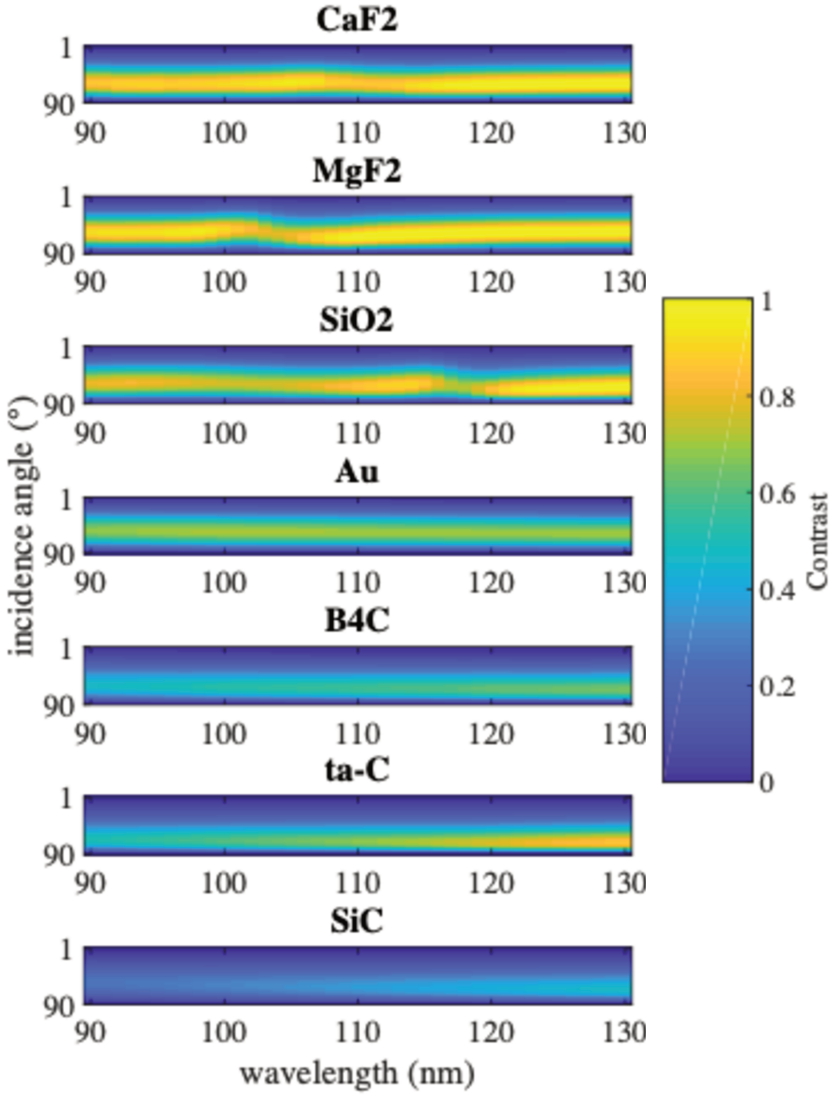

Figure 4.2: *Contrast after reflection on various materials as a function of wavelength, and angle of incidence. At a contrast of 1, the beam after reflection is fully polarized. At contrast=0, the beam is not polarized.*

reflectivity and contrast, but this decision could be modified for a CaF_2 or a SiO_2 plate to improve the contrast, and thus the efficiency of the polarimeter if the global SNR obtained with POLLUX permits it. These Figures show that at maximum contrast, a tolerance of 1 degree in the incidence angle creates a loss of contrast of less than 1%.

Considering the reflectivity, the best polarizer for the 90–130 nm wavelength domain is a plate of *ta-C* at 74.3° with a mean of 0.599 for the figure of merit and 0.6762 for

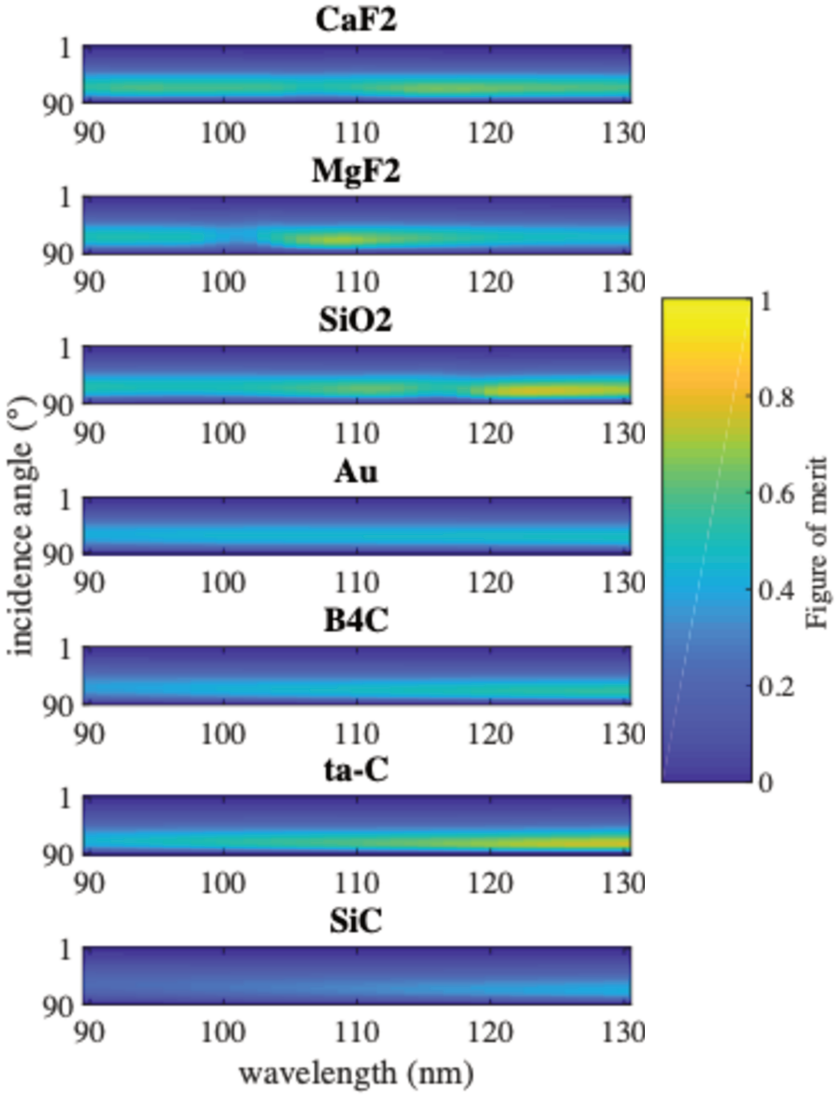

Figure 4.3: *Figure of merit after reflection on various materials as a function of wavelength, and angle of incidence. At a figure of merit of 1, the beam after reflection is fully polarized, and with no loss of flux. At contrast=0, the beam is not polarized, and/or the flux is lost.*

contrast. Nevertheless, if there were some spectral lines at specific wavelengths of particular scientific interest, the choice of the polarizer could be reconsidered by adding weights to those particular wavelengths. In addition, to study particularly bright objects, a plate of CaF_2 or SiO_2 could be a better choice as those materials improve the overall efficiency even though they decrease the reflectivity.

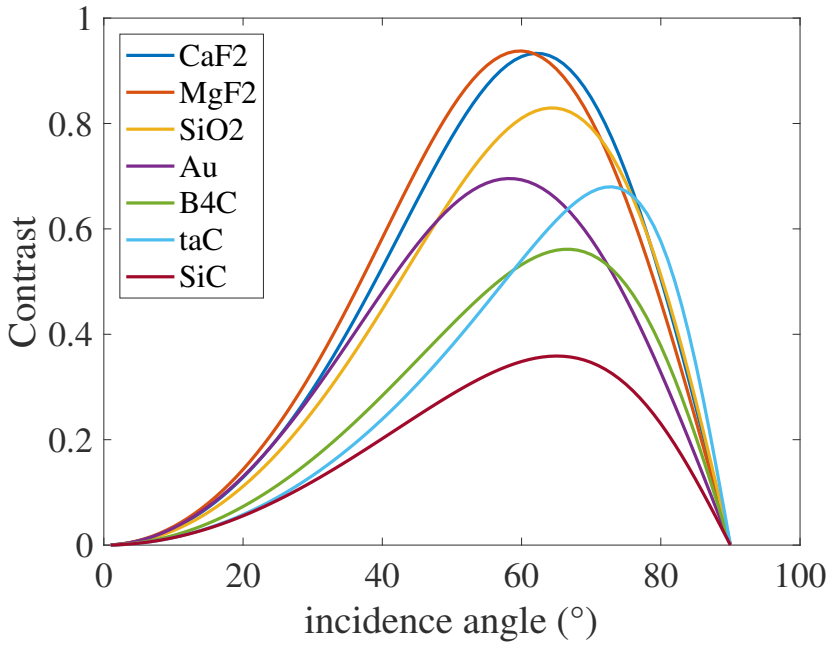

Figure 4.4: *Contrast of a polarizer (averaged across the spectrum) made with a reflection on various materials as a function of angle of incidence. At 1, the beam after reflection is fully polarized. At 0, the beam is not polarized.*

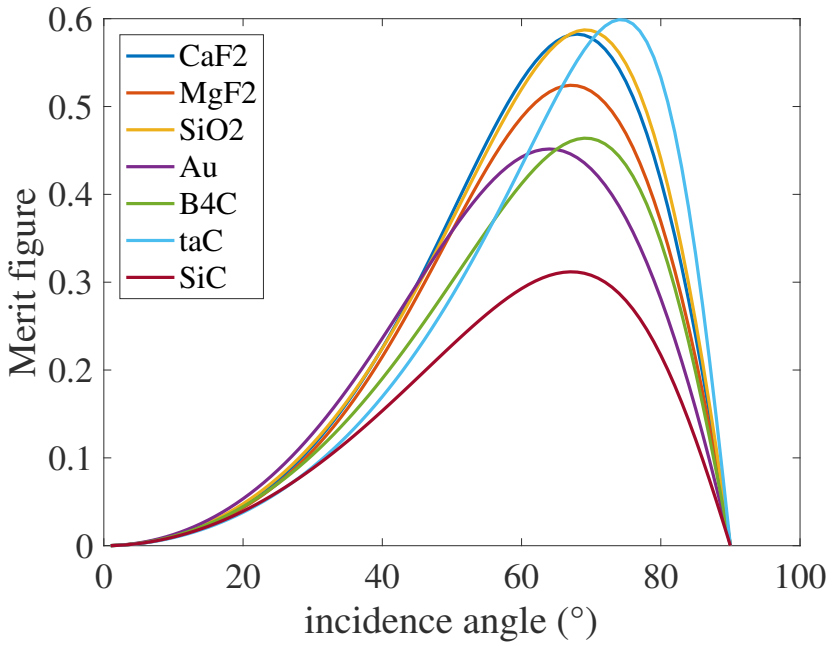

Figure 4.5: *Figure of merit of a polarizer (averaged across the spectrum) made with a reflection on various materials as a function of angle of incidence. At 1, the beam after reflection is fully polarized. At 0, the beam is not polarized.*

Study on coated materials

To simulate the use of a coated material, the thickness of the coating is another parameter to consider. Thicknesses between 5 and 90 nm are considered and cover the usual values. We decided to study a reflection on Al coated with MgF_2 as it is a well known combination to study UV light. To analyze the two relevant parameters (incidence angle and thickness), we plot the contrast averaged over wavelength as a function of incidence angle in Figure 4.6 for several thicknesses. Thicknesses were studied from 5 to 90 nm with a 1 nm step, but fewer values are displayed for clarity. A maximum contrast of 0.12 is obtained for a thickness of 32 nm, which is much lower than contrasts found for non-coated materials which are up to 0.9. This case is therefore discarded for the analyzer of POLLUX. Other combinations of materials for the substrate and coatings may be considered in the future, if an efficient combination appears from the current studies.

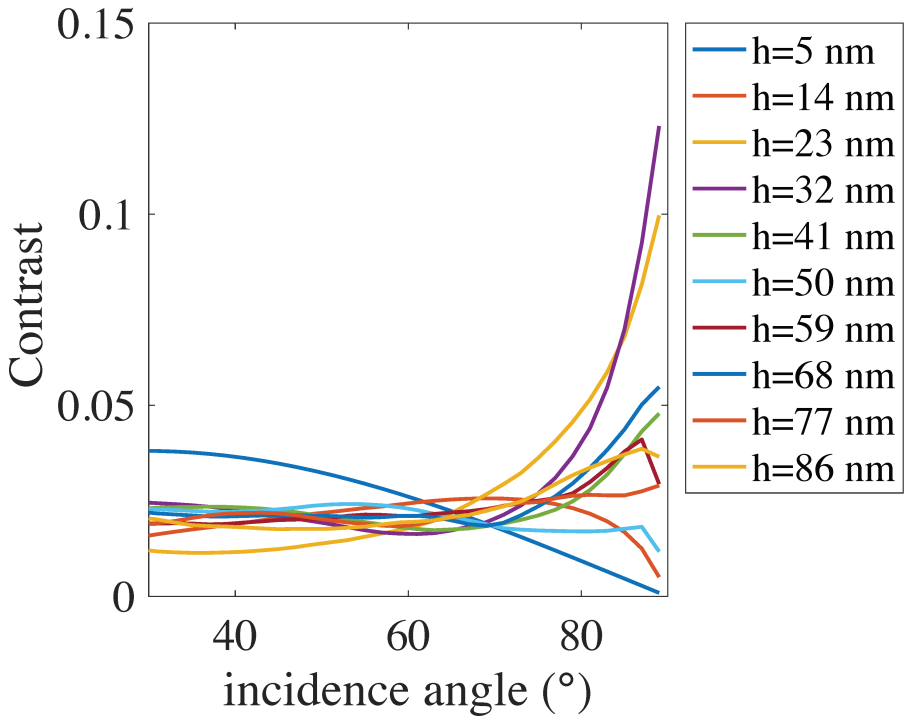

Figure 4.6: *Mean of contrast on wavelength of a reflective polarizer made with an aluminium mirror coated with different thicknesses (h) of MgF_2 as a function of angle of incidence. At 1, the beam after reflection is fully polarized. At 0, the beam is not polarized.*

4.2.4 FUV Polarimeter for POLLUX

Mueller matrix of the modulator

As already mentioned in Subsection 4.1, the modulator is formed by three reflections so that the beam is not deviated from the optical axis upon modulator rotation. The first and third reflections are then symmetrical with respect to the second one, which has its normal perpendicular to the optical axis of the instrument. The three reflections are studied as a whole, and not independently, since it is the total change of phase that is of interest. To that effect, the Mueller matrix of the modulator must be computed. The studied parameter is the incidence angle θ_m on the first surface, as denoted in Figure 4.7, θ_a is the angle of incidence on the analyzer, and m is the modulation angle. The incidence on the other surfaces can be computed from θ_m.

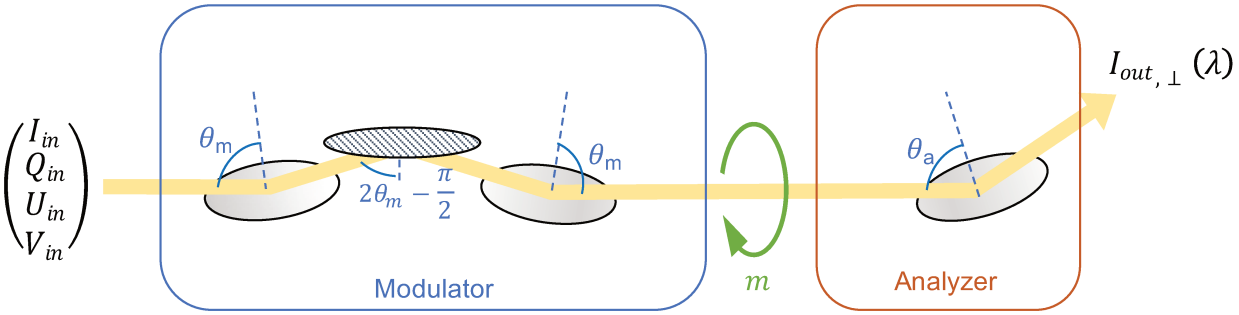

Figure 4.7: *Scheme of the reflective polarimeter.*

The Mueller matrix of the modulator is easily built up as the product of the matrices of these 3 reflections. Following the notation from Figure 4.7, we have $\mathbf{M_3} = \mathbf{M_R}(\theta_m, \lambda) * \mathbf{M_R}(2\theta_m - \frac{\pi}{2}, \lambda) * \mathbf{M_R}(\theta_m, \lambda)$.

The 3 reflecting surfaces rotate around the optical axis and the combined Mueller matrix is then modified by the rotation matrix of the angle of this rotation m:

$$\mathbf{R}(m) = \begin{pmatrix} 1 & 0 & 0 & 0 \\ 0 & \cos(2m) & \sin(2m) & 0 \\ 0 & -\sin(2m) & \cos(2m) & 0 \\ 0 & 0 & 0 & 1 \end{pmatrix} \tag{4.9}$$

The measurement of polarization with our current design consists in choosing a set of N angular positions for the modulator that differently encode polarization into intensity variations. Each one of the N measurements is differentiated by m, the rotation angle, and the resulting Mueller matrix for the full modulator is

$$\begin{aligned}\mathbf{M_{modulator}} &= \mathbf{R}(-m) * \mathbf{M_3} * \mathbf{R}(m) \\ &= \mathbf{R}(-m) * \mathbf{M_R}(\theta_m, \lambda) * \mathbf{M_R}(2\theta_m - \frac{\pi}{2}, \lambda) \\ &\qquad * \mathbf{M_R}(\theta_m, \lambda) * \mathbf{R}(m)\end{aligned} \tag{4.10}$$

However, as seen previously, we cannot find a perfect analyzer. The solution found for POLLUX polarizes light but not completely, and in the case of *ta-C* we even expect a retardance phase to appear between the reflected orthogonal polarizations. In other words, the analyzer may not just be polarizing, but also transforming, rotating one polarization into another, a role which in theory we reserve to the modulator. Because of this, we cannot study or optimize the modulator alone. We must consider the whole polarimeter made of the rotating 3-reflections modulator plus the non-perfect analyzer.

Optimizing the polarimeter

To study and optimize the modulator, we must also study the analyzer, i.e the Mueller matrix of the complete polarimeter must be studied. We can easily compute the Mueller matrix for the whole polarimeter from the modulator Mueller matrix computed above. The Mueller matrix for the whole polarimeter is

$$\begin{aligned}\mathbf{M_{polarimeter}} &= \mathbf{M_{analyzer}}(\theta_a) * \mathbf{R}(-m) * \mathbf{M_3} * \mathbf{R}(m) \\ &= \mathbf{M_{analyzer}}(\theta_a) * \mathbf{R}(-m) * \mathbf{M_R}(\theta_m, \lambda) \\ &\qquad * \mathbf{M_R}(2\theta_m - \frac{\pi}{2}, \lambda) * \mathbf{M_R}(\theta_m, \lambda) * \mathbf{R}(m)\end{aligned} \tag{4.11}$$

Choosing a set of modulation angles m, and keeping only the intensity of the resulting Stokes vector for each one of those angles, we can build the modulation matrix $\mathbf{O}$ as described in Section 1.3.3, which relates the incoming Stokes vector to the actual series of intensity measurements. An example of this modulation matrix is shown in Figure 4.8.

To quantify the performances of the whole polarimeter, and optimize it, we use the same polarimetric efficiencies introduced in equation 1.17. Optimizing the modulator consists in picking the material, incidence angle θ_m, and set of modulation angles m, that maximize these efficiencies ϵ_i. The need for a good reflectivity limits the materials available for the modulator to the same ones as those studied for the analyzer, i.e. SiC, *ta-C*, $Al + MgF2$... Crystals cannot be used for a reflective modulation because they do not introduce any phase shift between polarizations.
The incidence angle θ_m and modulation angles m have been optimized to minimize the difference between their computed efficiencies and the maximum theoretical one. The maximum theoretical efficiency is $\frac{1}{\sqrt{3}}$ in our case, since we choose to measure the Stokes Q, U, and V parameters with identical efficiencies. This can be tuned to highlight a particular

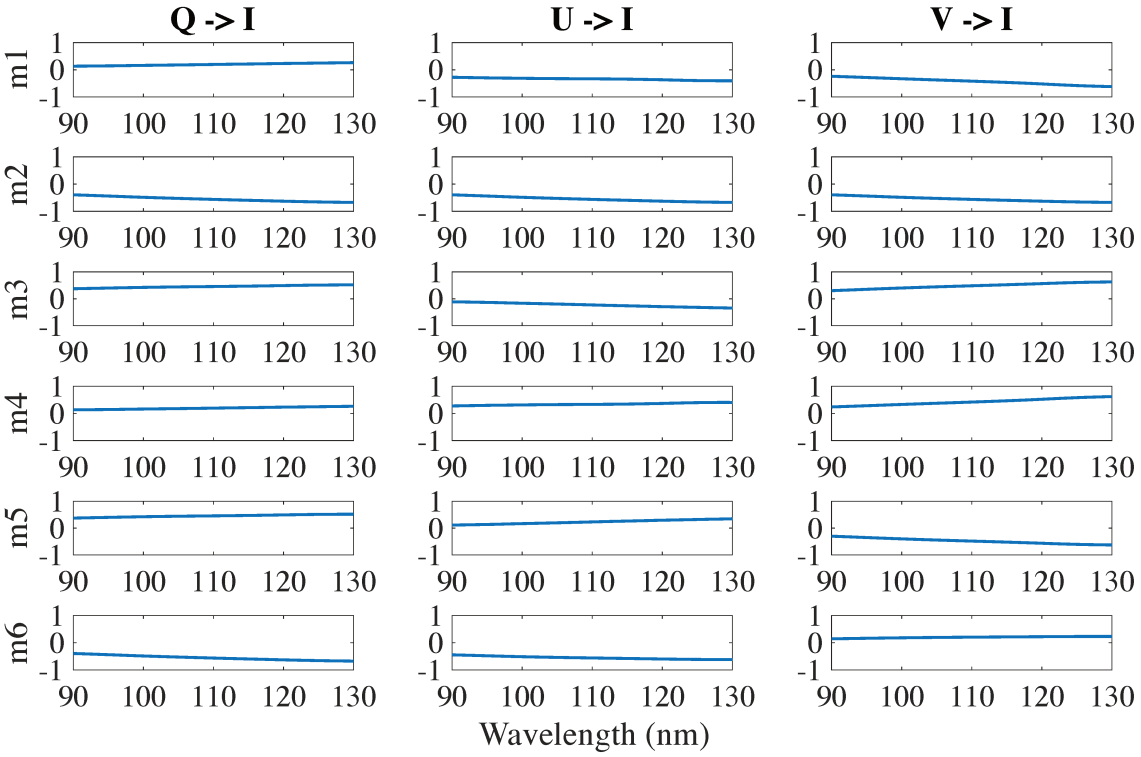

Figure 4.8: *Modulation matrix of the polarimeter for the FUV channel of POLLUX. made with one surface of B_4C, and two surfaces of SiC, and a ta-C analyzer.*

Stokes requirements. The incidence angle and modulation angles have been optimized for all combinations of materials for the three reflections including mixing and matching different materials in order to find the best polarimeter.
The actual number of measurements N, however, has been fixed by simple comparison of the best solutions obtained in each situation. A minimum of $N = 4$ is required to retrieve the 4 Stokes parameters, but increasing the number of measurements improves the SNR attributed to each Stokes vector. This may improve overall efficiency. To compromise between redundancy and convenience, we chose $N = 6$ for our polarimeter.

This optimization on the materials, incidence angle, and modulation angles has converged to one efficient modulator working from 90 to 130 nm. The first reflection is in B_4C and the two others are in SiC. The incidence angle is $\theta_m = 86.8°$. The modulator takes 6 angular positions: $15.8°, 48.4°, 66.0°, 114.0°, 131.6°$, and $164.2°$. Figure 4.9 shows the efficiencies in the 3 Stokes parameters Q, U, and V as a function of wavelength for this modulator and a *ta-C* analyzer. The black dotted line is the optimal efficiency $\frac{1}{\sqrt{3}}$ to measure the 3 Stokes parameters with the same efficiency. The efficiencies are around 0.3 at 90 nm and increase with wavelength to have a very satisfying result around 0.55 at 130 nm. The sensitivity of the modulator to the incidence angle is stronger than the one of the polarizer. Indeed, a

change of 0.1 degree in the incidence angle on the first mirror implies a change up to 0.04 in the polarization efficiencies.

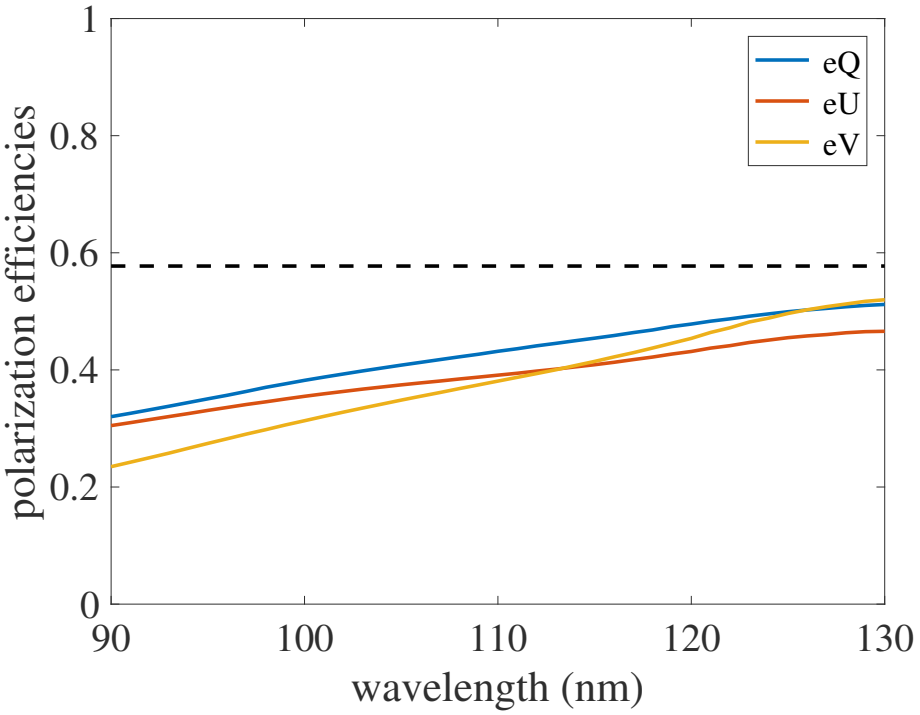

Figure 4.9: *Polarimetric efficiencies of the polarimeter for the FUV channel of POLLUX. It is made by reflection with a B_4C, and SiC modulator, and a ta-C analyzer. The black dotted line is the optimal efficiency at 57.7% we try to achieve.*

The theory of reflection polarimetry has been detailed and applied to the method for designing and optimizing UV polarimeters. A polarimeter operating in the FUV has been successfully designed and optimized. The results of the simulations are very encouraging and open the door to polarimetry in the FUV.

4.3 Testing equipment

As seen in the previous Section, complex indices have to be well known at every studied wavelength to optimize this polarimeter. Indeed, the equations in Section 4.2 show that the parameters of the modulation of the polarimeter are complex indices, wavelength, and incidence angles. At the present time, B_4C, SiC, and ta-C are being considered for POLLUX. Unfortunately, the indices found in the literature are not coherent between different sources, due to the dependence of the optical indices to the tested sample and measurement conditions. To measure indices at short wavelengths ourselves, it has thus been decided to

set up a gold reflective polarimeter. The polarimeter has the same design as the one studied above and is composed of pure gold. Gold has been chosen as it is a well-known material, and a gold polarimeter can then be precisely simulated. Moreover, the parameters of gold are constant with the supplier and process. The reflectivity is low, but since this is only for tests and material characterization, it is not important and can be compensated by long exposure times. Thanks to this experiment, a first prototype of a FUV reflection polarimeter is built and tested.

The experiment has been designed and built for tests in the FUV. However, only tests in the visible range have been performed so far. The experiment is presented in Section 4.3.1. The FUV polarimeter is presented in Section 4.3.2. The experiment and components for the FUV are introduced in Section 4.3.3 whereas the preliminary experiment carried out in the visible and its components are presented in Section 4.3.4. The challenging optical alignment is discussed in Section 4.3.5. Finally, the results of the experiment are presented in Section 4.4.

4.3.1 Experiment

The principle of measurement is the same as the polarimeter described for the FUV channel of POLLUX. The gold modulator rotates around the optical axis and modulates the light while a fourth gold mirror at the analog of the Brewster angle polarizes the light. The studied material sample is placed at the entrance of the gold polarimeter, and the Stokes vector is measured before and after reflection on the sample for several incidence angles. Knowing the Stokes vector before and after reflection enables us to retrieve the sample's complex indices.

It is very difficult to create polarization in the FUV in the same way as in the visible: quarter-wave plates or linear polarizers are not available. In order to change the incoming polarization on the sample without adding many reflections, it has been decided to rely on the instrumental polarization created by the monochromatic source. Indeed, the monochromatic source is obtained by using a windowless FUV source, a monochromator, and a collimator. These components are presented in Section 4.3.3. This set up creates instrumental polarization through the reflection on these components. As it is difficult to rotate the polarization of the incoming light, the optical bench was mounted on a rotating motor: the reference polarization axis rotates around the axis created by the incoming flux and thus simulates a rotation of the incoming polarization.

Our bench includes several rotations: the rotation of the modulator around the optical axis, the rotation of the sample on itself to change the angles of incidence and thus the tilt of the polarimeter around the sample in order to maintain the optical alignment, and the rotation of the whole bench around the axis created by the monochromatic source. The principle of the experiment is illustrated in Figure 4.10.

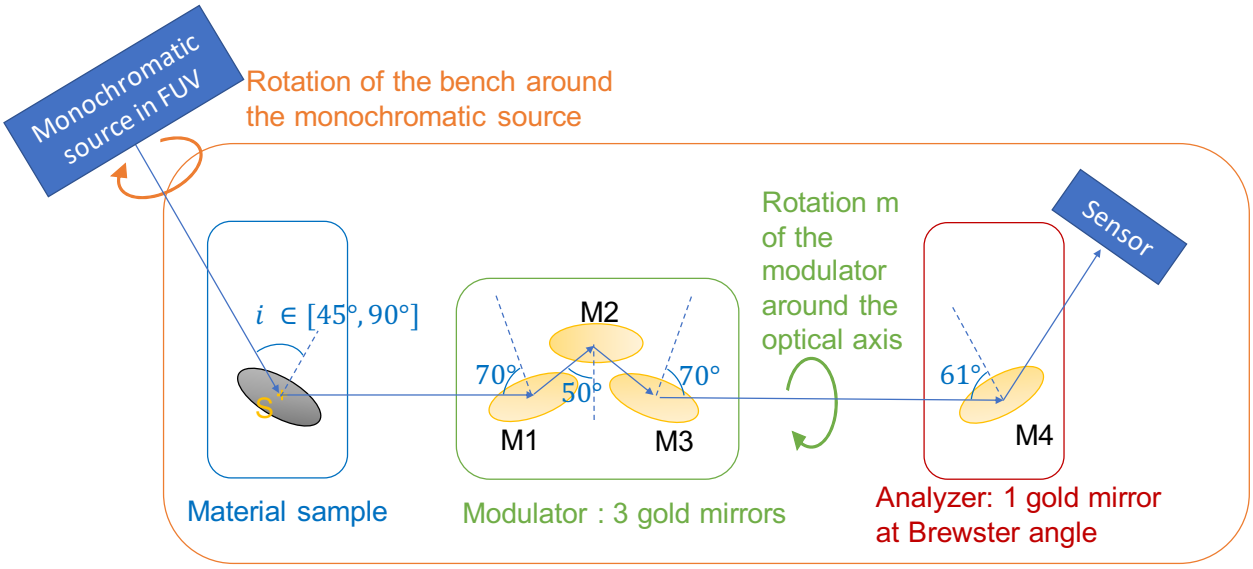

Figure 4.10: *Experiment using a gold polarimeter in order to retrieve the complex indices of samples of materials.*

4.3.2 Gold Polarimeter

The gold polarimeter was designed following the theoretical model explained in Section 4.2. First, the analyzer was optimised to find the angle that maximizes the contrast between the two orthogonal polarizations. The contrast is illustrated in Figure 4.11 as a function of the angle of incidence and the wavelength. The maximum average contrast over the considered wavelength range is 61°. Based on this analyzer, the modulator could be optimised to maximize polarimetric efficiencies. The angle of incidence on the first mirror of the modulator that maximizes the efficiencies is 70°. The most efficient gold polarimeter in the 90 - 120 nm wavelength range consists of a 3-mirror modulator with the first mirror angle at 70° and an analyzer at 61°. The optimisation of this polarimeter resulted in 4 modulation angles: 30°, 74°, 105°, and 149°. The extraction efficiencies of this polarimeter are shown in Figure 4.12. It can be seen that a very good extraction efficiency is obtained for the linear polarization Q, a very good one for the linear polarization U, and a rather poor one, less than 0.1, for the circular polarization V. The figure of merit for this polarimeter is shown in Figure 4.13. It is above 0.3 at 90 nm and almost reaches 0.4 at 130 nm.

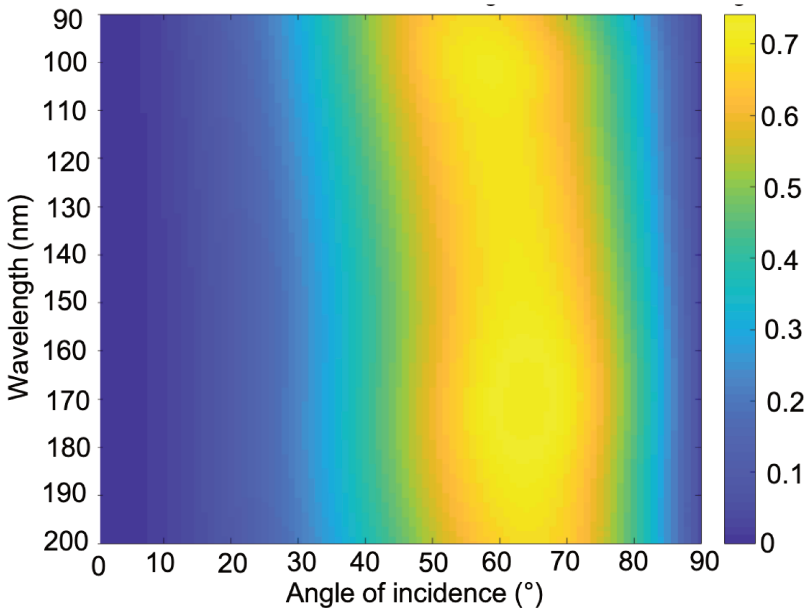

Figure 4.11: *Contrast between orthogonal polarizations as a function of incidence angle (in abscissa, from 0° to 90°), and as a function of wavelength (in ordinate, from 90 to 200 nm) for a gold mirror.*

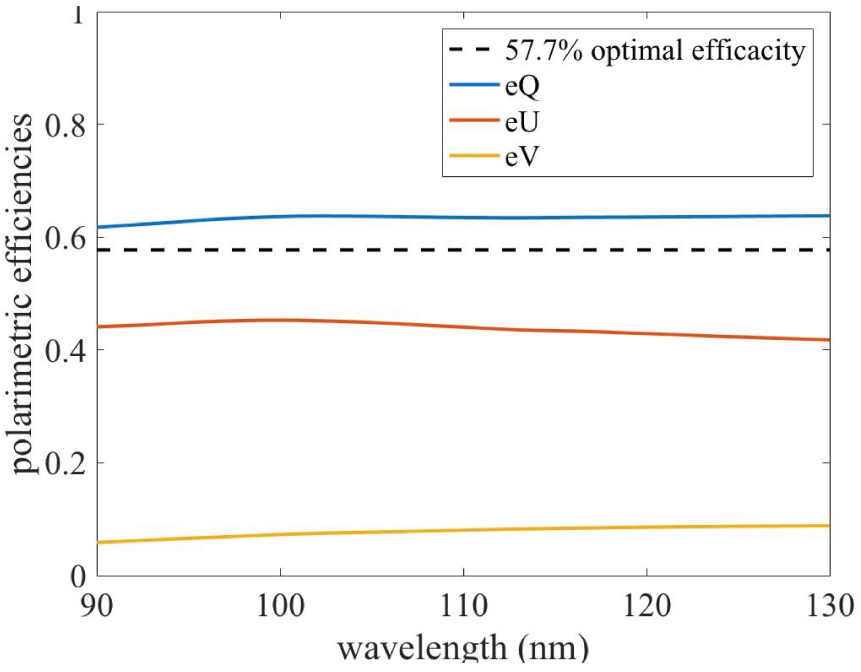

Figure 4.12: *Polarimetric efficiencies for a gold polarimeter with 4 angles of modulation (30°, 74°, 105°, and 149°).*

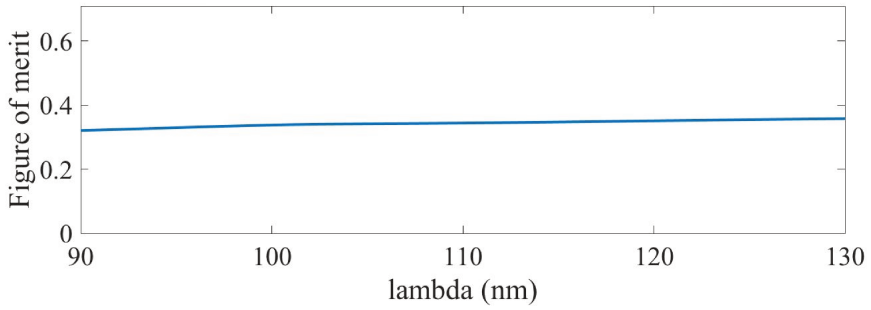

Figure 4.13: *Figure of merit of the gold Brewster-like analyzer (gold mirror at 61°) as a function of wavelength.*

4.3.3 Material test means for the FUV tests

This experiment was designed to be placed inside the FUV vacuum chamber at the Laboratoire ATMosphères, Observations Spatiales (LATMOS) at Guyancourt. The bench can be seen in Figure 4.14. It consists of a source entering a monochromator. The monochromator is a platinium (Pt) grating and reflects the light onto the collimator. The collimator is a curved Pt mirror which sends a collimated beam into the optical chamber. The experiment that has been set up here using a gold polarimeter will be placed in the test chamber. The LATMOS chamber was conceived for a use from 50 nm up to 300 nm.

Our optical bench consists of a modulator mounted on a rotating motor, an analyzer, a possible sample, and a detector, all of which are also on a rotating motor. The mechanical bench must also be able to adapt to the reflection on a sample: the optical axis must be able to tilt around the sample and must make two rotations. The mechanical bench was designed by Jean-Philippe Amans (GEPI, Observatoire de Paris), and is illustrated in Figure 4.15.

The UV optical bench is complete and uses the following components:

- Lamp Source: Resonance EUV - X - L Flow Lamp. It is a windowless source. The lamp has a gas inlet and outlet. Between the two, the gas is excited and emits light. The considered gas for this experiment is nitrogen.
- Monochromator: VUV grating referenced 549 00 201 from Horiba Jobin Yvon, made in Al, and covered with Pt. Groove density : 2726 gr/mm.
- Collimator: A toroidal mirror made with silica (BK7) and covered with a Pt coating.
- Gold mirrors: The four mirrors of the polarimeter are unprotected gold mirrors from Thorlabs, referenced PF10-03-M03.
- Samples: We have several materials available for testing. The first material sample is gold, i.e. the same Thorlabs mirror as the polarimeter. Secondly, REOSC lent us SiC

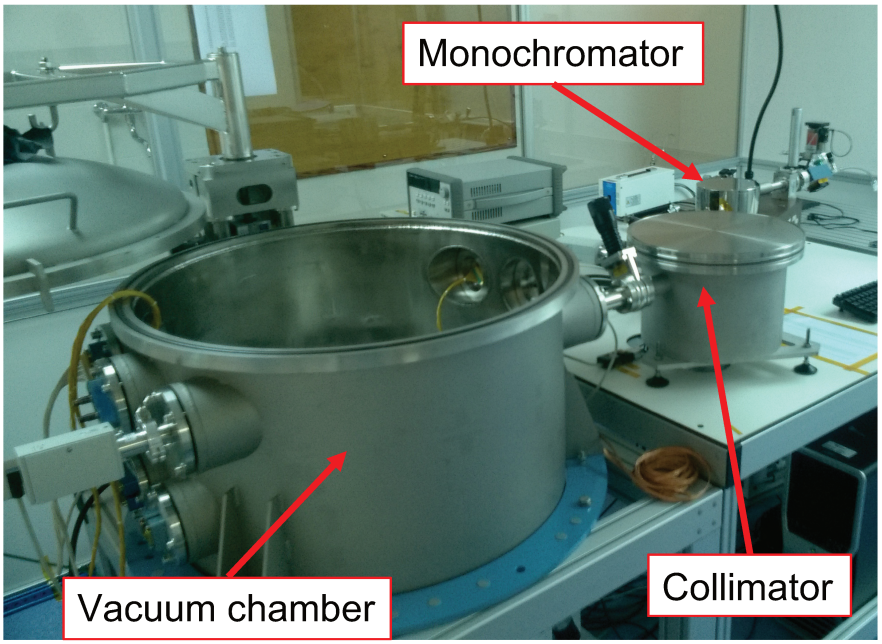

(a)

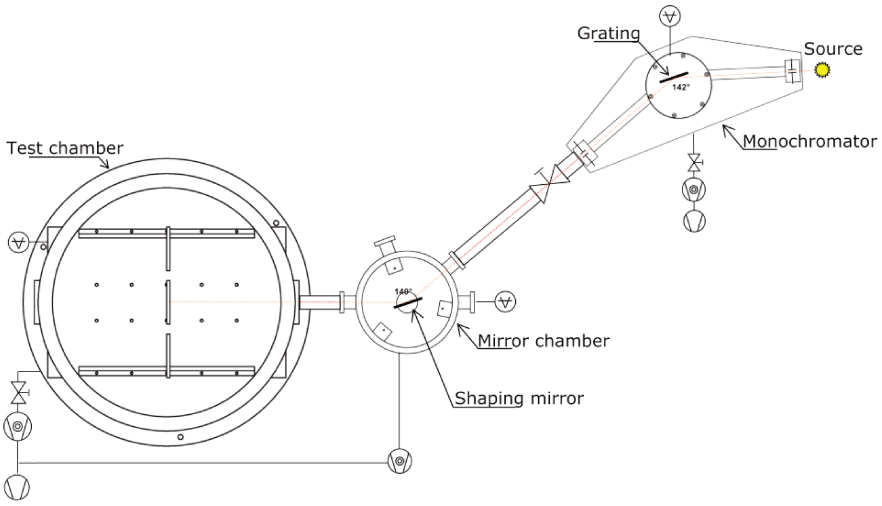

(b)

Figure 4.14: *4.14a: Picture of the vacuum chamber available at LATMOS. On the left, and in the foreground, one can see the main vacuum chamber. On the right, in the background of the picture, one can see the monochromator. The middle chamber hosts the collimator. 4.14b: Scheme of the same bench. Credit: Jean-François Mariscal (LATMOS).*

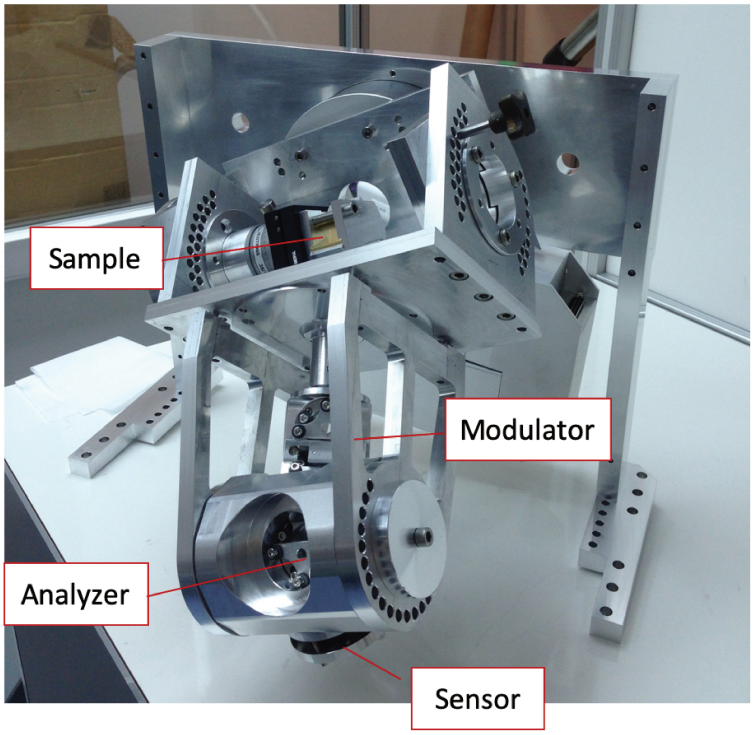

Figure 4.15: *Mechanical bench of the reflective polarimeter.*

and B4C samples, and finally, Avi Bendavid and Phil Martin at CSIRO provided us with samples of ta-C. We will therefore test Au, SiC, B4C, and ta-C.

- Detector: The detector is a channel electron multiplier (CEM) referenced 5901 with MgF_2 coating from Photonis, called a channeltron. The channeltron detects photons and particles directly, and amplifies them. The CEM is powered by a PF1053 power supply from Photonis. The detector is read out by the Ortec 550A Single Channel Analyzer.

- Electronic rotators: Several rotations are available on the bench. The first rotation, corresponding to the modulation, is performed by the Newport URS75PPV6 rotation stage. The second rotation, corresponding to the rotation of the whole polarimeter, is performed by the Newport RV160PE-FV6 rotation stage.

The optical alignment of this bench is very complex to set up. The center of the rotations must coincide perfectly with each other, and the 3 axes of the bench – the optical axis created by the mirrors, the mechanical axis created by the rotations, and the light axis created by the light source – must be identical to keep the bench aligned in all configurations. In order to achieve this complex alignment, it is preferable to start with visible light. Indeed, in visible light, the light beam is seen, but also the experiment can be performed in ambient air (rather than vacuum).

4.3.4 Material test means for the visible tests

For the visible experiment, the mechanical bench, the polarimeter, and the samples remain unchanged. However, the light source and detector were replaced by components adapted to visible light. The realization of the visible experiment also made it possible to carry out the first tests with controlled polarizations thanks to birefringent components. The visible bench follows the same principle as the bench set up for the UV transmission polarimeter (see Chapter 3). The light source is sent into an integrating sphere, which creates a depolarized source. This source is collimated by a lens. The collimated beam passes through a filter to obtain monochromatic light. The beam is then polarized by a linear polarizer and quarter-wave plate. The polarized beam then enters the polarimeter inside the mechanical structure described above. The components used specifically for this bench in the visible range are:

- Source: Fiber-Coupled Light Sources OSL2 from Thorlabs
- Integrating sphere: IS200 from Thorlabs
- Lens: singlet from Melles Griot, focal length 25 mm, diameter 1"
- Spectral filter: Thorlabs FL632.8-1 filter creating monochromatic light at 632.8 nm. The bandwidth is 1 nm.
- Linear polarizer: 1" diameter achromatic grid polarizers from Thorlabs
- Quarterwave plate: MgF2 achromatic plates from Bernhard Halle Nachfolger GmbH
- Camera: Edmund Optics camera EO-1312M

The pictures in Figures 4.17a and 4.17b show the experimental bench. At the front, the silver mechanical structure holds the polarimeter. In Figure 4.17a, the bench is in a direct polarization measurement, without reflection on a sample. The optical axis is not tilted. It is also the position in which the experimental modulation matrix is measured. In Figure 4.17b, the bench is in a position of measurement of a polarization after reflection on a sample, the bench is bent along the optical axis. In the background, an optical breadboard is visible. It is on this table that the visible source, the linear polarizer, and the quarter-wave plate are set up for the experiment.

4.3.5 Optical alignment

In order to align the optical bench, the rotation axis of the modulator, the axis of the light beam, and the optical axis created by the mirrors must coincide. In addition, these axes must pass through the center of the sample in order to be aligned at any reflection angle. A method has been developed and carried out, to perform a first non-perfect alignment. This method and the errors it generates are explained in this Section. A method achieving an

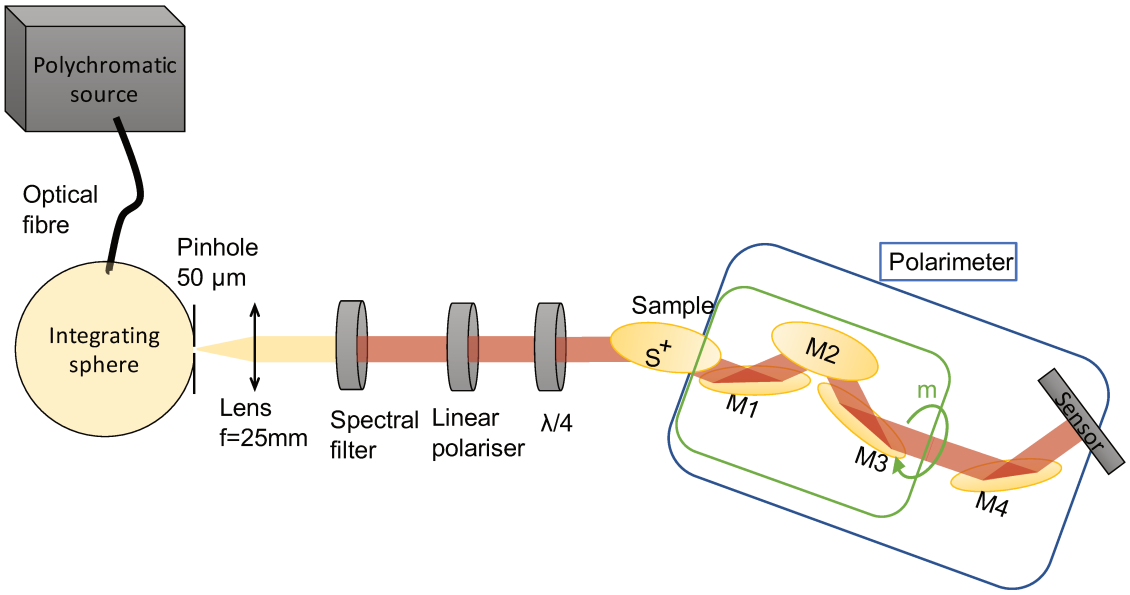

Figure 4.16: *Experiment performed in visible light using a gold polarimeter in order to retrieve the complex indices of material samples.*

extremely accurate alignment has been developed by the team working on a pupil de-rotator for the instrument Multi-AO Imaging Camera for Deep Observations (MICADO) for the Extremely Large Telescope (ELT) a ground-based telescope [63]. This method could not be implemented here due to time constraints, but should be used in the future to achieve better performances. It is briefly explained below.

Alignment carried out

The alignment is constrained by the settings available on the bench: the mechanical axis and the sample holder are not adjustable. The modulator cannot be removed as a single unit, only the mirrors can be removed independently. Removing the mirrors breaks their alignments. The polarizer, on the other hand, can be removed with its mechanical structure without affecting its optical alignment.

The alignment is done in several steps. First, a light source must be mounted to perform the alignment. This source must be aligned with the mechanical axis, defined by the rotation stage and the sample holder. This part is described in paragraph A below. Then, the polarizer should be adjusted, it defines the polarization axis. This alignment is described in paragraph B. Finally, the polarizer can be removed, and the modulator adjusted. This adjustment is explained in paragraph C and illustrated in Figure 4.18.

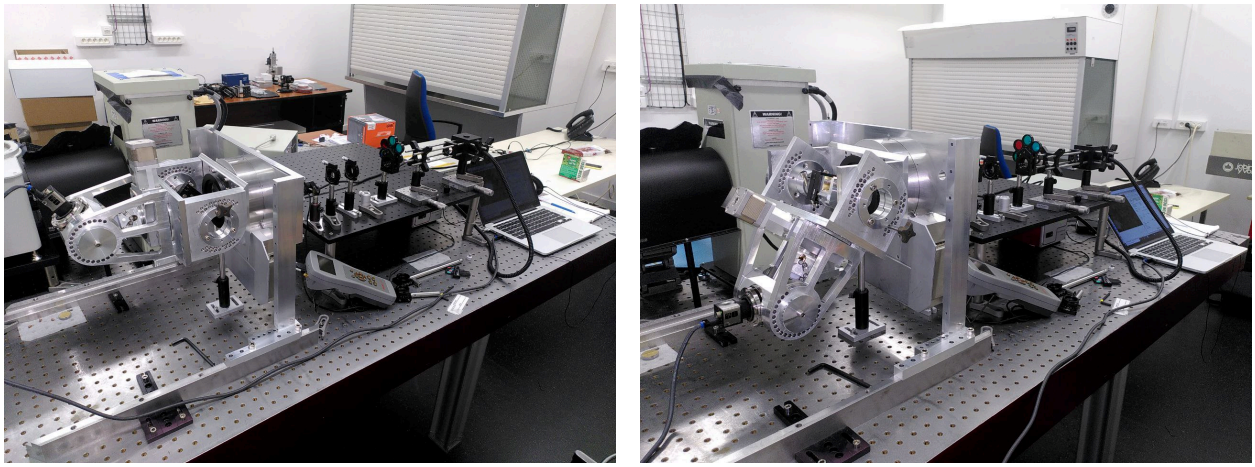

(a) (b)

Figure 4.17: *4.17a: Picture of the reflection polarimetry bench in position to measure the Mueller matrix. 4.17b: Picture of the reflection polarimetry bench in position to measure the polarization after reflection on a sample.*

A - Alignment of the source axis with the mechanical axis: The alignment of the bench requires the use of a laser source, which is the only source powerful enough to use reflections on the components. In order to align the axis of the light beam with the mechanical axis of rotation, the laser is centered on the diaphragms present on the mechanical structure. Then, a mirror is stuck at the output of the mechanical structure. The laser beam is reflected by the mirror. By confusing the laser beam with its reflection from the mirror, the tilt of the mirror is adjusted. This relies on the precision of the mechanics and induces small errors in the alignment.

B - Alignment of the analyzer and measurement of the polarimetric reference axis: Once the light axis is set, the analyzer can be installed without the modulator. M4, the analyzer mirror, is adjusted so that the beam is centered on the detector. The analyzer defines the polarization axis of the experiment. The polarization optics (linear polarizer and quarter-wave plate) must therefore be adjusted before adding the modulator. The laser being linearly polarized, it cannot be used for this alignment. The laser source is replaced by a non-polarized source (a polychromatic source and an integrating sphere, as described in the previous Section). By rotating the linear polarizer, a change in intensity is observed. When the light flux goes out, the linear polarizer and the analyzer are crossed. If the analyzer sets the zero axis, the linear polarizer is then at 90°. The quarter-wave plate is placed between the crossed linear polarizer and analyzer. A rotation of the quarter-wave plate also creates a change in intensity. The light flux is maximised when the plate is at 45° away from the reference axis. The optics (polarizer and quarter-wave plate) that we will use during

the experiment are now aligned to the analyzer. The analyzer can be removed to align the modulator.

C - Alignment of the modulator: Now that the analyzer and the polarization axis are set, the modulator can be aligned. A laser source should be used again, in order to see the reflections on the components. First, the middle mirror of the modulator, M2, is aligned using a cube beamsplitter. The beamsplitter is aligned without M2, using the reflection on its first side. Then M2 is added and the reflection of the laser is used to align it: the M2 mirror is then parallel to the optical beam and to the axis of rotation of the modulator. The last mirrors, M1 and M3, are adjusted together. The addition of M1 and M3 should not alter the axis of the light beam. Two methods are implemented to check the tip and the tilt of the axis. Before mounting M1 and M3, an auto-collimation mirror is mounted. The reflection of the laser source should be colinear with the light source. A screen with a target is mounted on an optical rail: the image spot must not move from the target. The screen is mounted on a rail so that it can be removed and replaced without misaligning it. M1 and M3 are then mounted. By going back and forth between the target and the reflection on the mirror, they can be adjusted so that the reflection of the laser source is still colinear to the laser source, and that the laser is still in the target. These 3 steps for the modulator adjustment are illustrated in Figure 4.3.5.

Once M1 and M3 are set, the alignment can be checked by rotating the modulator: the light axis should not be modified. With the modulator now adjusted, the analyzer can be placed again. The optical bench is ready to be used. However, we stress that this alignment is not perfect. Indeed, relying on mechanical alignment is never sufficient for an optical setup. Moreover, having to change the light sources during the adjustment introduces errors, since one is unlikely to place the source back at exactly the same place.

The intensity modulation is not extremely sensitive to the incidence angles on the mirrors. If the alignment is not done correctly, the risk is to have different mirror angles for each modulation angle. For angular errors of less than 3 degrees, numerical simulations give polarization measurements with errors of less than 10^{-12}. However, different incidence angles depending on the modulation angle also means that the beam is not at the same location on the detector for all modulation angles. The optical beam follows an epicycloid as the modulator rotates, which is visible on the detector. As the detector pixels do not have the same response, it will produce a signal detection error depending on the modulation angle. These photometric errors can have a great impact on the polarization errors but are difficult to estimate. Flat-field images have been acquired to reduce these errors, however these errors cannot be considered negligible. Finally, the misalignment of the optical bench makes it more difficult to measure polarization after reflection on the materials. Indeed, since the position of the sample is not adjustable, a prior misalignment is accentuated by the reflection on the sample.

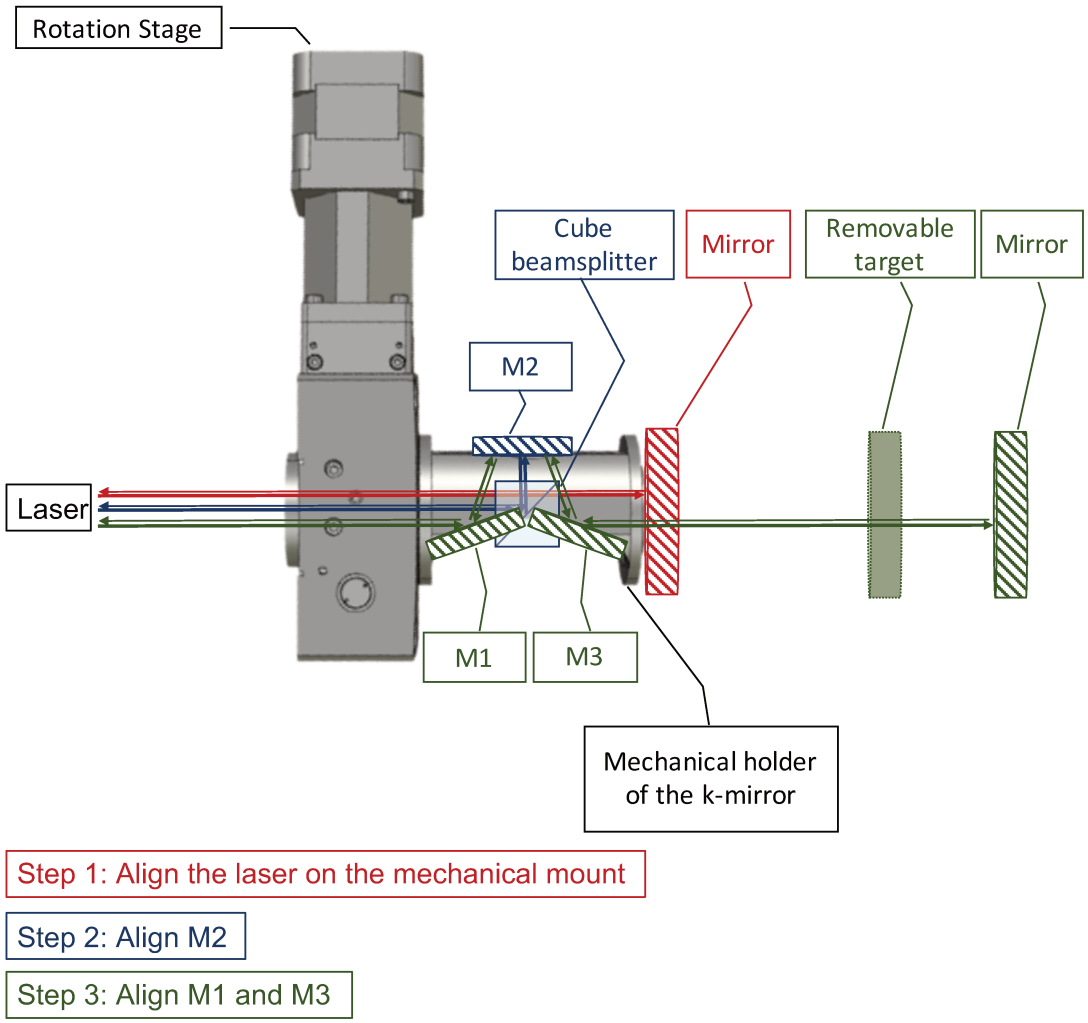

Figure 4.18: *Alignment method used to align the reflective modulator. The steps are represented by different colors. The first step is in red, the second in blue, and the third in green.*

Next step to reach a near-perfect alignment

The team working on the Multi-AO Imaging Camera for Deep Observations (MICADO) instrument, an adaptive optics instrument for the Extremely Large Telescope (ELT), uses a K-mirror as a pupil de-rotator. To align this K-mirror, they encounter the same challenges as for the alignment of the gold reflective polarimeter, and they developed a very precise alignment procedure. The K-mirror alignment performed by the MICADO team is described in [63]. This alignment is briefly described here in order to present its main features. When the K-mirror rotates, the beam forms an epicycloid: it describes a circle around a center C, which itself follows a circle. The epicycloid formed by the gold mirror is shown in Figure

4.19. The center C moves because the mechanical axis is misaligned with the optical axis. The complete characterisation of this epicycloid determines the mechanical axis, and thus can be used to merge it with the optical axis. To fully determine the epicycloid, two point sources are sent into the K-mirror. Using both sources, the rotations (centers and angles) can be precisely determined. Finally, to adjust the mirrors of the K-mirror simultaneously, several view points are required. In the case of the MICADO team, the M1 and M3 mirrors of the K-mirror are a single optical part: a prism. Therefore, they have two components to align: the prism and the M2 mirror. They are using two double sources, with two cameras at different distances (preferably one very close and one very far). Using these two optical paths and the two cameras, and by going back and forth, they can simultaneously align both components.

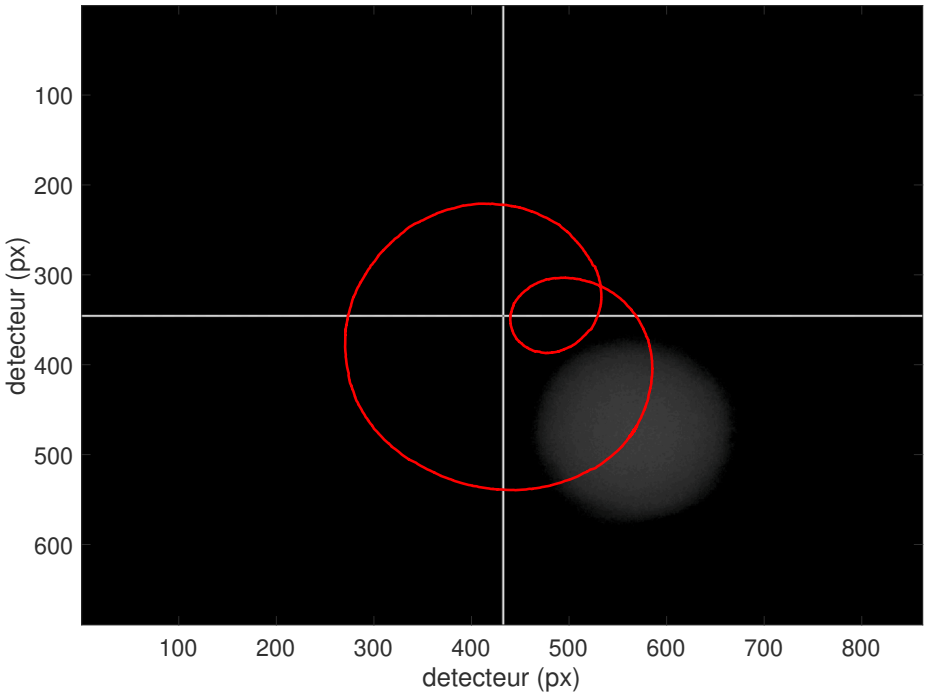

Figure 4.19: *Tracking the center of the image beam on the detector as the modulator rotates. The dimensions of the detector are 6.79 x 5.43 mm. The curve is drawn over an image of the detector. This image was taken without spectral filter, i.e. with polychromatic light.*

Before running the experiment in the UV, it will be necessary to proceed with this almost perfect alignment. In the UV, the detector is not a CDD but a photon counter; thus, a shift on the detector would greatly distort the measurement. Furthermore, this alignment is necessary to make reliable polarization measurements after reflection on material samples.

4.4 Acquisitions and measurements in the visible

The first results obtained in the visible range are presented in this Section. The tests were carried out at the wavelength $\lambda = 632.8$ nm. In Subsection 4.4.1, the visible gold polarimeter is simulated and experimentally characterised. Its modulation is measured. Then, in Subsection 4.4.2, polarization measurements after reflection on samples are performed.

4.4.1 Gold polarimeter test

Modulation

In order to see how the polarimeter works, a measurement of intensity versus modulation angle was made for a linear polarization of 100% Q. These measurements are shown in Figure 4.20. A sinusoidal curve is clearly visible. For a non-polarized light, no variation of intensity was observed. This intensity variation for polarized light shows that the polarimeter creates a polarization modulation in intensity. This proves the working principle of the polarimeter.

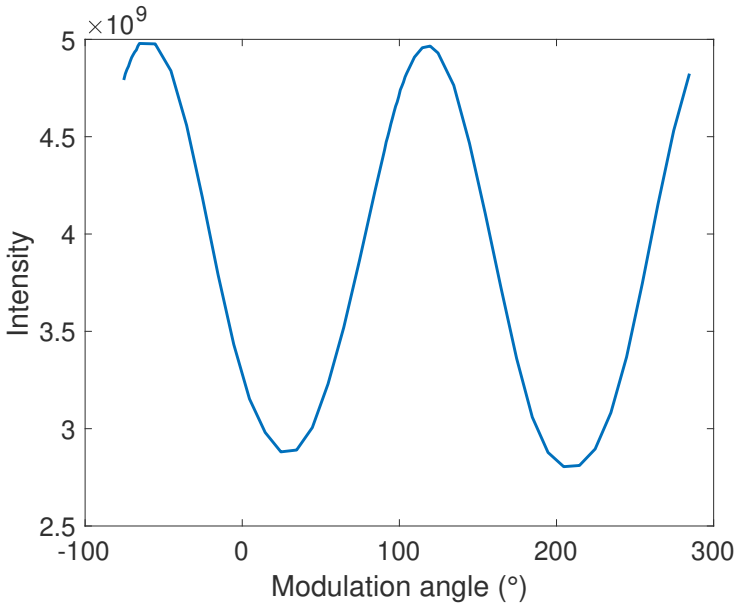

Figure 4.20: *Variation of intensity as a function of the modulation angles. The spectral filter was not included for this measurement.*

To test the polarimeter further, the experimental modulation matrix must be measured. Then, known polarizations are sent into the polarimeter, and the measured intensities are demodulated to verify the correct functioning of the polarimeter. First, the procedure to process the measured intensities is explained. Then, the experimental modulation matrix is compared with the theoretical one. Finally, the polarization measurements are presented.

Processing of measurements

For each incoming polarization and for each modulation angle, 50 images with an integration time of 2 seconds were recorded. All images are summed. Each stack of images is processed with a dark and a flat-field correction.

The dark is obtained by taking images in the same conditions on the camera (integration times, frame rate, etc) without any input light. It is the noise of the camera.

The flat-field is obtained by taking images of a uniform source. The global normalized flat-field T is then computed using N images following the equation:

$$T = \frac{\sum_{n=1}^{N} Flat_n - \sum_{n=1}^{N} Dark_n}{< \sum_{n=1}^{N} Flat_n - \sum_{n=1}^{N} Dark_n >} \tag{4.12}$$

The intensity measurement of a polarization I_{mes} are processed from the measurement $Image$ following:

$$I_{mes} = \sum_{(x,y)\in C_R} \frac{\sum_{n=1}^{N} Image_n - \sum_{n=1}^{N} Dark_n}{T} \tag{4.13}$$

where C_R is the circle of radius R around the beam image center, (x,y) are the coordinates of the pixel on the image, and N is the number of images. In our case, N=50 images were considered and the signal was summed on a circle of radius R=200 px.

For this experiment, calibration measurements were not performed. The source is considered stable and is not switched off during the time necessary for the experiment (∼1 day). The polarization measurements Q, U, and V are consistent with each other, only the level of intensity is unknown. Since the light is 100 % polarized, the formula 1.2 can be used to find the intensity I of the measured Stokes vector. As a reminder, the equation is:

$$I^2 = Q^2 + U^2 + V^2. \tag{4.14}$$

Error bars can be given for each measurement due to the large number of recorded images. The errors are found statistically. For each polarization measurement, demodulations are performed 1000 times using 25 random images out of the 50 recorded ones. Each demodulation gives a different result and the standard deviation of these results gives the statistical error on the measurement. This technique is used to compute error bars in the following paragraphs.

Modulation matrix

The UV performance of the polarimeter was studied in Section 4.3.2. Using the theory developed in Section 4.2, the modulation matrix and efficiencies are calculated at 632.8 nm.

The theoretical modulation matrix O_{th} is as follows:

$$\mathbf{O_{th}} = \begin{pmatrix} 1 & -0.0446 & -0.1486 & -0.0010 \\ 1 & 0.0928 & -0.0320 & -0.0006 \\ 1 & 0.0926 & 0.0295 & 0.0006 \\ 1 & -0.0382 & 0.1493 & 0.0010 \end{pmatrix} \tag{4.15}$$

The theoretical polarization extraction efficiencies are :

$$\begin{aligned} \epsilon_{Q,th} &= 0.06700 \\ \epsilon_{U,th} &= 0.03503 \\ \epsilon_{V,th} &= 0.00027 \end{aligned} \tag{4.16}$$

These efficiencies are extremely low, especially for V. Indeed, the polarimeter was not designed for the visible light and is not optimal in this range.
By sending 100%Q, 100%U, or 100%V polarized light, the experimental modulation matrix can be determined, similarly to what was done in Chapter 3. As the unpolarized intensity was not measured, an intensity was numerically estimated from the theoretical modulation matrix to obtain results. As seen in Chapter 3 in equation 3.9, in order to obtain the coefficients of the matrix $\alpha_{Q/U/V}$, the intensity measurement $I_{out,Q/U/V}$ for a polarization 100%Q, U, or V, must be normalized by the input intensity I_{in} and the transmission, then 1 must be subtracted:

$$\alpha_{Q/U/V} = \frac{I_{out,Q/U/V}}{T.I_{in}} - 1 \tag{4.17}$$

The intensity I_{in} was estimated numerically using the theoretical matrix:

$$I_{in} = mean_{m,QUV}\left(\frac{I_{out,Q/U/V}}{\alpha_{th,Q/U/V} + 1}\right) \tag{4.18}$$

where m are the modulation angles. This estimate leads to errors in the degree of polarization and in the determination of the parameter I of the Stokes vector. However, the coefficients Q, U, and V must each be found in the correct proportions. Parameter I can then be calculated using equation 4.14.

The experimental modulation matrix O_{exp} is:

$$\mathbf{O_{exp}} = \begin{pmatrix} 1 & -0.187 \pm 0.002 & -0.260 \pm 0.002 & -0.014 \pm 0.002 \\ 1 & 0.240 \pm 0.002 & -0.114 \pm 0.002 & 0.049 \pm 0.002 \\ 1 & 0.281 \pm 0.002 & 0.122 \pm 0.002 & -0.006 \pm 0.002 \\ 1 & -0.082 \pm 0.002 & 0.185 \pm 0.002 & -0.046 \pm 0.002 \end{pmatrix} \tag{4.19}$$

Experimental polarimetric efficiencies are:

$$\begin{aligned} \epsilon_{Q,exp} &= 0.0750 \\ \epsilon_{U,exp} &= 0.0756 \\ \epsilon_{V,exp} &= 0.0117 \end{aligned} \tag{4.20}$$

The experimental matrix is quite similar to the theoretical matrix, without taking into account the level of the intensity. The coefficients of V are very low, they cannot be compared because they are inside the instrumental errors. By looking only at the ratio between the values of the Q, U, and V coefficients, corresponding to the second, third, and fourth columns, the proportions between the coefficients seem to be similar to what is expected from the theoretical modulation matrix (4.15). For example, for the parameter Q (second column), the coefficients from modulation m2 and m3, corresponding to the second and third lines, have close values that are higher than the coefficient from modulation m1. The coefficient from modulation m4 is much lower. For the third column, we find the same effect: parameters 1 and 4 are larger than parameters 2 and 3. In addition, all the signs of columns Q and U are identical in the theoretical and experimental matrices.

The experimental polarimetric efficiencies ϵ_Q, ϵ_U, and ϵ_V are slightly higher than those calculated theoretically. Nevertheless, they are of the same order of magnitude. Based on this experimental matrix, polarization measurements can now be performed. The obtained polarization results should be normalized by the intensity calculated using equation 4.14.

Polarization measurement

Several polarization measurements were performed. Firstly, measurements of 100% Q, 100% V, and 100% U polarizations used in the matrix were demodulated. For this purpose, out of the 50 collected images, only 20 were randomly selected to compute the modulation and demodulation matrices, and another 20 were used as measurements. This test estimates the photometric errors that we obtain on our measurements. Indeed, no optics has been moved between the determination of the matrix and the measurements, so the alignment errors are negligible. These errors quantify the minimal errors that can be obtained with our polarimeter. These tests are called Q, U, and V, and are presented in Figure 4.21.

These results show the correct operation of the polarimeter. Indeed, all the polarizations Q, U, and V are retrieved as expected. However, the errors vary a lot depending on the input polarization. Indeed, one should note in particular a large error of 0.12 on V, likely due to the very low efficiency of the polarimeter for this parameter.On all other polarization measurements, the maximum error observed is 0.02.

Next, three particular polarizations, named A, B, and C, were sent to the polarimeter and then demodulated to check that the input polarization was found. These measurements have both alignment errors and photometric errors. The results are shown in Figure 4.22. The photometry errors are of the same level as the ones observed for the previous measure-

Name	S_{th}	S_{exp}	Photometry Errors
Q	$\begin{pmatrix}1\\1\\0\\0\end{pmatrix}$	$\begin{pmatrix}1\\0.994\\0\\0\end{pmatrix}$	$\begin{pmatrix}0\\0.009\\0.02\\0.12\end{pmatrix}$
U	$\begin{pmatrix}1\\0\\1\\0\end{pmatrix}$	$\begin{pmatrix}1\\0\\0.994\\0\end{pmatrix}$	$\begin{pmatrix}0\\0.02\\0.009\\0.12\end{pmatrix}$
V	$\begin{pmatrix}1\\0\\0\\1\end{pmatrix}$	$\begin{pmatrix}1\\0\\0\\0.999\end{pmatrix}$	$\begin{pmatrix}0\\0.02\\0.02\\0.005\end{pmatrix}$

Figure 4.21: *Measurements of 100% Q, U, and V polarizations, and their errors without optical misalignment with respect to the modulation matrix. S_{th} is the theoretical input polarization, and S_{exp} is the measured polarization. The column photometry results gives the results of the statistical demodulation.*

ments of Q, U and V with a maximal error of 0.1. Nevertheless, other errors are introduced. Indeed, when aligning the linear polarizer and the quarter wave plate to create the polarization, the alignment accuracy is expected to be $\pm 1°$. The error of alignment of the optical components creates a small change of the optical path inside the modulator, and thus the input polarization undergoes a different modulation than the one used to demodulate the signal. This induces errors in the polarization measurements. The difference between the theoretical polarizations and the measurements is given by $\Delta S = |S_{th} - S_{exp}|$. The maximal error is 0.26 in the measurement of polarization A. This error should decrease with a better alignment of the modulator.

Finally, Q, U, and V polarizations were performed again, after manipulation of the optics. In these measurements, both photometry and alignments errors are expected. These measurements are presented in Figure 4.23, as Qbis, Ubis, and Vbis. For the measurements of Qbis, Ubis, and Vbis, the errors ΔS are up to 0.5 and we see that there is a lot of crosstalk from linear polarization to circular polarization.

These tests have shown that the polarimeter works well. However, the photometry errors reach 0.12, and the alignment errors reach 0.5. The alignment errors should decrease significantly with a better alignment of the modulator. Alignment errors can be significant as the demodulation is done with a different matrix than the modulation. Despite these errors, all the injected polarizations were globally retrieved. The results are very encouraging and constitute the first measurements of reflection polarimetry in the visible.

Name	S_{th}	S_{exp}	Photometry Errors	$\Delta S = \lvert S_{th} - S_{exp} \rvert$
A	$\begin{pmatrix} 1 \\ -0.293 \\ 0.283 \\ 0.914 \end{pmatrix}$	$\begin{pmatrix} 1 \\ -0.25 \\ 0.54 \\ 0.8 \end{pmatrix}$	$\begin{pmatrix} 0 \\ 0.02 \\ 0.05 \\ 0.04 \end{pmatrix}$	$\begin{pmatrix} 0 \\ 0.043 \\ 0.257 \\ 0.114 \end{pmatrix}$
B	$\begin{pmatrix} 1 \\ -0.043 \\ 0.405 \\ 0.914 \end{pmatrix}$	$\begin{pmatrix} 1 \\ 0 \\ 0.56 \\ 0.83 \end{pmatrix}$	$\begin{pmatrix} 0 \\ 0.03 \\ 0.06 \\ 0.04 \end{pmatrix}$	$\begin{pmatrix} 0 \\ 0.043 \\ 0.155 \\ 0.084 \end{pmatrix}$
C	$\begin{pmatrix} 1 \\ 0.866 \\ 0.5 \\ 0 \end{pmatrix}$	$\begin{pmatrix} 1 \\ 0.946 \\ 0.30 \\ -0.07 \end{pmatrix}$	$\begin{pmatrix} 0 \\ 0.006 \\ 0.02 \\ 0.1 \end{pmatrix}$	$\begin{pmatrix} 0 \\ 0.08 \\ 0.2 \\ 0.07 \end{pmatrix}$

Figure 4.22: *Measurements of A, B, and C polarizations, and their errors. S_{th} is the theoretical input polarization, and S_{exp} is the measured polarization. The column photometry results gives the results of the statistical demodulation. ΔS is the difference between the theoretical input Stokes vector and the one measured.*

Name	S_{th}	S_{exp}	Photometry Errors	$\Delta S = \lvert S_{th} - S_{exp} \rvert$
Qbis	$\begin{pmatrix} 1 \\ 1 \\ 0 \\ 0 \end{pmatrix}$	$\begin{pmatrix} 1 \\ 0.86 \\ -0.15 \\ 0.5 \end{pmatrix}$	$\begin{pmatrix} 0 \\ 0.05 \\ 0.03 \\ 0.1 \end{pmatrix}$	$\begin{pmatrix} 0 \\ 0.14 \\ 0.15 \\ 0.5 \end{pmatrix}$
Ubis	$\begin{pmatrix} 1 \\ 0 \\ 1 \\ 0 \end{pmatrix}$	$\begin{pmatrix} 1 \\ -0.04 \\ 0.96 \\ 0.3 \end{pmatrix}$	$\begin{pmatrix} 0 \\ 0.02 \\ 0.03 \\ 0.1 \end{pmatrix}$	$\begin{pmatrix} 0 \\ 0.04 \\ 0.04 \\ 0.3 \end{pmatrix}$
Vbis	$\begin{pmatrix} 1 \\ 0 \\ 0 \\ 1 \end{pmatrix}$	$\begin{pmatrix} 1 \\ 0.07 \\ -0.14 \\ 0.99 \end{pmatrix}$	$\begin{pmatrix} 0 \\ 0.03 \\ 0.04 \\ 0.01 \end{pmatrix}$	$\begin{pmatrix} 0 \\ 0.07 \\ 0.14 \\ 0.01 \end{pmatrix}$

Figure 4.23: *Measurements of 100% Q, U, and V polarization, and their errors with optical misalignment with respect to the modulation matrix. S_{th} is the theoretical input polarization, and S_{exp} is the measured polarization. The column photometry results gives the results of the statistical demodulation. ΔS is the difference between the theoretical input Stokes vector and the one measured.*

4.4.2 Tests on material samples

The gold polarimeter being characterized, it is now possible to make polarization measurements of material samples to characterize them. To this aim, polarizations before and after reflections from materials should be measured. The materials we tested so far are SiC and $ta-C$. Two samples of each are shown in Figure 4.24. In addition to being excellent candidates for our UV reflection polarimeters, SiC and ta-C can be compared to the recent data measured in [29] and [33].

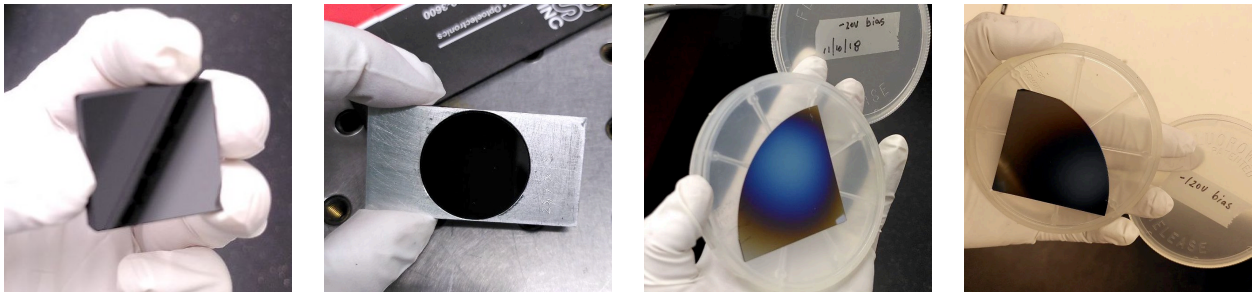

(a) **(b)** **(c)** **(d)**

Figure 4.24: *Samples of SiC, and ta-C are presented. Samples presented in subfigures 4.24a, and 4.24b are made in SiC. Samples presented in subfigures 4.24c, and 4.24d are made in ta-C.*

The measurements were made after a reflection at a 63° incidence angle on two samples of SiC, two samples of ta-C, as well as one sample of Au similar to the ones used for the polarimeter. The input Stokes vector before reflection was 100% Q. Based on the measurements made in Section 4.4.1, the errors on these measurements will be at least 0.5. The errors could be higher as the addition of the sample increases the optical misalignment. Moreover, the flux reflected by SiC and ta-C are very low in visible light. The photometric errors should thus also be higher than the ones detected in the previous Section. The results of polarization measurements after reflection on five samples are presented in Figure 4.25. For each sample, the theoretical Stokes vector is presented. The differences obtained between the measured and calculated polarizations can be explained by all the reasons listed above, but also by the difference in optical indices between the samples and the theoretical optical indices. It is interesting to note that the two SiC samples we tested give very different results, with notably opposite Stokes V parameters, but we recall that the polarimeter has a very low efficiency in V in the visible light. On the other hand, the two samples of ta-C give similar measured polarizations with a maximal difference of 0.06. It would be interesting to investigate whether ta-C is less sensitive to the sample processing conditions than SiC, as this could be an advantage in favour of the selection of this material. Of course, further measurements with more samples, various input polarizations, more incidence angles, and in the UV, will be needed to conclude on the properties of the material and stability of the

<table>
<tr><th>Sample</th><th colspan="2">S_{th}</th><th>S_{exp}</th></tr>
<tr><td>Au</td><td colspan="2">Palik
$\begin{pmatrix}1\\0.86\\0.32\\0.41\end{pmatrix}$</td><td>$\begin{pmatrix}1\\0.72\\-0.54\\-0.44\end{pmatrix}$</td></tr>
<tr><td>SiC 1</td><td>Palik
$\begin{pmatrix}1\\-0.40\\-0.27\\0.87\end{pmatrix}$</td><td>Larruquert
$\begin{pmatrix}1\\0.15\\-0.17\\0.97\end{pmatrix}$</td><td>$\begin{pmatrix}1\\0.12\\-0.33\\-0.94\end{pmatrix}$</td></tr>
<tr><td>SiC 2</td><td></td><td></td><td>$\begin{pmatrix}1\\-0.10\\0.05\\0.99\end{pmatrix}$</td></tr>
<tr><td>ta-C 1</td><td colspan="2" rowspan="2">Larruquert
$\begin{pmatrix}1\\-0.51\\-0.24\\0.83\end{pmatrix}$</td><td>$\begin{pmatrix}1\\0.06\\-0.26\\-0.96\end{pmatrix}$</td></tr>
<tr><td>ta-C 2</td><td>$\begin{pmatrix}1\\0.09\\-0.20\\-0.98\end{pmatrix}$</td></tr>
</table>

Figure 4.25: *Measurements of polarizations after reflexion on samples of Au, SiC and ta-C. S_{th} is the theoretical polarization computed from the database written, and S_{exp} is the measured polarization. If the database is Palik, the optical indices used are from [44]. If the database is Larruquert, the optical indices are from [29] and [33].*

material with respect to samples.

By measuring the polarization before, and after reflection, S_{in} and S_{out}, a system of four equations with two unknowns according to the following equation is achieved:

$$S_{out} = M_{reflection}(n, k) * S_{in} \tag{4.21}$$

with $M_{reflection}(n, k)$ the Mueller matrix of the reflection determined in Section 4.2. This Mueller matrix depends only on the complex optical indices n and k of the sample. This system can be resolved numerically.

4.4.3 Conclusion of the experiment

The experiment developed during this thesis enabled to design and build a gold reflective polarimeter operating in the FUV. The bench includes 3 rotations and 5 reflections which results in a real technical challenge in terms of alignment. Initial alignment methods were developed, but this slowed down the development of the experiment considerably. As a consequence, the tests carried out could only be done in the visible range so far. However, the modulation test and the polarizations measured during these first tests in the visible range serve as a proof of the polarimeter's operation. The accuracy of the polarimeter is currently limited by the errors induces by photometry and misalignment, as the bench was not designed for use in the visible. Polarization measurements after reflection on material samples have been performed using this experiment, as a proof of concept. In the future, we will perform a more accurate alignment, following the methods developed by the team working on the MICADO instrument. This alignment will enable the next steps of the material tests to be carried out. Once this alignment has been completed, the instrument can also be transferred to the test vacuum chamber and measurements in the FUV will be performed. These FUV measurements will be much more reliable than the ones performed in the visible domain.

4.5 Conclusions and prospects

First, the Mueller matrices of a reflection are presented in this Chapter, as well as the method to fully calculate them. Then, a FUV polarimeter was designed based on the theory presented. However, in order to improve the design of these reflection polarimeters, more information is needed on the optical indices of materials in the FUV. Indeed, it was noted that published information on materials in the FUV is often contradictory or unreliable. Thus, the material data seems to be highly dependent on its manufacturing and characterizing conditions. By testing the polarimetric efficiencies of selected materials, more realistic simulations of reflective polarimeters can be carried out.

To overcome this lack of information, an experiment using a gold reflective polarimeter was developed. This experiment measures the polarimetric properties of materials thanks to polarization measurements performed before and after a reflection. Moreover, a reflection polarimeter operating in the FUV has been built and tested in visible light for the first time thanks to this experiment. The progress of this experiment was greatly slowed down by the very complex optical alignment. The first measurements in the visible range are presented, and they demonstrate the operation of a reflective polarimeter. Measurements

of known polarizations were performed as well as polarization measurements after reflection on material samples. The precision of these measurements was degraded by the imperfect alignment of the experiment.

In the future, a precise alignment of the optical bench will be necessary. Indeed, as it stands, the alignment makes it impossible to accurately measure polarization after reflection on materials and thus to select the best material for FUV polarimeters. Moreover, it seems unthinkable to make UV measurements with a polarimeter that is out of alignment. Indeed, if measurements can be adapted in the visible range by noting the misalignment, it will be impossible to do the same in the FUV. Once this better alignment has been achieved, the gold polarimeter can be characterized in the UV and the polarimetric properties of the material samples can be properly measured. Finally, once the materials are better known in the FUV, the reflective polarimeters can be simulated more accurately, and FUV polarimeters can be optimised for space missions.

Chapter 5

Conclusions and prospects

Spectropolarimetry is a booming technology for astronomical instrumentation. Many infrared and visible spectropolarimeters have been deployed in recent years on ground-based telescopes, and many space mission projects are considering UV spectropolarimeters. However UV spectropolarimetry comes with many technical challenges such as the efficiency of detectors or materials. The subject of my thesis is the study of polarimeters for UV spectropolarimeters, a key part of the spectropolarimeter, still not easily accessible in the UV. My thesis focused on two types of polarimeters: transmissive polarimeters and reflective polarimeters. Both types of polarimeters use temporal modulation. My thesis was carried out in the context of the development of several space instruments such as POLLUX for LUVOIR, CASSTOR, and PolStar. Each polarimeter required for the development of these instruments was simulated according to one of these tw concepts. Both concepts have been first studied and simulated numerically, and then experiments were set up to test prototypes in real conditions.

5.1 Transmission

Chapter 3 of this thesis deals with the transmission polarimeter. This polarimeter is composed of a modulator and an analyzer, both made of birefringent material. The study in this Chapter highlights the use of MgF_2 for a polarimeter in the UV, down to 123 nm. An optimization based on polarimetric efficiency calculations was set up to design the modulator. This optimization aims at the best extraction of the polarization components from the measured intensities. The modulator is composed of thin MgF_2 plates, whose fast axis angle and thickness is specific to each plate. Each thin plate is doubled in order to be built by the supplier. The second plate of each pair is crossed to the first one so that only the difference of the thicknesses influences the polarization. The optimization of a transmission modulator consists in finding the parameters of the plates (number of plates, angles of the fast axis, thickness) which maximizes the extraction efficiencies for all polarizations: linear (Q and U) and circular (V). The analyzer is a birefringent prism also made of MgF_2. Since prisms are

perfect polarizers, separating physically orthogonal polarizations, only the output angle of the beams needs to be studied according to the optical design of the instrument. This part is not treated in this thesis. The work done on this prototype has improved the modulator optimization method and modulators made with only two double birefringent plates are now considered for our prototypes. The POLLUX NUV and MUV polarimeters, as well as the CASSTOR and PolStar polarimeters were designed using this technique.

Two experiments have been developed to test this transmission polarimeter. First, an optical experiment was set up to determine the polarimetric accuracy of a prototype in the UV. The tests were conducted with an existing high-resolution UV spectrometer. Unfortunately, many technical constraints were encountered, notably the tremendous loss of flux due to the degradation of the collimating mirror in front of the source. The cause of this degradation has not been clearly identified, but the formation of color centers is strongly suspected. Moreover, the non-stability of the lamp over the duration of the experiment, as well as the non-linearity of the response of the photosensitive detector generated significant errors in the measurement of the intensities. Finally, the extraordinary and ordinary beam measurements had to be done separately due to the optical configuration of the spectrometer. The separate treatment of the ordinary and extraordinary beams greatly complicated the data processing and added instrumental and photometric errors to the results. Nevertheless, all these difficulties are not in vain because they brought valuable lessons about the process of UV spectropolarimetry.

New tests will have to be performed with a spectrometer built specifically for this polarimeter and where both beams can be measured simultaneously. A digital detector should be used to better process the data with flat-fields and darks. Finally, I advise not to use a mirror with a coating too close to the UV source. At the wavelengths considered in the NUV, high quality MgF_2 or LiF lenses can be considered instead. All these modifications should allow us to overcome the problems of non-linearity as well as photometry encountered during the experiment. The simultaneity of the ordinary and extraordinary measurements should facilitate the treatment of the results, in particular it will not be necessary to have measurements of non-polarized intensities.

Finally, a thermal study has been carried out on the modulator. Indeed, in order to improve the transmission of the polarimeter, it is considered to use molecular bonding between the thin plates. Molecular bonding optically "glues" the elements in order to avoid Fresnel reflections at the diopters. The plates being composed of an anisotropic material, and each plate having a different axis, the structure is sensitive to thermal variations: each plate will expand or shrink in a different direction and thus create a stress on the molecular bonding. The purpose of the thermal study is therefore to observe the resistance or rupture of the bonding to thermal changes. Several modulators were thermally cycled between -20 and +55°C. The first test carried out included a real time monitoring of the bonding thanks to interferometry. The bonding of the tested plates broke down between -10 and -22°C. Then, several plates with different parameters (bonding numbers, presence or absence of optical

mount) underwent 8 identical cycles in a thermal chamber, without optical monitoring. During these thermal tests, one bonding of a plate out of the 7 tested broke. This set of plates was in an optical mount and included 4 plates and 3 bonding. These tests showed a weakness in molecular bonding. Moreover, the results of the tests are not repeatable, as a set identical to the one that broke in the first cycle survived the second series of tests. The origin of the resistance or not of the molecular bonding is not yet fully understood, however the quality and strength of the bonding should be studied. Further work including the strength of the molecular bonding as a function of various parameters, such as temperature and humidity, and the molecular bonding manufacturing process, such as the level of polishing and cleanliness, will need to be conducted to identify a repeatable process. If it turns out that 4 plates (2 double-plates) models are too fragile, then molecular bonding between the plates of a doublet only can be considered. Finally, it will also be necessary to check if the plates are distorted during temperature variations. A distortion of the plates would cause the light beam to pass through an inhomogeneous thickness of the plate and thus create an unwanted spatial modulation.

This prototype is the baseline for most space polarimeter projects. Before sending it in space, it will be necessary to qualify this prototype for measurements in the UV and for space conditions. Based on this thesis work, UV spectropolarimetry measurements can be made to demonstrate the expected accuracy of the measurements. Finally, thermal studies focusing on the manufacturing processes of molecular bonding will be conducted. The next step in the spatialization of this prototype will be the launch of CASSTOR, which will perform the first UV spectropolarimetry measurements with the prototype presented here. CASSTOR will also serve as a scientific demonstrator and will measure magnetic fields of hot stars in the UV. With all these technical advances on UV polarimeters, projects like POLLUX, PolStar, or other future UV polarimeters will give access to important astrophysical advances.

5.2 Reflection

Chapter 4 of this thesis discusses the prototype by reflection. Such polarimeters are less efficient than polarimeters by transmission but they are the only ones available in the FUV domain. First, the Mueller matrices of a reflection are presented, as well as the method to fully calculate them. Then, a FUV polarimeter was designed and optimized for the first time based on the presented theory. The optimization method is similar to that of the transmission polarimeter, but the parameters differ. Indeed, here the optimization parameters are the properties of the materials, the incident angles on the mirrors, and the modulation angles. The polarimeter optimized for the POLLUX FUV channel is composed of several materials: the modulator is made with two B4C mirrors and one SiC mirror, and the analyzer is made with one ta-C mirror. This polarimeter allows to reach an efficiency around 0.3 at 90 nm and around 0.5 at 130 nm using 4 modulation angles. These results are very encouraging and allow us to consider polarimetry measurements in the FUV.

However, in order to improve the design of these reflection polarimeters, it is necessary to have more information on the optical properties of materials in the FUV. Indeed, it was noted that the published information on materials in the UV is strongly dependent on the samples studied and on their manufacturing conditions. To overcome this problem, an experiment using a gold reflection polarimeter was developed. This experiment measures the optical indices (n,k) or the polarimetric properties (reflectivity and phase shift) of selected materials thanks to the measurement of the polarization before and after a reflection on the material. Characterizing the samples of promising materials would help us to design a realistic polarimeter with the considered materials. Moreover, thanks to this experiment, a broadband reflection polarimeter operating in the FUV was built for the first time. This polarimeter was built in gold in order to use a very well-known material. The progress of this experiment was strongly slowed down by the very complex optical alignment. A poor alignment was achieved but was sufficient to test the gold polarimeter in the visible. Intensity modulation with incoming polarization was confirmed and polarization measurements were performed. This experiment demonstrated the proper operation of the reflection polarimeter. The accuracy of the polarimeter could only be measured in the visible where the parameter extraction efficiencies are very low. The polarization errors in the visible range reach 0.5 for some measurements.

In the future, an accurate alignment of the optical bench will be necessary. Indeed, in the current state of alignment, UV measurements could not be performed. While the measurements can be adapted in the visible range by noting the misalignment, it will be impossible to do the same in the FUV. This accurate alignment method has been identified, but could not be implemented in this thesis due to lack of time. Once this alignment is achieved, the gold polarimeter can be characterized in the UV and the polarimetric properties of the material samples can be measured accurately. Finally, once the properties of the selected materials are better known in the UV, the reflection polarimeters can be optimized more precisely.

Conducting this UV experiment will greatly increase our knowledge on UV materials, making it much easier to simulate reflective polarimeters. Once the best materials are chosen, the POLLUX FUV and MUV reflection polarimeters will be designed and tested as well, using the methods employed in this thesis. These tests will characterize the efficiency of the POLLUX polarimeter in the FUV and measure its accuracy. Finally, the study of the polarimeter presented here was limited to 90 nm in the FUV because of the bandwidth of LUVOIR, but the theory of reflective polarimeters can be applied to all wavelengths. This study is the first step in the development of FUV polarimetry and shows that such instruments can be achieved and will open a new door for many scientific topics.

UV polarimeter studies have progressed thanks to the work done during this thesis. Indeed, broadband high-resolution spectropolarimetric measurements were performed for

the first time in the UV using the transmissive prototype. Moreover, an innovative reflective prototype for the FUV domain has been studied and built. The first experiment performed in visible light proves its operation. Using this reflective prototype, an experiment to measure polarimetric properties of material samples was set up and carried out in the visible, with the goal to select the best materials for FUV polarimeters. Many technical difficulties and their solutions have been identified to continue further investigations on UV polarimeters. Relying on this background, the next part of the adventure should focus on improving the current setups and implementing the proposed way forwards presented in this thesis. This will allow us to design the best UV polarimeters for high-resolution, wide spectral range spectropolarimeters onboard space missions. This is crucial as several mission projects including UV spectropolarimetric capabilities have already been proposed to ESA, NASA, and CNES.

Appendix A

Technical details on the experiments performed on the prototype by transmission

This appendix includes additional technical data to the work presented in Chapter 3. Section A.1 presents the optical indices used for the simulations. Section A.2 presents specificities of some components used for UV spectropolarimetric tests.

A.1 Data used to simulate the polarimeters

Transmission

Optical transmission is a key element in the study of UV polarimeters. In Figure A.1, the transmission of MgF_2 is presented. It was measured on a 5-mm plate by B. Halle.

In Figure A.2, the transmission of SiO_2 is presented. The beginning of the shaded region indicates 190 nm. This transmission curve has been measured by Thorlabs.

Optical indices and birefringence

The optical indices and the birefringence of the materials are essential to simulate the effect of the modulator on the polarization and calculate the polarimetric efficiencies. Depending on the data source, the optical indices differ up to 0.1. In Figure A.3, we can see different sets of indices for MgF_2. The first data set comes from Palik [44]. They can be compared with the data measured by Juan Larruquert [31]. The curves are very similar, but there is a difference of about 0.1 between the two data sets. Both ordinary and extraordinary indices are plotted from the Palik data. Only the ordinary index is plotted from the Larruquert data.

For the birefringence, we make a comparison between the birefringence calculated with

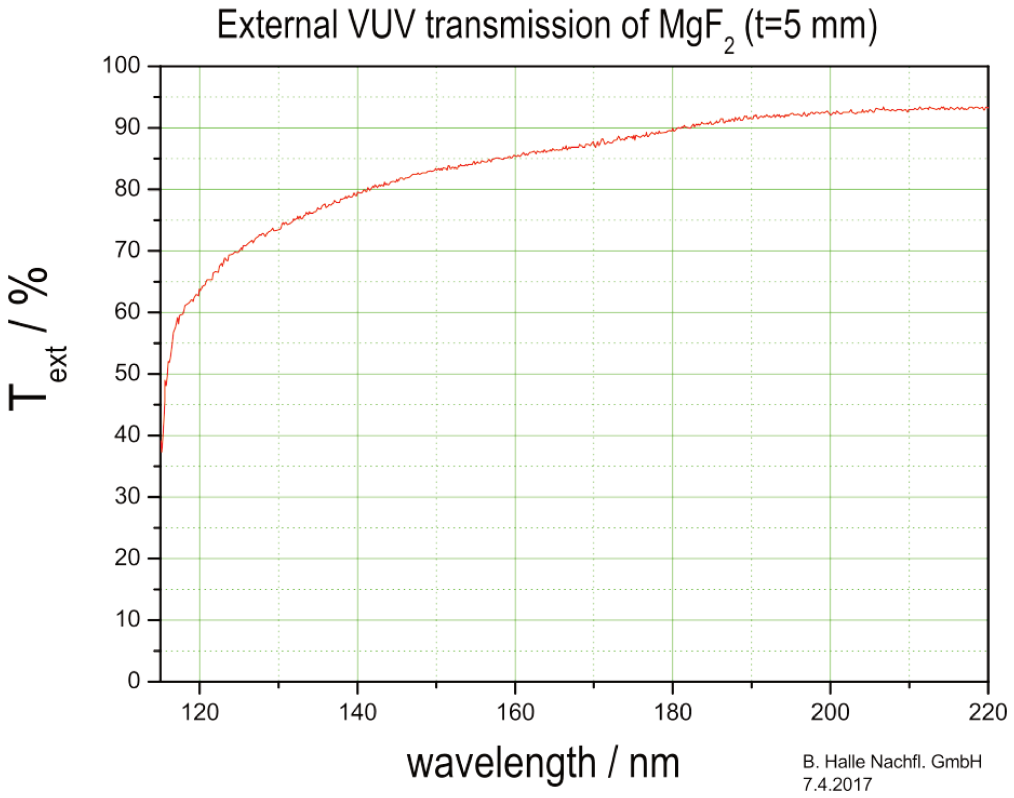

Figure A.1: *Transmission of a MgF_2-plate of 5 mm as a function of wavelength. Credit: B.Halle Nachfl. GmbH.*

the indices of Palik and the birefringence computed from the fit studied by Pertenais [46]. The birefringence computed from Pertenais incorporates several references depending on the studied wavelength. The birefringence computed from Pertenais decreases slowly and is 0 at 119.5 nm. On the contrary, using Palik data, the birefringence oscillates and reaches 0 just below 150 nm. In reality, MgF_2 is often used around 150 nm. Therefore Pertenais's fit seems like a more accurate database. The simulations for this thesis were thus done using the birefringence fit of Pertenais.

Figures A.5 and A.6 show the data for SiO_2. For SiO_2, only Palik's data were found. In Figure A.5, the ordinary and extraordinary indices are shown. In Figure A.6, the birefringence is presented. It can be seen that it is equal to 0 at 190 nm.

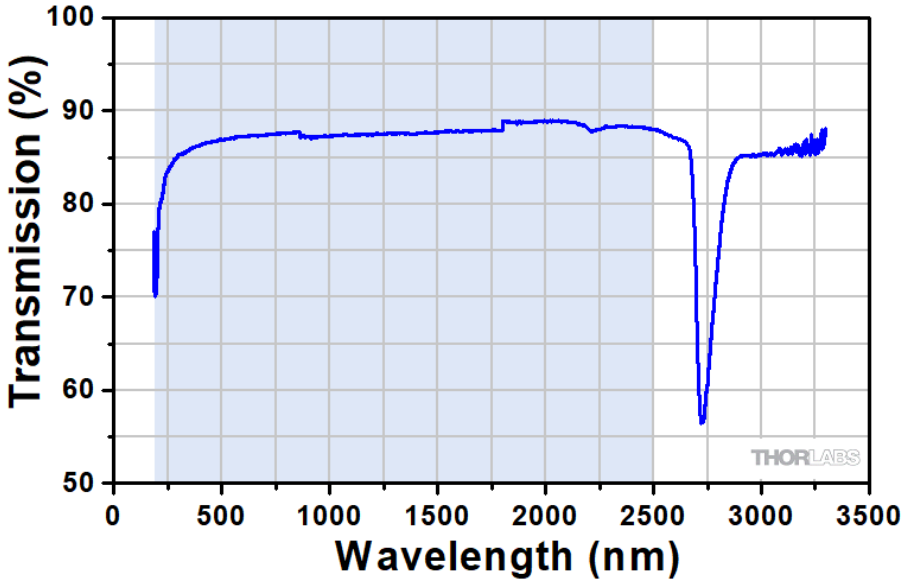

Figure A.2: *Transmission of a SiO_2-plate of 5 mm as a function of wavelength. Credit: Thorlabs.*

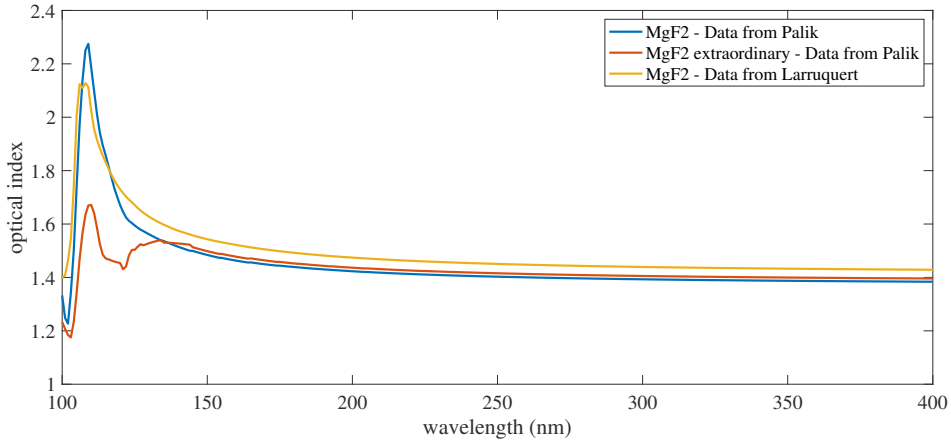

Figure A.3: *Index of MgF_2 as a function of wavelength.The blue line represents the ordinary optical index of MgF_2 extracted from Palik. The red corresponds to the extraordinary optical index of MgF_2 extracted from the Palik. The yellow line represents the ordinary optical index of MgF_2 extracted from Larruquert.*

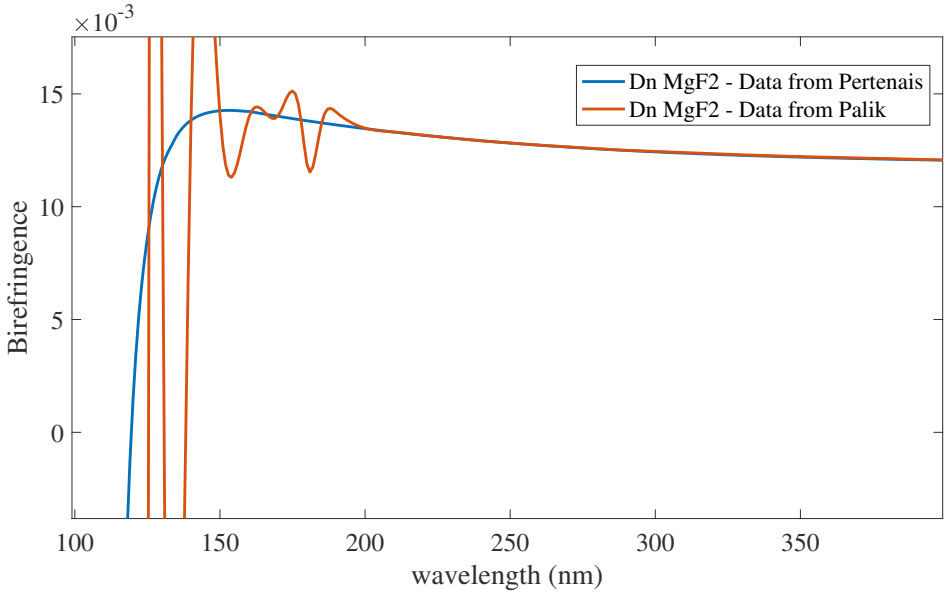

Figure A.4: *Birefringence of MgF_2 as a function of wavelength. The blue line is computed from Pertenais fit. The red line is computed from Palik data.*

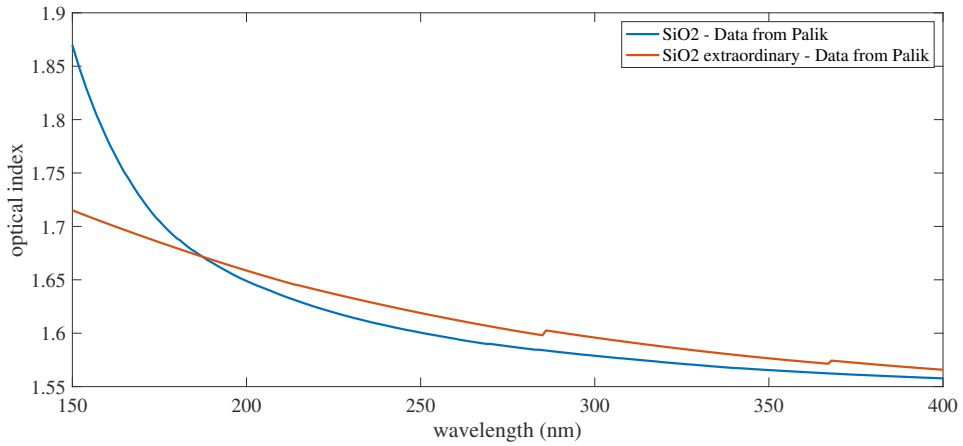

Figure A.5: *Index of SiO_2 as a function of wavelength. The indices are from [44]. The blue line corresponds to the ordinary index and the red line corresponds to the extraordinary index.*

A.2 Additional technical information of some components used for the experiment testing the polarimetric efficiencies

This Section describes some components used during the experiment described in Section 3.3. In particular, the spectrum of the lamp, the reflectivity curves of the mirrors, and the

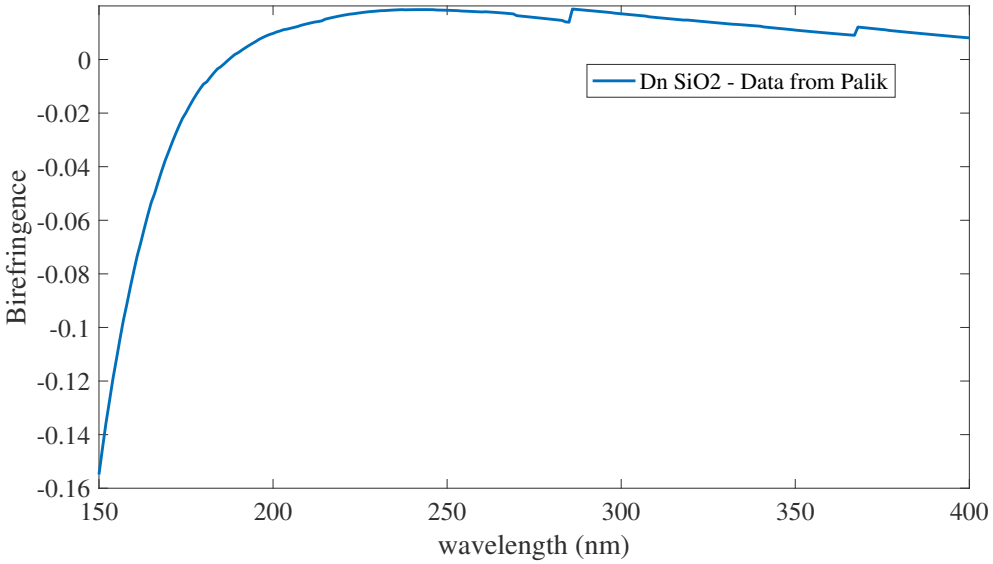

Figure A.6: *Birefringence of SiO_2 as a function of wavelength.*

retardation of the quarter wave plates are presented.

Spectrum of the source

The lamp source used for the experiment is a deuterium lamp from Hamamatsu referenced L15094. It is a VUV light source with high-performance. It has an air-cooled system. The window is in MgF_2.

The relative spectrum of the lamp is presented in Figure A.7. The maximum intensity of the source is between 120 and 170 nm with a maximum peak at 160 nm.

Mirrors reflectivity curves

The parabolic mirrors are off-axis parabolic mirrors from Thorlabs, with an angle of 45°, a diameter of 3", and a focal length of 12". The reference of the mirrors is MPD3124-P01. These mirrors were delivered without silver protection to our two suppliers, eSource Optics and Teledyne, in order to coat them with their UV coatings with Al/MgF2. The reflectivity of the coating from eSource Optics is presented in Figure A.8 whereas the one of Teledyne is presented in Figure A.9. The mirrors with eSource Optics coatings were used for the ordinary beam measurements. After the degradation of the coating was noted, as explained in Section 3.4.2, the Teledyne mirrors were used. The same effect was observed. The cause of this darkening has not been fully identified yet but is likely due to the too close proximity of the mirrors with the bright UV source.

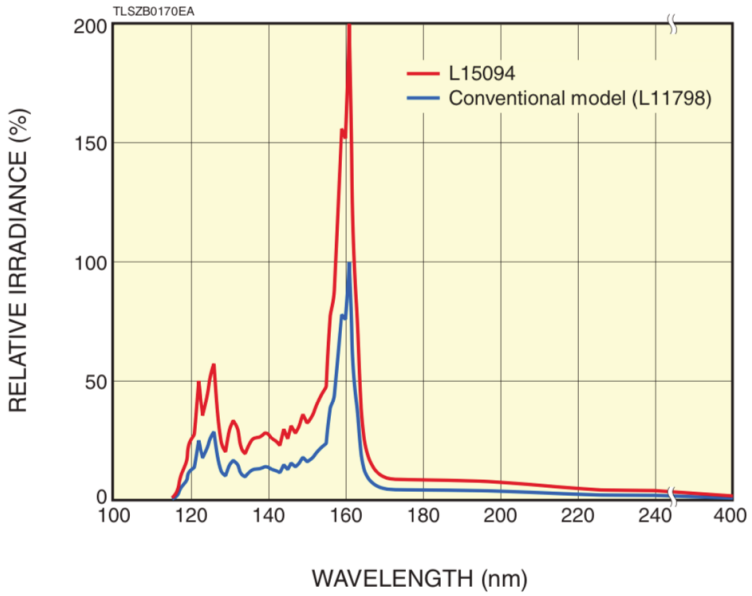

Figure A.7: *Spectrum of the D2 lamp. Credit: Hamamatsu.*

Figure A.8: *Reflectivity as a function of wavelength for the eSource Optics Al/MgF_2 coating. Credit: eSource Optics.*

Retardation created by the quarter waveplate

The waveplate used to create polarized light is from B.Halle Nachfl. GmbH. The plate was optimized to be a quarter wave at 157 nm. In the experiment performed in Chapter 3, the spectrum studied is from 143 to 163 nm. The quarter wave plate creates a delay between 0.24 and 0.275 λ. The action of the plate creates a chromatic effect. Indeed, the injection

of the polarizations Q, U, and V is not uniform over the range of wavelengths.

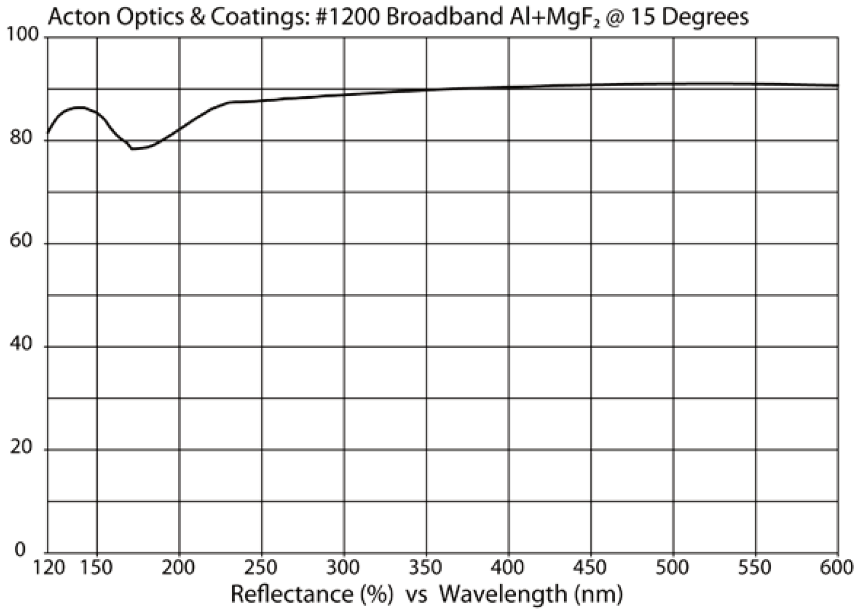

Figure A.9: *Reflectivity as a function of wavelength for the Teledyne Al/MgF_2 coating. Credit: Teledyne.*

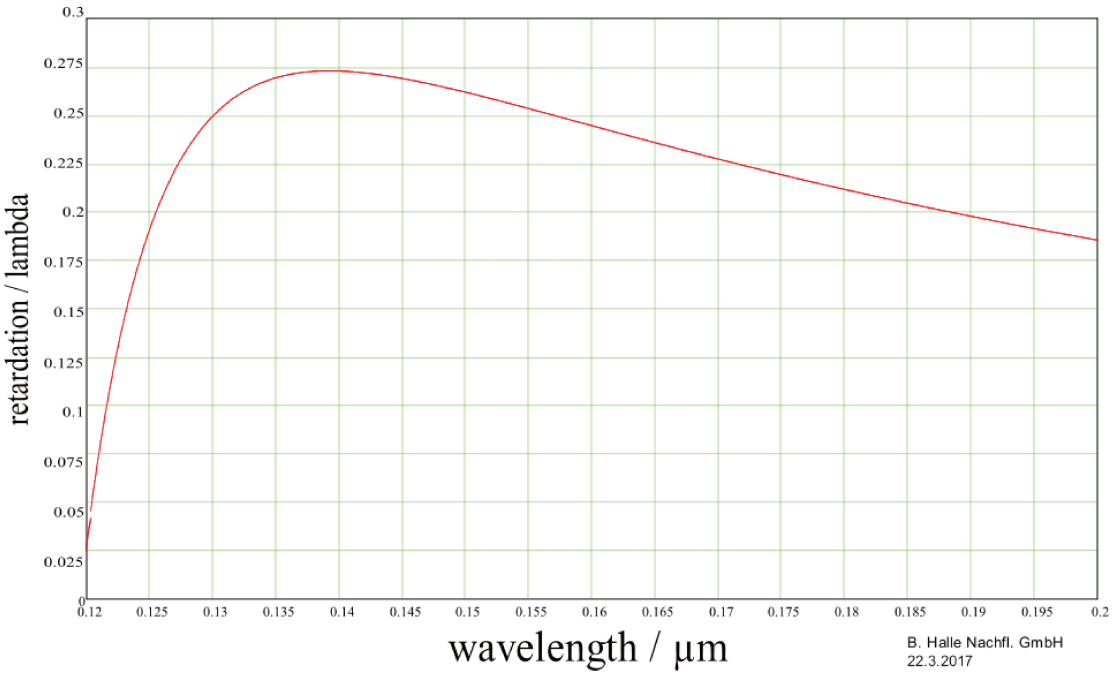

Figure A.10: *Phase shift between polarization for the MgF_2 quarter wave plate, optimized for a used around 157 nm. Credit: B.Halle Nachfl. GmbH.*

Appendix B

Optical indices used for the simulation of the reflective polarimeters

This appendix includes additional technical data to the work presented in Chapter 4.

Complex optical indices used for the reflection polarimeter simulations are presented. Figures B.1 and B.2 illustrate, respectively, the real n and complex k optical indices for different materials studied in Chapter 4. Data for the materials CaF_2, MgF_2, SiO_2, Au, $B4C$, $ta-C$, and SiC, used in the theoretical study of the polarimeter are presented as a function of wavelength. Some data come from the Palik database [44], others from papers produced by the GOLD team and directed by J. Larruquert [29, 32]. The origin of the data is indicated in the legend. One can observe the differences between the two databases for the materials MgF_2, SiC, and $B4C$. For the real indices n, the data from the two databases are quite different. The difference between the indices of SiC is up to 0.2. The difference between the values of $B4C$ reaches 0.1 and that of MgF_2 reaches 0.25. For the complex k indices, the $B4C$ data are very similar. On the other hand, the data on SiC reaches a difference of 0.2 and that of MgF_2 reaches 0.4. These differences are due to the great dependence of the optical index of the sample, of its manufacturing conditions but also of the measurement conditions. As a consequence, for accurate simulations, one must measure its own optical indices from its own samples.

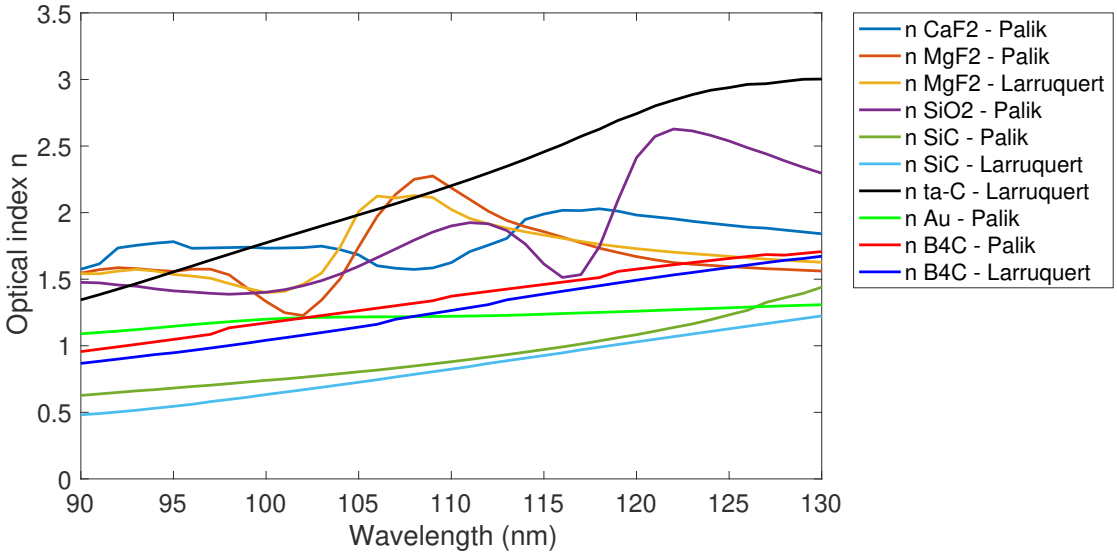

Figure B.1: *Optical index n as a function of wavelength for various materials: CaF_2, MgF_2, SiO_2, Au, B4C, ta − C, and SiC. Palik [44], Larruquert [29], and [32] are the sources of the displayed values.*

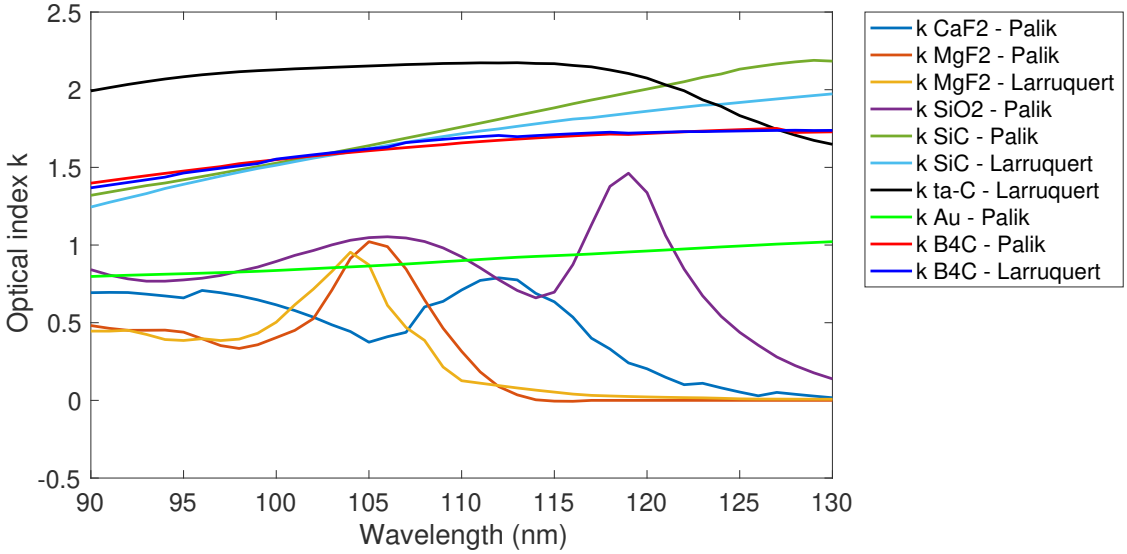

Figure B.2: *Same as Figure B.1 but for the optical index k.*

Bibliography

[1] F Arago. Mémoire sur une modification particuliere qu'eprouvent les rayons lumineux dans leur passage à travers certains corps diaphanes et sur plusieurs autres nouveaux phénomenes d'optique. *Moniteur*, 73:282–284, 1811.

[2] Erasmus Bartholinus and Werner Brandt. *Experiments with the double refracting Iceland crystal: which led to the discovery of a marvelous and strange refraction*. 1959.

[3] Max Born and Emil Wolf. *Principles of Optics: Electromagnetic Theory of Propagation, Interference and Diffraction of Light*. Elsevier, June 2013.

[4] Jean-Claude Bouret, Coralie Neiner, Ana Gómez de Castro, Chris Evans, Boris Gaensicke, Steve Shore, Luca Fossati, Cecile Gry, Stéphane Charlot, Frédéric Marin, et al. The science case for pollux: a high-resolution uv spectropolarimeter onboard luvoir. In *Space Telescopes and Instrumentation 2018: Ultraviolet to Gamma Ray*, volume 10699, page 106993B. International Society for Optics and Photonics, 2018.

[5] David Brewster. IX. On the laws which regulate the polarisation of light by reflexion from transparent bodies. By David Brewster, LL. D. F. R. S. Edin. and F. S. A. Edin. In a letter addressed to Right Hon. Sir Joseph Banks, Bart. K. B. P. R. S. *Philosophical Transactions of the Royal Society of London*, 105:125–159, January 1815. Publisher: Royal Society.

[6] Francoise Bridou, Mireille Cuniot-Ponsard, Jean-Michel Desvignes, Ivan Maksimovic, and Philippe Lemaire. VUV mirrors for the (80-120 nm) spectral range. In *Advances in Optical Thin Films*, volume 5250, pages 627–637. International Society for Optics and Photonics, February 2004.

[7] R. Cabanac. Telescope Bernard Lyot beyond Narval: Neo-Narval and SPIP. In J. Ballet, F. Martins, F. Bournaud, R. Monier, and C. Reylé, editors, *SF2A-2014: Proceedings of the Annual meeting of the French Society of Astronomy and Astrophysics*, pages 151–153, December 2014.

[8] C. Capitani, F. Cavallini, G. Ceppatelli, E. Landi Degl'innocenti, M. Landi Degl'innocenti, M. Landolfi, and A. Righini. Polarization properties of a 'Zeiss-type' coelostat: The case of the solar tower in Arcetri. *Solar Physics*, 120(1):173–191, 1989.

[9] Tengbo Chen, Yuxi Yu, Laichao Li, Jian Zhu, Minghui Cong, and Jingyuan Song. Eliminate of colour center and growth of large-size Tb3Ga5O12 crystals. *Journal of Crystal Growth*, 562:126090, May 2021.

[10] Russel A. Chipman. Polarimetry. *Chap. 22 in Handbook of Optics, 2(2nd edition.)*, 1994.

[11] David Clarke. *Stellar Polarimetry*. John Wiley & Sons, October 2009. Google-Books-ID: lioLCB1QktQC.

[12] Natacha Cocheteau. *Caractérisation et modélisation d'une adhérence moléculaire renforcée*. These de doctorat, Aix-Marseille, January 2014.

[13] Jose Carlos del Toro Iniesta and Manuel Collados. Optimum modulation and demodulation matrices for solar polarimetry. *Applied Optics*, 39(10):1637, April 2000.

[14] J-F Donati, Meir Semel, Brad D Carter, DE Rees, and A Collier Cameron. Spectropolarimetric observations of active stars. *Monthly Notices of the Royal Astronomical Society*, 291(4):658–682, 1997.

[15] Jean-François Donati, D Kouach, M Lacombe, S Baratchart, R Doyon, X Delfosse, Etienne Artigau, Claire Moutou, G Hébrard, Francois Bouchy, et al. Spirou: a nir spectropolarimeter/high-precision velocimeter for the cfht. *arXiv preprint arXiv:1803.08745*, 2018.

[16] ECSS Secretariat ESA-ESTEC. Thermal testing for the evaluation of space materials, processes, mechanical parts and assemblies. page 25, 2008.

[17] S. Fineschi. Presentation at polarimetric techniques and technology. 2014.

[18] Viktor Gruev, Rob Perkins, and Timothy York. Ccd polarization imaging sensor with aluminum nanowire optical filters. *Optics express*, 18(18):19087–19094, 2010.

[19] G. Hass and W. R. Hunter. Reflection polarizers for the vacuum ultraviolet using Al + MgF2 mirrors and an MgF2 plate. *Appl. Opt.*, 17(1):76–82, Jan 1978.

[20] Christiaan Huygens. *Traité de la lumiére, où sont expliquées les causes de ce qui lui arrive dans la reflexion, et dans la refraction: et particulierement dans l'étrange refraction du cristal d'Islande: avec un discours de la cause de la pesanteur*, volume 1. 1690.

[21] Institute of Semiconductor Physics, NAS Ukraine, 45 Prospect Nauki, Kyiv, 03028, Ukraine and S.A. Kovalenko. Descartes-Snell law of refraction with absorption. *Semiconductor Physics, Quantum Electronics and Optoelectronics*, 4(3):214–218, July 2001.

[22] R. Ishikawa, N. Narukage, M. Kubo, S. Ishikawa, R. Kano, and S. Tsuneta. Strategy for Realizing High-Precision VUV Spectro-Polarimeter. *Solar Physics*, 289(12):4727–4747, December 2014.

[23] Ryohko Ishikawa, Ryouhei Kano, Takamasa Bando, Yoshinori Suematsu, Shin-nosuke Ishikawa, Masahito Kubo, Noriyuki Narukage, Hirohisa Hara, Saku Tsuneta, Hiroko Watanabe, Kiyoshi Ichimoto, Kunichika Aoki, and Kenta Miyagawa. Birefringence of magnesium fluoride in the vacuum ultraviolet and application to a half-waveplate. *Applied Optics*, 52(34):8205, December 2013.

[24] Eric Josselin. Spectropolarimetry at pic du midi observatory. In *EGU General Assembly Conference Abstracts*, page 19525, 2017.

[25] Christoph U. Keller and Frans Snik. Spectropolarimetry. In *The WSPC Handbook of Astronomical Instrumentation*, World Scientific Series in Astrophysics, pages 239–255. WORLD SCIENTIFIC, April 2021.

[26] Raymond L. Kelly and Louis J. Palumbo. Atomic and Ionic Emission Lines below 2000 Angstroms - Hydrogen through Krypton. Technical report, NAVAL RESEARCH LAB WASHINGTON DC, June 1973. Section: Technical Reports.

[27] Oleg Kochukhov. Doppler and zeeman doppler imaging of stars. In *Cartography of the Sun and the Stars*, pages 177–204. Springer, 2016.

[28] John D Landstreet. Observing and modelling stellar magnetic fields-1. basic physics and simple models. *EAS Publications Series*, 39:1–20, 2009.

[29] J. I. Larruquert, L. V. Rodríguez-de Marcos, J. A. Méndez, P. J. Martin, and A. Bendavid. High reflectance ta-C coatings in the extreme ultraviolet. *Optics Express*, 21(23):27537, November 2013.

[30] Juan I. Larruquert and Ritva A. M. Keski-Kuha. Multilayer coatings with high reflectance in the extreme-ultraviolet spectral range of 50 to 1216 nm. *Applied Optics*, 38(7):1231, March 1999.

[31] Juan I Larruquert and Ritva AM Keski-Kuha. Far ultraviolet optical properties of mgf2 films deposited by ion-beam sputtering and their application as protective coatings for al. *Optics communications*, 215(1-3):93–99, 2003.

[32] Juan I. Larruquert, A. Marco Malvezzi, Angelo Giglia, José A. Aznárez, Luis Rodríguez-de Marcos, José A. Méndez, Paolo Miotti, Fabio Frassetto, Giuseppe Massone, Stefano Nannarone, Giuseppe Crescenzio, Gerardo Capobianco, and Silvano Fineschi. Reflective and transmissive broadband coating polarizers in a spectral range centered at 121.6 nm. *Journal of Optics*, 16(12):125713, November 2014.

[33] Juan I Larruquert, Antonio P Pérez-Marín, Sergio García-Cortés, Luis Rodríguez-de Marcos, José A Aznárez, and José A Méndez. Self-consistent optical constants of sic thin films. *JOSA A*, 28(11):2340–2345, 2011.

[34] Robert E. Lyle and Gloria G. Lyle. A brief history of polarimetry, June 1964. Archive Location: world Publisher: Division of Chemical Education.

[35] Jean-Marie Malherbe. Optique de polarisation et ses applications. 2014.

[36] Étienne Louis Malus. *Mémoire sur la mesure du pouvoir réfringent des corps opaque*. 1809.

[37] Kin F Man. Jpl thermal Testing Standards. page 9, 2011.

[38] Nadine Manset and Jean-Francois Donati. Espadons: an echelle spectropolarimetric device for the observation of stars. In *Polarimetry in Astronomy*, volume 4843, pages 425–436. International Society for Optics and Photonics, 2003.

[39] Luis Rodriguez-de Marcos, José A. Aznárez, José A. Méndez, Juan I. Larruquert, M. Vidal-Dasilva, A. Marco Malvezzi, Angelo Giglia, Gerardo Capobianco, Giuseppe Massone, Silvano Fineschi, and Stefano Nannarone. Advances in far-ultraviolet reflective and transmissive coatings for space applications. In *Advances in Optical and Mechanical Technologies for Telescopes and Instrumentation II*, volume 9912, page 99122E. International Society for Optics and Photonics, July 2016.

[40] Eduard Muslimov, Jean-Claude Bouret, Coralie Neiner, Arturo López Ariste, Marc Ferrari, Sébastien Vivès, Emmanuel Hugot, Robert Grange, Simona Lombardo, Louise Lopes, et al. Pollux: a uv spectropolarimeter for the luvoir space telescope project. In *Space Telescopes and Instrumentation 2018: Ultraviolet to Gamma Ray*, volume 10699, page 1069906. International Society for Optics and Photonics, 2018.

[41] C Neiner, D Baade, A Fullerton, C Gry, G Hussain, A Lèbre, J Morin, P Petit, JO Sundqvist, AA Vidotto, et al. Uvmag: stellar formation, evolution, structure and environment with space uv and visible spectropolarimetry. *Astrophysics and Space Science*, 354(1):215–227, 2014.

[42] KH Nordsieck, AD Code, MR Meade, BL Babler, CM Anderson, DE Michalski, RH Pfeifer, and TE Jones. The wisconsin ultraviolet photo-polarimeter experiment (wuppe). In *Bulletin of the American Astronomical Society*, volume 23, page 906, 1991.

[43] C.J. Overbeck, R. R. Palmer, R. J. Stephenson, and Marsh W. White. The concave grating spectrometer-rowland mounting. *Selective Experiments in Physics*.

[44] Edward D Palik. *Handbook of optical constants of solids*, volume 3. Academic press, 1998.

[45] José-Philippe Pérez. Optique: Fondements et applications. 7 édition, 2004.

[46] Martin Pertenais. *Spectropolarimétrie stellaire UV et visible depuis l'espace*. PhD thesis, Université de Toulouse, Université Toulouse III-Paul Sabatier, 2016.

[47] Martin Pertenais, Coralie Neiner, Pernelle Bernardi, Jean-Michel Reess, and Pascal Petit. Static spectropolarimeter concept adapted to space conditions and wide spectrum constraints. *Applied optics*, 54(24):7377–7386, 2015.

[48] Martin Pertenais, Coralie Neiner, and Pascal Petit. Full-Stokes polychromatic polarimeter design for Arago. In *Space Telescopes and Instrumentation 2016: Ultraviolet to Gamma Ray*, volume 9905, page 99052Y. International Society for Optics and Photonics, July 2016.

[49] Nikolai Piskunov, Frans Snik, Andrey Dolgopolov, Oleg Kochukhov, Michiel Rodenhuis, Jeff Valenti, Sandra Jeffers, Vitaly Makaganiuk, Christopher Johns-Krull, Eric Stempels, et al. Harpspol the new polarimetric mode for harps. *The Messenger*, 143(7), 2011.

[50] SB Potter, Ken Nordsieck, Encarni Romero-Colmenero, Steve Crawford, Petri Vaisanen, Éric Depagne, David Buckley, Anthony Koeslag, Janus Brink, Christian Hetlage, et al. Commissioning the polarimetric modes of the robert stobie spectrograph on the southern african large telescope. In *Ground-based and Airborne Instrumentation for Astronomy VI*, volume 9908, page 99082K. International Society for Optics and Photonics, 2016.

[51] Oscar G Rodriguez-Herrera and Neil Charles Bruce. Mueller matrix for an ellipsoidal mirror. *Optical Engineering*, 45(5):053602, 2006.

[52] D. S. Sabatke, M. R. Descour, E. L. Dereniak, W. C. Sweatt, S. A. Kemme, and G. S. Phipps. Optimization of retardance for a complete Stokes polarimeter. *Optics Letters*, 25(11):802–804, June 2000. Publisher: Optical Society of America.

[53] Maria Salatino, Paolo de Bernardis, and Silvia Masi. Modeling Transmission and Reflection Mueller Matrices of Dielectric Half-Wave Plates. *Journal of Infrared, Millimeter, and Terahertz Waves*, 38(2):215–228, February 2017.

[54] Paul Scowen, Richard Ignace, Coralie Neiner, Gregg Wade, Matt Beasley, Jon Bjorkman, Jean-Claude Bouret, Roberto Casini, Tanausu del Pino Alemán, Samantha Edgington, et al. Polstar–an explorer-class fuv spectropolarimetry mission to map the environments of massive stars. *arXiv preprint arXiv:1911.06724*, 2019.

[55] M Semel. Zeeman-doppler imaging of active stars. i-basic principles. *Astronomy and Astrophysics*, 225:456–466, 1989.

[56] M Semel, J-F Donati, and DE Rees. Zeeman-doppler imaging of active stars. 3: Instrumental and technical considerations. *Astronomy and Astrophysics*, 278:231–237, 1993.

[57] F Snik, Harpspol Team, et al. The polarimeters for harps and x-shooter. *370 Years of Astronomy in Utrecht*, 470:401, 2013.

[58] Frans Snik, Julia Craven-Jones, Michael Escuti, Silvano Fineschi, David Harrington, Antonello De Martino, Dimitri Mawet, Jérôme Riedi, and J Scott Tyo. An overview of polarimetric sensing techniques and technology with applications to different research fields. In *Polarization: measurement, analysis, and remote sensing XI*, volume 9099, page 90990B. International Society for Optics and Photonics, 2014.

[59] Frans Snik and Christoph U. Keller. Astronomical Polarimetry: Polarized Views of Stars and Planets. In Terry D. Oswalt and Howard E. Bond, editors, *Planets, Stars and Stellar Systems: Volume 2: Astronomical Techniques, Software, and Data*, pages 175–221. Springer Netherlands, Dordrecht, 2013.

[60] Frans Snik, Gerard van Harten, Ramon Navarro, Paul Groot, Lex Kaper, and Alfred de Wijn. Design of a full-stokes polarimeter for vlt/x-shooter. In *Ground-based and Airborne Instrumentation for Astronomy IV*, volume 8446, page 844625. International Society for Optics and Photonics, 2012.

[61] Donguk Song, Ryohko Ishikawa, Ryouhei Kano, Masaki Yoshida, Toshihiro Tsuzuki, Fumihiro Uraguchi, Kazuya Shinoda, Hirohisa Hara, Takenori J Okamoto, Frédéric Auchère, et al. Optical alignment of the high-precision uv spectro-polarimeter (clasp2). In *Space Telescopes and Instrumentation 2018: Ultraviolet to Gamma Ray*, volume 10699, page 106992W. International Society for Optics and Photonics, 2018.

[62] William Sparks, Thomas A Germer, John W MacKenty, and Frans Snik. Compact and robust method for full stokes spectropolarimetry. *Applied Optics*, 51(22):5495–5511, 2012.

[63] S Thijs, O Dupuis, E Gendron, F Vidal, V Deo, M Cohen, A Sevin, and V Lapereyre. K-mirror prototype for MICADO-SCAO module of the E-ELT.

[64] Jaap Tinbergen. *Astronomical polarimetry*. Cambridge university press, 2005.

[65] Steven Tomczyk, Roberto Casini, Alfred G de Wijn, and Peter G Nelson. Wavelength-diverse polarization modulators for stokes polarimetry. *Applied Optics*, 49(18):3580–3586, 2010.

[66] Marina Voisin. *Tenue aux chocs d'une adhérence moléculaire renforcée : application à des systèmes optiques spatiaux embarqués*. These de doctorat, Aix-Marseille, December 2017.

[67] H. Watanabe, N. Narukage, M. Kubo, R. Ishikawa, T. Bando, R. Kano, S. Tsuneta, K. Kobayashi, K. Ichimoto, and J. Trujillo-Bueno. Ly-alpha polarimeter design for CLASP rocket experiment. *Conference Name: Solar Physics and Space Weather Instrumentation IV*, 8148:81480T, October 2011. Conference Name: Solar Physics and Space Weather Instrumentation IV Place: eprint: arXiv:1407.4577.

[68] P. Zeeman. The Effect of Magnetisation on the Nature of Light Emitted by a Substance. *Nature*, 55(1424):347–347, February 1897. Bandiera_abtest: a Cg_type: Nature Research Journals Number: 1424 Primary_atype: News Publisher: Nature Publishing Group.

Publications

Journal publications

[1] **LE GAL Maëlle**, LÓPEZ ARISTE Arturo, NEINER Coralie and PERTENAIS Martin. Simulation and optimization of a broadband reflective far ultraviolet polarimeter. *Applied Optics*, VOL(59), 9320-9327., 2020.

Full papers in conference proceedings

[2] **LE GAL Maëlle**, NEINER Coralie, LOUVEL DE MONCEAUX Matthieu, NGUYEN TUONG Napoléon, PARISOT Jér ôme, COLLIN Claude, REESS Jean-Michel, BONAFOUS Marion, BLANCHARD Cyrille, PELLEAU Aurélien, BAUDOZ Pierre, PERTENAIS Martin, COSTES Vincent, BRACHET Frank, LOCATELLI Elsa and DESMARRES Jean-Michel. Thermal tests of birefringent plates in molecular adhesion for spatial ultravioletpolarimetry.. In *Advances in Optical and Mechanical Technologies for Telescopes and Instrumentation IV*, SPIE, 615-624, 2020.

[3] MUSLIMOV Eduard, BOURET Jean-Claude, NEINER Coralie, FERRARI Marc, LOMBARDO Simona, LÓPEZ ARISTE Arturo, and **LE GAL Maëlle** Thermal tests of birefringent plates in molecular adhesion for spatial ultravioletpolarimetry.. In *Advances in Optical and Mechanical Technologies for Telescopes and Instrumentation IV*, SPIE, 615-624, 2020.

[4] FERRARI Marc, BOURET Jean-Claude, NEINER Coralie, MUSLIMOV Eduard, **LE GAL Maëlle** and LÓPEZ ARISTE Arturo POLLUX, an innovative instrument providing a unique UV spectropolarimetric capability to LUVOIR.. In *American Astronomical Society*, AAS, 2019, vol. 233, p. 148.09.

[5] **LE GAL Maëlle**, LÓPEZ ARISTE Arturo, et NEINER Coralie. Far ultra-violet polarimeter by reflection for Pollux (LUVOIR).. In *International Conference on Space OpticsâĂŤICSO 2018*, International Society for Optics and Photonics, 2019. p. 111804V.

[6] **LE GAL Maëlle**, LÓPEZ ARISTE Arturo, PERTENAIS Martin, and NEINER Coralie. UV Polarimeters for Pollux onboard LUVOIR.. In *Société française d'astronomie et d'astrophysique 2018*, sf2a, 2018, p. Di.

[7] BOURET Jean-Claude, MUSLIMOV Eduard, NEINER Coralie, **LE GAL Maëlle**, LÓPEZ ARISTE Arturo and FERRARI Marc. POLLUX, a high-resolution UV spectropolarimeter for LUVOIR.. In *Société française d'astronomie et d'astrophysique 2018*, sf2a, 2018, p. Di.

[8] **LE GAL Maëlle**, PERTENAIS Martin, LÓPEZ ARISTE Arturo, NEINER Coralie, CHAMPION Norbert, YOUNES Youssef and REESS Jean-Michel. VUV test of a new polarimeter for spectropolarimetric measurements on board space missions.. In *Advances in Optical and Mechanical Technologies for Telescopes and Instrumentation III.*,International Society for Optics and Photonics, 2018. p. 107061M.

applied optics

Simulation and optimization of a broadband reflective far ultraviolet polarimeter

Maëlle Le Gal,[1,*] Arturo López Ariste,[2] Coralie Neiner,[1] and Martin Pertenais[3]

[1]LESIA, Observatoire de Paris, Université PSL, CNRS, Sorbonne Université, Université de Paris, 5 place Jules Janssen, 92195 Meudon, France
[2]IRAP, Université de Toulouse, CNRS, CNES, UPS. 14, Av. E. Belin., 31400 Toulouse, France
[3]Deutsches Zentrum für Luft- und Raumfahrt e.V. (DLR), Institute of Optical Sensor Systems, Rutherfordstr. 2, 12489 Berlin, Germany
*Corresponding author: maelle.le-gal@obspm.fr

Received 3 July 2020; revised 14 September 2020; accepted 16 September 2020; posted 17 September 2020 (Doc. ID 397984); published 14 October 2020

Traditional transmissive polarimetric methods can be used for wavelengths above 123 nm where birefringent materials transmit light and create significant birefringence. Below 123 nm, no suitable solution is known to measure the four Stokes parameters on a large wavelength range. Therefore, we study here an innovative reflective (rather than transmissive) polarimeter working in the far ultraviolet (FUV) range from 90 to 130 nm. We take advantage of the phase shift created by reflections as well as the different reflectivities for *p* (orthogonal ⊥) and *s* (parallel ∥ to the plane of incidence) polarizations to design an FUV polarimeter. Simulation of the analyzer and modulator using Mueller matrices coupled to polarimetric efficiencies calculations allowed optimization of reflective polarimeters for the first time, to the best of our knowledge. This opens up a new perspective for FUV polarimetry below 123 nm.

https://doi.org/10.1364/AO.397984

1. INTRODUCTION

A. POLLUX for LUVOIR

For the 2020 NASA decadal survey, the large ultraviolet optical infrared surveyor (LUVOIR) [1], a 15 m diameter space telescope in its version A, is being studied. LUVOIR has the ambition to become a serviceable space telescope working from ultraviolet (UV) to infrared (IR). It is proposed to harbor four instruments, including POLLUX, a high-resolution spectropolarimeter working in the UV domain from 90 to 400 nm. POLLUX would enable the study of various topics such as galactic and stellar formation and reflected light from exoplanets or stellar magnetosphere [2]. To do so, POLLUX requires us to measure the full Stokes vector (I, Q, U, V) and to have a spectral resolution of 120,000 and a polarimetric precision of 10^{-4} at all wavelengths. To maximize instrument performance, the wavelength range of POLLUX is divided into three channels: the FUV from 90 to 124.5 nm, the mid-UV (MUV) from 118 to 200 nm, and the near UV (NUV) [3] from 200 to 400 nm. For the NUV channel, transmissive polychromatic polarimeters are being considered [4,5]. For the MUV and FUV, such solutions are either not ideal or simply impossible. Therefore, we study here reflective polychromatic polarimeters.

B. General Principles

All polarimeters, which are currently considered for POLLUX, use temporal modulation, as illustrated in Fig. 1. As traditional sensors (e.g., CCD, CMOS, MCP) are not sensitive to the polarization of light but only to its intensity, we need to record the information of the polarization state into intensities. Modulating the polarization means to encode polarization information into the measured intensities. Temporal modulation means successive intensity measurements by the detector with different amounts of polarization encoded. The successive measurements are then combined to obtain the polarization of the source. In order to achieve that modulation, the polarimeter is made of two parts: the modulator, which takes several angular positions around the optical axis and rotates the polarization between the different Stokes parameters; and the analyzer, which filters the light polarized along one linear direction. To measure all four Stokes parameters, we need at least four measurements, which means four angular positions of the modulator. However, we decided to consider not only the four required angular positions of the modulator but a few more for redundancy reasons in case we have an outlier. This also allows us to improve the final polarimetric extraction efficiency. [6]

Commonly, polarimeters use birefringent materials such as calcite or magnesium fluoride. A waveplate of birefringent material acts as the modulator, and a linear polarizer or a prism works as the analyzer. Even though magnesium fluoride can be used for

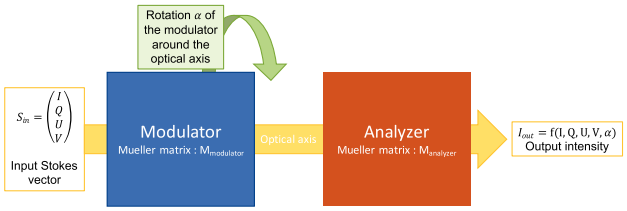

Fig. 1. General principle of a polarimeter using temporal modulation.

a waveplate almost near its transmission cutoff around 115 nm [7], its small and variable birefringence at these wavelengths makes it challenging to be used for a polychromatic polarimeter. Therefore, below ∼123 nm [4], one needs to find another way. To measure polarization as low as 90 nm, one must resort to reflection rather than the usual transmissive methods. Each reflection introduces a phase shift between p and s polarizations as well as a change in the total rate of polarization thanks to the different reflectivities. This makes it possible to use reflection for the modulator and analyzer functions. Here, we study a polarimeter made of four reflecting surfaces. Three surfaces are at a fixed position with respect to each other but free to rotate together around the optical axis; thus, they make the modulator. We choose to have three surfaces, as it is the minimum number that permits not to change the optical axis while maximizing the flux. The analyzer is made of a single reflecting surface (a dielectric crystal or a metal at a Brewster angle, which we define as the incidence angle at which the reflected beam is optimally polarized, though seldom polarized at 100% contrary to dielectrics), which polarizes the incoming light. Contrary to transmissive polarimeters, which can use dual-beam polarizers [8, 9], the use of the Brewster angle in this reflective polarimeter implies a single beam output. A scheme of this polarimeter is shown in Fig. 2. The alignment of such a device is tricky: the rotation of the modulator is likely to wobble the beam if not aligned exactly. In order to qualify for a space mission, the alignment should resist the vibration of a launch or be corrected in space. Thus, the accuracy and stability of the alignment are a major issue that will be studied later for the case of POLLUX.

C. Matrix Calculations/Mueller Calculus

In what follows, we study polarimetry using Stokes parameters and Mueller calculus. The simulation of polarimeters and the data processing involve Mueller matrices. We recall that a Mueller matrix is a 4×4 matrix that characterizes how a component, C, affects the polarization: the input Stokes vector S_{in} and the output Stokes vector S_{out} are linked by

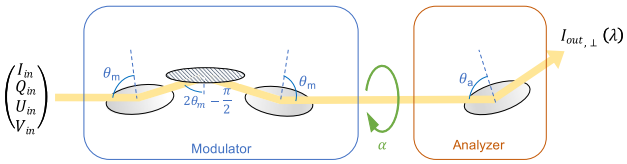

Fig. 2. Scheme of the reflective polarimeter.

$$\mathbf{S_{out}} = \begin{pmatrix} I' \\ Q' \\ U' \\ V' \end{pmatrix} = \mathbf{M_C} * \mathbf{S_{in}} = \mathbf{M_C} * \begin{pmatrix} I \\ Q \\ U \\ V \end{pmatrix}, \tag{1}$$

where $\mathbf{M_C}$ is the Mueller matrix of the optical component C. The four lines and four columns of the matrix correspond to the Stokes parameters I, Q, U, and V and show how the component changes the polarization among the four parameters. Each optical element has its own characteristic Mueller matrix. In particular, both the modulator and the analyzer are represented by such matrices. The Mueller matrix of the modulator can be computed with the Mueller matrix of each reflection as well as by using the rotation matrix, a 4×4 matrix that encodes the rotation of a component with respect to the optical axis. Mueller matrices form a group under matrix multiplication; therefore, the global Mueller matrix of the polarimeter can easily be obtained from Eq. (1) as

$$\mathbf{S_{out}} = \left(\prod_{i \in [C]} \mathbf{M_i} \right)_{\alpha} * \mathbf{S_{in}} = \mathbf{M_{polarimeter}}_{\alpha} * \mathbf{S_{in}}, \tag{2}$$

thus

$$\mathbf{M_{polarimeter}}_{\alpha} = \prod_{i \in [C]} \mathbf{M_{i\alpha}}, \tag{3}$$

where $\mathbf{M_{i\alpha}}$ is the Mueller matrix for a component in the ensemble of components $[C]$ in the system, and $\mathbf{M_{polarimeter}}_{\alpha}$ is the Mueller matrix of the whole polarimeter for the position of the modulation α. Since we measure only intensities, we are only interested in the first component of $\mathbf{S_{out}}$, which gives the total intensity measured on the detector. We define the modulation matrix $\mathbf{O}$, which is a matrix of dimensions $4 \times N$ formed by combining every first line of the polarimeter Mueller matrix for each of the N modulation angles (we shall often have $N = 6$ in the rest of this work).

This modulation matrix $\mathbf{O}$ allows us to write an equation for the measurement process:

$$\mathbf{I_{out}} = \begin{pmatrix} I'_{\alpha_1} \\ I'_{\alpha_2} \\ \vdots \\ I'_{\alpha_N} \end{pmatrix} = \mathbf{O} * \mathbf{S_{in}}, \tag{4}$$

with $\mathbf{I_{out}}$ the vector of the series of N intensity measurements made for each angle α of modulation and $\mathbf{S_{in}}$ the Stokes vector we want to measure. To retrieve the Stokes vector, we need the demodulation matrix $\mathbf{D}$, which is the pseudo-inverse of the modulation matrix $\mathbf{O}$ [10]:

$$\mathbf{D} = (\mathbf{O}^T * \mathbf{O})^{-1} * \mathbf{O}^T. \tag{5}$$

We then have

$$\mathbf{S_{in}} = \mathbf{D} * \mathbf{I_{out}} \tag{6}$$

to retrieve directly the initial Stokes vector from the N intensity measurements. The demodulation matrix also allows us to determine the efficiency of the polarimeter (see Section 4).

After fully studying the reflection in Section 2, we first simulate and optimize the analyzer independently using the contrast and figures of merit in Section 3. Using the results obtained for the analyzer, we finalize the polarimeter by optimizing the modulator according to the global polarimetric efficiency in Section 4.

2. SIMULATING A REFLECTION AS A MUELLER MATRIX

A. Mueller Matrix of a Reflection

To simulate and optimize a reflective polarimeter, we need to calculate its modulation and demodulation matrices from the Mueller matrices of the components, i.e., with Mueller matrices of a reflection. The Mueller matrix of a reflection $\mathbf{M_R}$ at an incidence angle θ and for a wavelength λ is given by [11]

$$\mathbf{M_R}(\theta,\lambda)=\begin{pmatrix} X(\theta,\lambda)^2+1 & X(\theta,\lambda)^2-1 & 0 & 0\\ X(\theta,\lambda)^2-1 & X(\theta,\lambda)^2+1 & 0 & 0\\ 0 & 0 & 2X(\theta,\lambda)\cos(\tau(\theta,\lambda)) & 2X(\theta,\lambda)\sin(\tau(\theta,\lambda))\\ 0 & 0 & -2X(\theta,\lambda)\sin(\tau(\theta,\lambda)) & 2X(\theta,\lambda)\cos(\tau(\theta,\lambda)) \end{pmatrix} \tag{7}$$

with $X^2=r_{\parallel}^2/r_{\perp}^2$ the squared ratio of Fresnel amplitude reflection coefficients and τ the difference of phase shift between p and s polarizations. To study the modulation and efficiency of the reflective polarimeter, these two parameters must be known. This matrix is obviously dependent on the angle of incidence θ and the wavelength λ but also on the material used (optical indices of the substrate, of the coating, and of its thickness).

We present below three cases, depending on the surface used to reflect (absorbing or not) and with or without a coating. We did not consider the case of multilayer coatings.

B. Phase Shift and Amplitude of a Reflection on an Absorbing Surface with a Nonabsorbing Coating

A reflection on an absorbing material creates a phase shift in addition to the polarization-dependent reflectivities. As shown in Fig. 3, we call 1 the environment of the instrument, vacuum in our case; 2 the coating; and 3 the substrate of the surface. The indices of all the parameters in this section will refer to this notation. One may notice that the calculation of the refraction angle using Snell–Descartes equations should use the complex optical index to take the absorption into account and may provide mathematical complex refraction angles [12].

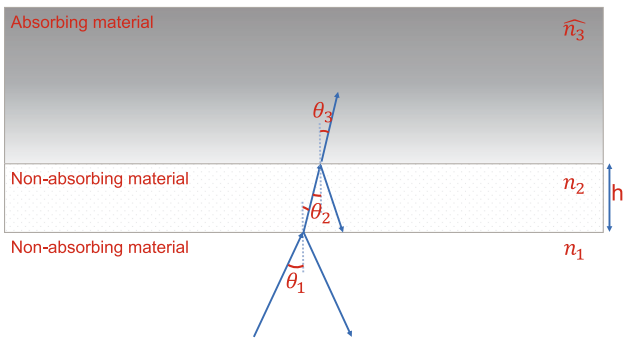

Fig. 3. Reflection on a coated absorbing surface.

The rate of reflectivities χ and the phase difference τ in this case can be directly found in [13]. Explicitly, they are calculated using the reflection coefficient r:

$$r=\frac{r_{12}+\rho_{23}e^{i(\phi_{23}+2\beta)}}{1+r_{12}\rho_{23}e^{i(\phi_{23}+2\beta)}}, \tag{8}$$

with $\beta=2\pi n_2\frac{h}{\lambda}\cos(\theta_2)$, where r_{12} is the reflection ratio at the interface between 1 and 2, and ρ_{23} and ϕ_{23} are the amplitude ratio and phase change at the interface between 2 and 3. The amplitude and phase of this reflection coefficient give the reflectivities and phases for p or s polarizations, using the appropriate expressions.

Using Born and Wolf equations [13], it is now possible to calculate χ and τ and retrieve the Mueller matrix of a reflection in the case of a coated reflecting surface.

C. Phase Shift and Amplitude of a Reflection on an Absorbing Surface Without Coating

Although a particular case of a coated surface, it is worth to recall here also the case of an uncoated substrate, which, obviously, can be computed with simpler expressions. These can also be found in [11]:

$$\chi^2=\frac{f^2+g^2-2f*\sin(\theta_1)*\tan(\theta_1)+\sin^2(\theta_1)*\tan^2(\theta_1)}{f^2+g^2+2f*\sin(\theta_1)*\tan(\theta_1)+\sin^2(\theta_1)*\tan^2(\theta_1)} \tag{9}$$

and

$$\tan(\tau)=\frac{2g*\sin(\theta_1)*\tan(\theta_1)}{\sin^2(\theta_1)*\tan^2(\theta_1)-(f^2+g^2)} \tag{10}$$

with θ_1 the angle of incidence, and where

$$f^2=\frac{1}{2}(n^2-k^2-\sin^2(\theta_1)+\sqrt{(n^2-k^2-\sin^2(\theta_1))^2+4n^2k^2} \tag{11}$$

and

$$g^2=\frac{1}{2}(k^2-n^2+\sin^2(\theta_1)+\sqrt{(n^2-k^2-\sin^2(\theta_1))^2+4n^2k^2} \tag{12}$$

help to simplify the expressions, and k is defined by $\hat{n}=n+ik$. Other terms use the same notations as in Section B.

D. Phase Shift and Amplitude of a Reflection on Nonabsorbing Material ($k=0$)

In the particular case of a nonabsorbing medium, such as crystal, where k is considered null, the expressions for reflectivities reduce to the well-known expressions. We stress that, in this case, there is no phase shift between the polarizations. Indeed, at each reflection of light coming from vacuum into the crystal, the phase shift is 0, unless the crystal is finite with width d and transparent enough so that multiple reflections occur [14]. Total reflections impose another different phase shift, used in Fresnel rhombs, but this is beyond application in our present study. Therefore, nonabsorbing media cannot be used for the modulator but can make a good polarizer.

For any given wavelength, it is indeed possible to find an angle for which the reflected beam is 100% polarized: the Brewster angle $\theta_B = \arctan(n)$. Such a Brewster angle is wavelength-dependent, which complicates its use in a broadband polarimeter if the available materials have chromatic optical indices. In addition, even if the reflection at the Brewster angle is 100% polarized, the actual reflectivity may be too small, jeopardizing the throughput of any polarimeter based upon it. This will be studied further in Section 3.

3. SIMULATING THE ANALYZER

A. Polarization Contrast and Figure of Merit

Usually, above 123 nm, beam splitters are used as transmissive analyzers, as they separate the incoming beam into two linear polarization states. This has the advantage to use all the incoming flux and to have a perfect polarizer, with two 100% polarized beams. Using a reflection is more complicated. First, this FUV analyzer only reflects one linear polarization, so we lose some flux, which is precious in the UV domain. Also, the efficiency of the polarimeter decreases, as the output beam is not 100% polarized.

Our goal is to simulate and then optimize the analyzer in order to restrict these two drawbacks, i.e., to maximize the degree of polarization, the ratio of one linear polarization with respect to its orthogonal polarization, and the transmission, i.e., to retain a sufficient signal-to-noise ratio.

Two parameters are going to help us quantify their efficiency. First, we can define a contrast as the ratio between p and s polarizations:

$$C = \left| \frac{R_s - R_p}{R_s + R_p} \right|. \tag{13}$$

The contrast can help us to determine the degree of polarization of the reflection, which is linked to the efficiency of the polarimeter. This is, however, not sufficient to characterize a good analyzer, since the reflection can be fully polarized but with an extremely low reflectivity. Thus, reflectivity should be part of our characterization. To combine both parameters, reflectivity and contrast, we introduce a figure of merit (as found in a presentation of *S*. Fineschi at the workshop *Polarimetric Techniques & Technology* in March 2014):

$$\epsilon = C * \sqrt{\max(R_s, R_p)} = \left| \frac{R_s - R_p}{R_s + R_p} \right| * \sqrt{\max(R_s, R_p)}. \tag{14}$$

The figure of merit helps us to quantify and compare analyzers according to their efficiencies and reflectivities. The square root is used on the reflectivity to minimize its variation and give a larger weight to contrast.

Now that we have a way to quantify the quality of a polarizer, we can study different solutions and compare them. The study is divided in two parts: first, the solutions, including only one material (no coating) with only one parameter to study, i.e., the incidence angle; second, the study of a coated substrate, for which there is then two parameters, i.e., the incidence angle and the thickness of the coating.

B. Uncoated Surface

For a reflection made with a material without coating, we have just one parameter: the angle of incidence. For a given material and a given wavelength, a particular angle of incidence, which optimizes polarization contrast or transmission or, ideally, both, can be computed. However, the values of the optimal angle of incidence are chromatic; at best, for a given material, we can find a compromise at the price of some trade-offs. The previously defined figure of merit in Eq. (14) will help us to define that optimal solution, but it will also be used to compare different materials. The contrast alone has also been studied to underline the benefit of the defined figure of merit.

For the spectral range of POLLUX in the FUV and MUV, we have studied the following materials: calcium fluoride (CaF_2), magnesium fluoride (MgF_2), silicon dioxide (SiO_2), gold (Au), boron carbid (B_4C), tetrahedral amorphous carbon (ta-C, a diamond-like carbon), and silicon carbide (SiC). We identified those materials in the literature, as they seem to have good reflectivity in the considered wavelength range [15–17]. The contrast as a function of incidence angle and wavelength is shown in Fig. 4. The figure of merit as a function of incidence angle and wavelength is given in Fig. 5.

Figure 4 shows that the contrast is sufficiently high for some materials such as CaF_2, MgF_2, SiO_2, Au, and ta-C to consider them. Moreover, the variation of the contrast with wavelength is acceptable in the considered wavelength range. However, in Fig. 5, one can see that, in spite of the good contrast, the reflectivity is not very high and is mostly responsible for the degradation of the efficiency of these polarizers.

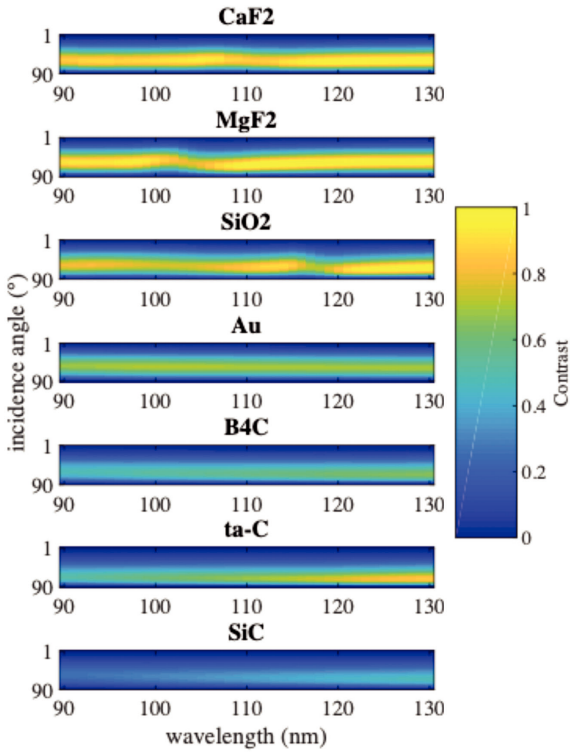

Fig. 4. Contrast after reflection on various materials as a function of wavelength and angle of incidence. At a contrast of 1, the beam after reflection is fully polarized. At a contrast of 0, the beam is not polarized.

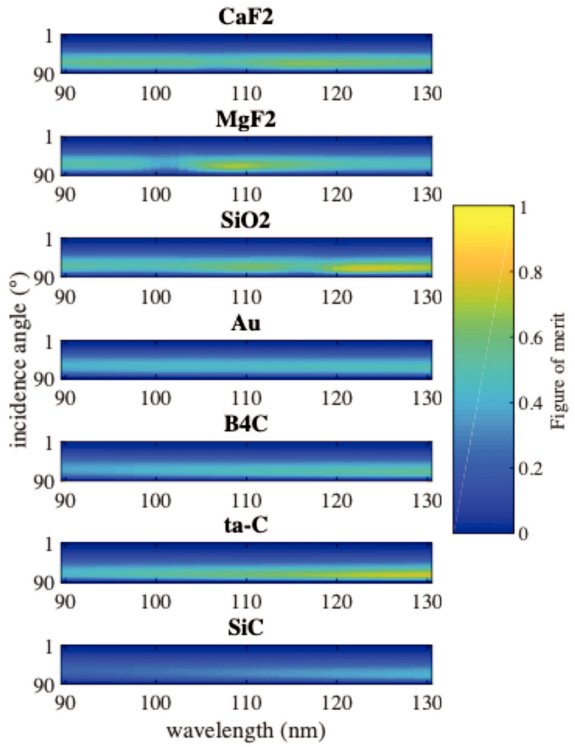

Fig. 5. Figure of merit after reflection on various materials as a function of wavelength and angle of incidence. At a figure of merit of 1, the beam after reflection is fully polarized and with no loss of flux. At a contrast of 0, the beam is not polarized and/or the flux is lost.

To compare our solutions, the mean contrast (Fig. 6) and figure of merit (Fig. 7) averaged over the considered wavelength range are plotted as a function of incidence angle. On those graphs, one can see clearly that, even though ta-C isn't the best analyzer based on contrast, reaching almost 0.7, it is the best choice when based on the figure of merit, where it hits 0.6. CaF_2 and SiO_2 seem to be good backup solutions since they have good figures of merit almost reaching 0.6. One may notice that they also have good contrast, around 0.9 for CaF_2 and 0.8 for SiO_2. The figure of merit helps us to choose ta-C reflection as

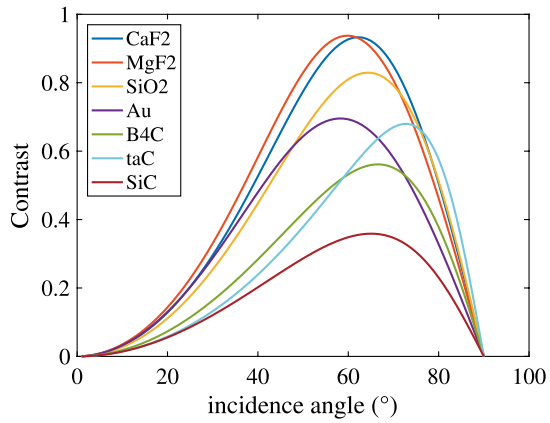

Fig. 6. Contrast of a polarizer (averaged across the spectrum) made with a reflection on various materials as a function of angle of incidence. At 1, the beam after reflection is fully polarized. At 0, the beam is not polarized.

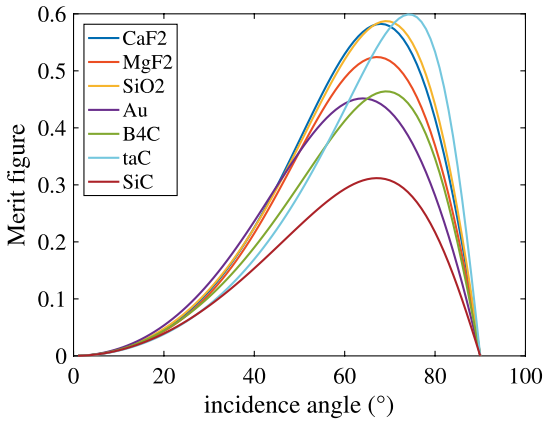

Fig. 7. Figure of merit of a polarizer (averaged across the spectrum) made with a reflection on various materials as a function of angle of incidence. At 1, the beam after reflection is fully polarized. At 0, the beam is not polarized.

the analyzer for POLLUX, as it is the best compromise between reflectivity and contrast, but this decision could be modified for a CaF_2 or a SiO_2 plate to improve the contrast and thus the efficiency of the polarimeter if the global signal-to-noise ratio obtained with POLLUX permits it. These figures show that, at maximum contrast, a tolerance of 1 deg in the incidence angle creates a loss of contrast of less than 1%.

Considering the reflectivity, we conclude that the best polarizer for the 90–130 nm wavelength domain is a plate of ta-C at 74.3° with a mean of 0.599 for the figure of merit and 0.6762 for the contrast. Nevertheless, if there were spectral lines at specific wavelengths of particular scientific interest, the choice of the polarizer could be reconsidered by adding weights to those particular wavelengths. In addition, to study particularly bright objects, a plate of CaF_2 or SiO_2 could be a better choice, as those materials improve overall efficiency, even though they decrease reflectivity.

C. Study on Coated Materials

To simulate the use of a coated material, the thickness of the coating is another parameter to consider. Thicknesses between 5 and 90 nm are considered and cover the usual values. We decided to study a reflection on aluminum coated with MgF_2 [18], as it is a well-known combination to study UV light. To analyze the two relevant parameters (incidence angle and thickness), we plot the contrast averaged over wavelength as a function of incidence angle in Fig. 8 for several thicknesses. Thicknesses were studied from 5 to 90 nm with a 1 nm step, but fewer values are displayed for clarity. A maximum contrast of 0.12 is obtained for a thickness of 32 nm, which is much lower than contrasts found for noncoated materials, which are up to 0.9. This case is therefore discarded for the analyzer of POLLUX.

Other combinations of materials for the substrate and coatings may be considered in the future, if an efficient combination appears from the current LUVOIR R&D studies.

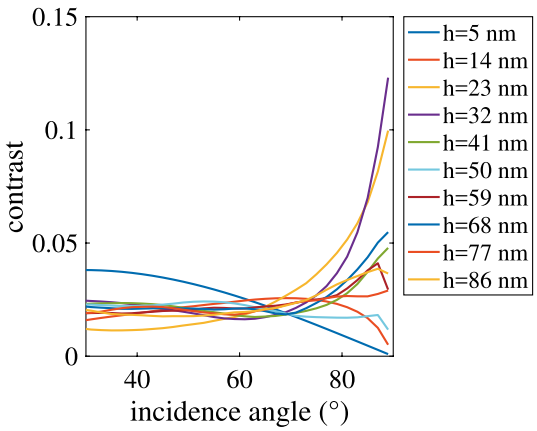

Fig. 8. Mean of contrast on wavelength of a reflective polarizer made with an aluminium mirror coated with different thicknesses (h) of MgF_2 as a function of angle of incidence. At 1, the beam after reflection is fully polarized. At 0, the beam is not polarized.

4. POLARIMETER MODULATION

A. Mueller Matrix of the Modulator

As mentioned in Subsection 1B, the modulator is formed by three reflections, so that the beam is not deviated from the optical axis, and the output beam does not move with the rotation of the modulator. The first and third reflections are then symmetrical with respect to the second one, which has its normal perpendicular to the optical axis of the instrument. The three reflections are studied as a whole and not independently, since it is the total change of phase that is of interest. To that effect, the Mueller matrix of the modulator must be computed. The studied parameter is the incidence angle θ_m on the first surface, as denoted in Fig. 2. The incidence on the other surfaces can be computed from θ_m.

The Mueller matrix of the modulator is easily built up as the product of the matrices of these three reflections. Following the notation from Fig. 2, we have $\mathbf{M_3} = \mathbf{M_R}(\theta_m, \lambda) * \mathbf{M_R}(2\theta_m - \frac{\pi}{2}, \lambda) * \mathbf{M_R}(\theta_m, \lambda)$.

The three reflecting surfaces are allowed to rotate around the optical axis, and the combined Mueller matrix is then modified by the rotation matrix of the angle of this rotation α:

$$\mathbf{R}(\alpha) = \begin{pmatrix} 1 & 0 & 0 & 0 \\ 0 & \cos(2\alpha) & \sin(2\alpha) & 0 \\ 0 & -\sin(2\alpha) & \cos(2\alpha) & 0 \\ 0 & 0 & 0 & 1 \end{pmatrix}. \tag{15}$$

The measurement of polarization with our present design consists in choosing a set of N angular positions for the modulator that differently encode polarization into intensity variations. Each one of the N measurements is differentiated by α, the rotation angle; further, the resulting Mueller matrix for the full modulator is

$$\begin{aligned} \mathbf{M_{modulator}} &= \mathbf{R}(-\alpha) * \mathbf{M_3} * \mathbf{R}(\alpha) \\ &= \mathbf{R}(-\alpha) * \mathbf{M_R}(\theta_m, \lambda) * \mathbf{M_R}\left(2\theta_m - \frac{\pi}{2}, \lambda\right) \\ &\quad * \mathbf{M_R}(\theta_m, \lambda) * \mathbf{R}(\alpha). \end{aligned} \tag{16}$$

However, as seen in previous sections, we cannot find a perfect analyzer. The solutions found for POLLUX polarizes light but not completely; in the case of ta-C, we even expect a retardance phase to appear between the reflected orthogonal polarizations. In other words, the analyzer may not just be polarizing but also transforming, rotating one polarization into another, a role that, in theory, we reserved to the modulator. Because of this, we cannot study or optimize the modulator alone. We must consider the whole polarimeter made of the rotating three-reflections modulator plus the nonperfect analyzer.

B. Optimizing the Polarimeter

To study and optimize the modulator, we must also study the analyzer, i.e., the Mueller matrix of the complete polarimeter must be studied. We can easily compute the Mueller matrix for the whole polarimeter from the modulator Mueller matrix computed in Section B. The Mueller matrix for the whole polarimeter is

$$\begin{aligned} \mathbf{M_{polarimeter}} &= \mathbf{M_{analyzer}}(\theta_a) * \mathbf{R}(-\alpha) * \mathbf{M_3} * \mathbf{R}(\alpha) \\ &= \mathbf{M_{analyzer}}(\theta_a) * \mathbf{R}(-\alpha) * \mathbf{M_R}(\theta_m, \lambda) \\ &\quad * \mathbf{M_R}\left(2\theta_m - \frac{\pi}{2}, \lambda\right) * \mathbf{M_R}(\theta_m, \lambda) * \mathbf{R}(\alpha). \end{aligned} \tag{17}$$

Choosing a set of modulation angles α and keeping only the intensity of the resulting Stokes vector for each one of those angles, we can build the modulation matrix $\mathbf{O}$, as described in Section C, which relates the incoming Stokes vector to the actual series of intensity measurements. An example of this modulation matrix is shown in Fig. 9.

To quantify the performances of the whole polarimeter and optimize it, we define, following [10], a polarimetric efficiency as

$$\epsilon_i = \left(N \sum_{j=1}^{N} \mathbf{D}_{ij}^2\right)^{-1/2} \tag{18}$$

of a given demodulation scheme made of N measurements and represented by matrix $\mathbf{D}$, the pseudo-inverse of the modulation matrix $\mathbf{O}$, for every Stokes parameter $i \in [I, Q, U, V]$. It is important to stress that the three efficiencies for Q, U, and V obey the relationship

$$\sum_{Q,U,V} \epsilon_i^2 \leq 1. \tag{19}$$

Our work in optimizing the modulator has been to pick the material, incidence angle θ_m, and set of modulation angles α, which maximize these efficiencies ϵ_i. The need for good reflectivity limits the materials available for the modulator to the same ones as those studied for the analyzer, i.e., SiC, ta-C, Al + MgF2… Crystals cannot be used for modulation because they do not introduce any phase shift between polarizations.

The incidence angle θ_m and modulation angles α have been fixed through a Marquardt–Levenberg iteration scheme with the constraint to minimize the difference between their value

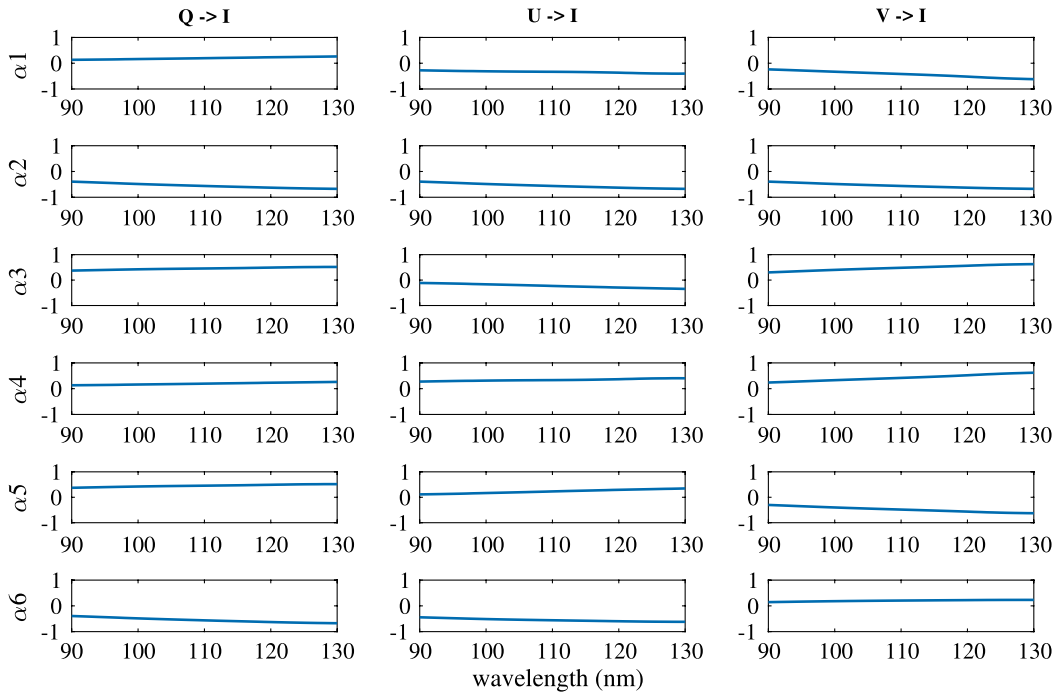

Fig. 9. Modulation matrix of a polarimeter made with one surface of B_4C and two surfaces of SiC and a ta-C analyzer.

and the maximum theoretical one. The maximum theoretical efficiency is $1/\sqrt{3}$ in our case, since we choose to measure the three Stokes parameters with identical efficiency. This can be changed to highlight a particular Stokes parameter to satisfy scientific specification. The incidence angle and modulation angles have been optimized for all combinations of materials for the three reflections, including mixing and matching different materials in order to find the best polarimeter.

The actual number of measurements N, however, has been fixed by simple comparison of the best solutions obtained in each situation. A minimum of $N = 4$ is required to retrieve the four Stokes parameters, but increasing the number of measurements will improve the signal-to-noise ratio attributed to each Stokes vector. This may improve overall efficiency. To compromise between redundancy and convenience, we chose $N = 6$ for our polarimeter.

This optimization on the materials, incidence angle, and modulation angles has converged to one efficient modulator working from 90 to 130 nm. The first reflection is in B_4C and the two others are in SiC. The incidence angle is $\theta_m = 86.8°$. The modulator takes six angular positions: 15.8°, 48.4°, 66.0°, 114.0°, 131.6°, and 164.2°. Figure 10 shows the efficiencies in the three Stokes parameters Q, U,

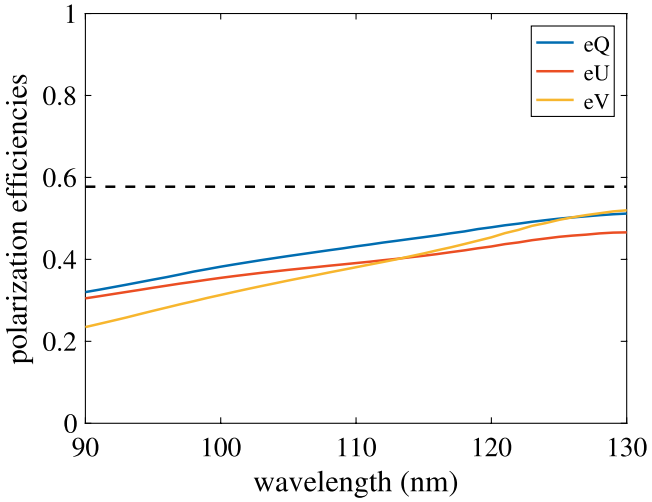

Fig. 10. Polarimetric efficiencies of a polarimeter by reflection with a B_4C and SiC modulator and a ta-C analyzer. The black dotted line is the optimal efficiency at 57.7% we try to achieve.

and V as a function of wavelength for this modulator and a ta-C analyzer. The black dotted line is the optimal efficiency to measure the three Stokes parameters with the same efficiency. The efficiencies are around 0.3 at 90 nm and increase with wavelength to obtain a satisfying result around 0.55 at 130 nm. The sensibility of the modulator is thinner than the one of the polarizer. Indeed, a change of 0.1 degree in the incidence angle on the first mirror implies a change up to 0.04 in the polarization efficiencies.

5. CONCLUSION

We have studied and optimized, for the first time to our knowledge, a new polarimeter design using only reflection on different surfaces and working in the FUV on a large spectrum. The modulator is made with three surfaces, fixed with respect to one another, and rotating as a block to create a temporal modulation of the polarization. The analyzer is the critical part of the design, as one has to make a trade-off between efficiency and reflectivity. A plate at the Brewster angle or a reflecting surface at a similar angle can play the role of the analyzer. This design has the benefit of not deviating the optical axis with the rotation of the modulator. The optimal polarimeter for the wavelength range 90–130 nm calculated for POLLUX is made of one reflection in B_4C and two reflections in SiC for the modulator. The analyzer has several options, the one maximizing the flux is a reflection in ta-C. A plate of CaF_2 or SiO_2, increasing the efficiency but decreasing the reflectivity of the polarimeter, can be used for bright sources. In the case of POLLUX, we need to maximize the flux; thus, the choice of a ta-C reflection has been made, decreasing a bit the efficiency but increasing a lot the reflectivity. To confirm those theoretical results, an experiment has been set up to measure complex optical indexes for the considered materials. This experiment should be conducted in the coming year and will be the subject of a subsequent paper.

6. DATA

For calculations, the optical indexes used to compute CaF_2, MgF_2, SiO_2, Au, B_4C, and SiC are from Palik and to compute ta-C are from Juan Larruquert.

Funding. Centre National d'Etudes Spatiales.

Acknowledgment. The authors would like to thank Juan Larruquert (CSIC, Spain) for sharing his data on optical indexes, allowing these first calculations.

Disclosures. The authors declare no conflicts of interest.

REFERENCES

1. M. R. Bolcar, S. Aloezos, V. T. Bly, C. Collins, J. Crooke, C. D. Dressing, L. Fantano, L. D. Feinberg, K. France, G. Gochar, Q. Gong, J. E. Hylan, A. Jones, I. Linares, M. Postman, L. Pueyo, A. Roberge, L. Sacks, S. Tompkins, and G. West, "The large UV/optical/infrared surveyor (LUVOIR): decadal mission concept design update," Proc. SPIE **10398**, 79–102 (2017).
2. J.-C. Bouret, C. Neiner, A. I. G. de Castro, C. Evans, B. Gaensicke, S. Shore, L. Fossati, C. Gry, S. Charlot, F. Marin, P. Noterdaeme, and J.-Y. Chaufray, "The science case for POLLUX: a high-resolution UV spectropolarimeter onboard LUVOIR," Proc. SPIE **10699**, 106993B (2018).
3. M. Le Gal, M. Pertenais, A. L. Ariste, C. Neiner, N. Champion, Y. Younes, and J.-M. Reess, "VUV test of a new polarimeter for spectropolarimetric measurements on board space missions," Proc. SPIE **10706**, 107061M (2018).
4. M. Pertenais, C. Neiner, and P. Petit, "Full-Stokes polychromatic polarimeter design for Arago," Proc. SPIE **9905**, 99052Y (2016).
5. S. Tomczyk, R. Casini, A. G. de Wijn, and P. G. Nelson, "Wavelength-diverse polarization modulators for Stokes polarimetry," Appl. Opt. **49**, 3580–3586 (2010).
6. D. S. Sabatke, M. R. Descour, E. L. Dereniak, W. C. Sweatt, S. A. Kemme, and G. S. Phipps, "Optimization of retardance for a complete Stokes polarimeter," Opt. Lett. **25**, 802–804 (2000).
7. R. Ishikawa, R. Kano, T. Bando, Y. Suematsu, S.-N. Ishikawa, M. Kubo, N. Narukage, H. Hara, S. Tsuneta, H. Watanabe, K. Ichimoto, K. Aoki, and K. Miyagawa, "Birefringence of magnesium fluoride in the vacuum ultraviolet and application to a half-waveplate," Appl. Opt. **52**, 8205–8211 (2013).
8. H. Watanabe, N. Narukage, M. Kubo, R. Ishikawa, T. Bando, R. Kano, S. Tsuneta, K. Kobayashi, K. Ichimoto, and J. Trujillo-Bueno, "Ly-alpha polarimeter design for CLASP rocket experiment," Proc. SPIE **8148**, 81480T (2011).
9. R. Ishikawa, N. Narukage, M. Kubo, S. Ishikawa, R. Kano, and S. Tsuneta, "Strategy for realizing high-precision VUV spectro-polarimeter," Sol. Phys. **289**, 4727–4747 (2014).
10. J. C. del Toro Iniesta and M. Collados, "Optimum modulation and demodulation matrices for solar polarimetry," Appl. Opt. **39**, 1637–1642 (2000).
11. C. Capitani, F. Cavallini, G. Ceppatelli, E. L. Degl'innocenti, M. L. Degl'innocenti, M. Landolfi, and A. Righini, "Polarization properties of a 'Zeiss-type' coelostat: the case of the solar tower in Arcetri," Solar Phys. **120**, 173–191 (1989).
12. S. Kovalenko, "Descartes-Snell law of refraction with absorption," Semicond. Phys. Quantum Electron. Optoelectron. **4**, 214–218 (2001).
13. M. Born and E. Wolf, *Principles of Optics: Electromagnetic Theory of Propagation, Interference and Diffraction of Light* (Elsevier, 2013).
14. M. Salatino, P. de Bernardis, and S. Masi, "Modeling transmission and reflection Mueller matrices of dielectric half-wave plates," J. Infrared Millim. Terahertz Waves **38**, 215–228 (2017).
15. J. I. Larruquert, L. V. Rodríguez-de Marcos, J. A. Méndez, P. J. Martin, and A. Bendavid, "High reflectance ta-C coatings in the extreme ultraviolet," Opt. Express **21**, 27537–27549 (2013).
16. R. Keski-Kuha, J. Larruquert, J. Gum, and C. Fleetwood, "Optical coatings and materials for ultraviolet space applications," in *Ultraviolet-Optical Space Astronomy Beyond HST* (1999), Vol. **164**, p. 406.
17. P. Zetner, A. Pradhan, W. B. Westerveld, and J. W. McConkey, "Polarization analysis techniques in the VUV," Appl. Opt. **22**, 2210–2212 (1983).
18. G. Hass and W. R. Hunter, "Reflection polarizers for the vacuum ultraviolet using Al+MgF_2 mirrors and an MgF_2 plate," Appl. Opt. **17**, 76–82 (1978).

RÉSUMÉ

Plusieurs projets de missions spatiales, tels que LUVOIR, Arago, PolStar ou CASSTOR, prévoient l'utilisation d'un spectropolarimètre fonctionnant dans le domaine de l'ultra-violet (UV). Parmi les objectifs principaux de ces instruments on trouve l'étude des étoiles et leurs environnements, en particulier leurs champs magnétiques et leurs magnétosphères, ainsi que le milieu interstellaire et les exoplanètes. Cependant, les spectropolarimètres haute résolution fonctionnant sur une large gamme spectrale n'existent que sur des instruments sur Terre et dans le domaine des longueurs d'onde visibles ou infrarouges. Le travail réalisé au cours de cette thèse vise à étudier des prototypes de polarimètres afin de les concevoir et de les optimiser sur les longueurs d'onde UV d'intérêt. Plusieurs gammes de longueurs d'onde ont été considérées, en fonction des instruments étudiés, entre 90 et 400 nm. Deux prototypes de polarimètres ont été étudiés : un prototype utilisant des matériaux biréfringents et fonctionnant par transmission et un prototype fonctionnant exclusivement par réflexion. Une méthode d'optimisation a été développée pour maximiser l'efficacité des polarimètres pour les gammes de longueurs d'onde choisies. Enfin, trois expériences ont été mises en place pour tester ces deux prototypes sur le plan optique et thermique. Deux expériences ont été conçues pour tester le polarimètre par transmission. Tout d'abord, il a été testé dans l'UV et sous vide afin de mesurer l'efficacité du prototype dans ses conditions de fonctionnement. Ensuite, des exemplaires du modulateur utilisé dans ce polarimètre ont été soumis à une série de cycles thermiques pour étudier la résistance de l'adhésion moléculaire de ses lames. Enfin, la troisième expérience permet de tester un prototype par réflexion utilisant des miroirs en or. Cette expérience permet également de mesurer les propriétés polarimétriques de certains matériaux pressentis pour de tels polarimètres par réflexion et ainsi mieux simuler les polarimètres étudiés. Les méthodes utilisées pour l'étude et la conception des polarimètres ainsi que les expériences réalisées et leurs résultats sont présentés dans cette thèse.

MOTS CLÉS

ultra-violet, polarimétrie, spectropolarimétrie, polarisation

ABSTRACT

Several space mission projects, such as LUVOIR, Arago, PolStar or CASSTOR, plan to use a spectropolarimeter operating in the ultraviolet (UV) range. The main goals of these instruments is the study of stars and their environment, in particular their magnetic fields and magnetospheres, as well as the interstellar medium and exoplanets. However, high-resolution spectropolarimeters operating over a wide spectral range only exist on instruments on Earth and in the visible or infrared wavelength ranges. The work carried out in this thesis aims at studying prototype polarimeters in order to design and optimize them over the wavelengths of interest. Several wavelength ranges were considered, depending on the studied instruments, between 90 and 400 nm. Two prototypes were studied: one using birefringent materials and operating by transmission, and one operating exclusively by reflection. An optimization method was developed to maximize the efficiency of the polarimeters for the chosen wavelength ranges. Finally, three experiments were set up to test these two prototypes optically and thermally. Two experiments were designed to test the transmission polarimeter. First, it was tested in the UV and in vacuum in order to measure the polarimetric efficiencies of the prototype under its operating conditions. Then, examples of the modulator used in this polarimeter underwent a series of thermal cycles to study the resistance of molecular bonding of its plates. Finally, the third experiment tests a prototype by reflection using gold mirrors. This experiment also allows us to measure the polarimetric properties of some materials foreseen for such polarimeters and thus better simulate the studied polarimeters. The methods used to optimize and design the polarimeters as well as the experiments carried out and their results are presented in this thesis.

KEYWORDS

ultra-violet, polarimetry, spectropolarimetry, polarization